UNIVERSITÉ DU LUXEMBOURG

PhD-FSTM-2024-077
The Faculty of Science, Technology and Medicine

DISSERTATION

Defence held on 23/10/2024 in Esch-sur-Alzette

to obtain the degree of

DOCTEUR DE L'UNIVERSITÉ DU LUXEMBOURG

EN PHYSIQUE

by

Marco António Mesquita MOREIRA

Born on 2nd June 1992 in Vila Franca de Xira (Portugal)

THE INFLUENCE OF INDUCED STRAIN ON ELECTRIC PROPERTIES OF NONSTOICHIOMETRIC COPPER CHROMIUM OXIDE

Dissertation Defence committee

Dr. Petru Lunca-Popa, dissertation supervisor
Luxembourg Institute of Science and Technology

Dr. Susanne Siebentritt, Chairwoman
Professor, University of Luxembourg

Dr. Silviu Colis, Vice Chairman
Professor, University of Strasbourg

Dr. Pedro Barquinha
Professor, NOVA School of Science and Technology (FCT-NOVA)

Dr. Vincent Rogé
Luxembourg Institute of Science and Technology

Acknowledgements

My PhD journey at the Luxembourg Institute of Science and Technology marked my first experience living abroad, far from home and family. This transition brought me many challenges, both in my research and in daily life. Adapting to a new culture and academic environment tested my resilience but also helped me grow personally and professionally. The support from my colleagues, friends, and mentors was invaluable, guiding me through these challenges and helping me succeed in my research.

I express my deepest gratitude to my PhD supervisor, Dr. Petru Lunca-Popa, for granting me the opportunity to work at LIST. His patience, vast knowledge, and invaluable guidance, combined with his good humour, were vital throughout my PhD journey. His mentorship has been instrumental in shaping my research skills and academic growth, providing the support and inspiration I needed to overcome the challenges of my doctoral studies. I am especially thankful for the time he dedicated to reviewing my articles and this manuscript, offering constructive criticism that guided me through these four years.

I am also grateful to the CET committee: Professor Susanne Siebentritt from the University of Luxembourg and Professor Silviu Colis from the University of Strasbourg, for closely following the progress of my thesis over these four years. Their insightful comments and challenging questions have broadened my research, allowing me to explore it from various perspectives.

I am thankful to STEERMOB project team members who supported me during my stay at LIST: Damien Lenoble, Jérôme Polesel, Renaud Leturcq, Jorge Iñiguez and Natalya Fedorova.

A special thanks to all the co-workers that helped me regarding the fabrication and characterisation techniques and interpretation of results, and laboratory work: Yves Fleming, Jérôme Guillot, Adrian-Marie Phillipe, Christèle Vergne, Vincent Rogé, Jonathan Crêpellière, Marc Michel, Patrick Grysan, Kevin Menguelti, Noureddine Adjeroud, Mathieu Gerard, Didier Arl, Nathalie Valle, Stéphanie Girod, Julien Jacob and Jérémy Raguin.

A special thanks to the TOT group and the line manager Emanuele Barborini for all support that provided me during the group meetings.

I cannot forget my gratitude to the office friends I met during these four years: Alfredo, Poorani, John, Longfei, Rutuja, Nikhar, Julien, Raoul, Alireza, Artenis, Aymane and Sukriti for the enjoyable moments with them at the office. In addition, a special thanks to many friends I met throughout this journey: Ashwath, Chérif, Thiago, Pablo, Kilian, Enrique, Alexander, Andreas, Marko, João, Naveen, Gustavo, Laurent, Vishnu, Victor, Olivier, Luca, Hasan, Beatriz, Pooria and Ricardo. In addition, a special thanks to the Persian gang for the enjoyable times in FoodHouse.

A very special thanks to all the Portuguese friends I encountered here in Luxembourg and helped me to integrate into both LIST and the local environment: Francisco, Marta, João Afonso, Shiv, Adriano, André Madureira, David Pêra, Ana, Ricardo, Diogo, Tânia and Hélder.

I have special gratitude for the people from LIST football group that contributed for competitive Wednesdays playing football. Additionally, I am grateful for the people from the Magic: The Gathering community in Luxembourg for the enjoying playing sessions with them.

I have a great gratitude for all my friends from Portugal that accompanied and supported me throughout this journey.

Lastly and importantly, my gratitude from my heart to my family. Without their love and support I would not be the happy and realised person I am today.

I would like to acknowledge the Luxembourg National Research Fund (FNR) for their support, as this manuscript is based on work funded by FNR under the project STEERMOB (C19/MS/13577628).

List of publications

- *A review on the p-type transparent Cu–Cr–O delafossite materials*

Marco Moreira, João Afonso, Jonathan Crêpellière, Damien Lenoble, Petru Lunca-Popa
Journal of Materials Science 57 (5), 3114-3142 (2022)

- *Electrical properties of strained off-stoichiometric Cu-Cr-O delafossite thin films*

Marco Moreira, Jonathan Crêpellière, Jérôme Polesel-Maris, Renaud Leturcq, Jerome Guillot, Yves Fleming, Petru Lunca-Popa
Journal of Physics: Condensed Matter 36 215702 (2024).

- *On the charge transport models in high intrinsic defect doped transparent and conducting type Cu-Cr-O delafossite thin films*

Jonathan Crêpellière, Marco Moreira, Petru Lunca-Popa, Renaud Leturcq, Damien Lenoble
Journal of Physics D: Applied Physics 58 015310 (2024)

Contributed talks

- *Effect of thermal induced strain on electrical properties off-stoichiometric $Cu_{2/3}Cr_{4/3}O_2$ delafossite*
  EUROCVD/Baltic ALD, May-June 2023, Leuven, Belgium.
- *Effect of thermal induced strain on electrical properties of off-stoichiometric $Cu_{2/3}Cr_{4/3}O_2$ delafossite thin films*
  FEMS EUROMAT 2023, September 2023, Frankfurt am Main, Germany.

Conference poster presentations

- *Deposition and characterisation of off-stoichiometric Cu-Cr-O thin films on flexible substrates*
  13th International Conference on Physics of Advanced Materials, September 2021, Sant Feliu de Guíxols, Spain.
  - ❖ *Ioan Ursu* Prize for the best poster presentation delivered by a young scientist.

Abstract

Transparent p-type semiconductors with optoelectronic properties comparable to those of n-type semiconductors are essential for advancing transparent electronics applications. The development of a completely transparent p-n junction remains a significant challenge due to the lack of high-performing p-type transparent (semi)conducting materials. These materials often exhibit low carrier mobilities, making them unsuitable for industrial-scale applications in modern "invisible" circuitry. Enhancing mobility is essential for improving the speed, efficiency, and overall performance of transparent electronic devices, which are increasingly relevant as technology evolves. Achieving a high figure of merit for p-type materials is regarded as the 'holy grail' for fabricating technologically relevant, fully invisible electronic devices.

One promising approach to enhance carrier mobility is strain engineering, which can significantly improve mobility by altering the band structure due to interatomic displacement. This thesis focuses on the effect of strain on the hole mobility of delafossite copper chromium oxide (CCO). Various mechanisms to induce strain were reviewed and applied, including mechanical bending, magnetostriction, thermal expansion and extrinsic doping.

We synthesised thin films using metal-organic chemical vapour deposition. Thermal strain was induced by growing CCO on substrates with different coefficients of thermal expansion. Mechanical bending resulted in minimal changes in mobility for very small strain values, as higher strains were unattainable due to substrate breakage. No changes were observed in the electrical properties of CCO grown on a magnetostrictive nickel substrate when strain was induced. For thermally induced strain, the electrical conductivity exhibited semiconductive behaviour, while the temperature-dependent Seebeck coefficient indicated energy dispersion within the polaronic states in these polycrystalline films. A distinct feature in the electrical conductivity curve emerged at the deposition temperature, indicating the shift between tensile and compressive strain regimes in the thin films. This feature is more pronounced in thinner films and nearly vanishes in thicker films due to reduced average strain. This observation suggests that strain could influence mobility, although definitive quantitative conclusions cannot yet be drawn.

This study also explored the effect of doping CCO with trivalent (Al, Mn, Sc, Y) and divalent (Mg, Zn) cations. Although doped films exhibited off-stoichiometry characterised by excess oxygen, all doped films exhibited similar room-temperature electrical conductivities. X-ray diffraction $\sin^2\Psi$ profile analysis revealed compressive strain in all doped films, but the differences were too negligible to conclude a linear variation of strain with dopant cation radii. The $\sin^2\Psi$ method also indicated compressive strain in both (006) and (012) reflections at room temperature, suggesting that the first epitaxially grown layers altered the effect of thermal strain.

The findings indicate that strain engineering in polycrystalline CCO can influence mobility, but not significantly enough to achieve the high values required for technological applications. The results confirm that the hole effective mass in polaronic materials is inherently high and challenging to manipulate. The peculiar behaviour of the Seebeck coefficient was investigated, and a method to extract accurate values of optoelectrical parameters may provide insights that could resolve ongoing debates regarding mobility values in small polaronic materials.

Abbreviations

ALD – Atomic Layer Deposition
APCVD – Atmospheric Pressure Chemical Vapour Deposition
ATM – Atmospheric Pressure
AZO – Zinc-doped Aluminium Oxide
CB – Conduction Band
CBM – Conduction Band Minimum
CCO – Copper Chromium Oxide (both on and off-stoichiometric)
Ch – Chalcogen
CL – Condenser lens
CMVB – Chemical Modulation of the Valence Band
CPS – Counts Per Second
CTE – Coefficient of thermal expansion
CVD – Chemical Vapour Deposition
DFT – Density Functional Theory
DLI – Dynamic Liquid Injection
DOS – Density of States
EDOS – Electronic Density of States
EDS – Energy-dispersive X-ray Spectroscopy
FFT – Fast Fourier Transform
FPD - Flat Panel Display
FTO – Fluorine-doped Tin Oxide
GGA – Generalised Gradient Approach/Approximation
GI – Grazing Incidence
GW – Green Functions Correlated with Coulomb Interactions
HH – Heavy Hole
HRTEM – High-Resolution Transmission Electron Microscopy
HRSTEM – High-Resolution Scanning Transmission Electron Microscopy
HSE06 – Screened Hybrid Functional Approach of Heyd, Scuseria, and Ernzerhof
ICDD – International Center for Diffraction Data
IR – Infrared
ITO – Tin-doped Indium Oxide
LED – Light-emitting Diode
LH – Light Hole
LPCVD – Low-pressure Chemical Vapour Deposition
MOCVD – Metal-organic Chemical Vapour Deposition
NNH – Nearest-neighbour Hopping
OMCVD – Organometallic Chemical Vapour Deposition
PBE + U – Generalised Gradient Approach of Perdew, Burke, and Ernzerhof Corrected for On-site Coulomb Interactions
PEDOS – Projected Electronic Density of States
PDF – Powder Diffraction File
PECVD – Plasma Enhanced Chemical Vapour Deposition

PLD – Pulsed Laser Deposition
PVD – Physical Vapour Deposition
RMS – Root Mean Square
RSF – Relative Sensitivity Factor
RTCVD – Rapid Thermal Chemical Vapour Deposition
sX-LDA – Screened Exchange Local Density Approximation
SEM – Scanning Electron Microscopy
STEM –Scanning Transmission Electron Microscopy
TACVD – Thermal Activated Chemical Vapour Deposition
TCM – Transparent Conductive Material
TCO – Transparent Conductive Oxide
TEM – Transmission Electron Microscopy
TFT – Thin Film Transistor
TSO – Transparent Semiconductive Oxide
UV – Ultraviolet
VB – Valence Band
VBM – Valence Band Maximum
VRH – Variable-range Hopping
XPS – X-ray Photoelectron Spectroscopy
XRA – X-ray Stress Analysis
XRD – X-ray Diffraction

Symbols

a – Lattice parameter along the x-axis
A – Dimensionless parameter that depends on the primary scattering mechanism
B – Magnetic field
B.E., E_b – Binding energy
c – Fraction of sites occupied by polarons, and lattice parameter along the z-axis
c_l – Average longitudinal elastic constant
d – Interplanar spacing, deflection, and thickness of the sample
D – Diffusion coefficient, average crystallite size
E – Electric field
E – Energy, and Young modulus
E_b – Average small polaron binding energy
E_B – Potential barrier height
E_C – Conduction band edge
E_d – Deformation potential of the band edge per unit dilation of the lattice
E_F – Fermi level
E_g – Optical band gap
E_g^{dir} – Direct band gap
E_g^{dir} – Indirect band gap
E_h – Activation energy for carrier hopping
E_H – First ionisation energy of the hydrogen atom
E_{kin} – Kinetic energy
E_n – Activation energy for charge carriers
E_p – Characteristic polaron binding energy
E_T – Average vibrational energy transported with a carrier as it hops
E_V – Valence band edge
E_σ – Activation energy for conduction
E_0 – Band edge energy
f – Geometric correction factor, and occupancy probabilities
f_C – Cauchy-Lorentz function
f_G – Gaussian function
F_{ii} – Screening function for ionised impurity scattering for a non-parabolic conduction band
f_{pV} – Pseudo-Voigt fitting function
g – Probability of successful hopping
g_m – Transconductance
g_n – Spin degeneracy
$g(E_F)$ – Density of states in the vicinity of the Fermi energy
h – Planck's constant
h_f – Film thickness
h_s – Substrate thickness
ħ – Reduced Planck's constant
H_{AC} – AC magnetic field
I – Current

j – Current density
J – Inter-site transfer energy, and half of the rigid-lattice bandwidth
K – Scherrer constant
k – Wavevector
k – Strain gauge factor
k_B – Boltzmann constant
l – mean free path, and length
L – Lateral grain size
m_e – Electron mass in vacuum
m* – Effective mass
m_0* – Effective mass of the electron at the conduction band edge
n – Charge carrier concentration, diffraction order, Tauc exponent, and transport dimensionality parameter
n_a – Average free carrier concentration in the grain
N – Total density of conducting sites, and number of orbital configurations
N_i – Ionised impurity concentration
N_{Cu} – Total density of copper sites in the crystal
N_v – Effective density of states per unit volume in the valence band
p – Hole concentration
P – Tunnelling probability, and pressure
P_0 – Pre-factor associated with the phonon frequency
q – Elementary charge
r – Distance between electrons and nuclei
R – Transition rate
R_H – Hall coefficient
R_S – Sheet resistance
S – Seebeck Coefficient, and global spin
T – Temperature
T_d – Deposition temperature
T_M – Mott temperature
t_d – Deposition time
U(r) – Independent motion potential of an electron
v_d – Drift velocity
V – Voltage
V_{cell} – Unit cell volume
V(r) – Interaction potential felt by an electron in the crystal
w – Width
z – Number of nearest neighbours
Z – Charge of impurities, and atomic number of nucleus
α – Polaron coupling constant, a parameter reflecting the overlap of wavefunctions, and absorption coefficient
α_f – Coefficient of thermal expansion of film
α_s – Coefficient of thermal expansion of substrate
β – Non-parabolicity parameter, and integral breadth of Bragg peak
Γ –Parameter related to the strength of charge-lattice coupling

ΔE_d – Activation energy required to raise an electron from the donor level to the bottom of the conduction band
$\Delta Ev_{v,i}$ – Change in energy of heavy holes and light holes branches under the strain
ΔL – Change in length
ΔH – Energy formation enthalpy
ΔT – Temperature gradient
ΔV – Potential difference
ε – Strain
ε_∞ – Dielectric constant at high frequency
ε_s – Static dielectric constant
ε_0 – Permittivity in vacuum
ε_{th} – Thermal strain
$\tilde{\varepsilon}$ – Microstrain
η – Profile shape factor, and reduced Fermi energy
θ – Bragg angle
λ – Wavelength, and magnetostriction coefficient
λ_S – Saturation magnetostriction coefficient
μ – Electrical mobility
ν – Poisson's ratio
ν_0 – Hopping frequency
ξ – Carrier localisation length, and strain components
ξ_0 – Reduced scattering length
ξ_1 – Non-parabolicity parameter of the conduction band
ρ – Electrical resistivity
σ – Electrical conductivity and stress
σ_{avg} – Average stress
σ_{ext} – External stress
σ_i – Intrinsic stress
σ_0 – Pre-exponential factor
σ_{res} – Residual stress
σ_{th} – Thermal stress
σ_{tot} – Total stress
τ – Free scattering time
ϕ – Work function
ω_p – Plasmon frequency
ω_0 – Angular phonon frequency
Ω – Number of microstates available to the system

Table of Contents

List of Figures

List of Tables

General introduction

In the 21st century, society has become increasingly reliant on electronic technologies. One field that has seen remarkable advancements is transparent electronics. At the heart of this domain lie thin films, which have permeated nearly every aspect of our daily lives. This widespread adoption of transparent electronics has had a profound impact on modern society. For instance, transparent displays have transformed the way we consume information, allowing for the creation of sleek, unobtrusive interfaces that blend seamlessly into our surroundings. Additionally, transparent electronics have also played a crucial role in advancing renewable energy technologies, such as solar panels and energy-harvesting windows, which are poised to revolutionise the way we generate and consume power. As a result, transparent electronics have become an integral part of our modern infrastructure, shaping the way we live, work, and interact with the world around us.

The development of materials for transparent electronic devices relies on achieving both high visible transparency and high electrical conductivity (σ). These fundamental properties of materials appear contradictory from the from the traditional band-structure perspective. Typically, transparent materials possess wide band gaps of at least 3.0 eV, preventing visible photons from exciting electrons from the valence band (VB) to the conduction band (CB) and thus allowing the transmission of visible light. However, by virtue of their band gap, they are usually insulators and difficult to dope. Conversely, semiconductors exhibit low activation energy for charge carriers to participate in band conduction, but this is often at the cost of having a narrow band gap (less than 2 eV) [1]. Transparent conductive materials (TCM) represent a unique category that combines these desirable properties. These materials can be either n-type or p-type, depending on the predominant charge carriers (electrons or holes) and exhibit with high carrier concentrations (n) up to the order of 10^{21} cm^{-3}, along with band gaps exceeding 3 eV. This combination of properties enables TCMs to maintain high electrical conductivity while allowing visible light to pass through, making them essential for a variety of applications in transparent electronic devices.

Most industry-standard TCMs, such as Sn-doped In_2O_3 (ITO) [2], Al-doped ZnO (AZO) [3], and F-doped SnO_2 (FTO) [4], are oxides with n-type conductivity and belong to the subcategory of transparent conductive oxides (TCOs). Among these, ITO is the most important n-type TCM in the market, standing out with an electrical conductivity up to 10^3 S/cm and transparency exceeding 80% in the visible range [2], [5]. For applications involving active devices, such as thin-film transistors (TFTs), charge carriers are controlled; thus, TCOs in this context are usually referred to as transparent semiconductive oxides (TSOs), as their key properties may lie within the limited to non-conductive regime [6]. The primary applications of these materials in the market include their use as transparent electrodes for flat panel displays (FPDs) and photovoltaic cells, as well as active layers in TFTs, ultraviolet (UV) light-emitting diodes (LEDs), gas sensors, and other transparent electronic devices.

All these applications rely exclusively on n-type TCMs, as the performance of investigated p-type TCMs has not matched the advancements of their n-type counterparts. Despite decades of research, challenges remain in identifying a reliable p-type TCM. Since the report of the first p-type TCO, nickel oxide (NiO) [7], numerous materials have been investigated as potential p-type TCMs for industrial applications. However, to date, they have failed to fully meet the required optoelectronic characteristics for large-scale applications, often due to inadequate electrical properties or insufficient optical transparency in the visible range.

Obtaining a p-type TCM exhibiting properties on par with their n-type counterpart for high-scale production is a challenging task, mainly due to intrinsic limitations such as the localisation of VB holes and difficulties in introducing holes through p-type doping while minimising compensating defects. The scientific community has focused on strategies to improve p-type mobility. Low mobility in p-type TCMs is primarily due to several factors, including the localised nature of the VB holes, which hinders their ability to move freely. Additionally, introducing sufficient p-type doping while avoiding compensating defects is difficult, as these defects can trap charge carriers and further reduce mobility. Furthermore, the structural and electronic properties of many p-type materials inherently limit the ease with which charge carriers can traverse the material, resulting in lower overall mobility compared to n-type materials [8]. Low mobility in TCMs restricts the speed at which charges can move through the material, limiting the performance of electronic devices. Increasing mobility can be achieved through material engineering, such as optimising crystallinity and reducing defects, or by exploring alternative materials with inherently higher mobilities, such as organic semiconductors or novel hybrid materials. These approaches are crucial for achieving high-performance transparent electronics capable of competing with traditional opaque counterparts.

In 1997 the theory of “chemical modulation of valence band” (CMVB) was proposed for designing p-type TCMs to optimise the mobility and was implemented in p-type delafossite copper aluminate ($CuAlO_2$) [9]. This theoretical advancement significantly boosted research into a wide array of materials as potential high figure-of-merit p-type TCMs for large-scale applications, including other materials with delafossite structures. Among these, copper chromium oxide delafossite was intensively studied due to its superior properties [10]. Off-stoichiometric Cu-Cr-O, in particular, has garnered attention due to its enhanced electrical conductivity and improved transparency. The slight deviation from stoichiometry can introduce defects that act as acceptors, thereby increasing the hole concentration and improving p-type conductivity. These properties make off-stoichiometric Cu-Cr-O a promising candidate for advanced transparent electronic applications.

One of the strategies to improve the electrical mobility is by engineering the strain to alter the band valence edge dispersion. This approach has been proven successful for the optimisation of the active channels of metal-oxide-semiconductor field-effect transistors (MOSFETs). More recently, the advent of flexible electronics has boosted the research into the properties of thin films with induced strain [11], [12].

Fabricating a high figure of merit p-type TCM would transform transparent electronics by making possible applications that cannot be achieved with n-type TCMs alone. These applications include transparent p-n heterojunctions, which are the fundamental block of active devices [13]–[15], and complementary transistors [16]–[18]. This advancement would pave the way for a new range of fully transparent devices, such as smart windows [9],[19]–[21], transparent UV LEDs [22], [23], solar cell heterojunctions [24], [25], gas sensors [26]–[29], and electromagnetic shielding [30].

Objectives and outline of work

The goal of this work is to understand how the electronic mobility is affected by the induced strain on off-stoichiometric delafossite copper chromium oxide ($Cu_{1-x}Cr_{1+x}O_2$) thin films. Strain was induced by various methods and the influence on delafossite thin films was investigated.

Chapter 1 begins with a general description of p-type TCMs reported in literature. Next, a general description of delafossite materials is given, with an emphasis on their physical and functional properties. It then narrows down to Cu-based delafossites, considered one of the most promising p-TCM candidate. The chapter ends with the state of the art of delafossite copper chromium oxide, the material of interest for this work.

Chapter 2 examines on charge carrier transport mechanisms semiconductors, with a particular focus on those reported on delafossite structure. It begins by introducing fundamental concepts, including conductivity, carrier concentration doping, and the degeneracy in semiconductors, highlighting their impact on mobility. Both band conduction and hopping mechanism are thoroughly discussed, with an emphasis on their roles in determining mobility. The chapter also explores the effects of strain on critical parameters such as effective mass and band structure. Finally, it concludes with an analysis of the Seebeck effect in semiconductors, paying special attention to the Emin-Wood formalism, which is characteristic of semiconductors exhibiting semi-metallic behaviour.

Chapter 3 is consecrated to the deposition and characterisation techniques of delafossite thin films used in this work. The first section details the dynamic liquid injection metal-organic chemical vapour deposition technique used in this thesis for the synthesis of copper chromium delafossite thin films. The second section describes the characterisation techniques assessed for the investigation of the chemical composition, morphology, optical and structural properties of delafossite thin films. The next section discusses the electrical measurements methods engaged during the work. The last section is dedicated to the description of the methods to induce and measure the strain in thin films.

Chapter 4 presents a detailed characterisation of delafossite thin films, examining their morphology, chemical composition, and structural properties, specifically for undoped films. Special attention is given to the stability of these films through investigations involving thermal treatments.

Chapter 5 provides an in-depth analysis of the experimental data on delafossite films under strain. It begins with a discussion of the results on the impact of strain induced by magnetostriction and mechanical bending, placing these findings in a broader scientific context. This is followed by an exploration of strain effects due to extrinsic doping, achieved through the incorporation of various elements. Next, studies on thermally induced strain are presented, using substrates with different thermal expansion coefficients. Electrical measurements are then analysed to determine the effects of strain on electrical properties. The chapter concludes with an in-depth discussion of the films' electrical properties, using the interpretive framework of the Emin-Wood model for a detailed evaluation of the Seebeck coefficient in semi-metallic materials.

Chapter 6 concludes by summarising the results obtained throughout this work and discusses the quest of finding a p-type TCM with properties matching their n-type counterpart. It suggests new candidate materials and strategies to improve the actual ones.

Chapter 1 – p-type transparent conductive materials: fundamentals and state of the art

This chapter begins with a comprehensive overview of p-type Transparent Conducting Materials (TCMs) to date. It starts by categorising the main types of p-type oxide and non-oxide TCMs and discussing their primary limitations. The chapter then narrows its focus to the family of chalcogenide semiconductors, which includes the material under study in this work, copper chromium oxide. The focus is on the significance of chemically modulating the valence band to design the band structure of p-type TCMs. The chapter concludes with a comprehensive overview of the functional properties of the delafossites family and summarises the current state of knowledge on copper chromium oxide delafossite.

1.1. P-type transparent conductive materials

Transparent semiconductors can be divided into the material classes as depicted in Figure 1, depending on the periodic table group containing their respective anions. Mixed anion compounds are composed by at least two chalcogens or one chalcogen and one halide (e.g. AgBiISeO, BaCuSF and CuSCN).

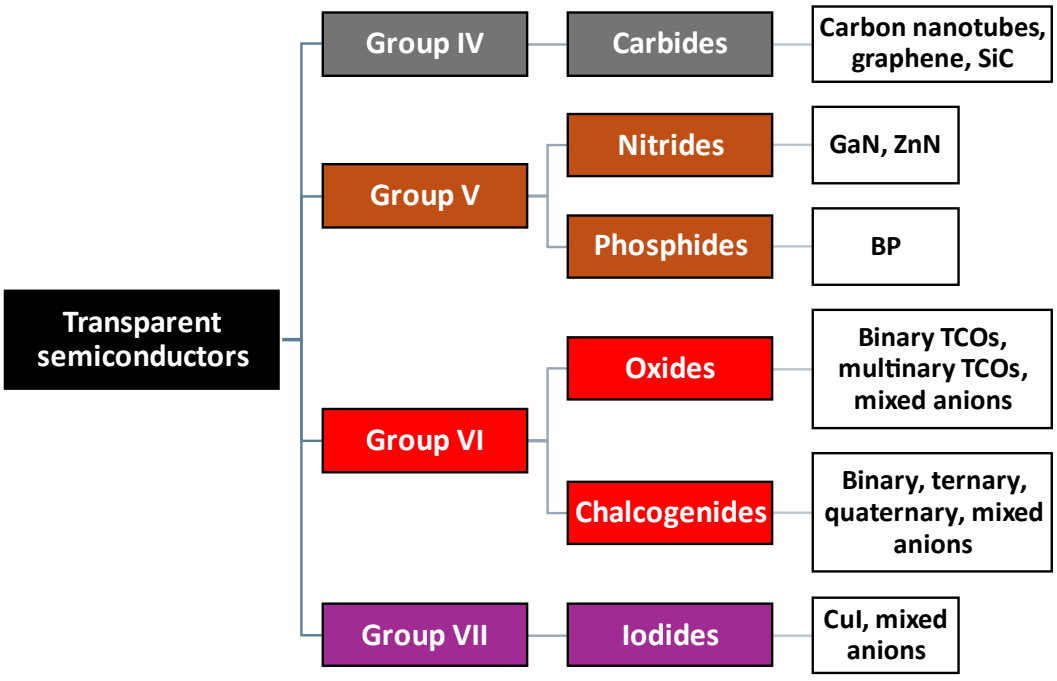

Figure 1 – Schematic network diagram of wide band gap semiconductor's categories. They are categorised according to the periodic table group of the compound's anions. Adapted from [8] and revised.

A panoply of materials has been identified by high-throughput computational screening as potential candidates as p-type TCMs with low effective mass, based on the delocalisation of the VB, combined with a favourable defect formation for doping. Materials featuring mixed-anion chemistry and non-oxide compositions have emerged as promising candidates for next-generation p-type

TCMs [31]. Non-oxides have limitations such as experimental difficulty of safely and controllably source elements for thin film deposition, avoiding formation of secondary phases, and ensuring air stability to avoid the formation of competing oxide phases [31].

1.1.1. Non-oxide p-type transparent semiconductors

Non-oxide p-type transparent semiconductors have received considerable attention in recent years for their potential to address the limitations of traditional oxide-based transparent conducting materials. Most of these non-oxide TCMs were proposed through high-throughput ab initio calculations. They can be categorised as follows:

- Carbides (Group IV): Graphene, carbon nanotubes, SiC
- Nitrides and phosphides (Group V): GaN, ZnN, BP
- Non-oxide chalcogenides (Group VI): binary (MCh): ZnS, ZnSe, ZnTe, CdS, SnS_2, In_2S_3, Cu_2S; ternary (M_1M_2Ch): $CsZn_3Se_4$, $CsZn_3Te_4$, $CuAlS_2$, $CuAlSe_2$, $CuAlTe_2$, $CuGaS_2$, $AgAlS_2$, $AgAlSe_2$, $AgAlTe_2$, $AgGaS_2$, α-$BaCu_2S_2$, Cu_3TaS_4; 2D chalcogenides (MoS_2)
- Halides (VII): CuI
- Mixed anions (Groups VI/VII): BaCuSF, BaCuSeF, CuSCN

1.1.2. Oxide p-type transparent semiconductors

All p-type TCOs belong to groups VI and/or VII. Since the first report of a semi-transparent p-type oxide, NiO [7], numerous materials have been proposed and investigated as potential p-type TCOs for novel materials design. Compared to non-oxides, p-type TCOs are distinguished by their high negative formation enthalpy, wide band gaps and chemical stability [6]. They can be categorised as follows:

- Chalcogenides: binary oxides (Cu_2O [32],[33], ZnO [34]–[36] B_6O [37], In_2O_3 [38], NiO [7], [39]–[41] SnO/SnO_x [42]–[45] and β-Ga_2O_3 [46]–[48]); delafossites ($CuAlO_2$, $CuScO_2$, $CuCrO_2$, $CuFeO_2$, $CuGaO_2$, $CuInO_2$, $CuYO_2$) [9], [49]–[57]; chromium based oxides ($LaCrO_3$ [58], Cr_2O_3 [59],[60] and CuSrO [61]); spinel-based oxides ($NiCo_2O_4$ [62],[63], $ZnCo_2O_4$ [64],[65] $ZnIr_2O_4$ [64] and $ZnRh_2O_4$ [64], [66], [67])
- Mixed anions: mixed oxides (In_2O-Ag_2O [68],[69]); oxychalcogenides (LaCuOS [70]–[73], LaCuOSe [74] and (Cu_2S_2)($Sr_3Sc_2O_5$) [75], SnSeO [76]
- Others, notably Ba_2BiTaO_6 [77] and $SrCu_2O_2$ [78]–[80]

Similar to non-oxide TCMs, these materials, from a broad perspective, have not completely met the criteria for a high figure of merit p-type TCO: they typically exhibit either low mobilities or low transparency, both of which are essential for advancing novel applications in optoelectronics. A fully functional transparent p-n junction, the fundamental block of active devices, requires a p-type TCM matching the high figure of merit n-type TCMs already available. The actual n-type semiconductors used at technological level shows electrical mobility of the carriers around 100 $cm^2 V^{-1}s^{-1}$), electrical conductivities of 10^3 S/cm and visible transparencies beyond above 80% [2], [5].

1.1.3. Chalcogenides

Chalcogenide-based transparent semiconductors are notable for their ability to be p-type doped, high mobility, and high valence band (VB) positions. They typically include at least one chalcogen (Ch) anion (oxygen[1], sulphur, selenium, tellurium) and at least one metallic cation.

There are several differences between non-oxide and oxide chalcogenides. Moving down group XVI (O 2p, S 3p, Se 4p, Te 5p), the chalcogenides demonstrate higher mobilities due to the stronger hybridisation of their p orbitals with s,d metallic cation orbitals, forming more disperse, delocalised VBM than oxides (O 2p), leading to lower hole effective mass. Moreover, chalcogenides show greater propensity for p-type doping compared to oxides due to their valence levels being closer to the vacuum, resulting in lower ionisation energy. Additionally, M-O bonds in chalcogenides are stronger than other M-Ch bonds, facilitating synthesis.

However, chalcogenides are more susceptible to degradation and instability in air and aqueous environments compared to oxides. Additionally, they have narrower band gaps compared to oxide TCOs, which correlates with the electronegativity of the chalcogen anion.

Oxychalcogenides, compounds mixing oxygen with another chalcogen, have also been investigated. O 2p orbitals at the VBM hybridise with more dispersed 3p orbitals from the chalcogenide, enhancing hole conductivity while maintaining the transparency imparted by oxides. For example, Mg-doped LaCuOSe exhibits high p-type conductivity (910 S cm^{-1}), yet lacks sufficient transparency (Eg < 2.8 eV) and electrical mobility (3.5 cm^2 V^{-1} s^{-1}) [74].

Chemical modulation of the valence band

The concept of Chemical Modulation of the Valence Band (CMVB), proposed by Kawazoe et al. in 1997, serves as a design framework for developing p-type TCMs [9]. CMVB aims to enhance valence band delocalisation through the hybridisation of nd^{10} metal cations and chalcogen p orbitals. This approach seeks to create a dispersed VBM and a shallow ionisation potential, essential for effective p-type doping without self-compensation, resulting in lower effective hole masses and higher carrier mobility. CMVB follows three main criteria to optimise the VBM of p-type TCOs while maintaining optical transparency [81]:

- **Selection of Cations**: Cations with closed nd-orbitals and energy levels similar to anion p-orbitals are chosen to foster hybridisation in the valence band, forming covalent bonds. This hybridisation produces a more dispersive VBM that rises above the non-bonding anion 2p level or metallic cation nd states, thereby enhancing hole delocalisation and increasing carrier mobility (Figure 2). Moreover, the closed electronic shells nd^{10} prevent colouration due to d-d excitations.
- **Linear Coordination**: These cations are arranged in a linear coordination with the anions, ensuring chalcogen ligands remain at a distance due to strong repulsion between the 2p electrons on the nd^{10} cations and anion ligands.
- **Tetrahedral Coordination**: Structures with anions in tetrahedral coordination are selected, which minimises the non-bonding character of the metal-anion bonds. In this arrangement, all eight electrons around the anions are in σ, sp^3 hybrid orbitals, which reduces the localisation of the VBM edge.

[1] when the chalcogen is oxygen, the compounds are called oxides.

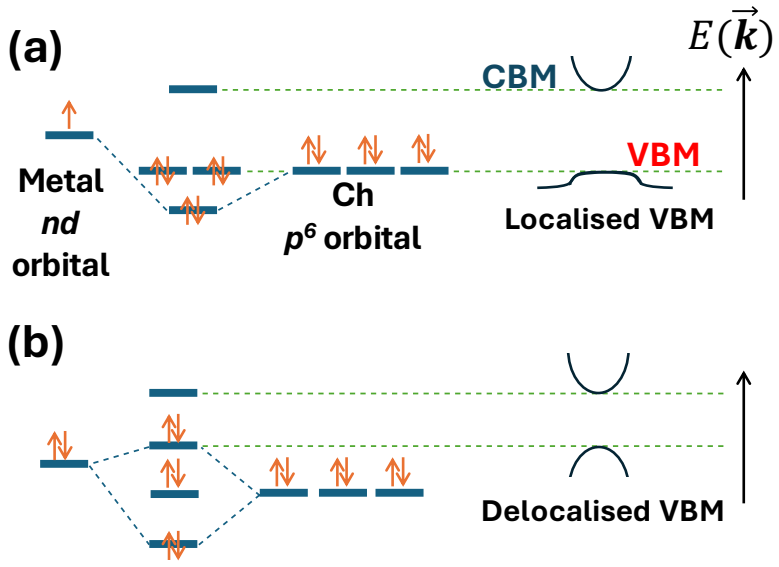

Figure 2 – (a) Localised and (b) delocalised due to covalent bonds between nd metallic cations and oxygen (chalcogen). Adapted from [82].

The group explored and implemented these criteria by fabricating a stable p-type undoped copper aluminate ($CuAlO_2$) with delafossite structure. At the time they obtained considerable electrical conductivity and optical band gap (E_g) for a p-type TCM candidate (σ = 1 S cm^{-1} and E_g = 3.5 eV). Although the results were promising, the electrical conductivity was still too low for large-scale p-type TCM applications. The design concept of Kawazoe work fuelled the hope that invisible circuits might be feasible and sparked the research on several p-type transparent conducting oxides, and also device fabrications using them [15], [83].

1.1.4. Delafossite materials

Among p-type semiconducting materials, those possessing a delafossite structure have been extensively studied for their exceptional properties and wide-ranging applications. The origins of materials with this structure trace back to Charles Friedel's identification of $CuFeO_2$ in 1873, named in tribute to the French mineralogist and crystallographer Gabriel Delafosse [84]. However, it took more than a century for these materials to attain scientific prominence, when in 1997 p-type conductivity and transparency in delafossite $CuAlO_2$ were demonstrated experimentally by applying the CMVB principles [9]. Subsequently, p-type TCOs with this structure underwent thorough investigation due to their promising electrical conductivity, reasonable optical transparency and stability. In absence of intentional doping, their p-type[2] conduction is attributed to acceptor defects, but the high formation energies of the defects and the large transition/activation energy lead to poor electrical conductivity [85],[86].

[2] Delafossite $CuInO_2$ [153] was reported to have either p- or n-type conductivity, due to its favourable band edge positions.

Structure and composition

Delafossite compounds are ternary oxides characterised by a layered AMO_2 structure[3], where A and M represent monovalent and trivalent cations, respectively. The A cations exhibit linear coordination with two oxygen atoms, while the M cations have octahedral coordination with six oxygen atoms. The oxygen atoms are tetrahedrally coordinated, forming pseudo-tetrahedral structures with one A and three M cations, as M_3AO. The delafossite structure consists of two alternating layers: one layer of slightly distorted, edge-shared MO_6 octahedra and another layer of tightly packed A cations arranged in a triangular pattern, which forms the conduction path for charge carriers. The two-fold coordination of A-O induces a dumbbell-shaped structure O-A-O parallel to the c-axis, connecting adjacent MO_6 octahedra. Additionally, each oxygen atom from the dumbbell is coordinated to three M cations, arranged such that the MO_6 octahedra form MO_2 layers parallel to the ab plane. The MO_6 and A layers can form two different polytypes depending on the stacking sequence along the c-axis [86]–[90]:

- The 3R rhombohedral structure (space group symmetry R-3m, No. 166) consists of duplicated three-layer stacks arranged in an "ABCABC" sequence (Figure 3a,c). The A layers are oriented in the same direction relative to each other but are offset from each other in a three-layer sequence. Its unit cell contains 12 atoms (3 A cations, 3 M cations, and 6 oxygens), equivalent to 3 formula units.
- The 2H hexagonal structure (space group symmetry P63/mmc, No. 194) consists of duplicated two-layer stacks with alternating A layers oriented 180° relative to each other, arranged in an "ABAB" sequence (Figure 3b,d). Its unit cell contains 8 atoms (2 A cations, 2 M cations, and 4 oxygens), equivalent to 2 formula units.

Palladium and platinum-based delafossites, $CuAlO_2$, $CuGaO_2$, $CuInO_2$ and $CuCrO_2$ crystallise in 3R, whereas delafossites with unoccupied 3d levels (M = Sc, Y, La) are more stable with 2H polytype. This layered structure leads to highly anisotropic physical properties. Hence, delafossites represent natural nanolaminates offering a wide array of design possibilities, determined by the selection of monovalent and trivalent cations [91]–[95].

Lattice parameters in delafossites

The dimensions of both cations contribute significantly to the lattice parameters of delafossites. Specifically, the A cation exerts a notable influence on the c-axis parameter due to the dumbbell-shaped O-A-O bond length being aligned parallel to the c-axis. The A cations have small size – the interatomic distance between these cations ranges between 2.8 and 3.0 Å for most compounds – favouring a linear coordination. On the other hand, the M cations have larger size and oxidation state +III, leading to a stronger M-M repulsion compared the smaller A cations with +I oxidation state. This results in an increase of the M-O distance, increasing the a-axis parameter, whereas the O-O distance is barely altered. Therefore, the M cations have negligible influence on the c-axis lattice parameter [92].

[3] Non-oxide chalcogenides with the structure $AMCh_2$ (such as copper aluminium sulphide $CuAlS_2$) have similar stoichiometry but crystallise as a chalcopyrite and not as a delafossite.

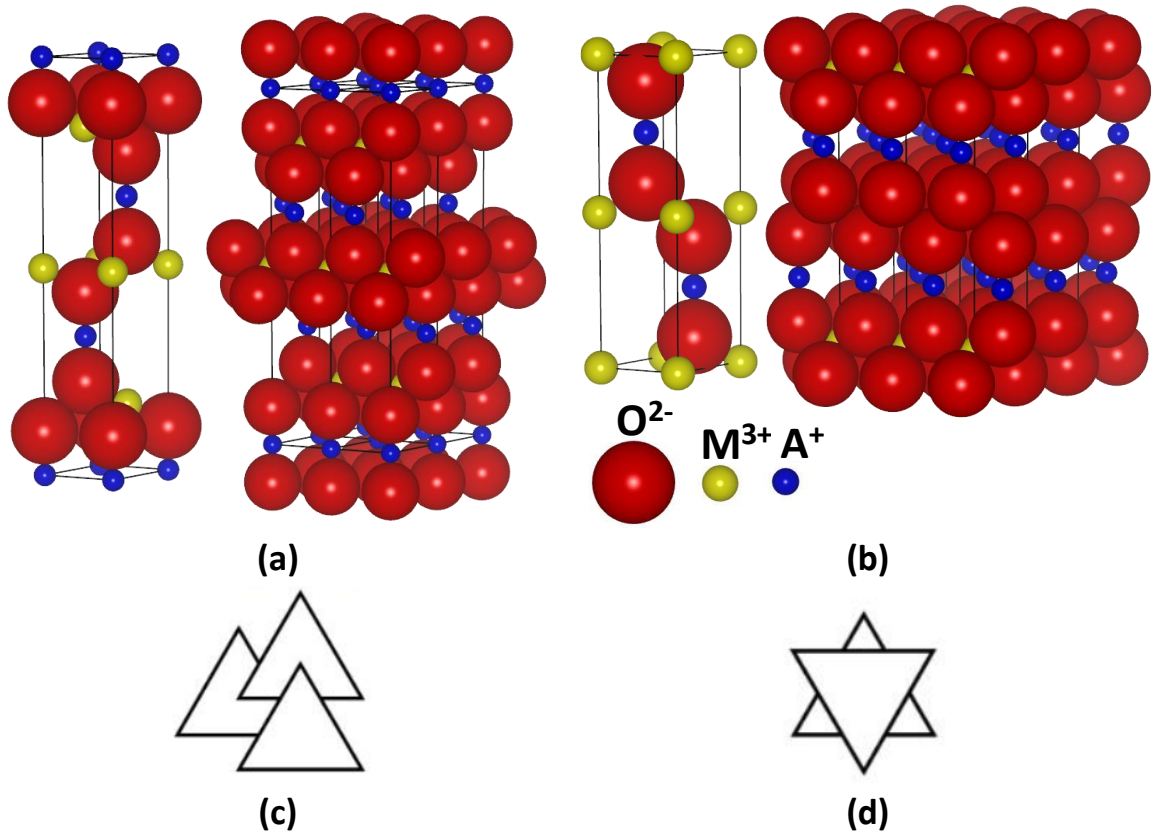

Figure 3 – Unit cells and 2 x 2x1 stacks for delafossite structure. (a) Rhombohedral α-3R polymorph (R-3m); (b) Hexagonal α-2H polymorph ($P6_3/mmc$). In R-3m the layers stack in ABCABC (c), whereas in 2H they stack in ABAB sequence (d). Adapted from [96].

Monovalent cations in delafossites

Figure 4 depicts the structure field map of AMO_2 oxides in ambient conditions, including the ones that crystallise in delafossite phase. It shows that the delafossite structure is stable only when the A site is a cation with small size – noble metals from group X or XI (Pd, Pt, Ag and Cu). Delafossites can be classified into two groups based on the electronic configuration of these cations:

- nd^9 ions from group X: Pd^+ and Pt^+ [93], [97]–[100]
- nd^{10} ions from group XI: Cu^+ and Ag^+ [95], [101], [102]

Depending on these cations, delafossites can exhibit behaviours ranging from insulating to metallic. Figure 5 depicts the reported highest electrical conductivities of selected delafossites. The values vary widely, spanning approximately eight orders of magnitude, and are heavily influenced by both the A and M cations. It is clearly remarkable that the A cation plays a crucial role in the conductivity [103]–[106].

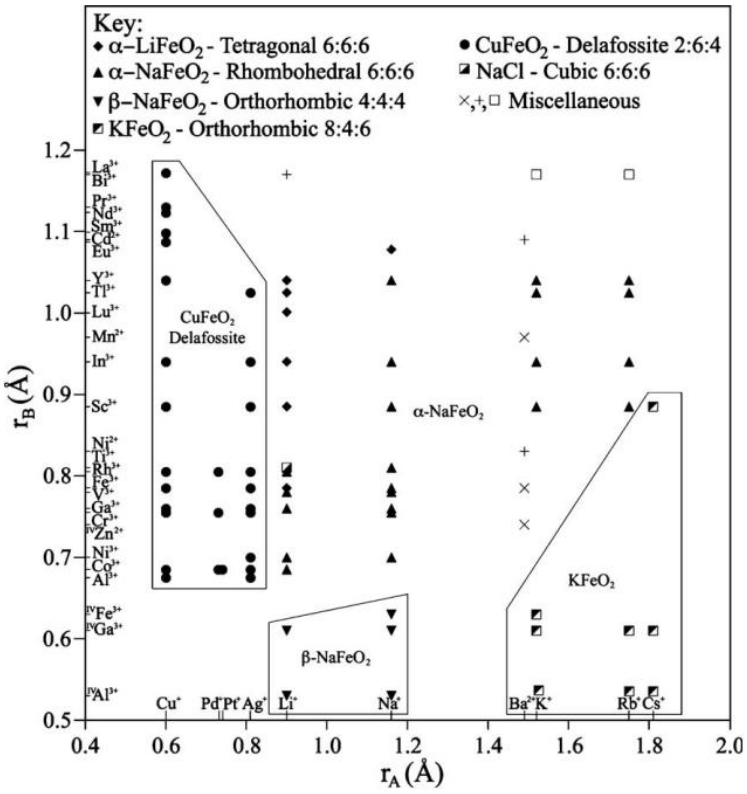

Figure 4 – Structure field map of AMO_2 oxides. r_B and r_A correspond to the cations' radius of trivalent and monovalent cations, respectively. Adapted from [92].

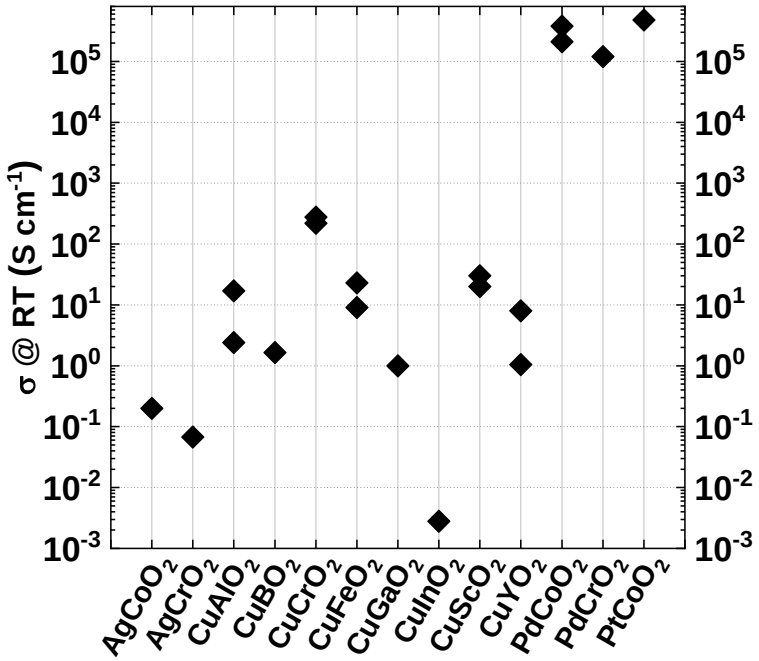

Figure 5 – Values of highest reported electrical conductivities at room temperature, for various non-doped and doped delafossite materials. Adapted from [107].

Palladium and platinum-based delafossites

Figure 5 shows that Pd and Pt-based delafossites comprise the ones with highest reported electrical conductivities (> 10^5 S cm^{-1}). This phenomenon arises from an unconventional oxidation state stabilised by a metal-metal bonding within these delafossites. They show high reflectivity (optical metallic behaviour), although ultrathin films have reasonably low sheet resistance (even at critical thicknesses) and high transmittance (particularly in the near infrared (IR) region), making these delafossites as potential candidates for application as transparent electrodes. Moreover, the high cost and scarcity of Pd and Pt impede their widespread use in semiconductor applications [54]–[57], [98], [102].

Silver and copper-based delafossites

When A = Ag or Cu, the delafossites typically present semiconducting or insulating behaviour and reasonable optical transparency. They satisfy all the required criteria outlined by the CMVB approach to achieve high-performing p-type TCOs [108]–[110]:

- The A cations have a closed electronic d-shell (Cu $3d^{10}$ and Ag $4d^{10}$), which are free from visible colouration arising from a d-d transition;
- The Cu $3d^{10}$ and Ag $4d^{10}$ energy levels are proximate to the O $2p^6$ level, fostering covalent bonding between these levels and leading to a significant dispersion in the valence band or a reduction in the localisation of positive holes;
- The oxygen ions are in tetrahedral coordination.

Ag-based delafossites are expected to exhibit wider band gaps and reduced visible-light absorption due to the lower energy position of the VBM influenced by the Ag $4d^{10}$ states. However, synthesising these materials in open systems has proven difficult due to the low free energy of formation of Ag_2O (2.6 kcal mol^{-1}) [111], which decomposes into metallic silver and oxygen at 300°C before any reaction occurs [53], [101], [104]. Consequently, the most effective deposition methods to date involve closed-system or low-temperature techniques. These include ion-exchange methods such as hydrothermal synthesis in sealed autoclaves [111], [112], metathetical cation exchange [113], and oxidising flux [114], rather than conventional solid-state reactions [51].

The binding interactions of O 2p orbitals with holes are strong, with the Ag $4d^{10}$ orbitals playing a minimal role in the VB. The low electrical conductivity stems from exceptionally low carrier mobility due to the unfavourable energy alignment between O p and Ag $4d^{10}$ levels [115]. Consequently, Ag-based delafossites have been reported with low electrical conductivities [10], [52], [112]. Nagarajan et al. reported doped and non-doped Ag-based delafossites in powder form with very low conductivities (10^{-6}-10^{-4} S cm^{-1}) [102]. Wei et al. [53] reported a facile chemical solution synthesis under open conditions (spin-coating and annealing) of 12% Mg-doped $AgCrO_2$, achieving a conductivity of approximately $7x10^{-3}$ S cm^{-1}.

Finally, following the experimental results of CMVB on $CuAlO_2$, a multitude of Cu-based delafossites with different trivalent cations but similar properties were discovered [9]. Doped and undoped Cu-based delafossites have renewed interest in optoelectronic technology due to the potential fabrication of all-oxide transparent active devices [116]. In this regard, they have been extensively reported as potential candidates as high-conductive transparent p-type semiconductor. Figure 6 shows that, with the exception of $CuInO_2$, Cu-based delafossites exhibit enhanced

conductivity attributed to the alignment of Cu $3d^{10}$ energy levels with O 2p, resulting in a more dispersed VBM and consequently a lower effective mass.

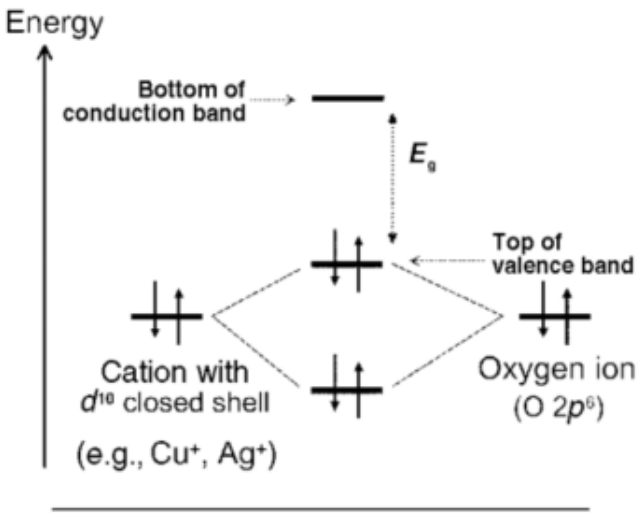

Figure 6 – Hybridisation of cations with Cu $3d^{10}$ with O 2p energy levels in Cu based delafossites. Adapted from [9].

Trivalent cations in Cu-based delafossites

The delafossite structure features octahedral coordination for the M cation site, which can accommodate trivalent M cations with ionic radii ranging from 0.5 to over 1.0 Å [92]. This flexibility enables the tuning of properties in delafossites. Consequently, these materials have been extensively investigated due to their intriguing properties in various fields: antibacterial [117], [118], electrical [119], [120], luminescent [121]–[124] magnetic [125]–[131], ferroelectric [132], optoelectronic [133], [88], superconducting [134], [135], and thermoelectric properties [126], [136], [137], as well as for sensors [138], supercapacitors [139],[140], (photo)catalysis [136], [141]–[144] and batteries [145].

The M trivalent cation is generally an element from the p-block, a transition metal or a lanthanide [92], [146]. Numerous publications reported this structure hosting a multitude of M cations, namely:

- p-block: Al [9], [80], [109], [147], B [148]–[150], Ga [51], [80], [91], [152], [153] and In [153]–[156].
- Transition metals: Co [139], [157], [158], Cr [49], [159], [160], Fe [161]–[163], Mn [140],[164], Rh [165], Sc [166]–[169] and Y [102], [121], [167], [170], [171].
- Lanthanides: La [94], [121], [122], [172], Nd [173], Pr [174], Sm [174] and Eu [175].

Table 1 includes these cations' radii in coordination six [176]. The optoelectronic properties of Cu-based delafossites can be engineered depending on the size of the trivalent cation. Firstly, the Cu-Cu basal planes make up the path for conducting holes, giving anisotropic conductivity [126]. As the radii of M cation decreases, The M-M repulsion is decreased and the lattice parameter a as well. Therefore, the Cu-Cu distance decreases accordingly [177]. This in turn increases the overlap of Cu $3d^{10}$ orbitals, improving the hole mobility. For this reason $CuBO_2$ is the reported undoped delafossite

with highest conductivity (1.65 S cm^{-1}), as the B ionic radii is the smallest among the trivalent cations in delafossites [150].

Secondly, when the trivalent cations have larger ionic radii (e.g., Sc and Y), the delafossite structure becomes more amenable to extrinsic doping and oxygen intercalation along the Cu triangular planes. The expanded lattice can accommodate more excess oxygen, leading to tail states within the band gap and reducing transmittance [1], [51], [167]. Conversely, for smaller M cations, the compact lattice makes oxygen intercalation difficult, hindering oxygen penetration. The oxygen conditions and annealing process during film deposition also significantly influence this phenomenon [170]. For smaller cations (such as Fe), forced oxygen intercalation generates structural shear and defects [178]. Beyond a certain level of oxidation, the structure transforms into CuO and spinel oxide phases (CuM_2O_2) [1].

Table 1 - Trivalent cations' radii in coordination VI [176].

p-block	$r(M^{3+})$ (Å)	Transition metals	$r(M^{3+})$ (Å)	Lanthanides	$r(M^{3+})$ (Å)
B	0.270	Cr	0.615	Pr	0.990
Al	0.535	Mn	0.645	Nd	0.983
Ga	0.620	Fe	0.645	Sm	0.958
In	0.800	Rh	0.665	Eu	0.947
		Co	0.685	La	1.032
		Sc	0.745		
		Y	0.900		

Ultimately, the mixing of the M d orbital with O 2p orbitals diminishes the binding effect on Cu atoms surrounding the Cu vacancy (V_{Cu}). By enhancing this covalent bond, the delocalisation of Cu atom around V_{Cu} is reinforced as well, increasing the hole density [179]. Among the reported M cations in delafossites, Cr has the strongest covalent bonding interaction with oxygen, which explains the better conductivities reported on $CuCrO_2$ than other Cu-based delafossites. It is worth mentioning here that the Cu-O distance is confined within a very narrow range (1.83 ± 0.02 Å) regardless the size and nature of the M^{3+} cation [121].

1.2. Delafossite copper chromium oxide

Among the wide range of delafossites, $CuCrO_2$ and its out-of-stoichiometry derivatives are considered the most promising one to achieve the desired optoelectronic properties of a p-type TCO, mainly due to its foremost trade-off between optical and electrical properties. Figure 5 shows that, apart from metallic delafossites, $CuCrO_2$ is the only one reported to surpass an electrical conductivity above 100 S cm^{-1}. As mentioned earlier, within Cu-based delafossites, chromium stands out as the trivalent cation with the most pronounced covalent bonding interaction with oxygen. As a result, the $CuCrO_2$ structure benefits from advantageous covalent mixing between Cr 3d and O 2p states, leading to improved hole mobility, a high density of Cr 3d states near the valence band maximum (VBM), and a wide band gap [180], Furthermore, its optoelectrical properties are highly tuneable, allowing for easy substitution with aliovalent and/or isovalent cations at the Cr site due to its moderate ionic radius [86], [160], [180]–[184] It also features a low synthesis temperature and favourable thermal stability in air, remaining the most stable delafossite when heated in air up to at least 1000 °C [185].

Currently, the highest reported electrical conductivity for delafossite materials is 278 S cm^{-1} for Mg-N co-doped $CuCrO_2$ produced via solid-state reaction, with a transmittance of 69% over the visible spectrum [49], and 220 S cm^{-1} for Mg-doped $CuCrO_2$ deposited by sputtering, with approximately 30% transmittance [159]. Despite these advancements, the conductivity remains an order of magnitude lower than that of state-of-the-art n-type TCOs.

1.2.1. Crystalline structure

Spatial representation and lattice parameters

Similar to other delafossite structures, in $CuCrO_2$ the CrO_6 and Cu layers can exist in both 3R (R-3m) and 2H ($P6_3/mmc$) polytypes, as documented in the International Center for Diffraction Data (ICDD) powder diffraction files (PDF 04–010-3330 and PDF 04–010-3329, respectively). The transition between these phases typically occurs during crystallisation at elevated temperatures, with the 3R phase demonstrating greater stability and higher electrical conductivity compared to the 2H phase [10],[92],[186]. The primitive rhombohedral unit cell of $CuCrO_2$ consists of four atoms: one copper, one chromium, and two oxygen atoms [187], [188]. Despite this, the hexagonal cell is often employed to describe rhombohedral structures due to its conventional usage in crystallography [132]. Among Cu-based delafossites, $CuCrO_2$ is characterised by relatively compact a and c axes. Nonetheless, variations in lattice parameters arise from different deposition or computational methods, resulting in a significant range of reported values. Table 2 summarises the lattice parameters and unit cell volumes obtained from various experimental and theoretical studies.

Table 2 - Reported values in the literature for the lattice parameters and unit cell volume of $CuCrO_2$. Data adapted from [82] and revised accordingly.

a (Å)	c (Å)	V (Å³)	System	Exp./Theory	Reference
2.962	17.01	129.24	3R	Experimental	[189]
2.97	17.24	-	3R	Experimental	[190]
2.9748(1)	17.1016(5)	131.06	3R	Experimental	[136]
2.975	17.10	-	3R	Experimental	[191]
2.970	11.40	87.09	2H	Experimental	[192]
2.9734(3)	17.100(4)	130.9	3R	Theoretical	[188]
3.050	17.09	-	3R	Theoretical	[191]
2.9740(3)	11.400(1)	87.32	2H	Theoretical	[187]
3.01-3.05	11.40-10.47	89.73-92.25	2H	Theoretical	[180]

The computed bond lengths for Cu-O and Cr-O are 1.881 Å and 1.972 Å, respectively, aligning well with the values derived from Shannon's atomic radii ($^{II}O^{2-}$ = 1.38 Å, $^{II}Cu^{+}$ = 0.46 Å, $^{VI}Cr^{3+}$ = 0.615 Å [176]). Notably, significant deviations from these values have been reported in doped films.

Band structure

Theoretical analyses of the band structure of $CuCrO_2$ have employed several methodologies. Common approaches include Density Functional Theory (DFT) with a screened exchange local density approximation (sX-LDA) [193], the Heyd-Scuseria-Ernzerhof hybrid functional (HSE06) [180], the Generalized Gradient Approximation (GGA) with Perdew, Burke, and Ernzerhof correction for on-site Coulomb interactions (PBE + U) [180], the LDA+U method [184], and many-body perturbation theory using Green functions with Coulomb interactions (GW approximation) [194]. These approaches generally predict a direct band gap (E_g^{dir}) ranging from 2 to 4 eV and an indirect band gap (E_g^{ind}) between 1 and 3 eV. A summary of these results is shown in Table 3.

Table 3 - Calculated direct and indirect band gaps for $CuCrO_2$ using various theoretical methods.

Method	E_g^{dir} (eV)	E_g^{ind} (eV)	Ref.
sX-LDA	3.10	2.90	[193]
HSE06	-	3.09	[180]
GGA	1.97	1.12	[193]
GGA	-	2.14	[195]
GGA+U	2.55	2.04	[160]
PBE	-	1.06	[180]
PBE	1.83	1.07	[196]
PBE	1.30	0.96	[194]
PBE+U	-	2.06	[180]
PBE+U	2.39	1.71	[196]
PBE+U	1.72	1.67	[197]
GW	3.42	3.29	[194]
GW	3.42	3.42	[198]

The variation in predicted values arises from the differing assumptions and specifics of each theoretical method. For instance, the PBE method tends to overestimate lattice parameters and underestimate self-interaction, while HSE06 provides more accurate structural and band gap data compared to LDA/GGA [180]. Nonetheless, these models primarily address bulk materials with ideal crystalline structures, whereas deposited films often exhibit random defects that are challenging to model accurately.

The nature of the band gap in $CuCrO_2$ remains debated. Some experimental studies indicate an indirect band gap [199], while others report direct band gaps, both within the range of 2.95 to 3.30 eV, which correlates with the material's optical transparency.

Density of states

Analysis of the total electronic density of states (EDOS) for the delafossite $CuCrO_2$ reveals several distinct features (Figure 7). The electronic states below -4 eV are predominantly composed of broad, intense O 2p states. These are succeeded by narrower, yet still significant, Cu 3d nonbonding states centred around -2 eV. The Cu 3d states in this range are energetically degenerated with the weakly dispersive nonbonding O 2p states observed at the same energy level. The interaction between bonding Cu 3d and O 2p states results in the formation of a mixed Cu-O state that is positioned above the less dispersed background at the VBM.

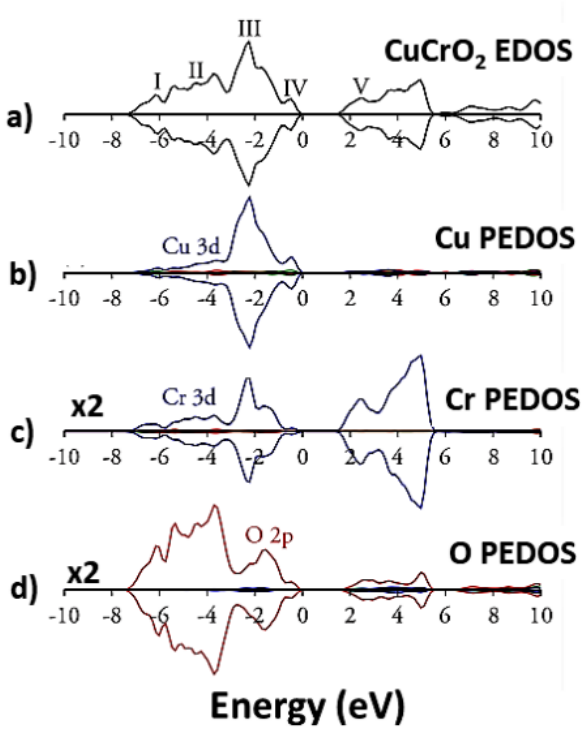

Figure 7 - EDOS for $CuCrO_2$. (a) Overall EDOS; (b) EDOS projected onto Cu (Cu-PEDOS); (c) EDOS projected onto Cr (Cr-PEDOS), with magnification of 2x; (d) EDOS projected onto O (O-PEDOS), with magnification of 2x. In the plots, d states are depicted by blue lines, s states by green lines, and p states by red lines. Adapted from [180].

This characteristic has been corroborated by experimental data from X-ray resonant photoemission and X-ray absorption spectroscopy studies conducted by Yokobori [184] and Arnold

[160]. Their investigations, which focused on Mg-doped $CuCrO_2$, revealed the simultaneous presence of copper in both +1 and +2 oxidation states. Additionally, Cr 3d states primarily contribute to the conduction band minimum (CBM), with some minor contribution to the VBM arising from hybridized Cr-O bonds formed between three Cr ions and one O ion [86].

1.2.2. Electrical conductivity and sources of charge carriers

In undoped, stoichiometric $CuCrO_2$, intrinsic point defects are typically the primary source of hole carriers, yet the material exhibits low electrical conductivity. This is attributed to the low concentration of acceptor defects and their high energy levels [131], [200].

Reported conductivity values vary based on the synthesis method used. For instance, Poienar et al. [201] observed a conductivity of $3x10^{-4}$ S cm^{-1} in a single crystal produced via the flux technique. Yu et al. [202] measured a conductivity of 0.2 S cm^{-1} in films prepared by radio frequency sputtering, while Sadik et al. [203] reported a significantly lower value of $1x10^{-4}$ S cm^{-1} for films grown by pulsed laser deposition (PLD). It is widely acknowledged that pure $CuCrO_2$ has low conductivity, whereas non-stoichiometric or doped delafossites can achieve better electrical performance. Notably, the highest conductivity reported is 278 S cm^{-1} for a Mg and N co-doped delafossite [49], and 100 S cm^{-1} for a non-stoichiometric variant [190].

TCMs can be modified either through extrinsic or intrinsic doping. Extrinsic doping involves the incorporation of aliovalent or isovalent ions, whereas intrinsic doping involves altering the electronic properties through the introduction of native defects. In the case of $CuCrO_2$, several defects can enhance conductivity based on the processing conditions and type of dopants used. These include copper vacancies (V_{Cu}), interstitial oxygen atoms (O_i''), and dopants substituting at the chromium site (X_{Cr}). These modifications can be achieved either during the initial synthesis or through post-synthesis processes such as rapid thermal annealing or ion implantation [8].

Extrinsic doping

The primary function of dopants is to enhance carrier concentration while maintaining the integrity of the delafossite structure [49]. Typically, doping is more straightforward when the size difference between the dopant and the substituted cation, as well as the M cations, is minimal. However, Marquadt et al. elucidated that the difference in electronegativity between the M cation and the dopant plays a more significant role in stabilising the delafossite structure than the size of the cations [92]. It is noteworthy that extrinsic doping does not invariably enhance electrical conductivity due to the limited solubility of certain dopant cations within the delafossite structure, a limitation likely attributed to non-stoichiometric constraints.

The valence state of dopant cations significantly impacts the electrical properties of delafossites. Notably, several studies have reported substantial enhancements in electrical conductivity upon the incorporation of divalent cations at the Cr site. This enhancement is attributed to an increase in hole concentration due to the charge discrepancy at the substitutional site, involving Cu^+/Cu^{2+} [126], [204] and/or Cr^{3+}/Cr^{4+} [136] hole mechanisms, thereby enhancing the conductivity. It is generally accepted that hole conduction in delafossites predominantly occurs via the Cu^+/Cu^{2+} hole mechanisms [126], [130], [136], [147], [180]. Additionally, internal stress might play a role on divalent cations' effect on delafossite: for instance, the lattices parameters of $CuCrO_2$ increase with the doping of Mg, as it allocates on the octahedral site, replacing Cr^{3+} which has a

smaller ionic radius (0.720 Å and 0.615 Å, respectively) [205]. Note that aliovalent dopants can lead to formation of compensation ionic defects or defect associates [92].

Doping with a trivalent cation X^{3+} (isovalent doping) results in a compound that exhibits properties of both $CuCrO_2$ and $CuXO_2$ [92]. The carrier concentration remains constant due to the identical oxidation states of the cations; however, notable changes in electrical properties are often observed [134], [206]. These changes can be attributed to the difference in ionic radii between the dopant and the substituted atom. The resulting internal stress can alter the band structure, thereby affecting electronic charge mobility. This phenomenon has been demonstrated in polycrystalline films of Ge [207], Si [208] or graphene [209].

Table 4 provides a summary of studies on extrinsic doping of $CuCrO_2$ delafossite. Commonly reported $CuCrO_2$ dopants are Cd, Co, Fe, Mg, Mn, N, Ni, Sc, Sn and Zn. Among these, Mg has demonstrated the most significant improvement in the electrical properties of delafossite [51], [205], [210]. There is an extensive list of reported dopants in $CuCrO_2$

Table 4 – Summary of various extrinsic dopants for copper chromium delafossite and their reported effects. Adapted from [107].

Dopant	Doped-$CuCrO_2$ reported characteristics	Ref.
Al	Destabilise Cr^{3+} antiferromagnetic order, inducing weak ferromagnetism. Substitutional randomness reduces conductivity.	[125], [127]
Fe	Enhances electrical and optical properties slightly. Fe induces hole-mediated Fe^{3+}-Cr^{3+} super-exchange coupling, leading to room-temperature ferromagnetism. Fe doping does not directly create holes, but alters the delafossite structure, increasing interstitial oxygen in the lattice. Superconductivity in Fe-doped $CuCrO_2$ has been reported up to 118 K.	[134], [211], [212]
Mg	Mg-doped $CuCrO_2$ exhibits enhanced conductivity compared to other p-type TCOs. Mg^{2+} substitutes at the Cr^{3+} site, converting Cu^{+} to Cu^{2+}, and this substitution reduces both resistivity and the Seebeck coefficient. However, if Mg^{2+} occupies a Cu^{+} site instead of a Cr^{3+} site, it may act as a donor rather than an acceptor.	[211], [213]–[215]
Mg + Ag	The dopants are not localised at grain boundaries. Mg^{2+} substitutes Cr^{3+}, and Ag^{+} substitutes Cu^{+}, increasing the electrical conductivity up to 560 times.	[216]
Mg + Mn	Incorporation of Mg^{2+} generates mixed valence states Mn^{3+} and Mn^{4+}, facilitating a hole-mediated double-exchange mechanism between Mn^{3+}-Cr^{3+} and Mn^{3+}-Mn^{4+}, resulting in a noteworthy diluted magnetic semiconductor.	[217]
Mg + Ni	Enhance thermoelectric properties.	[137]
Mg + S	Sulphur incorporation enhances mobility values.	[218]
Mg + N	Despite being undetectable in films, the best optoelectronic properties are observed when N_2 is present during deposition. Nitrogen acts as an acceptor, increasing hole carriers in the delafossite lattice as follows: $$N \rightarrow N_O^- + h^+$$	[49], [219]
Mn	The material shows a ferromagnetic transition. Conductivity improves slightly with Mn content up to 10%.	[220], [221]
Ni	An increased electrical conductivity was observed with Ni^{2+} doping in $CuCr_{1-x}Ni_xO_2$ for $0 \leq x \leq 0.6$.	[222],[223]
Rh	There is good matching in oxidation states and ionic radii, and weak ferromagnetism is induced at low temperatures.	[224]
Sc	Local lattice distortions disrupt the residual magnetic degeneracy.	[206],[225]
Sc + Mg	Incorporation of Sc and Mg into the delafossite structure introduces microstrain with anisotropic characteristics. The substitution of (Sc, Mg) creates additional space for oxygen intercalation.	[206]
Sn	The emergence of mixed Cr^{3+}/Sn^{4+} states impacts the thermoelectric properties, resulting in decreased electrical conductivity.	[226]
Ti	A dilution of spin is observed, with corresponding magnetic properties reported.	[227]
Zn	The delafossite phase remains stable with up to 3% Zn content, and electrical conductivity improves as Zn concentration increases.	[228],[229]

Intrinsic doping

Defect chemistry significantly impacts the p-type conductivity of delafossites. In non-stoichiometric delafossites, metal deficiency or excess oxygen are common introduced defects that alter stoichiometry and introduce holes within the material to enhance conductivity. However, the formation energies of cation vacancies and excess (interstitial) oxygen anions are relatively high. Consequently, they are counterbalanced by native compensating defects, such as anion vacancies [76]. Adjusting the preparation conditions can control the stoichiometry of the material [116], [230]. Copper vacancies act as hole donors and introduce shallow acceptor states according to [180], [234]:

$$V_{Cu} \longrightarrow h^{+} \quad \textbf{(1)}$$

Excess oxygen atoms might be substituted in the lattice sites (Cu and Cr sites) and produce holes or intercalate within the crystal structure to form $CuCrO_{2+\delta}$ phases. This process traps electrons and leaves behind empty states in the valence band, which act as holes, according to [116]:

$$O_2(g) \longrightarrow 2O_i'' + 4\,h^{+} \quad \textbf{(2)}$$

This defect behaviour is more pronounced for larger M cations, because a bigger lattice would accommodate more excess of oxygen [232]. Conversely, smaller M cations with radii less than 0.7 Å shrink the lattice, hindering oxygen penetration [170]. Consequently, the structure cannot accommodate oxygen intercalation without distortion, as the M octahedron defines the cell edge [178]. Additionally, the extent of oxygen intercalation is influenced by the oxygen environment and annealing conditions during film deposition. Under oxidising conditions, oxygen intercalates into the Cu triangular layers. At elevated temperatures, the lattice expands to accommodate oxygen intercalation, but this can sometimes lead to the formation of spinel and copper oxide phases [96]. Oxygen intercalation introduces tail states into the band gap, reducing optical transmittance.

Off-stoichiometric copper chromium delafossite

Off-stoichiometric delafossite materials are characterised by a significant excess or deficit of copper, chromium, and/or oxygen [120], [190], [233], [234]. Despite these deviations from the ideal 1:1:2 stoichiometry, structural analysis using techniques such as X-ray diffraction (XRD), Raman spectroscopy, X-ray photoelectron spectroscopy (XPS) confirm that the delafossite structure remains intact. For instance, Ling et al. [235] fabricated Cr deficient $CuCr_{1-x}O_2$ films ($0 < x < 0.1$) via solid-state reactions, achieving a minimum resistivity of 2 kΩ cm for $CuCr_{0.92}O_2$. This behaviour, similar to Mg-doped $CuCrO_2$, is attributed to an increased carrier concentration resulting from excess holes created by chromium deficiency, where each missing Cr atom might introduce three holes.

Subsequent research using Chemical Vapor Deposition (CVD) techniques revealed the synthesis of Cu-Cr-O delafossite layers with significant copper deficiencies. Farrell et al. [233] first reported such a material exhibiting a 20% copper deficit, synthesised via spray pyrolysis with acetylacetonate precursors for copper and chromium in methanol. These 90 nm thin films demonstrated an electrical conductivity of 12 S cm^{-1} and an optical transmittance of 55%.

Additionally, the same group fabricated $Cu_{0.4}CrO_2$ films with notable optoelectronic properties [244]. Raman, XPS, and XRD analyses confirmed the delafossite structure, although an increased number of Cr-O octahedra were observed compared to crystalline $CuCrO_2$. Furthermore, off-stoichiometric copper chromium delafossite films exhibiting both copper deficiency and chromium excess ($Cu_{1-x}Cr_{1+x}O_2$) were synthesized using dynamic liquid injection metal-organic chemical vapour deposition (DLI-MOCVD) [236],[82]. These films have a unique 2/3:4/3:2 stoichiometry, with one-third of the copper atoms missing and an additional one-third of chromium atoms present. These films currently show the highest conductivity values (102 S cm^{-1} [190]) for a non-intentionally doped copper chromium delafossite.

The doping mechanisms in these off-stoichiometric delafossite materials cannot be solely attributed to point defects, and ongoing research aims to elucidate the charge sources and transport mechanisms. Recently, chains of copper vacancies were identified and investigated as potential doping sources [190]. Using positron annihilation spectroscopy on $Cu_{2/3}Cr_{4/3}O_2$ samples, Lunca-Popa et al. [237] linked the reduction in conductivity to a decrease in the size of these vacancy chains. They proposed that a ripening mechanism occurs, where the dissolution of copper vacancy chains during annealing leads to decreased electrical conductivity. This hypothesis is supported by theoretical work from Art and Zunger [238], [239], which suggests that in transparent conductors, the formation of such defects is thermodynamically favoured as it incurs no energy cost.

Despite significant differences between extrinsically doped $CuCrO_2$ and highly conductive $Cu_{2/3}Cr_{4/3}O_2$, their electric properties show notable similarities. For instance, in Mg-doped $CuCrO_2$, Okuda et al. [126] observed different temperature dependencies of the Seebeck coefficient (S) for undoped (x = 0) and doped samples (Figure 8). The Seebeck coefficient for x = 0 is about 350 µV K^{-1} at 300 K, with a broad peak in the temperature dependence. As the Mg content increases, the Seebeck coefficient decreases significantly, and the broad peak structure gradually disappears. With 2% Mg, the Seebeck coefficient becomes nearly proportional to temperature up to 300 K, indicating reduced resistivity. A similar behaviour was observed in $Cu_{2/3}Cr_{4/3}O_2$ films. As-deposited samples exhibit an almost linear temperature dependence, while annealed samples display a bell-shaped curve, akin to undoped $CuCrO_2$. This similarity suggests that chained copper vacancies in $Cu_{2/3}Cr_{4/3}O_2$ act as dopants in a manner similar to Mg in standard $CuCrO_2$.

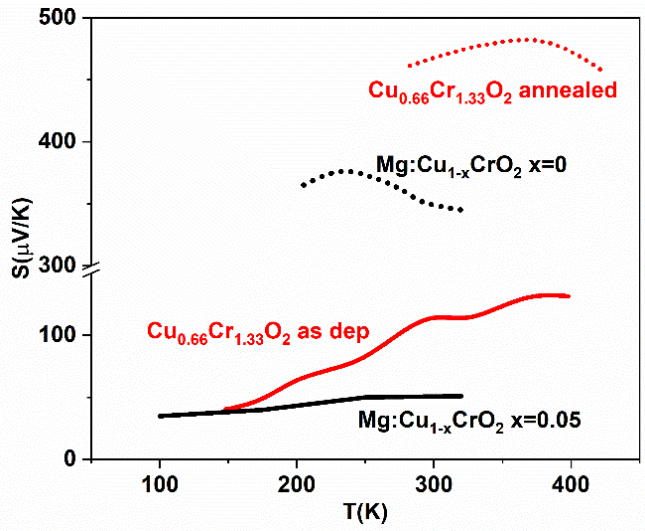

Figure 8 – Seebeck coefficient temperature dependence for $CuCr_{1-x}Mg_xO_2$ (black curve, x = 0 and 0.05) and $Cu_{2/3}Cr_{4/3}O_2$ (red curve, as-deposited and annealed). Adapted from [126] and [190].

The formation enthalpy (ΔH) of different defects in $CuCrO_2$ was evaluated with HSE06, LDA, PBE and PBE+U theoretical approaches [180],[240] (Table 5).

Table 5 – Formation energy calculations for various defects and Mg doping in $CuCrO_2$ different theoretical approaches.

Defect	Calculation Method	ΔH (eV)	Ref.
Mg_{Cr}	LDA	-2.13	[240]
V_{Cu}		-2.5	
O_i''		-2.1	
Mg_{Cr}	HSE06	0.62	[180]
V_{Cu}		1.45	
O_i''		1.63	
Mg_{Cr}	PBE	-0.54	
V_{Cu}		0.16	
O_i''		1.27	
Mg_{Cr}	PBE+U	0.46	
V_{Cu}		0.95	
O_i''		1.38	

The results indicate that the most thermodynamically favourable defect is chromium substitution by magnesium (Mg_{Cr}), followed by copper vacancies (V_{Cu}) and oxygen interstitials (O_i'').

However, recent theoretical models indicate long chains of metallic vacancies as the primary source of p-type doping in complex oxides. These defects were observed for the first time in thoroughly analysis, previously performed by our group. High-Resolution Scanning TEM (HRSTEM) images from earlier studies detected regions with chains of Cu vacancies in off-stoichiometric $Cu_{2/3}Cr_{4/3}O_2$ [190], as shown in Figure 9.

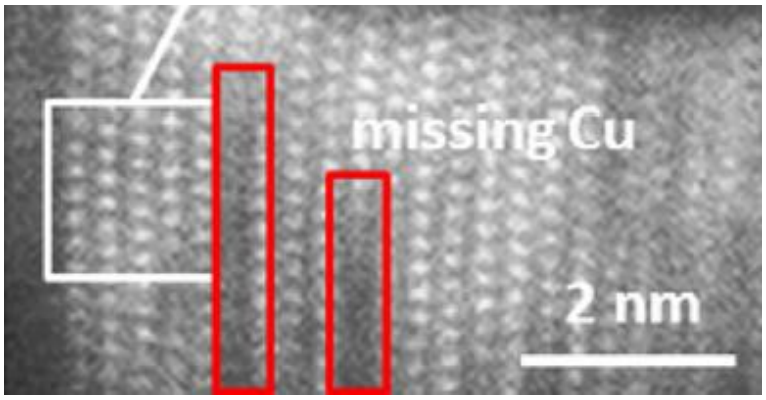

Figure 9 - High angle annular dark field images from STEM of as-deposited Cu-Cr-O. The missing planes of Cu are shown inside the red rectangles. Adapted from [190].

HRSTEM shows also a significant rearrangement of Cu and Cr due to the annealing of the thin films. Bright-field images of the samples before and after annealing (Figure 10) were obtained. In the as-deposited sample, a density of approximately 18 structural defects/µm was observed. Vertical columns separated by these defects are visible, corresponding to twinned domains. After annealing, a decrease in the number of defects is observable, and the thickness of crystallographic domains increased, characterised by having the same crystalline structure as before the treatment. The Fast Fourier transform (FFT) patterns (inset of Figure 10) display the typical distance of the main delafossite plane (012), supporting the previous statement [237].

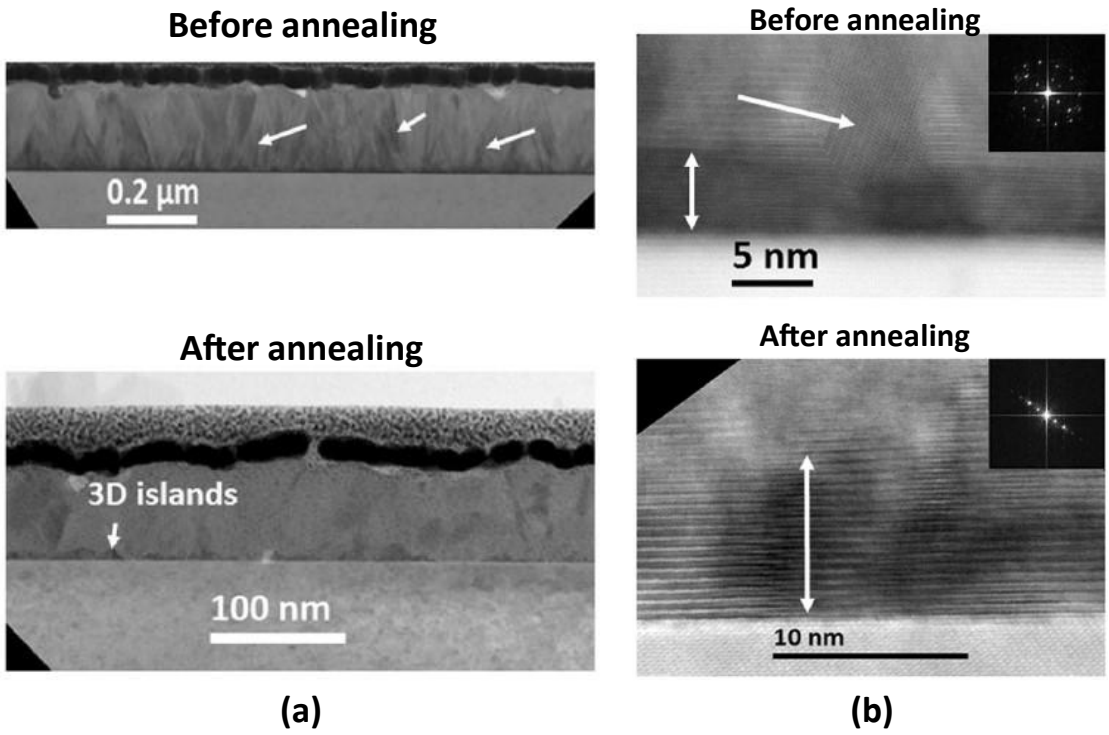

Figure 10 – (a) Cross-sectional bright-field STEM images of Cu-Cr-O. Structural defects are indicated by the arrows; (b) high resolution images; the epitaxial layer and the twinned domain are shown, with the arrows representing their thickness. Inset: FFT patterns of as-deposited and annealed samples. Adapted from [237].

In Figure 10b (top), STEM image shows the growth of similar crystallographic planes at the interface with the substrate, with a different contrast observed beyond a thickness of around 5 nm. This behaviour likely results from the epitaxial growth of $Cu_{2/3}Cr_{4/3}O_2$ on α-Al_2O_3 substrate. It should be noted that the thickness of this layer might vary in some regions, affecting the density of defects. Far from the interface, the structure appears bulky due to the relaxation of structural strain correlating with the lattice constant shrinkage observed after thermal annealing, as evidenced by XRD data. Dark-contrast 3D islands are visible at the interface with the substrate, suggesting the diffusion of atoms in the crystallographic defects, which rearranges the epitaxial layer at the interface [237].

Chapter 2 – Electronic transport in semiconductors

This chapter offers an in-depth examination of the core main concepts underpinning the optoelectronic properties and electronic transport mechanisms in conductive materials. It starts with an introduction to fundamental properties, such as electrical conductivity, carrier concentration and doping, and the differences between non-degenerate and degenerate semiconductors. The discussion then shifts to carrier scattering mechanisms, which play a crucial role in determining mobility and overall charge transport. Following this, various charge transport mechanisms are presented, with particular attention to band conduction and the hopping mechanism. The chapter then addresses the electrical mobility, describing distinct cases of free carriers and small polarons. The next section concerns the influence of strain on effective mass and band structure. Finally, the chapter explores thermoelectric effects, focusing on the Seebeck effect and the theoretical framework of the Emin-Wood expression for semiconductors exhibiting semi-metallic behaviour.

2.1. Electrical conductivity

According to Drude's transport model, the electrical conductivity (σ) and its reciprocal, electrical resistivity (ρ), are directly proportional to the carrier concentration (n), the elementary charge (q) and carrier electrical mobility (μ):

$$\sigma = \frac{1}{\rho} = \mu q n \qquad \textbf{(3)}$$

In simple terms, two main "knobs" can adjust electrical conductivity. The first, fairly straightforward, is carrier concentration, which relates to the number of charge carriers. The second, more complex, concerns electrical mobility, which refers to how fast these carriers can move in the material [241]. The electrical mobility in semiconductors is influenced by the intrinsic band dispersion, which is characterised by the charge carrier effective mass. It depends on the carrier scattering time (τ) and effective mass, and can be expressed by the following relation:

$$\mu = \frac{q\tau}{m^*} \qquad \textbf{(4)}$$

The electrical mobility can be improved by decreasing the effective mass and/or increasing the carrier scattering time [8].

2.1.1. Carrier concentration and doping

Doping is the process of intentionally introducing impurities into a semiconductor material to modify its electrical properties. This is a common strategy to increase the carrier concentration and thereby improve the electrical conductivity. To facilitate the process of doping, n-type semiconductors should have the CBM far from the vacuum level (i.e. large electron affinity); for p-type doping, the VBM should be close to the vacuum level (i.e. small ionisation energy – higher position of p-orbital derived VBs).

Figure 11 depicts the band offsets of oxides in the "Schottky limit," where electron affinities and ionisation potentials are assessed via photoemission spectroscopy or electrochemical methods. The pinning-limit energies define the range within which the Fermi level (E_F) can be adjusted without inducing compensating defects that halt doping. For an oxide to be doped n-type, the n-type limit must lie above the conduction band edge (E_C) of that oxide, allowing E_F to shift to E_C without defect formation. Conversely, for p-type doping, the p-type limit must be below the valence band edge (E_V), enabling doping without defect formation.

Figure 11 emphasizes that for effective n-type doping, a high electron affinity is required, indicating that the E_C should be significantly below the vacuum level. Conversely, for p-type doping, a low valence band ionisation potential is preferred, meaning the E_V should not be excessively below the vacuum level. These criteria ensure that the material can be effectively doped n-type or p-type without causing the formation of compensating defects [242], [243].

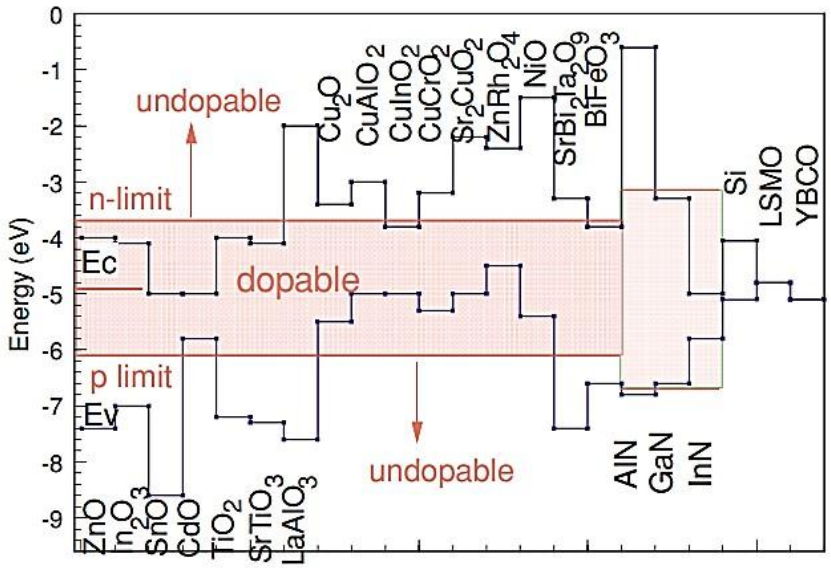

Figure 11 - Band energies of various oxides relative to the vacuum level, depicting doping limits and categorising dopable versus undopable cases. Adapted from. Adapted from [243].

Importantly, there is a fundamental trade-off to engineer between carrier concentration and mobility, as the former influences both the transparency and the conductivity of the material. The plasmon frequency (ω_p) is a fundamental property that describes the natural oscillation frequency of the free carriers in a material. This parameter is essential for understanding the optical and electronic properties of materials, as it determines how the material interacts with electromagnetic radiation. The plasmon frequency is defined as:

$$\omega_p = \sqrt{\frac{nq^2}{m^*\varepsilon_\infty\varepsilon_0}} \qquad \textbf{(5)}$$

where m* is the charge carrier effective mass, ε_∞ is the high-frequency dielectric constant and ε_0 the permittivity of vacuum. High carrier concentrations (greater than 5 x 10^{21} cm^{-3}) can shift the plasmon frequency from the near infra-red (NIR) towards visible wavelengths, leading to reduced optical transparency. Consequently, a TCM cannot be doped too heavily as this can lead to a visible light

reflection. Additionally, increasing the carrier concentration through introduction of defects might decrease the free scattering time (τ) due to increased scattering processes. At elevated doping levels, intraband scattering and free carrier absorption can result in diminished transparency in both the NIR and visible spectra. Additionally, dopants might create defect states within the band gap, further reducing optical transparency, and excitonic absorption may also become pronounced in certain materials. Therefore, increasing the electrical mobility is the realistic alternative strategy to improve the electrical conductivity [242].

Several key factors must be considered to achieve a high hole concentration in a p-type semiconductor, when doping is based on point or extended defects engineering [81], [244], [245]:

- The point or extended defects responsible for creating holes, such as native acceptors like cation vacancies or oxygen interstitials, should have low formation energies.
- The defects should have a low ionisation energy to effectively release holes, meaning they should have shallow acceptor levels relative to the host valence band.
- It is crucial to ensure that native defects which neutralize holes, such as native donors like anion vacancies, have a high formation energy to minimise their impact.

Additionally, doping can enhance the material's transparency near the band edge. When the CBM is occupied, optical transitions require higher energy levels. This phenomenon, known as the Burstein-Moss shift, is observed in heavily doped transparent conducting oxides [200].

2.1.2. Non-degenerate and degenerate semiconductors

Semiconductors can be classified into non-degenerate and degenerate types based on the level of doping and the concentration of charge carriers. In non-degenerate semiconductors, the doping level is relatively low, resulting in a concentration of charge carriers (electrons in the CB and holes in the VB) that is much less than the density of states (DOS) in their respective bands. Consequently, the Fermi level lies within the band gap (Figure 12a). The behaviour of charge carriers follows classical Boltzmann statistics, and the distribution function (F(E)) can be approximated by the Boltzmann function under these conditions:

$$F(E) = \exp\left(-\frac{E - E_F}{k_B T}\right) \quad \textbf{(6)}$$

where E is the energy of the charge carrier.

Degenerate semiconductors are heavily doped, leading to a high concentration of charge carriers. In such cases, the Fermi level may move into the CB for n-type semiconductors or into the VB for p-type semiconductors (Figure 12b). Under these condition, with the energy levels of the carriers close to the Fermi level, the behaviour of charge carriers follows Fermi-Dirac statistics. Here the distribution function is given by:

$$F(E) = \left[1 + \exp\left(\frac{E - E_F}{k_B T}\right)\right]^{-1} \quad \textbf{(7)}$$

For non-degenerate semiconductors, therefore, F(E) approaches classical Boltzmann behaviour, while in degenerate semiconductors, the carrier behaviour more closely resembles that of metals, following the full Fermi-Dirac function.

Degenerate semiconductors exhibit metallic-like conductivity and are employed in applications requiring high conductivity, such as certain types of sensors and thermoelectric devices. The major differences between the non-degenerate and degenerate semiconductors can be summarised as follows:

- Doping level: Non-degenerate semiconductors have moderate doping levels, whereas degenerate semiconductors have high doping levels.
- Impurity interactions: In non-degenerate semiconductors, dopant atoms are well-separated and do not interact with each other. In degenerate semiconductors, the high concentration of dopant atoms causes them to interact and merge into an impurity band.

These differences lead to distinct electrical properties. Non-degenerate semiconductors are used in applications where high thermal conductivity and electrical conductivity are important, while degenerate semiconductors are used in high-power and optical applications where high carrier concentrations are necessary [246], [247].

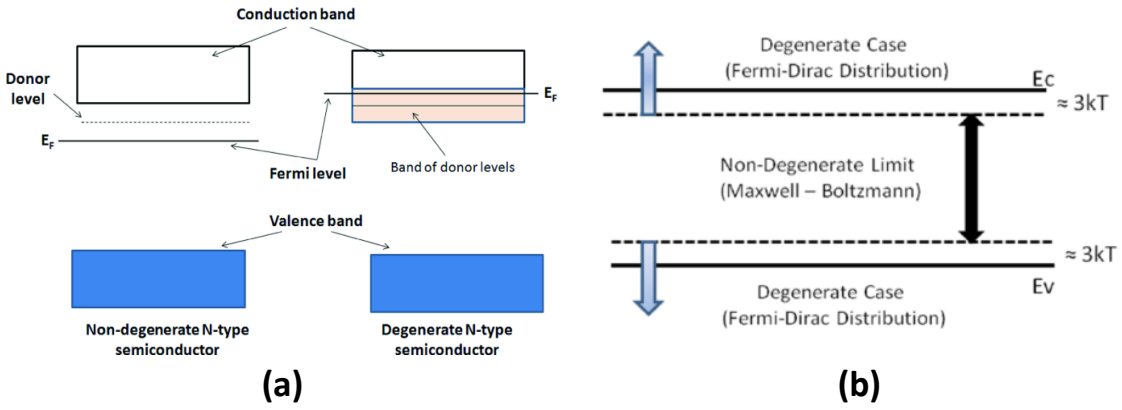

Figure 12 – (a) Position of the Fermi level in non-degenerate n-type and degenerate n-type semiconductor; (b) Non-degenerate limit and degenerate case for n-type and p-type semiconductor.

2.1.3. Carrier scattering mechanisms

Carrier scattering leads to a finite mobility. The carrier scattering time is influenced by several scattering mechanisms, as charge carriers can be scattered by various phenomena. These mechanisms differ significantly by material and depend on several factors, such as crystal film microstructure, processing conditions, crystal purity, and doping level. The mobility varies inversely with the number of scattering events taking place; thus, an increase in motion-impeding collisions decreases the mobility. Carriers in a semiconductor are scattered by their interaction with the following excitations [246],[247]:

- Phonons (both acoustic and optical);
- Ionised impurities;
- Grain boundaries;
- Neutral defects;
- Surfaces and interfaces;
- Scattering between charge carriers.

In polycrystalline TCM films, the total τ is typically decomposed into three main scattering components: ionised impurity (τ_{ii}), grain boundary (τ_{gb}) and lattice (phonon) scattering (τ_l). According to the Matthiessen's rule, the total τ is given by [248]:

$$\frac{1}{\tau} = \frac{1}{\tau_{ii}} + \frac{1}{\tau_{gb}} + \frac{1}{\tau_l} \quad \textbf{(8)}$$

Phonon scattering

Phonon scattering, also known as lattice scattering, originates from interactions between charge carriers and thermally vibrating lattice atoms. This scattering mechanism is influenced by intrinsic material parameters and is dominant at low carrier concentrations ($n < 10^{16}$ cm^{-3}) and in the high-temperature range. Within phonon scattering, polar-optical phonon scattering occurs in polar semiconductors with partially ionic bonding, arising from the dipole moment induced by lattice vibrations that interact with electromagnetic waves. Acoustic phonon scattering, often termed deformation potential scattering, results from atomic displacements that create local compressions and extensions in the crystal lattice, causing shifts in the band edges.

Phonon scattering is unavoidable but can be mitigated by operating at lower temperatures, as the scattering rate is highly temperature-dependent [249].

Scattering on ionised impurities

This extrinsic scattering mechanism occurs in all doped semiconductors due to ionised impurities, which deflect carrier trajectories via the Coulomb potential. It is particularly significant at low temperatures and is typically the dominant scattering mechanism in degenerately doped semiconductors with carrier concentrations exceeding 10^{18} cm^{-3} [248]

Grain boundary scattering

Grain boundary scattering is commonly the predominant mechanism affecting polycrystalline TCO thin films, resulting in lower mobility relative to single-crystal materials. A polycrystalline material is composed of crystallites joined together by grain boundaries, which are transitional regions between different orientations of neighbouring crystallites. Each crystallite has atoms in a periodic manner, so they can be considered single crystals. The grain boundary is a complex structure containing typically few atomic layers of disordered atoms [250].

2.2. Charge carrier transport mechanisms

Charge carrier transport mechanisms are the fundamental processes that govern the flow of electric current through various materials. These mechanisms involve the movement of charge carriers, within a material in response to external stimuli like electric fields and thermal gradients. The transport of charge carriers can occur through two primary mechanisms: carrier drift, where the carriers move under the influence of an electric field, and carrier diffusion, driven by thermal energy and random motion. Charge carrier mechanisms include the following ones [248]:

- **Band conduction**: it occurs in crystalline semiconductors and metals. Charge carriers move freely through delocalised energy states.
- **Hopping transport**: it is observed in disordered solids, polycrystalline, and amorphous semiconductors. Charge carriers move by hopping between localised sites via tunnelling or overcoming potential barriers. The mobility is typically lower than in band transport and depends on the electric field.
- **Thermally activated conduction**: it is observed in disordered materials where charge transport occurs through thermally activated transitions between localised states. The conductivity is temperature-dependent and follows an Arrhenius-like behaviour.
- **Space charge limited current**: it is observed in "trap-free" materials with a high concentration of charge carriers. The current is limited by the space charge region formed by the accumulation of charge carriers near the electrodes.
- **Poole-Frenkel conduction**: it is observed in materials with a high concentration of charge carriers. The conductivity is influenced by the electric field and temperature, following an Arrhenius-like behaviour. It involves the reduction of the potential barrier for charge carrier emission due to the applied electric field.
- **Schottky emission**: it occurs at metal-semiconductor junctions where the charge carriers surmount a potential barrier at the interface. The current increases exponentially with the applied voltage and temperature, exhibiting an Arrhenius-like behaviour.
- **Fowler-Nordheim tunnelling**: it involves quantum mechanical tunnelling of charge carriers through a potential barrier under a high electric field. It is characterized by a strong dependence on the electric field and follows an exponential relationship with the applied voltage.

The most common mechanisms are the band conduction and hoping conduction. In band conduction, "free carriers" – electrons in the conduction band and holes in the valence band – are not strongly bound to atoms or localised lattice distortions, allowing them to move freely. Small polaron hopping, however, becomes important in materials with strong charge-lattice interactions, where charge carriers are more localised due to coupling with lattice distortions, affecting their mobility and conduction behavior.

2.2.1. Band conduction

Band transport mechanisms in semiconductors involve charge carriers moving through the crystal lattice, where their motion is primarily governed by the band structure of the material. In ideal cases where scattering events are minimal or negligible, this process can approach ballistic transport, a regime characterised by charge carriers traversing the material without scattering [246]. However, in typical band transport, some degree of scattering due to impurities, phonons, or lattice imperfections is present.

The mobility of charge carriers in band transport is generally high and, within certain limits, independent of the electric field strength, making it a crucial mechanism for high-performance electronic devices. In this regime, charge carriers possess a mean free path that exceeds the inter-atomic spacing, leading to mobilities often surpassing 1 $cm^2V^{-1}s^{-1}$.

In the band conduction mechanism, charge carriers move freely under the influence of an external electric field. As the temperature increases, thermal energy contributes to the excitation of charge carriers (as shown in Figure 13, red curve, for a doped semiconductor). At low temperatures, dopants are gradually ionised, releasing free carriers (electrons or holes) into the conduction process. This ionisation enhances the number of charge carriers, thereby increasing the material's electrical conductivity (as shown in Figure 13, violet curve).

However, as the temperature continues to rise and all dopants become fully ionised, the electrical conductivity begins to decrease due to a reduction in carrier mobility. This reduction is attributed to increased thermal scattering, where interactions with lattice vibrations (phonons) become more frequent, hindering the free movement of charge carriers.

At very high temperatures, the conductivity experiences a sharp increase due to the significant generation of intrinsic carriers. This occurs because a substantial number of electrons and holes are thermally excited across the band gap, leading to a dramatic rise in overall conductivity as more semiconductor atoms become ionised. This intrinsic carrier generation dominates over the effects of scattering, thereby increasing the conductivity despite the presence of phonon interactions. The electrical conductivity in such a scenario is often described by:

$$\sigma = \sigma_0 \exp\left(-\frac{E_\sigma}{k_B T}\right) \quad \textbf{(9)}$$

where σ_0 is a pre-exponential factor that includes the effects of carrier mobility and density, and E_σ is the activation energy for conduction [205], [241], [251].

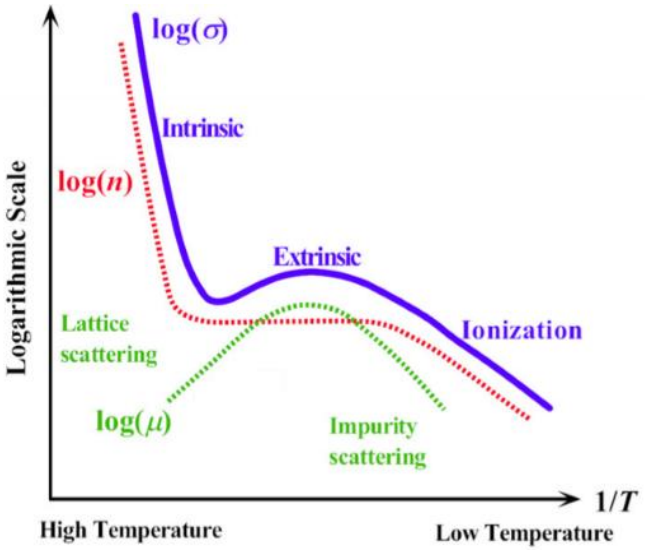

Figure 13 - Temperature dependence of electrical conductivity, carrier concentration, and mobility in band conduction semiconductors.

2.2.2. Hopping conduction

In certain semiconductors, free carriers do not exist in the traditional sense. Instead, charge carriers "hop" between localised states. This hopping occurs between different oxidation states of the same chemical element, which are localised at equivalent sites within the crystal structure. The following redox equation illustrates this process, where the charge hops between site A and site B, both occupied by M atoms:

$$M_{(A)}^{n+} + M_{(B)}^{(n+1)+} \Leftrightarrow M_{(A)}^{(n+1)+} + M_{(B)}^{n+} \quad \textbf{(10)}$$

These semiconductors exhibit thermally activated conductivity behaviour; however, in this case, the carrier concentration remains constant or varies slowly, while the mobility is exponentially dependent on temperature. Thermal energy assists in overcoming potential barriers between states, thereby increasing the probability of charge carriers hopping from one localised state to another without significantly increasing the carrier concentration [252].

The localised states can result from the absence of any long-range order – a phenomenon known as Anderson localisation – or from lattice-distortion localisation caused by a strong electron-phonon interaction, commonly referred to as small polaron hopping. This process, known as thermally activated hopping, is typically observed in disordered solids, polycrystalline, and amorphous semiconductors [253],[254].

Main categories of hopping transport mechanisms

Nearest-neighbour hopping

In nearest-neighbour hopping (NNH), charge carriers hop to the nearest available localised state. This mechanism typically dominates at higher temperatures, where thermal energy is sufficient to overcome the energy barriers between adjacent states. The conductivity follows an Arrhenius-type temperature dependence, where it increases exponentially with temperature [255].

Variable-range hopping

In variable-range hopping (VRH), charge carriers hop to localised states that are not necessarily the nearest neighbours but may be energetically more favourable. It becomes significant at lower temperatures, where the thermal energy is insufficient to facilitate NNH. The carriers hop over larger distances to find states closer in energy. This mechanism occurs in disordered correlated systems and mixed valence compounds such as those involving transition metals, lanthanides or actinides, oxides with delafossite and spinel structure [252],[256]. There are two main categories of VRH: Mott VRH and Efros-Shklovskii VRH.

Mott VRH occurs when the DOS near the Fermi level is constant. At low temperatures (below 200 K), the conductivity dependence on temperature is given by [257], [258]:

$$\sigma = \sigma_0 \exp\left(-\frac{T_M}{T}\right)^{\frac{1}{n+1}} \quad \textbf{(11)}$$

where σ_0 and n are an exponential pre-factor and the transport dimensionality parameter, respectively. T_M is the Mott temperature, related to the degree of disorder and the density of localised states, and is expressed as [258], [255]:

$$T_M = \frac{18}{k_B N(E_F)\xi^3} \quad \textbf{(12)}$$

where $N(E_F)$ is the DOS in the vicinity of the Fermi energy and ξ is the carrier localisation length.

Efros-Shklovskii VRH occurs when Coulomb interactions create a gap in the DOS at the Fermi level, leading to a $T^{-1/2}$ dependence [259].

Polaron hopping

Polaron hopping describes a mechanism where charge carriers are coupled with lattice distortions, known as polarons. There are two primary categories of polarons: small polarons and large polarons. Small polarons form when the charge carriers are tightly bound to the lattice distortion, and hopping occurs through a thermally activated process. In contrast, large polarons are more loosely coupled with the lattice, allowing for higher mobility. Materials that conduct via large polaron hopping exhibit behaviour similar to conventional band materials, where the activation energies of thermopower and resistivity are comparable.

The differences between these polaronic mechanisms are illustrated in Figure 14, which depicts the polaron potentials.

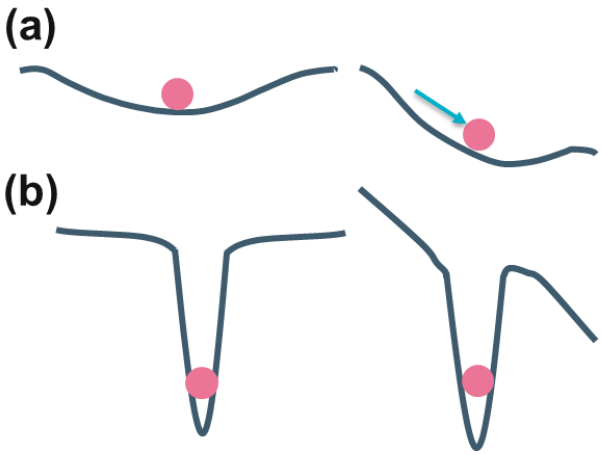

Figure 14 – Schematic representation of potentials of (a) large polaron and (b) small polaron. Adapted from [260].

The potential of a large polaron is wide and shallow, allowing it to 'roll' down smoothly under an electric field, which results in high mobility. In contrast, the narrow and deep potential of a small polaron causes it to become trapped, requiring it to escape either by tunnelling or by thermally hopping to adjacent wells [260].

Phonon-assisted hopping

Phonon-assisted hopping involves phonons assisting charge carriers in hopping between localised states. This mechanism can occur in both nearest-neighbour hopping and variable-range hopping, depending on the energy landscape and temperature [261].

Tunnelling-assisted hopping

This mechanism is significant at very low temperatures, where thermal activation is minimal. In this scenario, charge carriers may hop via quantum tunnelling, bypassing energy barriers through quantum mechanical effects. This mechanism is particularly important in highly disordered systems, where direct tunnelling between localised states becomes feasible [262].

Band conduction vs hopping mechanisms

Figure 15 illustrates the main distinctions between band conduction and hopping mechanisms in solids under an applied electric field. In band conduction (Figure 15a), charge carriers move freely across energy bands with relatively minimal scattering, primarily interacting with lattice vibrations (phonons). As a result, mobility generally decreases with increasing temperature due to phonon scattering, making band conduction slightly temperature-dependent. In contrast hopping transport (Figure 15b) involves charge carriers moving between localised states rather than extended energy bands. Lattice vibrations assist carriers in overcoming potential barriers, leading to thermally activated transport. The hopping rate thus increases with temperature, making this mechanism highly temperature-dependent.

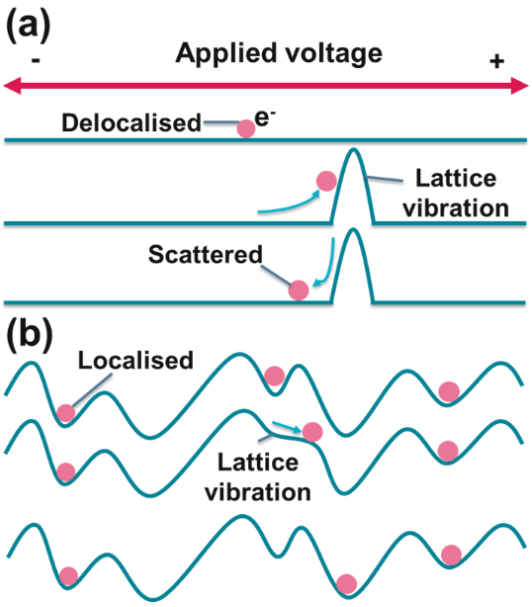

Figure 15 - Illustration of the transport mechanisms in solids with applied electric field. (a) Band-like conduction. (b) Hopping between localised states. Adapted from [263].

They key differences between these transport mechanisms can be summarised according to the following:

- **Scattering**: Band transport involves minimal scattering of charge carriers, while hopping transport involves significant scattering due to the localised nature of the sites.
- **Carrier Mobility**: Band transport typically exhibits higher carrier mobility than hopping transport due to the delocalised nature of the charge carriers.
- **Temperature Dependence**: Hopping transport is highly temperature-dependent, with the hopping rate increasing with temperature. This is because thermal energy helps overcome potential barriers between localised sites. In contrast, band transport is less temperature-dependent, with mobility often decreasing with increasing temperature due to increased phonon scattering.
- **Energy Gaps**: Band transport involves transitions between energy bands, while hopping transport involves transitions between localised sites [255], [259].

2.3. Electrical mobility

The electrical mobility is a fundamental property in solid-state physics, describing the ease with which charge carriers move through a material when an electric field is applied. This property reflects the average drift velocity of charge carriers per unit electric field, effectively quantifying their response rate to an applied field. Mathematically, mobility (μ) is defined as the ratio of the drift velocity (v_d) to the electric field (E) [264]:

$$v_d = \mu E \tag{13}$$

2.3.1. Electrical mobility of the free carriers

Several factors influence the electrical mobility, and their effects can vary depending on whether free carriers or polarons are considered. In the simpler case of free carriers, the primary factors affecting mobility are the following:

- **Crystal structure**: A more ordered crystal structure generally leads to higher mobility due to fewer scattering events.
- **Doping concentration:** While doping can increase the number of charge carriers, it also introduces impurities that act as scattering centres, potentially reducing mobility. In non-degenerate semiconductors, increased doping concentration usually leads to decreased mobility due to enhanced ionised impurity scattering. In contrast, in degenerate semiconductors where the Fermi level lies within the conduction band, mobility behaviour becomes more complex and can sometimes improve due to screening effects.
- **Scattering mechanisms**: The scattering mechanisms impact significantly the mobility. Each mechanism contributes differently depending on temperature and carrier concentration (see Equation (8)).
- **Effective mass**: Carriers with lower effective mass demonstrate higher mobility.

Additionally, the presence of defects, impurities, and grain boundaries in the material can significantly reduce mobility by acting as scattering centres for both free carriers and polarons. Even with free carriers, the temperature dependence of mobility is complex, influenced by various scattering mechanisms that dominate over different temperature ranges, each contributing distinct mobility behaviours.

To illustrate the fundamental principles underlying temperature-dependent mobility, a selection of widely studied models will be presented, each describing mobility in systems with free carriers. These models serve as foundational examples, demonstrating how mobility may be characterised under various regimes and assumptions. In contrast, carrier mobility in small polaron systems is governed by distinct mechanisms, differing significantly from those of free carriers and necessitating a specialised approach to address the effects of temperature on polaron dynamics.

In non-degenerate semiconductors, simpler models can be used to describe mobility, particularly at lower doping levels. In nonpolar semiconductors such as Ge and Si, scattering primarily results from acoustic phonons and ionised impurities. At low temperatures, ionised impurity scattering often dominates, resulting in a mobility (μ_{ii}) with a $T^{3/2}$ dependency [264]:

$$\mu_{ii} = \frac{64\sqrt{\pi}\varepsilon_s^2(2k_BT)^{3/2}}{N_i q^3\sqrt{m^*}}\left\{ln\left[1+\left(\frac{12\pi\varepsilon_s k_BT}{q^2\sqrt[3]{N_i}}\right)^2\right]\right\}^{-1} \quad \textbf{(14)}$$

where ε_s is the static dielectric constant, and N_i is the ionised impurity concentration.

As temperature increases, phonon (lattice) scattering becomes more significant. For acoustic phonon scattering, common in many semiconductors at room temperature, the mobility typically follows the power law $\mu_{ac} \propto T^{-3/2}$ [264]:

$$\mu_{ac} = \frac{\sqrt{8\pi}q\hbar^4 c_l}{3E_d^2 m^{*5/2}(k_BT)^{3/2}} \quad \textbf{(15)}$$

where c_l is the average longitudinal elastic constant, and E_d is the deformation potential of the band edge per unit dilation of the lattice. The temperature dependence of mobility due to these scattering mechanisms is illustrated in Figure 16.

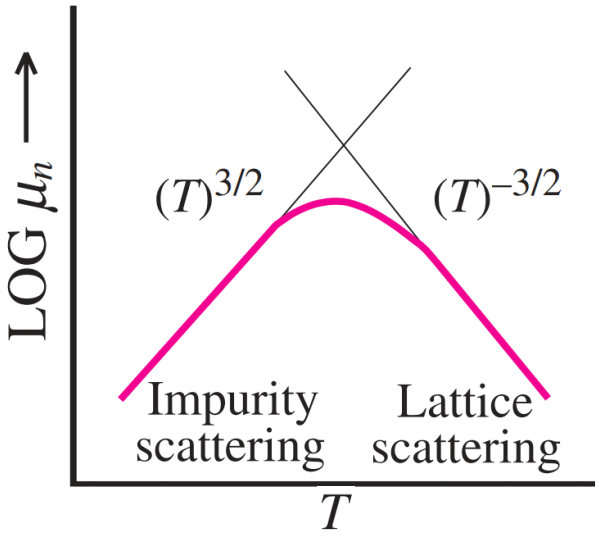

Figure 16 – General diagram of mobility-temperature dependence in ionised impurity and lattice scattering mechanisms. Adapted from [248].

The models to describe scattering mechanisms for degenerate semiconductors are more complex and less common. The mobility due to ionised impurities ($\mu_{ii,deg}$) for degenerate semiconductors with non-parabolic bands was derived by Zawadzki and simplified by Pisarkiewicz, assuming statistically homogeneously distributed scattering centres (i.e. dopants):

$$\mu_{ii,deg} = \frac{3(\varepsilon_s\varepsilon_0)^2h^3}{Z^2m^{*2}q^3}\frac{n}{N_i}\frac{1}{F_{ii}(\xi_0,\xi_1)} \quad \textbf{(16)}$$

where h is the Planck's constant, Z is the charge of the impurities in units of the elementary charge q (usually +1), and $F_{ii}(\xi_0,\xi_1)$ is the screening function for ionised impurity scattering for a non-parabolic conduction band:

$$F_{ii}(\xi_0, \xi_1) = \left[1 + \frac{4\xi_1}{\xi_0}\left(1 - \frac{\xi_1}{8}\right)\right]\ln(\xi_0 + 1) - \frac{\xi_0}{\xi_0 + 1} - 2\xi_1\left(1 - \frac{5\xi_1}{16}\right) \quad \textbf{(17)}$$

where ξ_0 is the reduced scattering length, which depends on the electron density and is given by:

$$\xi_0 = (3\pi^2)^{\frac{1}{3}}\frac{\varepsilon_s\varepsilon_0 h^2 n^{\frac{1}{3}}}{q^2 m^*} \quad \textbf{(18)}$$

and ξ_1 describes the non-parabolicity of the conduction band and is given by:

$$\xi_1 = 1 - \frac{m_0^*}{m^*} \quad \textbf{(19)}$$

where m_0^* is the effective mass of the electron at the conduction band edge. The variation of the effective mass with electron energy is described by:

$$m^* = m_0^*[1 + 2\beta(E - E_C)] \quad \textbf{(20)}$$

where β denotes the non-parabolicity parameter. A temperature-independent mobility is usually indicative that this is the dominant scattering mechanism, as according to Equation (16), $\mu_{ii,deg}$ is proportional to the intrinsic material parameter $[\varepsilon_s/(Zm^*)]^2$. Note that for very high dopant concentrations ($n > 5x10^{20}$ cm^{-3}), the dopants tend to form clusters, leading to even lower mobilities ($\mu_{ii} \approx Z^{-2}$) owing to their higher charge ($Z > 1$) and the model is no longer valid [265]–[267].

Bardeen and Shockley derived an expression for the mobility associated with acoustic phonon scattering in degenerate semiconductors ($\mu_{ac,deg}$), given by [268], [269]:

$$\mu_{ac,deg} = \left(\frac{\pi}{3n}\right)^{\frac{1}{3}}\frac{\hbar^3 c_l q}{E_d^2 m^{*2} k_B T} \quad \textbf{(21)}$$

According to Askerov, under the conditions $k_BT << \hbar\omega_0$ and $E << \hbar\omega_0$ (where E is the CB electrons' energy and $\hbar\omega_0$ is the average energy of the longitudinal optical phonons) the electrical mobility from polar optical phonon ($\mu_{opt,deg}$) scattering is given by [270]:

$$\mu_{opt,deg} = \frac{q}{4\alpha\omega_0 m^*}\left[\exp\left(\frac{\hbar\omega_0}{k_B T}\right) + 1\right] \quad \textbf{(22)}$$

where ħ is the reduced Planck's constant and α is the polaron coupling constant, given by:

$$\alpha = \left(\frac{1}{\varepsilon_\infty} - \frac{1}{\varepsilon_s}\right)\sqrt{\frac{m^* E_H}{m_e \hbar\omega_0}} \quad \textbf{(23)}$$

where E_H is the first ionisation energy of the hydrogen atom (13.595 eV), and m_e denotes the electron mass in vacuum. It is important to note that there is no suitable formula in literature available to explain this mobility for $n > 10^{19}$ cm^{-3}, as at this carrier concentration range the condition $E << \hbar\omega_0$ is actually violated [271].

Finally, in polycrystalline materials, grain boundary scattering introduces an additional layer of complexity, each with its own temperature dependence. The overall temperature dependence of mobility can often be approximated by combining these mechanisms. This combined effect typically results in a decrease in mobility as temperature rises within the usual operating range of most semiconductor devices. However, the exact relationship can vary depending on material properties, doping levels, and the temperature range. In certain instances, more sophisticated models are required to accurately describe the temperature dependence, particularly when considering additional factors such as intervalley scattering or when addressing complex semiconductor structures. The mobility associated with grain boundaries (μ_{gb}) is given by:

$$\mu_{gb} = \frac{4q\pi L m^* k_B T}{n_a h^3} \ln\left[1 + \exp\left(\eta - \frac{E_B}{k_B T}\right)\right] \quad \textbf{(24)}$$

where L is the lateral grain size, n_a is the average free carrier concentration in the grain (including the depletion region and the bulk), E_B is the potential barrier height, and η is the reduced Fermi energy, given by (for an n-type semiconductor):

$$\eta = \frac{E_F - E_C}{k_B T} \quad \textbf{(25)}$$

This model describes the mobility as function of both the free carrier concentration and temperature, applicable for both non-degenerate and degenerate semiconductors across a range of carrier concentrations [271].

2.3.2. Case of small polarons

In delafossite materials, conduction electrons occupy incomplete inner shells (d or f). Due to limited electron overlap, they form extremely narrow bands, leading to the emergence of small polarons [272]. This mechanism is commonly used to explain charge carrier transport in Cu-based delafossites.

Small polaron transport involves the thermal "diffusion" or hopping of a charge carrier and its associated lattice polarisation field between equivalent sites with different valence states. Key characteristics include [256]:

- **Activated mobility**: The mobility of small polarons increases with temperature due to thermally activated hopping.
- **Thermal diffusion**: Charge carriers jump from one atom or ion to a neighbouring one, facilitated by thermal energy that helps overcome potential barriers from lattice distortions.
- **Effective mass**: Polaronic interactions significantly increase the effective mass of charge carriers, as they must drag local lattice distortions along while moving.

Small polaron transport properties are strongly temperature-dependent. At high temperatures (where $k_BT > ½ h\nu_0$, with ν_0 as the phonon frequency), the polaron band collapses, leading to diffusive transport via thermally activated hopping. Thermal-induced atomic distortions around trapping sites destabilise charge carrier localisation, facilitating hopping between neighbouring sites and enhancing electrical mobility. Conversely, at low temperatures ($k_BT < ½ h\nu_0$), charge carriers move more freely through the crystal but with increased effective mass, resembling behaviour within a band of large effective mass, albeit with tunnelling possibilities .

The mobility behaviour of polarons differs significantly from that of free carriers. Polarons, as quasiparticles coupled with lattice distortions, exhibit increased mobility with temperature due to thermally activated hopping mechanisms. The strength of electron-phonon coupling influences polaron mobility; stronger coupling generally leads to lower mobility as polarons become more localised. Additionally, the frequency of lattice vibrations and the lattice's ability to relax around the charge carrier also affect polaron mobility.

Unlike free carriers, which are hindered by lattice vibrations at elevated temperatures, polarons benefit from increased thermal energy to overcome potential barriers between localised states. The temperature dependence of polaron mobility can be described by various models, such as the small polaron hopping model, where mobility follows an Arrhenius-like behaviour: $\mu T \propto \exp(-E_h/k_BT)$, with E_h as the activation energy for hopping. More complex relationships, such as Mott's variable range hopping model, may apply, where conductivity (and consequently mobility) follows $\sigma = \sigma_0 \exp[-(T_0/T)^{1/4}]$. The fundamental difference in charge transport arises from the nature of these carriers: free carriers move through delocalised band states and are hindered by lattice vibrations at higher temperatures, whereas polarons, as quasiparticles coupled to lattice distortions, take advantage of increased thermal energy to overcome potential barriers between localised states [252], [273]–[276].

Electrical mobility in small polarons

The activation energy for polarons participating in electrical conduction varies between adiabatic and non-adiabatic regimes, which represent the two limiting cases of the Holstein model [277]. Adiabatic hopping occurs when the hopping rate is slower than the phonon frequency. During this period, the charge carrier tunnels multiple times between potential wells while experiencing an excited lattice state. Given the total density of conducting sites (N) and the fraction of sites (c) occupied by polarons, the Nernst-Einstein equation yields the following relation:

$$\sigma = Ncq\mu = \frac{NcqD}{k_B T} \quad \textbf{(26)}$$

where D is the small polaron diffusion coefficient, given by:

$$D = \mu k_B T = g(1-c)qa^2\nu_0 \exp\left(-\frac{E_h}{k_B T}\right) \quad \textbf{(27)}$$

Here, g is the probability of successful hopping (close to 1 in the adiabatic regime), a is the hopping distance between equivalent sites, ν_0 is the maximum frequency for carrier jumps (generally 10^{13} Hz), 1-c represents the probability that the adjacent site is unoccupied for exchange to occur (assuming that the two states are randomly distributed), and the exponential factor $\exp(-E_h/k_BT)$ is the probability that a given site will possess the thermal energy necessary for the hopping. The relationships above yield the temperature dependence of electrical conductivity:

$$\sigma = \frac{gNc(1-c)q^2a^2\nu_0}{k_B T}\exp\left(-\frac{E_h}{k_B T}\right) \quad \textbf{(28)}$$

This expression demonstrates that the thermally activated mobility in adiabatic regime is given by:

$$\mu = \frac{(1-c)qa^2\nu_0}{k_B T}\exp\left(-\frac{E_h}{k_B T}\right) \quad \textbf{(29)}$$

The overall activation energy for conduction (E_σ) in small polarons is the sum of two terms:

$$E_\sigma = E_h + E_n \quad \textbf{(30)}$$

where E_n is the energy associated with carrier generation, which is typically zero. This assumption arises because small polarons are formed from charge carriers that are already localised due to electron-phonon interactions, meaning that no additional energy is required for their generation in the system. Therefore $E_\sigma \approx E_h$.

In the non-adiabatic regime, where the hopping rate is much slower than the phonon frequency, mobility is given by:

$$\mu = \frac{P(1-c)qa^2}{k_B T}\exp\left(-\frac{E_h}{k_B T}\right) \quad \textbf{(31)}$$

where P is the tunnelling probability, given by:

$$P = \frac{J^2}{2\hbar}\left(\frac{\pi}{E_h k_B T}\right)^{1/2} \ll 1 \qquad \textbf{(32)}$$

Here, J represents half of the rigid-lattice bandwidth. In this regime, the rapid ion vibrations coupled with slower carrier hopping yield a low probability of transfer during each excitation ($J << \omega_0$). In conclusion, the low probability of charge transfer per phonon excitation in the non-adiabatic regime significantly limits carrier mobility. This inefficiency arises because the charge hopping rate is much slower than the frequency of ion vibrations, resulting in a reduced likelihood of successful carrier transfer and, consequently, lower overall mobility in the material [147], [256], [261], [278]–[280].

2.4. Strain-engineering the electrical mobility of semiconductors

2.4.1. Effective mass and electronic band structure

The effective mass describes the apparent mass of a charge carrier as it moves through a lattice under the influence of external forces. This intrinsic property of materials can be characterised in relation to a specific crystal direction, averaged over all directions, or aligned with the least favourable direction to reflect a more detrimental impact. The effective mass is closely linked to the electronic band structure of the material, particularly the dispersion at the band edges, where free carriers reside, such as the CBM for electrons and the VBM for holes. The parabolic approximation used to model the energy of these bands is expressed as follow:

$$E(\boldsymbol{k}) = E_0 + \frac{\hbar^2 \boldsymbol{k}^2}{2m^*} \quad \textbf{(33)}$$

where E(**k**) denotes the energy of a band as a function of the wave vector **k** (which represents the momentum of electrons within the crystal lattice), and E_0 is the band edge energy. In this quadratic approximation, m* is determined by the second partial derivative of E(**k**) with respect **k** according to:

$$m^* = \left[\frac{1}{\hbar^2}\frac{d^2E(\boldsymbol{k})}{d\boldsymbol{k}^2}\right]^{-1} \quad \textbf{(34)}$$

The second derivative term represents the band edge dispersion, providing important information regarding m*. The higher $d^2E/d\mathbf{k}^2$, the sharper the curvature of the energy band, meaning lower m*. Conversely, smaller $d^2E/d\mathbf{k}^2$ causes flatter curves, leading to higher m*. Both cases are illustrated in Figure 17 in an E-**k** diagram.

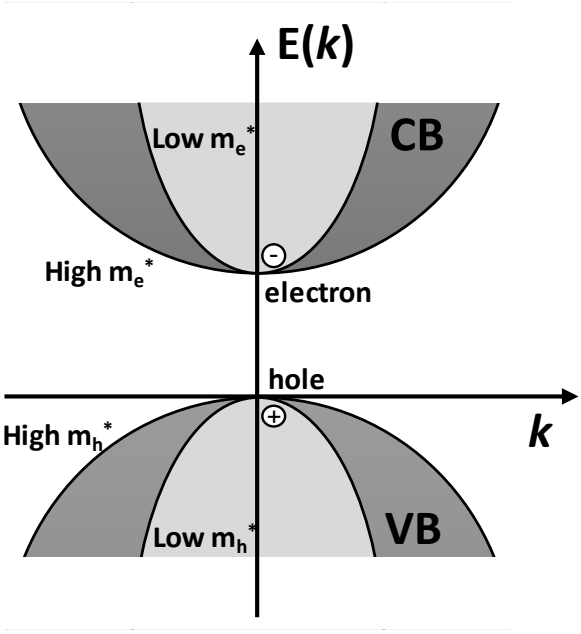

Figure 17 – Relationship between band dispersion and effective mass in an in E-**k** diagram.

From the chemical perspective, the CBM in current n-type TCOs is mainly formed by of two spherical ns^0-orbitals (that are less localised and have spherical symmetry) from a p-block heavy metal cation and chalcogen p-orbital. This leads to strong chemical hybridisation resulting in very dispersive bands (with very low m*) and hence high electrical mobility [295]–[297].

TCOs primarily exhibit n-type conductivity due to the favourable formation of oxygen vacancies or cation interstitials, which serve as donor states. These defects contribute additional electrons to the CB, thus enhancing n-type conductivity [6]. In contrast, the VBMs of many p-type TCMs are formed through the hybridisation of d-orbitals from metallic cations with p-orbitals from chalcogens. The d-orbitals, being highly localised and directionally dependent, result in weak bonding with the chalcogen p-orbitals, leading to nearly flat VBs at the VBM [281]. Furthermore, the p-orbitals of chalcogens are significantly lower in energy compared to the valence orbitals of the metallic cations and possess high electronegativity, which traps holes and thereby hampers the introduction of shallow acceptors while increasing the hole effective mass [37], [110], [281]. Consequently, enhancing the mobility of p-TCMs primarily involves engineering the band structure to reduce the effective mass, which is generally more feasible than improving the scattering time.

2.4.2. Strain in semiconductors

The wave vector and effective mass in semiconductors are closely intertwined with strain, which alters the electronic band structure. Strain (ε) in semiconductors arises from various sources, such as phonon-induced lattice vibrations in homogeneous semiconductors, lattice-mismatched film growth in epitaxial heterostructures, intrinsic stress in deposited thin films, or applied external stress [251], [285], [286]. Strain modifies bond lengths and lattice parameters at the atomic level, perturbing the material's band structure by modifying the interaction potential (energy) felt by an electron in the crystal (V(r)) [265]:

$$V(r) = U(r) - \sum_J \frac{Z_J q^2}{r_{iJ}} \qquad \textbf{(35)}$$

where U(r) represents the time-averaged potential, in which the electrons move independently. The summation term accounts for electron-nucleus interactions over distances r_{iJ} between the electron at position i and each nucleus J. Here, q is the elementary charge at position I, and Z_J is the atomic number of nucleus J. These interactions contribute to variations in the effective mass, which is critical because free carriers are situated at the minima or maxima of the CB and VB, corresponding electrons and holes, respectively.

With the advent of flexible electronics applications, understanding the impact of mechanical strain on devices performance has become crucial. The relationship between mobility and strain has been used to optimise the active channels in silicon metal–oxide–semiconductor field-effect transistors (MOSFETs). For instance, early 1990s studies reported enhancement factors of 2.2 [11] and 1.5 [12] in transconductance (g_m) (channel mobility) for n- and p-channels, respectively (Figure 18).

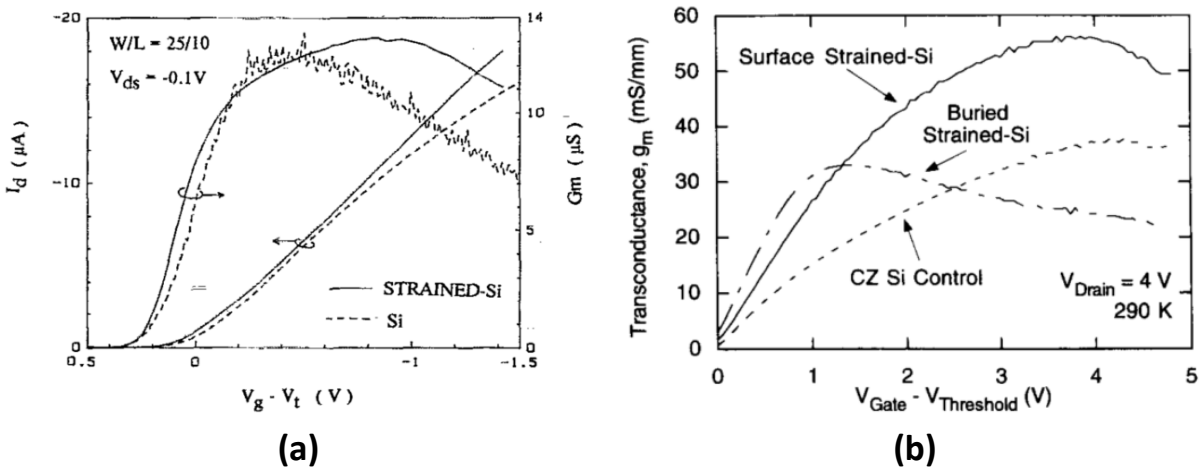

Figure 18 – Comparison of transconductance vs gate voltage in (a) n-type and (b) p-type strained-silicon MOSFETs. Adapted from [11], [12].

Applied stress in semiconductors can positively impact physical properties such as magnetoelasticity [287] or piezoelectricity [288], [289], where mechanical energy is converted into magnetic or electrical energy, respectively. Consequently, the manipulation of electrical mobility through strain has been extensively studied. For instance, DFT predicts a 3000% increase in mobility for monolayers of phosphorus allotropes subjected to -6% strain [290]. Experimental studies frequently report mobility enhancements of up to an order of magnitude with increasing stress in semiconducting thin films [285].

2.5. Thermoelectric effects

2.5.1. Seebeck effect overview

The Seebeck effect (S) is a fundamental thermoelectric phenomenon that describes the generation of an electric potential in a conducting material when exposed to a temperature gradient (ΔT). When a temperature gradient is applied, charge carriers at the hotter end gain additional thermal energy, causing them to diffuse toward the cooler end. This movement of carriers generates a charge buildup, resulting in an electric potential difference (ΔV) expressed as:

$$S = \frac{\Delta V}{\Delta T} \quad \textbf{(36)}$$

The Seebeck effect is inherently linked to charge transport mechanisms in materials. The sign of S indicates the dominant charge carrier type, with a negative S signifying n-type (electron-dominant) conduction and a positive S indicating p-type (hole-dominant) conduction. The Seebeck coefficient's sensitivity to the energy dependence of scattering mechanisms provides valuable insights into a material's electronic structure. Generally, the magnitude of S is inversely related to carrier concentration under specific conditions, due to the influence of the Fermi level. In non-degenerate p-type semiconductors, S can be approximated as:

$$S = +\frac{k_B}{q}\left[\frac{E_F - E_V}{k_B T} + A\right] = +\frac{k_B}{q}\left[ln\left(\frac{N_v}{p}\right) + A\right] \quad \textbf{(37)}$$

where E_F-E_V is the Fermi energy relative to the VB edge, N_v is the effective DOS per unit volume in the VB, and A is a dimensionless parameter that depends on the primary scattering mechanism [291]. For degenerate semiconductors, the Fermi level is within or near the VB, and carrier statistics must consider Fermi-Dirac behaviour, which leads to a Seebeck coefficient approximated by [254]:

$$S \approx \frac{\pi^2 k_B^2 T}{3qE_F} \quad \textbf{(38)}$$

Here, S exhibits a weaker linear dependence on temperature due to the lower sensitivity of carrier concentration with temperature near the Fermi level. For narrow-band or polaronic semiconductors where carriers undergo hopping conduction, the Seebeck coefficient is described by Heikes' formula [292]:

$$S = +\frac{k_B}{q} ln\left(\frac{g_1}{g_2}\frac{1-c}{c}\right) \quad \textbf{(39)}\ [4]$$

[4] The sign of S can change for a given type of small polaron conduction when $c > g_1/(g_1+g_2)$. In $CuCrO_2$, $S < 0$ if $c > 0.2$ [256]. However, this never occurs in the experimental data of this work.

where g_1 and g_2 are the spin degeneracies of two distinct charge states (e.g., Cu^+ and Cu^{2+} in $CuCrO_2$), and c is the fraction of sites occupied by carriers. This form, sensitive to carrier concentration rather than temperature, indicates no temperature dependence in small polaron conductors.

2.5.2. Emin-Wood expression for Seebeck coefficient in semiconductors with semi-metallic behaviour

The dependence of the Seebeck coefficient on temperature in copper chromium delafossite remains a contentious topic in the literature, with various values and behaviours reported for this material. For instance, Sinnarasa [293] demonstrated that the Seebeck coefficient remains invariant with temperature between 40 and 220 °C in magnesium-doped $CuCrO_2$ thin films, with values around 300 μV K^{-1} measured across this entire temperature range for films exhibiting a conductivity of 0.60 S cm^{-1}. In contrast, Tripathi [294] observed a linear dependence of the Seebeck coefficient within the same temperature range for ALD-deposited pure delafossite films, which displayed similar conductivity values. As previously discussed, our off-stoichiometric delafossite samples exhibit a Seebeck behaviour comparable to that of Mg-doped $CuCrO_2$ films deposited by Okuda [126], where an increase in dopant concentration induces a linear temperature dependency in the Seebeck coefficient.

To investigate these aspects further, a more in-depth analysis of the Seebeck coefficient is necessary. Emin and Wood [295] proposed that the Seebeck coefficient can be derived independently of scattering mechanisms by focusing on shifts in the electron chemical potential due to temperature changes. Their theoretical framework provides valuable insight into the Seebeck coefficient within the context of small polaron hopping conduction, helping to explain the unusually high Seebeck coefficients observed in semiconductors with substantial charge carrier densities – a combination rarely seen in conventional semiconductors. Diverging from the traditional Boltzmann kinetic transport model, the authors adopted a thermodynamic approach, suggesting that the Seebeck coefficient could be determined solely by the EDOS. Their work highlights how localised carriers can displace surrounding atoms from their equilibrium positions and reduce their vibrational frequencies, thereby significantly influencing carrier conductivity. Emin and Wood proposed that the Seebeck coefficient can be expressed as the sum of two terms:

$$S = \frac{T\Delta S + E_T}{qT} \qquad \textbf{(40)}$$

The first term represents the classical contribution, linked to the average change in entropy (ΔS), associated with the thermal energy transported by the charge carriers. The second term relates to the thermal energy transported by phonons (vibrational energy) during the hopping process. Carrier hopping between localised states is a common transport mechanism in disordered materials, such as semiconductors with low carrier densities.

The probability of a carrier hopping between two sites, i and j, $P_{i,j}$, depends on the spatial separation r_{ij} and the energy difference ΔE_{ij} between these sites:

$$P_{i,j} = P_0 \exp\left(-2\alpha r_{ij} - \frac{\Delta E_{ij}}{k_B T}\right) \qquad \textbf{(41)}$$

where P_0 is a pre-factor associated with the phonon frequency, and α is a parameter reflecting the overlap of wavefunctions [296]. At high temperatures, transport is primarily driven by nearest-neighbour hopping with activated behaviour. As temperature decreases, variable-range hopping becomes more favourable, allowing carriers to hop over longer distances but with smaller energy differences.

The localisation length ξ of the localised states is typically on the order of a few angstroms, related to the lattice constants. This short localisation length indicates that hopping occurs between highly localised states around defects or impurities within the material.

Several factors influence the Seebeck coefficient, with the most significant being the entropy change: the Seebeck coefficient is proportional to the average entropy change when a charge carrier is introduced into the material. In most cases, this entropy term is the primary factor considered. However, other influences also contribute, such as the vibrational energy transported with the carrier during hopping, and charge carrier asymmetry at the Fermi level, which is crucial in determining both the sign and magnitude of the Seebeck coefficient. Emin and Wood [295], and Tewari [297] considered a probabilistic approach of the phonon-assisted hopping.

In copper chromium delafossite, the polarons are related to the copper sites. These are not energetically equivalent, especially in the presence of a significant off-stoichiometry. Furthermore, the polarons are strongly coupled with phonons, making it essential to consider the second term of the Seebeck coefficient. The vibrational energy transferred during the jump of a polaron from site i to site j is [295]:

$$E_T^{i\to j} = \frac{1}{2}\frac{(E_j - E_i)(\Gamma_i - \Gamma_j)}{\Gamma_i - \Gamma_j} \qquad \textbf{(42)}$$

where E_i and E_j are the energies of the system when the polaron is located at site i and site j, respectively, and Γ_i and Γ_j are parameters related to the strength of charge-lattice coupling. The net current (I_p) associated with a particle moving from site i to site j can be described in terms of Einstein diffusion as [295]:

$$I_p^{i\to j} = f_i(1 - f_j)R_{i,j} - f_j(1 - f_i)R_{j,i} \qquad \textbf{(43)}$$

where f_i and f_j are the occupancy probabilities of sites i and j, respectively, with 1-f_i and 1-f_j representing the probabilities of these sites being vacant $R_{i,j}$ and $R_{j,i}$ denote the transition rates between the two sites. When a temperature gradient is applied, the system moves out of equilibrium. Following Emin's reasoning [295], the vibrational energy transported depends on temperature and on the temperature derivatives of the transition rates at equilibrium:

$$E_T^{i\to j} = k_B T^2 \left[\frac{d\ln(R_{i,j}/R_{j,i})}{dT_i} + \frac{d\ln(R_{j,i}/R_{i,j})}{dT_j}\right]_{T\Delta_{ji} at\ 0\ K} \qquad \textbf{(44)}$$

If the transition occurs between two states with the same energy or identical phonon coupling strength, this term is zero. Since the hole-lattice coupling depends on the energy of the states, Emin approximated:

$$\Gamma_i - \Gamma_j \approx E_j - E_i \quad \textbf{(45)}$$

thus simplifying E_T to:

$$E_T^{i\to j} = C\left(E_j - E_i\right)^2 \quad \textbf{(46)}$$

Where C is a constant calculated by Wood [295] as:

$$C = \frac{zJ^2}{16E_b^3} \quad \textbf{(47)}$$

where z is the number of nearest neighbours, E_b is the average binding energy of the small polaron, and J is the inter-site transfer energy. Averaging the term from Equation (46), assuming a broad distribution of energy, the vibrational energy transferred is:

$$E_T^{i\to j} = \frac{k}{q} 8Ck_BT^2 \quad \textbf{(48)}$$

When replacing E_T in Equation (40), the complete expression for the Seebeck coefficient becomes:

$$S = \frac{\Delta S}{q} + \frac{8k_B^2C}{q^2}T \quad \textbf{(49)}$$

In this expression, only the temperature-independent part relates to carrier concentration, as per the Boltzmann entropy formula:

$$S = k_B \ln(\Omega) \quad \textbf{(50)}$$

where Ω is the number of microstates available to the system – the thermodynamic probability. Hence, Equation (49) can thus be used to determine carrier concentration and, further, to assess electrical mobility. Figure 19 illustrates this discussion.

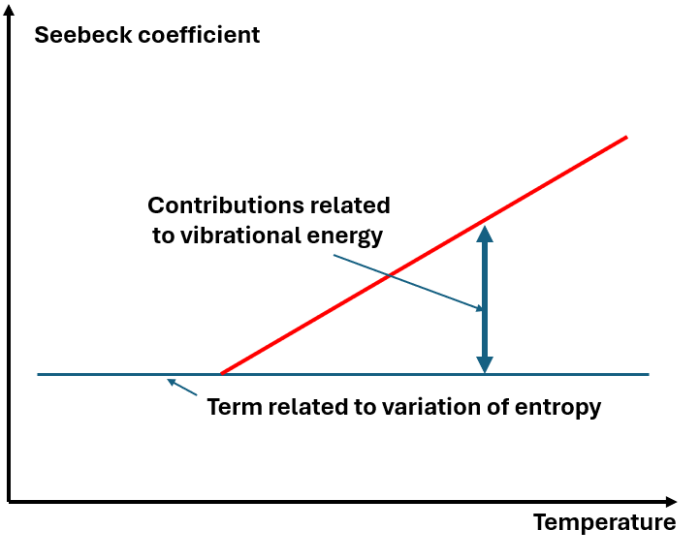

Figure 19 – Temperature dependence of Seebeck coefficient, accounting for contributions from to vibrational energy and entropy variation.

In typical experiments, what is measured is the combined contribution from both the energy transported by carriers and by phonons. For accurate carrier concentration estimation, the contribution due to vibrational energy transfer must be isolated. This approach by Wood and Emin provides a broad physical insight into the increase in S with temperature, applicable even for non-metallic samples.

Tewari [297] developed a similar approach, focusing on intrinsic semiconductors with donor impurity levels. For $CuCrSe_2$, Tewari demonstrated the following expression for the Seebeck coefficient:

$$S = \frac{k_B}{q}\left[A + B\ln(T) + \frac{\Delta E_d}{2k_B T}\right] \qquad \textbf{(51)}$$

where ΔE_d is the activation energy required to excite an electron from the donor level to the conduction band minimum. This approximation for doped semiconductors remains valid in our case, as $CuCrO_2$ is a semiconductor with a defined DOS, although its conduction mechanism is that of a small polaron. We can assume that the carrier density approximates the defect density, as most defects would be ionised at high temperatures. In Tewari's work, the 1/T term only accounts for the low-temperature part of the curve, so we can infer that at higher temperatures, the Seebeck coefficient comprises two contributions, as in Emin's model. However, Tewari does not assign physical meanings to the constants A and B, though his conclusions align with those of Emin, indicating a Seebeck coefficient with both a temperature-independent component a ln(T) dependent term.

These approaches offer a deeper understanding of the Seebeck coefficient in complex semiconductors, such as boron carbides. They provide explanations for atypical phenomena, including high Seebeck coefficients at elevated charge carrier densities and the behaviour of the Seebeck coefficient in materials exhibiting small polaron hopping conduction.

Chapter 3 – Experimental methods and approaches

This chapter outlines the experimental methods and approaches utilised in this work. It begins with a detailed description of the Metallo-Organic Dynamic Liquid Injection Chemical Vapour Deposition (MODLI-CVD) method employed to synthesise the films under study, including a discussion of both the experimental setup and the deposition process. A special section is devoted to the characterisation methods, covering established techniques such as X-ray Diffraction (XRD), Scanning Electron Microscopy (SEM), Transmission Electron Microscopy (TEM), and electrical characterisation. Additionally, emphasis is given to specific methods and in-house developed setups for inducing strain, including those utilising magnetostriction and mechanical bending. The chapter also describes the specific techniques used for data interpretation in this thesis, such as the Pseudo-Voigt and $\sin^2\Psi$ methods for investigating strain, as well as methods for estimating thermally induced strain.

3.1. Chemical vapour deposition

Chemical vapour deposition (CVD) is a versatile vacuum deposition technique widely employed in the semiconductor industry for the growth of thin films. It involves the dissociation and/or chemical reactions of gaseous reactants in an environment containing a source that initiates the reaction, typically in the form of heat, light or plasma. The deposition process involves homogeneous gas-phase reactions and/or heterogeneous chemical reactions occurring on a heated substrate, leading to the formation of powders or films, respectively.

The conventional CVD method – thermal activated CVD (TACVD) – uses thermal energy to activate chemical reactions. There are a multitude of thin film growth techniques relying on the CVD principles, including atmospheric pressure CVD (APCVD), low-pressure CVD (LPCVD), plasma enhanced CVD (PECVD) rapid thermal CVD (RTCVD) and atomic layer deposition (ALD). All these variations share the main sequential steps of a CVD deposition, as described below and identified in Figure 20:

1) Generation of active gaseous reactant species through processes such as sublimation of powder, liquid evaporation, or gas introduction.
2) Transport of the generated gaseous species into the reactor chamber.
3) Gaseous reactants undergo gas phase reactions forming intermediate species.
    a) If the temperature exceeds the decomposition temperatures of intermediate species, a homogeneous gas phase reaction may occur. In this process, species decompose or chemically react to form powders and volatile by-products, with the powders collecting on the substrate surface potentially serving as crystallisation centres. The by-products are evacuated from the chamber, and poor adhesion of the deposited film may result.
    b) At temperatures below the dissociation point of intermediate species, diffusion or convection transports these species through a boundary layer near the substrate surface, where they proceed to subsequent stages (4-7).
4) Absorption of gaseous reactants onto the heated substrate. heterogeneous reaction at the gas-solid interface leads to the formation of adatoms or solid clusters and additional gaseous by-products.

5) The adatoms diffuse across the substrate surface, initiating crystallisation and film growth.
6) Gaseous by-products are removed from the boundary layer through diffusion or convection.
7) Unreacted gaseous precursors and remaining by-products are transported out of the deposition chamber.

Engineering of the process conditions is necessary to favour either a more heterogeneous or homogeneous reaction. The former promotes the growth of dense films (as in the case of this work), whereas the latter is more suitable for porous coatings.

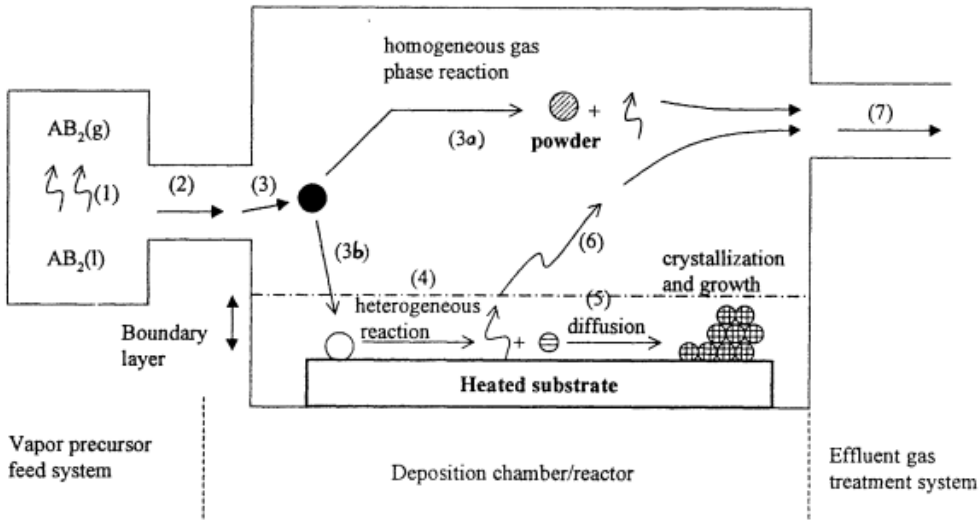

Figure 20 - Schematic illustration of the main CVD steps during a deposition. Adapted from [298].

The main advantages of CVD methods are as follows:

- Growth of highly dense, pure films, with good reproducibility and adhesion at reasonably high deposition rates.
- Possibility for high conformality depositions, making them suitable for substrates with complex 3D geometries.
- Control over crystal structure, surface morphology and orientation by adjusting the process parameters.
- Adjustability of deposition rate, enabling for instance the preference for growth of epitaxial films.
- Availability of a wide range of chemical precursors, including organometallics.
- Relatively lower deposition temperatures than those for other conventional growth techniques, such as PVD or PLD, hence achieving smaller energetic costs [299],[300].

On the other hand, significant challenges with this technique include the handling of toxic, corrosive, flammable, and/or explosive precursor gases, as well as challenges in controlling the stoichiometry of multicomponent-materials. Furthermore, the adoption of more sophisticated reactors for CVD variants may introduce drawbacks related to advanced reactor designs and the associated costs of ultra-high vacuum systems [298].

3.1.1. Metal-organic chemical vapour deposition

Common precursors used in the CVD process include metals, metal hydrides, halides, halohydrides, and metal-organic compounds. When employing the latter, the process is known as Metal-organic CVD (MOCVD). These compounds consist of metal atoms bonded to organic radicals[5]. Their primary feature is the lower decomposition/pyrolysis temperature compared with other precursors. Consequently, they enable film growth at temperatures lower than those typically reported by conventional CVD. Moreover, these precursors tend to be less toxic and pyrophoric, making them safer to handle. These advantages propelled MOCVD for wider applications, particularly in the growth of II-VI and III-V semiconductors. In contrast, the precursors for this method tend to be more expensive and often require specialised synthesis tailored to specific applications. Furthermore, as they are volatile liquids, precise pressure control is essential during the process. MOCVD enables the growth of uniform thin films with excellent crystallinity, mechanical stability, good adhesion and easy mass production on large substrates [301]. Additionally, it offers versatility in utilising a wide range of materials to grow amorphous, epitaxial, and polycrystalline films. It can be effectively employed for depositing semiconductors, metallic and dielectric films. The specific properties of the resulting film are determined by the choice of precursors and the reactions involved [302]. In this work, a variant of MOCVD is used – Dynamic Liquid injection MOCVD (DLI-MOCVD), also referred to as pulsed injection CVD. This was developed by Senateur et al. [303]. It involves the sequential direct injection of the precursor solution into an evaporator via a high-speed microelectrovalve, assisted by a pressurised inert gas at room temperature within the container, causing the solution to vaporize instantly. The flow rate is regulated by successive fast opening of the valve. This approach offers unique advantages, including [298]:

- Reduction in the number of process parameters.
- More precise control over the thickness, stoichiometry and growth rate of the films.
- Enhancement of the reproducibility of the properties of the grown films.

3.1.2. DLI-MOCVD Setup

In this work Cu-Cr-O thin films were grown using DLI-MOCVD (MC-200 Annealsys). The main sequential steps of DLI-MOCVD deposition are outlined below:

1) Precursor injection: A pressure of 5 mbar pressure is applied to the cannister to drive the precursor liquid into the injector head (at 100 °C). Here the carrier gas (N_2) mixes with the liquid.
2) Introduction of precursor and reactant gases into the reactor: when the precursor enters the reactor, it instantly evaporates due to the sudden decrease of pressure and the elevated temperature within the reactor. Oxygen as reactant gas is introduced separately at the same time in this step.
3) Both the precursor and oxygen are transported to the substrate holder vicinity due to the vacuum pumping line below the substrate holder.

[5] Precursors containing one or more direct metal-carbon covalent bonds are termed organometallics. When these are used, the CVD technique is referred to as Organometallic CVD (OMCVD).

4) The heated substrate, which in the presence of the precursor gas and oxygen at the vicinity, triggers the chemical reaction near the substrate surface, leading to film growth.

The DLI-MOCVD reactor parameters that were tuned throughout this work are described in Table 6. Here the parameters were tailored to promote the growth of crystalline and dense films without formation of powders, with an electrical conductivity of at least 5 S cm^{-1} [182], [190], [236], [237], [304], [305].

Table 6 - DLI-MOCVD parameters used for Cu-Cr-O film growth.

Parameter	Value
Substrate holder temperature	580-630 K
Reactor pressure	12 mbar
Precursor flow	2 g min^{-1} (2.6 mL min^{-1})
O_2 flow	1000 sccm
N_2 flow	75 sccm
N_2 precursor carrier flow	350 sccm
Injector frequency	2.5 Hz
Substrate holder height	10 – 16 cm
Substrate holder rotation	10 rpm
Deposition time	10 – 60 min

The reactor was operated at temperatures of 580 or 630 K, with N_2 serving as the carrier gas. A continuous flow of 30% nitrogen and 70% oxygen was introduced into the reactor to sustain a total pressure of 12 mbar throughout the deposition process.

All precursors used are metalorganic compounds belonging to the metal β-diketonates class, with the formula $M(THMD)_x$ (tetramethyl heptanedionato), where M = Cu or Cr for delafossite (Merck Life Science BV, Belgium) and M = Al, Mg, Mn, Sc, Y, Zn for dopants (STREM Chemicals, Massachusetts, USA) and x = 2 or 3. Solutions with an equimolar Cu/Cr concentration $[Cu(THMD)_2]$ = $[Cr(THMD)_3]$ = 2.5 mM were prepared using cyclohexane (≥ 99%, Merck Life Science BV, Belgium) as solvent. Due to the limited solubility of the dopants and to prevent precipitation of secondary phases that could affect the physical properties, their concentration was fixed at 5 at.% [306].

Prior to deposition, all substrates were cleaned in an ultrasonic bath with acetone for 15 min, followed by cleaning in isopropyl alcohol for 15 min. Subsequently, the substrates were cleaned with deionised water and dried under N_2.

3.2. Chemical, morphological, optical and structural characterisation techniques

3.2.1. Scanning electron microscopy

Scanning electron microscope (SEM) technique used to analyse the morphology and topography of a specimen. The principle of this technique is based on an electron beam that interacts with the specimen, losing energy in the form of heat, secondary electrons, backscattered electrons, cathodoluminescence or X-rays. Each of these emitted energies allows to obtain different information about the sample. For instance, the detected secondary electrons allow for the production of an image of the specimen's surface. Since SEM image relies on surface processes, it can image bulk samples [248].

SEM analyses were conducted using a Helios 650 FIB-SEM (FEI Company, USA) High Resolution system. The observations were carried out under vacuum conditions (10^{-6} mbar), and images were captured through secondary electron detection. Both top-view and cross-sectional imaging configurations were used to examine surface morphology and verify film thickness. The electron source voltage and current were adjusted according to surface charging effects, ranging from 2 to 5 kV and 25 to 100 pA, respectively.

3.2.2. Atomic force microscopy

Atomic force microscopy (AFM) is a high-resolution imaging technique used to analyse the surface topography of materials at the nanoscale. It operates by scanning a sharp tip, mounted on a cantilever, very close to the sample surface. As the tip moves across the surface, forces between the tip and the sample cause the cantilever to deflect. These deflections are measured by a laser beam reflected from the top of the cantilever onto a photodetector. By recording these deflections, AFM generates a detailed three-dimensional map of the surface. AFM is widely used in materials science, biology, and nanotechnology due to its ability to provide atomic-scale resolution without requiring extensive sample preparation [307].

The surface morphology of the doped films was investigated using an MFP-3D Atomic Force Microscope (Oxford Instruments, UK) operating in tapping mode, by maintaining the amplitude of the cantilever's first resonance constant. Scans were acquired over a 1 µm × 1 µm area at a scan rate of 2 Hz. The tip used was an OPUS 160AC (MikroMasch, Bulgaria), with a cantilever stiffness of 26 N/m and an apex diameter of 8 nm. Data post-treatment for roughness measurement and grains segmentation was performed using MountainsSPIP software (DigitalSurf, France).

3.2.3. X-ray photoelectron spectroscopy

X-ray photoelectron spectroscopy (XPS) is a surface analysis technique used to determine the elemental composition and chemical states of elements within a material, based on the photoelectric effect. When the surface of the specimen is irradiated by X-rays with energy hν, the core electrons are ejected with a kinetic energy (E_{kin}), which can be related to the binding energy of the electrons the following way:

$$E_b = h\nu - E_{kin} - \phi \quad \textbf{(52)}$$

where ϕ denotes the work function of the detector. XPS typically probes a depth of up to approximately 5 nm from the surface, allowing for a detailed surface analysis. The relative intensity of the peaks in the XPS spectrum enables the quantitative determination of the elemental composition.

The technique also allows for the identification of binding and oxidation states. Chemical composition in the bulk of the material is possible by a sequential use of argon sputtering and XPS measurements. XPS is capable of detecting elemental concentrations down to approximately 1% [8], [308].

In this study, XPS analysis was performed using a Kratos Axis Ultra DLD system equipped with a monochromated Al Kα X-ray source (hν = 1486.6 eV) and an argon gun for depth profiling, with a power setting of 150 W. The analysis was conducted over an area of 300 µm x 400 µm, while the depth profiles were obtained from a 3 mm x 3 mm etched area using an Ar^+ ion beam operating at 2 kV. Elemental quantification was carried out using the Cu $2p_{3/2}$, Cr $2p_{1/2}$ and O 1s peaks, with their relative sensitivity factors (RSF) detailed in Table 7.

Table 7 - RSF of the peaks considered for XPS quantification.

Peak	RSF
Cu $2p_{3/2}$	3.547
Cr $2p_{1/2}$	0.809
O 1s	0.780

3.2.4. Transmission electron microscopy

Transmission electron microscopy (TEM) is a powerful imaging technique that uses a focused beam of electrons to investigate the internal structure of thin specimens at high resolution. In a TEM, an electron beam is accelerated at high voltages (100-300 kV) towards the specimen down a column held under vacuum. As the electrons interact with the thin specimen, typically less than 100 nm thick, some are transmitted through it, while others are scattered or absorbed. This interaction allows to gather information regarding the specimen's structure and composition.

Unlike SEM, which relies on secondary electrons emitted from the surface, TEM images are formed based on the transmitted electrons. This enables much higher resolution imaging, down to the atomic scale, due to the shorter wavelength of the high-energy electrons that penetrate between the atomic columns. However, this advantage comes at the cost of requiring meticulous sample preparation to achieve the necessary thinness.

TEM can be operated in two primary modes: TEM mode and Scanning TEM (STEM) mode, as described below.

Transmission electron microscopy mode

In this mode, a broad electron beam illuminates a large area of interest. The transmitted electrons form an image that reveals microstructure details of the sample. Two imaging techniques were employed in this work. The electron beam itineraries for both are illustrated in Figure 21.

- **Bright Field Images**: These images are produced by allowing the central beam of electrons to pass through the objective aperture, providing high contrast images.
- **Dark Field Images**: In contrast, dark field images are generated by allowing only the diffracted electrons to pass through the objective aperture, emphasising differences in structural features based on electron scattering.

Another specialised mode within TEM mode, High-Resolution Transmission Electron Microscopy (HRTEM), enables the visualisation of atomic arrangements within a sample. In HRTEM, the electron beam is focused to achieve extremely high resolution, allowing for the observation of features as small as 0.1 nm. This technique relies on the interference of electron waves, where both transmitted and scattered electrons contribute to the formation of high-contrast images. HRTEM is particularly useful for analysing crystal structures, defects, and interfaces at the atomic level [309], [310].

Scanning transmission electron microscopy mode

In STEM mode, the electron beam is focused to a nanometre-scale diameter and scanned across the area of interest. This method enables high-resolution imaging and the collection of elemental information through Energy Dispersive X-ray Spectroscopy (EDS), as the probe position can be precisely controlled [309], [310].

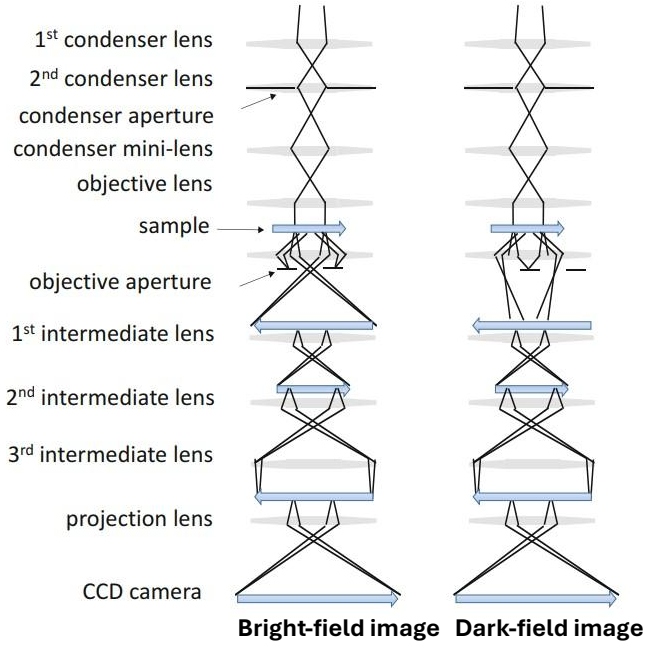

Figure 21 – Electron beam itineraries for bright-field and dark-field imaging in TEM. Adapted from [311].

Experimental procedures

The TEM equipment used in this work was a JEOL F200 Cold Field Emission Gun (FEG) TEM/STEM operating at an acceleration voltage of 200 kV. Sample preparation was conducted using a Focused Ion Beam (FIB) SEM technique. For bright field and dark field imaging analysis, high-contrast apertures with three different hole sizes (120 µm, 60 µm, and 20 µm) were used to optimise image quality.

HRTEM was performed using a condenser lens (CL) aperture of 200 µm and a beam current of 20 nA. This setup allowed for the acquisition of detailed micrographs, particularly at the interfaces of the substrate and film.

STEM imaging was conducted with a CL size of 40 µm and a camera length of 300/120 mm, resulting in a beam current of 95 pA. This configuration enabled the collection of high-resolution images and EDS data, facilitating a comprehensive analysis of the sample's composition and structure.

3.2.5. Energy dispersive X-ray spectroscopy

Energy-dispersive X-ray spectroscopy (EDS) is a powerful analytical technique used to identify the elemental composition of a sample. It relies on the interaction X-ray source with the sample, which stimulates the emission of characteristic X-rays from the atoms within the material. Each element has a unique atomic structure, resulting in a unique set of peaks on its electromagnetic emission spectrum. The positions of these peaks are predicted by Moseley's law, enabling the elemental analysis of a sample. EDS was performed to determine the chemical composition and evaluate the distribution of the chemical elements on delafossite extrinsically undoped and doped films.

In this study, EDS was performed under the STEM mode as mentioned previously. This method is particularly advantageous for providing precise elemental quantification at specific beam scanning positions.

3.2.6. Ultraviolet-visible-infrared spectroscopy

Transmittance and reflectance measurements of the films were conducted using a Perkin Elmer Lambda 950 Ultraviolet-Visible-Near Infrared (UV-Vis-NIR) spectrometer. This instrument employs a deuterium lamp for UV and a tungsten lamp for visible light, along with a photomultiplier for UV-Vis detection and an InGaAs detector for NIR detection. The setup utilises an integrating sphere to collect diffuse light transmittance and reflectance from the sample, covering a range from 2500 nm to 250 nm with a 5-nm interval. The optical band gap of the films was determined using Tauc plots, based on the equation [312],[313]:

$$(\alpha h\nu)^{\frac{1}{n}} = C\left(h\nu - E_g\right) \quad \textbf{(53)}$$

where α is the absorption coefficient, hν the photon energy, E_g the optical band gap and C a constant. The exponent n depends on the nature of the optical transition: its value is 1/2, 2, 3/2 or 3 for direct allowed transitions, indirect allowed transitions, direct forbidden transitions, or indirect forbidden transitions respectively [312].

3.2.7. X-ray diffraction

X-ray diffraction (XRD) is a non-destructive technique commonly used to determine the crystal structures of films and their defects introduced during the film growing. The principle of this technique relies on the interaction of X-rays with a specimen, as the atomic distances in condensed matter are of the same order as the wavelength of X-rays. By directing monochromatic X-rays into the specimen, the interaction of X-ray photons with the lattice atoms leads to scattering in all directions. Then, the photons scattered coherently will be in phase, forming diffracted beams that obey the Bragg's law (Figure 22), given by:

$$2d_{hkl}\sin(\theta) = n\lambda \quad \textbf{(54)}$$

where d_{hkl} is the distance between two adjacent planes (interplanar spacing) with the indices specifying the Miller indices of the appropriate lattice planes, θ is the Bragg angle where the constructive interference (maximum intensity) occurs, n is the diffraction order and λ is the wavelength of the X-ray beam incident on the specimen.

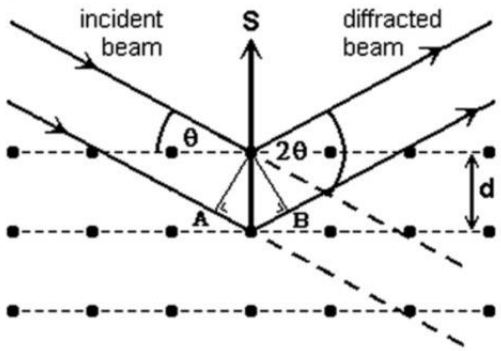

Figure 22 - Visualisation of Bragg's law in a crystalline sample. Constructive interference occurs between scattered X-rays when the path difference AB (nλ) equals $2d_{hkl}\sin(\theta)$. Adapted from [314].

The main characteristics of a Bragg peak include position and intensity. The ideal XRD pattern of a polycrystalline material consists of a narrow, symmetrical, delta function-like peaks at the positions of the Bragg angles according to the crystal unit cell. An X-ray line profile analysis is crucial to analyse the deviations from an ideal powder pattern. These deviations can be attributed to numerous microstructural properties of the specimen, summarised in Table 8 [315], [316].

Table 8 - Peak characteristics and the corresponding information.

Peak characteristic	Concerning information
Position (2θ)	Lattice spacing (d_{hkl})
Broadening	Crystallite size and lattice faults, grains and microstresses
Intensity	Texture

The crystalline structure of the thin films was analysed using a Bruker D8 Discover diffractometer equipped with a Cu Kα radiation source (λ = 1.54184 Å) and operated at 40 kV and 40 mA. Grazing incidence X-ray diffraction (GIXRD) measurements were conducted with an incident angle of 0.5° and a step size of 0.02°.

3.3. Electrical characterisation of delafossite thin films

3.3.1. Electrical measurements at room temperature

Four-point probe

The four-point probe technique is a method used to measure the sheet resistance (R_S) of bulk or thin film semiconductors. If the film thickness (h_f) is known, the in-plane conductivity can also be determined. Conceptually a source current (I_{DC}) passes through two (external) terminals while a generated voltage (V) from the other two (inner) terminals is measured [8], [246]. Considering the geometric correction factor of the sample (f = 4.532), the sheet resistance is given by:

$$R_S = \frac{V.f}{I_{DC}} \quad \textbf{(55)}$$

and then the conductivity by:

$$\sigma = \frac{1}{R_S h_f} \quad \textbf{(56)}$$

The electrical measurements were conducted using a Multiheight four-point probe system from Jandel Engineering Limited (UK), which features a linear probe arrangement with a 1 mm spacing between probes. The setup was connected to a Keithley 2401 SourceMeter® (Keithley Instruments, USA).

Hall effect

In classical semiconductors, both the carrier concentration and electrical mobility can be obtained through Hall effect measurements. The Hall effect measures the response of drift carriers in a magnetic field [6]. However, applying this technique to degenerate semiconductors with very low charge carrier mobilities presents significant challenges and is generally considered questionable, particularly in semiconductors that rely on hopping conduction [51], [85], [258], [272], [317], [318].

In such cases, accurately determining the carrier concentration and identifying the dominant carriers require either very high magnetic fields or complex mathematical models, which are not always reliable [205], [319]. The general formulas for the Hall coefficient (R_H) and the Hall mobility (μ_H) are given by:

$$R_H = \frac{\boldsymbol{E_y}}{\boldsymbol{j_x} \times \boldsymbol{B_z}} = \frac{V_H h_f}{I_x \times \boldsymbol{B_z}} = \frac{1}{nq} \quad \textbf{(57)}$$

$$\mu_H = \frac{\sigma}{nq} = \frac{\rho^{-1}}{q(qR_H)^{-1}} = \frac{R_H}{\rho} \quad \textbf{(58)}$$

where R_H is the Hall coefficient, $\mathbf{E_y}$ is the y-component of the electric field, I_x current in the x-direction, $\mathbf{j_x}$ is the x-component of the current density of the charge carriers, V_H is the Hall voltage, and $\mathbf{B_z}$ is the z-component of the magnetic field [246].

In the case of high carrier concentrations, the Hall signal is very small compared to sizable offset voltages, leading to significant errors and uncertainties. Previous measurements on off-stoichiometric copper chromium delafossites reveals values around 0.01 $cm^2V^{-1}s^{-1}$ after numerous approximations and corrections (Figure 23) [319]. In such cases, the Seebeck effect is more reliable.

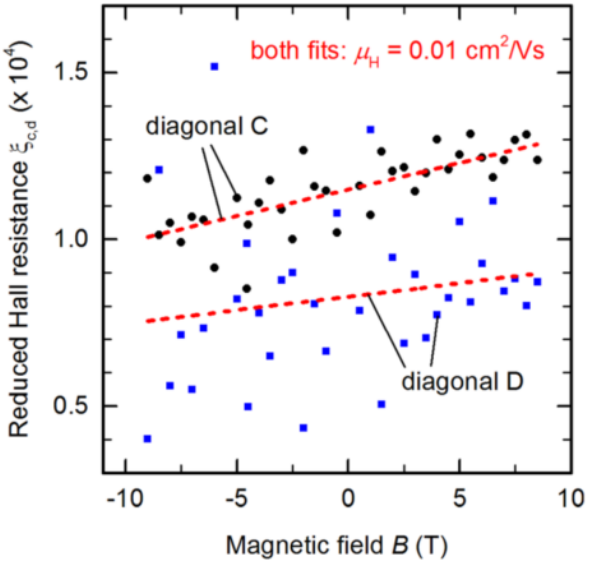

Figure 23 - Limiting case for the offset correction for Hall measurements of a non-intentionally-doped $CuCrO_2$ thin film. The linear fits yielded a p-type conduction with a mobility of the order of 0.01 $cm^2V^{-1}s^{-1}$. Adapted from [319].

Seebeck effect

The Seebeck effect, also known as thermopower (S) is defined as the open-circuit potential difference (ΔV) generated across a sample in response to an imposed temperature gradient:

$$S = -\frac{V_h - V_c}{T_h - T_c} = -\frac{\Delta V}{\Delta T} \qquad \textbf{(59)}$$

where the subscripts h and c refer to the hot and cold terminals, respectively. Thermoelectric measurements are valuable for providing information regarding the predominant charge carriers and the dominant scattering mechanisms. The Seebeck effect arises from an electric field established under steady-state conditions, balancing the diffusion current caused by a temperature gradient with the counteracting current. The direction of the field tells the type of dominant carriers [6], as the predominant charge carriers diffuse to the colder side; therefore, the sign of S is negative (positive) for a n (p)-type material. The carrier concentration is typically inversely related to the magnitude of the Seebeck coefficient. This relationship is influenced by electrical conductivity, with higher conductivity generally resulting in a lower Seebeck coefficient.

Room-temperature thermoelectric measurements were performed using a home-built Seebeck effect setup. The sample was clamped between two copper plates as electrical contacts. A temperature gradient was applied across the sample by heating and cooling the extreme opposite

sides of the sample. The potential difference across each side was measured using a Keithley 2614B SourceMeter® (Keithley Instruments, USA). The Seebeck coefficient was then determined by analysing the slope of the plot of the voltage potential difference (ΔV) as a function of the temperature difference (ΔT), as described by Equation (58).

3.3.2. Thermoelectric and electrical measurements with temperature

Measurements of the electrical resistivity ρ(T) and Seebeck coefficient S(T) as functions of temperature were both performed using a Linseis LSR-3 system, utilising the steady-state DC-method/slope-method. In this setup, a rectangular sample (15 mm x 5 mm) is placed vertically between two electrodes. The lower electrode block contains a heating coil, referred to as the secondary heater. When the furnace heats up and reaches the target measurement temperature, the secondary heater generates a predefined temperature gradient along the sample. Two thermocouples, in lateral contact with the sample, measure the temperature gradient between the hot (T_h) and cold (T_c) contacts on the sample. Additionally, one of the two thermocouples measures the potential difference (ΔV) (Figure 24a). The Seebeck coefficient is then calculated according to Equation (58).

Electrical resistivity is measured using the DC four-point probe method, with a 4-mm distance between the inner probes. Under thermal equilibrium conditions (ΔT = 0 K), the measurement principle is the same as that described for the four-point probe technique. The resistivity is calculated using the following equation:

$$\rho = \frac{1}{\sigma} = \frac{V}{I_{DC}} \frac{w_f . h_f}{l} \qquad \textbf{(60)}$$

where V is the measured voltage, I_{DC} is the applied DC current, w_f and h_f are the width (0.5 cm) and thickness of the delafossite film, and l is the distance between the thermocouples (Figure 24b) [320].

Before the measurements, helium was purged and pumped into the closed furnace twice. Then the vacuum was then achieved up 10^{-3} bar. The temperature gradient was set to 2 K, and the absolute Seebeck coefficient value was adjusted using a platinum wire reference.

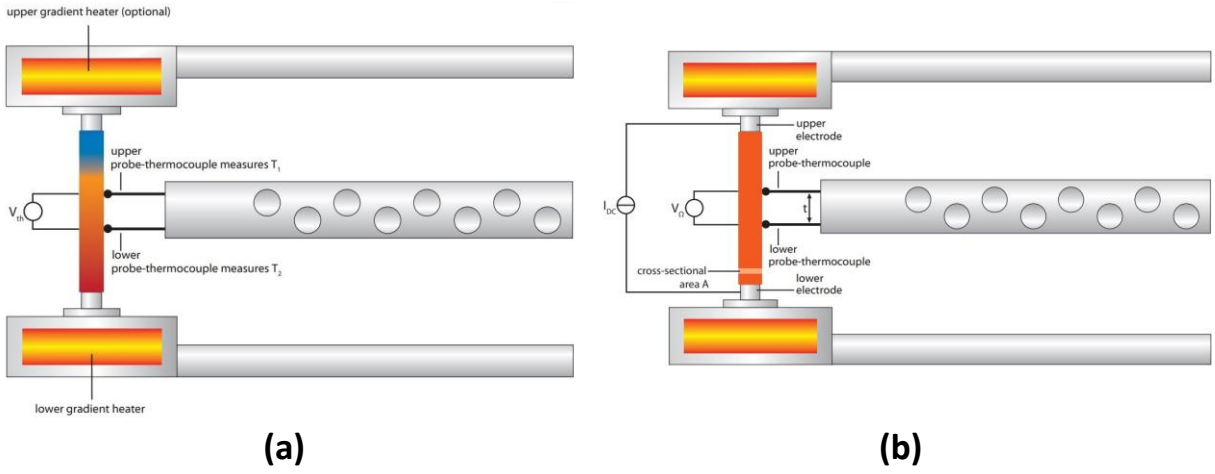

Figure 24 – (a) Seebeck coefficient and (b) resistivity measurement modes in LSR - 3 system [320].

3.4. Techniques for inducing and measuring strain

The following techniques were employed in this work to induce strain and study its effects on the electrical properties of delafossite thin films:

- Applying an external magnetic field on a delafossite film deposited on a magnetostrictive material (nickel).
- Bending the substrate using a home-built strain gauge setup, where the change in the resistivity of the delafossite film was measured as a function of the applied external stress.
- Thermal strain generated by the mismatch between coefficients of thermal expansion of the film and substrates.
- Extrinsic doping.

In this thesis, the focus is on polycrystalline delafossite thin films deposited on planar substrates, where a thin-film approximation is applied. Except in the case of doping, strain is transferred from the planar substrate into the thin film, which exhibits a randomly oriented polycrystalline structure. The strain components in the substrate can be transferred to the film, affecting its structural properties. To analyse this, we use two orthogonal reference systems: one attached to the substrate strain and the other to the film (Figure 25). We represent a crystalline grain within the film to understand how strain is transferred.

In the substrate, the strain components in an orthogonal reference system are related to the lattice parameters of the substrate and are denoted as:

$$\xi_{sub} = (\xi_x, \xi_y, \xi_z) \quad \textbf{(61)}$$

In the orthogonal system associated with the film, the components correspond to the lattice parameters (a, b and c) of the film:

$$\xi_f = (\xi_u, \xi_v, \xi_w) \quad \textbf{(62)}$$

The relationship between the strain in the substrate and the film is given by:

$$\xi_f = R \cdot \xi_{sub} \quad \textbf{(63)}$$

where R is the 3 x 3 rotation matrix that transforms vectors from the substrate's coordinate system to the film's coordinate system. This matrix is constructed from the direction cosines between the old and new coordinate axes:

$$R = \begin{pmatrix} \cos(\alpha) & \cos(\beta) & \cos(\gamma) \\ \cos(\alpha') & \cos(\beta') & \cos(\gamma') \\ \cos(\alpha'') & \cos(\beta'') & \cos(\gamma'') \end{pmatrix}$$

where:

- α, β, γ are the angles between the u-axis and the x, y, z axes, respectively.
- α', β', γ' are the angles between the v-axis and the x, y, z axes, respectively.

- α'', β'', γ'' are the angles between the w-axis and the x, y, z axes, respectively.

For epitaxially grown films, the rotation matrix R simplifies to the identity matrix, making the strain transfer straightforward. However, for polycrystalline films, the strain components in the film can be expressed in terms of the substrate strain components:

$$\xi_{(f,u)} = cos(\alpha) \cdot \xi_x + cos(\beta) \cdot \xi_y + cos(\gamma) \cdot \xi_z \quad \textbf{(64)}$$

$$\xi_{(f,v)} = cos(\alpha') \cdot \xi_x + cos(\beta') \cdot \xi_y + cos(\gamma') \cdot \xi_z \quad \textbf{(65)}$$

$$\xi_{(f,w)} = cos(\alpha'') \cdot \xi_x + cos(\beta'') \cdot \xi_y + cos(\gamma'') \cdot \xi_z \quad \textbf{(66)}$$

In most cases, $\xi_z \approx 0$ as this component acts perpendicular to the film's surface, not deforming the film significantly. Importantly, the magnitudes of the strain vectors should be conserved, assuming no energy losses:

$$\xi_{sub,x}^2 + \xi_{sub,y}^2 = \xi_{f,u}^2 + \xi_{f,v}^2 + \xi_{f,w}^2 \quad \textbf{(67)}$$

This implies that the strain in the x and y directions of the substrate is distributed among the u, v, and w directions of the film, converting the substrate's surface strain into a volumetric strain in the film. Consequently, the deformation in the film's planar directions (u and v) is typically smaller than the substrate's planar deformation.

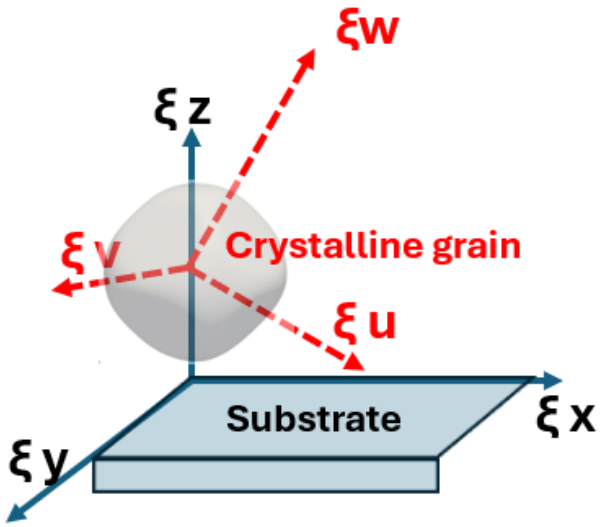

Figure 25 – Orthogonal reference systems considered for the strain transferred from the substrate to a polycrystalline film.

Let us consider the TEM results discussed earlier. Initially, the film grows epitaxially with respect to the substrate for the first few nanometres, meaning that the x and y strain components of the substrate are fully transferred to the u and v strain components in the film. However, as the growth proceeds, the random orientation of the grains results in a redistribution of strain in all crystallographic directions.

It is important to note that there are limited reports on the elastic properties of delafossite thin films, and none on off-stoichiometric ones. For bulk stoichiometric delafossite, the Young's modulus is approximately 0.045 GPa. Such a low Young's modulus indicates that delafossite is relatively elastic or flexible, meaning that it requires minimal stress to induce strain within the elastic region.

3.4.1. Magnetostriction

Magnetoelastic effects refer to the coupling between the magnetic and elastic properties of a material and can be classified into direct and inverse effects. Magnetostriction is a direct magnetoelastic effect observed exclusively in ferromagnetic materials. In the absence of an external magnetic field, the spins in a ferromagnetic material are aligned within magnetic domains, but these domains are oriented randomly with respect to each other, resulting in no net magnetization. Upon application of a magnetic field, these spins gradually align in the direction of the field, causing a change in the material's shape or dimensions. This phenomenon is known as the Joule magnetostriction effect. The magnetostriction coefficient (λ) quantifies this effect and is defined as the ratio of the change in length Δl to the original length (l_0) of the material:

$$\lambda = \frac{\Delta l}{l_0} \quad \textbf{(68)}$$

In a saturated field, λ is known as the saturation magnetostriction (λ_S). This discussion focuses solely on the longitudinal effect; other effects such as induced volume changes, torsion, or bending under a magnetic field are beyond the scope of this work. The inverse magnetoelastic effect is known as the Villari effect [321].

In this study, the effect of strain on delafossite was investigated by applying a magnetic field to a delafossite film grown on a magnetostrictive nickel substrate. Prior to the magnetoelastic (ME) measurements, a 50 nm insulating layer of Al_2O_3 was deposited on the nickel substrate (λ_S = – 11.2 ppm) using ALD. Subsequently, a 70-nm thick delafossite film was grown atop the of Al_2O_3 layer via MOCVD.

The magnetostriction coefficient was measured using a custom-built magnetoelastic measurement setup comprising Helmholtz coils and an electromagnet to produce both a small alternating current (AC) magnetic field and a direct current (DC) bias magnetic field, respectively (Figure 26). The sample was secured in a holder positioned between the coils, and a Hall probe (Hirst Magnetics, GM08) was placed near the sample to measure the magnetic field. The AC and DC bias fields were generated using a dual-channel frequency generator (Tektronix, AFG1062).

The output signal from the ME sample was analysed using a lock-in amplifier (Stanford Research Systems, SRS865A, 4 MHz) and data were collected with an oscilloscope (Teledyne LeCroy, WaveAce 2024). The key specifications of the ME measurement setup are summarised in Table 9. For electrical contacts, the sample was mounted on a printed circuit board (PCB), and silver glue was used to attach wires to the top and bottom electrodes of the ME chip.

The ME voltage (V_{out}) was measured with the lock-in amplifier while the sample was subjected to a DC magnetic field (H_{DC}) ranging from -200 to 200 Oe, combined with a small AC

magnetic field of 8.5 Oe at a constant frequency of 46 Hz. The magnetostriction coefficient was calculated using the following equation:

$$\lambda = \frac{V_{out}}{h_s H_{AC}} \quad (69)$$

where h_s is the thickness of the nickel substrate (600 µm), and H_{AC} is the magnitude of the applied AC magnetic field.

Table 9 - Capabilities of ME bench setup.

Parameter	Range
AC field max. with Helmholtz coils	± 20 mT (± 200 Oe, ± 16 kA m^{-1})
DC field max. with electromagnet	± 0.25 T (± 2500 Oe, ± 200 kA m^{-1})
AC field frequency range	1 Hz – 5 kHz

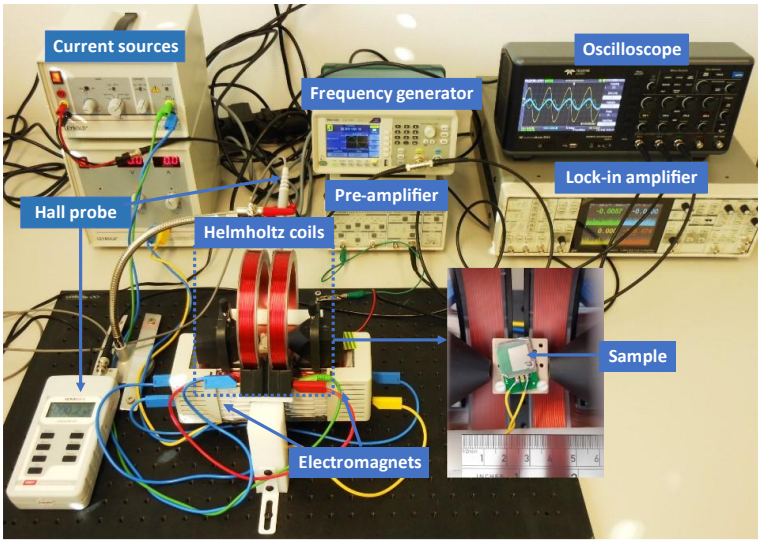

Figure 26 - Magnetostriction bench setup.

3.4.2. Strain induced by mechanical bending

Piezoelectric effect

When an external uniaxial or hydrostatic stress is applied to a material, resulting in a change in its electrical resistivity, the material exhibits piezoresistive behaviour [322]. This phenomenon is closely related to the direct piezoelectric effect, wherein mechanical stress induces an electric charge within material. Additionally, mechanical strain can alter the film's geometry – such as causing it to contract – which, in turn, affects its resistance. This geometric alteration interacts with the piezoresistive effects, leading to a complex overall response of the material to the applied stress.

Before the development of heteroepitaxy and CVD, variable strain transducers were developed to exploit the piezoresistive effect in silicon and germanium, enabling the construction of strain gauges and stress transducers that responded to strain or stress [286]. The gauge factor (k) measures the ratio of the relative change in electrical resistance to the applied mechanical strain.

This resistance change has two primary components: one due to changes in the physical dimensions of the resistor (such as length and cross-sectional area) and another due to semiconductor-specific effects, including changes in resistivity effects, including changes in resistivity (Δρ) and mobility (Δμ), relative to their unstrained values (ρ_0 and μ_0).

$$k = \frac{\Delta R}{R_0}\frac{1}{\varepsilon} = 1 + 2\nu_f + \frac{\Delta\rho}{\rho_0}\frac{1}{\varepsilon} = 1 + 2\nu_f - \frac{1}{\varepsilon}\frac{\Delta\mu}{\mu} \qquad \textbf{(70)}$$

where ΔR is the change in resistance, R_0 is the resistance of the unstrained sample, ε is the mechanical, ν_f is the Poisson's ratio. The term $1+2\nu_f$ is associated with changes in dimensions of the semiconductor due to its Poisson ratio, while $\Delta\rho/(\rho_0\varepsilon)$ and $\Delta\mu/(\mu\varepsilon)$ are attributed to the piezoresistive effect. In semiconductors, k is primarily influenced by Δρ, with the geometric factor playing a minor role. For instance, in silicon and germanium, the piezoresistive term is 50-100 times larger than the geometric term. Consequently, strain gauges are commonly used for experimental stress analysis [288], [289], [323].

A custom-built strain gauge bench setup was employed to measure the electrical resistance variation of the semiconducting sample under externally induced strain through controlled bending (Figure 27 and Figure 28). This setup consists of an aluminium double clamped cantilever (140 mm length, 30 mm width, 0.5 mm thickness) where the test sample is glued (Loctite 401, RS) in the middle of the beam. The deflection in the centre of the cantilever is precisely controlled by a differential micrometer drive (DRV304, ThorLabs) with a coarse adjustment range of 13 mm with a resolution of 5.0 µm, along with a fine adjustment range of 300 µm with a resolution of 0.5 µm. To calibrate deflection-to-strain values, reference strain gauges (RS PRO, 120 Ω, ref.: 865-6226, RS) with Cu/Ni electrodes embedded in polyimide foil are also glued on the same cantilever location. The setup allows for a controlled strain sensitivity of $3\text{x}10^{-7}$ μm^{-1} with a maximum applied strain limit of $4\text{x}10^{-3}$ [304].

A 200-nm thick $Cu_{2/3}Cr_{4/3}O_2$ film was deposited on Schott D 263® T eco glass (length = 55 mm, width = 7 mm and R_0 = 4.9 kΩ), and subsequently glued in the centre of the aluminium bar with a test cantilever attached. The relationship between the deflection (d) applied at the centre of the beam and the strain at the same point is described by:

$$\varepsilon = -\frac{12td}{l^2} \qquad \textbf{(71)}$$

where t is the combined thickness of the aluminium bar and the sample, d is the deflection and l the length of the beam [304],[324].

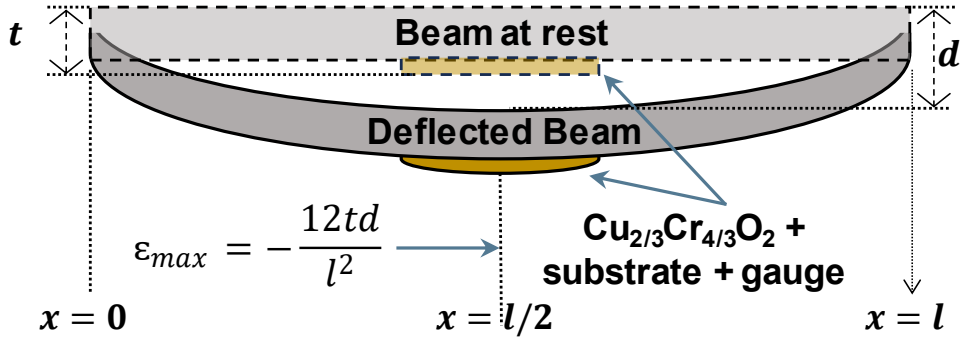

Figure 27 – Schematic of the home-built strain gauge bench setup used to apply stress on the semiconducting sample (t = thickness of bar + delafossite sample, d = deflection, l = beam length) [304].

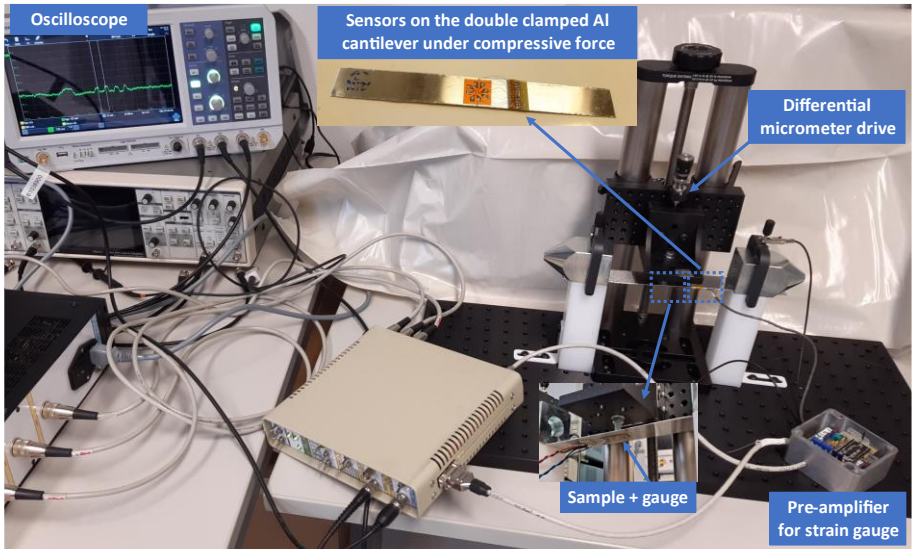

Figure 28 - Strain gauge bench setup.

Figure 29 depicts the schematic of the pre-amplifier for the strain gauge. The calibration curves of the strain gauge are depicted in Figure 30.

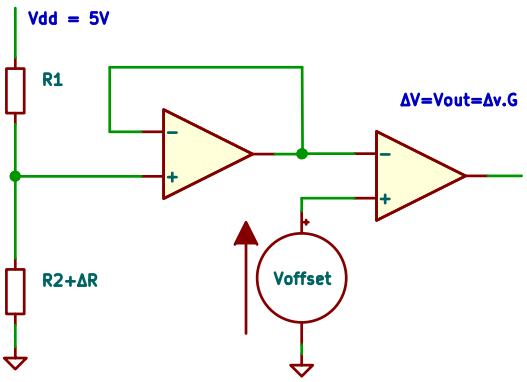

Figure 29 - Schematic of the pre-amplifier for strain gauge.

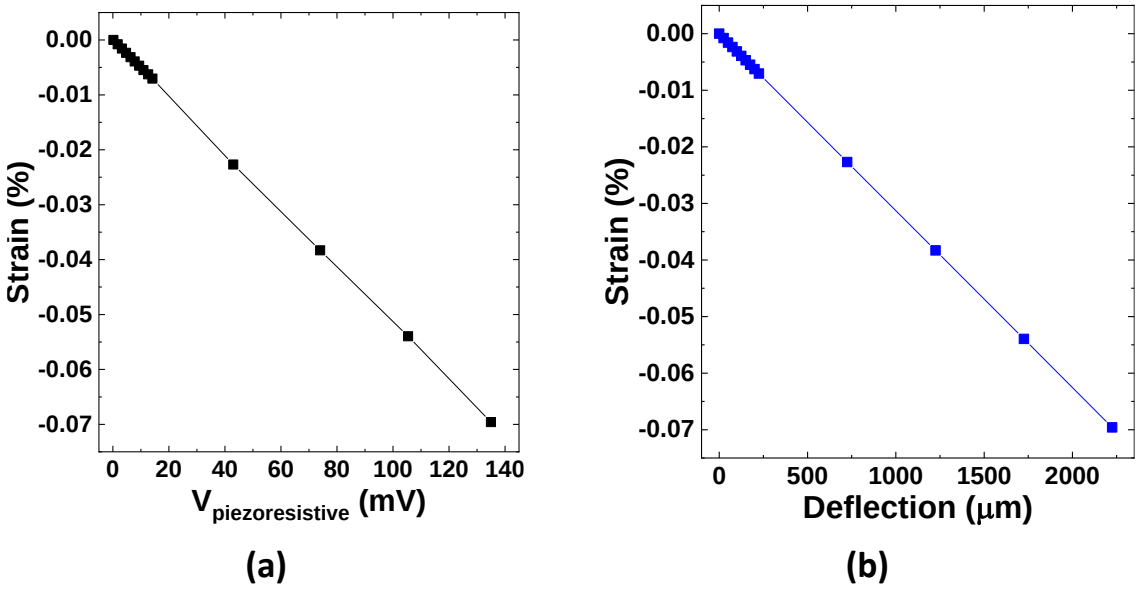

Figure 30 - Calibration of strain gauge.

The variation of resistance of the sample (ΔR/R) is obtained as described below. For V_{out} = 0:

$$V_{offset} - \frac{R_2}{R_1 + R_2} V_{DD} = 0 \quad \textbf{(72)}$$

For V_{out} = ΔV:

$$V_{offset} - \frac{R_2 + \Delta R}{R_1 + R_2 + \Delta R} V_{DD} = \Delta v = \frac{\Delta V}{G} \quad \textbf{(73)}$$

This yields the following expression for ΔR:

$$\Delta R = -\frac{(R_1 + R_2)^2}{\left(1 + \frac{V_{DD}}{\Delta v}\right) R_1 + R_2} \quad \textbf{(74)}$$

When R_1 = R_2 = R, it yields:

$$\frac{\Delta R}{R} = -2\left(1 + \frac{\frac{V_{dd}}{2\Delta V}}{G}\right)^{-1} \quad \textbf{(75)}$$

3.4.3. Thermal strain

Nearly all materials undergo a change in volume or dimensions with temperature, as the increase in thermal energy leads to an increased amplitude of atomic vibrations [96]. The fractional change in the lattice parameter per unit temperature is defined as the coefficient of thermal expansion (CTE or α):

$$\alpha = \frac{1}{a_0}\left(\frac{\partial a}{\partial T}\right)_{T_0} \quad \textbf{(76)}$$

where a_0 is the original lattice parameter of the substance at temperature T_0, and ∂a/∂T is the rate of change of the lattice parameter with respect to temperature T_0 [248]. It is more commonly represented as a cumulative expansion coefficient α along each lattice direction, referred to as the linear coefficient of thermal expansion (α_{lin}):

$$\alpha_{lin} = \frac{a - a_0}{(T - T_0)a_0} = \frac{\varepsilon}{T - T_0} \quad \textbf{(77)}$$

The lattice parameters can be calculated from XRD measurements using the Rietveld method [325]. Common values for α are on the order of 10^{-5} K^{-1}. Typically, α can be determined using the dilatometry method. α is strongly dependent on multiple factors such as the synthesis method, particle size, morphology and crystal phases [326].

Typically, the substrate material and the growth film have different CTEs. This mismatch results in thermal strain (ε_{th}) due to the difference between the film's CTE (α_f) and that of the substrate (α_s). The thin film approximation assumes that the film's thickness is negligible compared to the substrate's dimensions, allowing the substrate to dominate the mechanical behaviour and simplifying the strain analysis. This strain can be tensile ($\varepsilon_{th} > 0$) or compressive ($\varepsilon_{th} < 0$), depending on whether α_f is larger or smaller than α_s, respectively, at room temperature (Figure 31). For a continuous, non-epitaxially film deposited at a temperature T_d, ε_{th} can be calculated (within the elastic regime) using the following expression [327]–[329]:

$$\varepsilon_{th} = \int_{T_d}^{T_m} (\alpha_s - \alpha_f)\, dT \cong \left(\alpha_s - \alpha_f\right)(T_m - T_d) \quad \textbf{(78)}$$

where T_m is the temperature at which the thermal strain is measured post-deposition, typically room temperature. The resulting thermal stress (σ_{th}) is given by [328],[330],[331]:

$$\sigma_{th} = \frac{E_f}{1 - \nu_f}\left(\alpha_s - \alpha_f\right)(T_m - T_d) \quad \textbf{(79)}$$

where E_f is the Young modulus of the film. Additionally, it is crucial to consider the strain distribution along the z-axis. The maximum strain occurs at the film-substrate interface, after which the film begins to relax. The average stress across the film thickness (σ_{avg}) can be obtained by integrating the in-plane stress (σ_{in}) from the film-substrate interface (z = 0) to the film's surface ($z = h_f$) [327]:

$$\sigma_{avg} = \frac{E_f}{1 - \nu_f}\varepsilon_{avg} = \frac{1}{h_f}\int_0^{h_f} \sigma_{in}(z)\, dz \quad \textbf{(80)}$$

where ε_{avg} represents the average strain within the film. In thicker films, the impact of strain may be less significant due to the predominant elastic behaviour of the entire film [304].

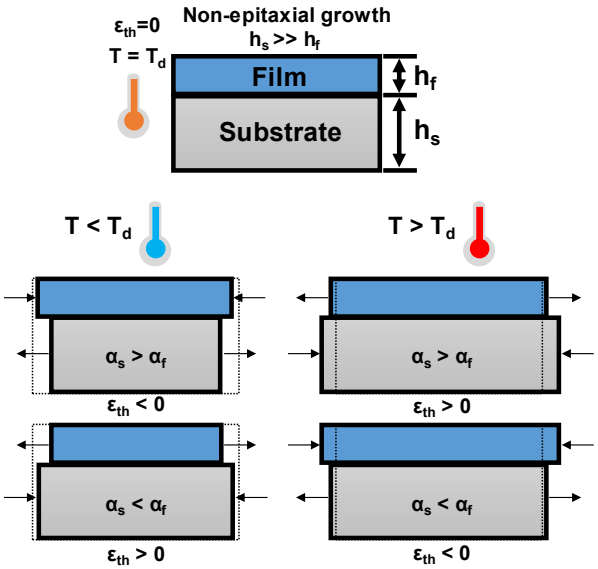

Figure 31 – Schematic representation of thermal strain development in a thin film deposited on a substrate with differing CTEs. The films are stress-free at T_d. When $T_d \neq 0$, the films experience either compressive or tensile strain based on the difference between α_s and α_f. Adapted from [304].

Considering these factors, the influence of thermal strain on the electrical properties of delafossite was evaluated by depositing films with thicknesses of approximately 70 nm and 200-300 nm onto six different substrates. The CTEs, thicknesses and suppliers of the substrates are detailed in Table 10. Given the limited data on reported CTEs of $CuCrO_2$, this study used the value reported by Ross, which indicates a nearly linear thermal expansion for $CuCrO_2$ with α_f = 10.26 ppm K^{-1} [96]. The calculated thermal strain of $CuCrO_2$ on different substrates, as derived from Equation (78) is illustrated on Figure 32.

Table 10 - Properties of the substrates used throughout this work.

Substrate	α_s (ppm K^{-1})	Thickness (µm)	Orientation	Supplier
Fused-silica quartz	0.54	500 ± 20	Amorphous	Siegert Wafer GmbH, Germany
α-Al_2O_3	6.7 (||a)	480 ± 20	Hexagonal (0001)	
Schott AF 32® eco glass	3.2	70	Amorphous	Schott Benelux B.V., The Netherlands
Schott D 263® T eco glass	7.2	50		
$SrTiO_3$	9.0	500	Cubic	Crystal GmbH, Germany
MgO	12.8			

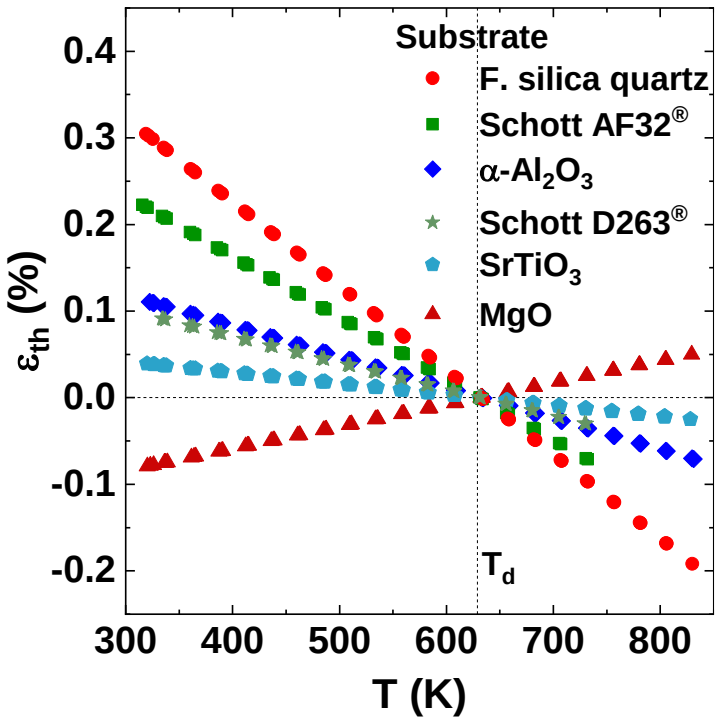

Figure 32 - Expected thermal strain on delafossite film in the temperature range T = 300 - 850 K, for a deposition at 630 K [304].

Equation (78) implies that ε_{th} is zero when $T_m = T_d$. At temperatures below T_d, the stress is positive if $\alpha_f > \alpha_s$, and negative if the opposite is true. This suggests the presence of thermal strain during room-temperature measurements on thin films. Among the used substrates, only MgO exhibits a $\alpha_s > \alpha_f$, provided the referenced values are accurate.

3.4.4. Strain measurements by X-ray diffraction

sin²ψ method

Residual stresses can be assessed by X-ray Stress Analysis (XSA), where the strain is derived by comparing the interplanar spacing of the stressed sample with that of the unstressed reference (d_0). The in-plane strain can be quantified using a direct strain assessment via the $\sin^2\psi$ method, a widely used technique for XSA. In films under stress, by measuring the position of a Bragg reflection at various tilt angles[6] (ψ) of the sample with respect to the scattering plane, the Bragg peak shifts with varying orientation. Considering the biaxial strain model (which is valid for the thin film approximation), for various tilt angles, the strain ε_ψ is determined according to:

$$\varepsilon_\psi = \frac{d_\psi - d_0}{d_0} \qquad (81)$$

[6] The tilt angle ψ quantifies the amount of tilting of the sample normal with respect to the scattering vector or with respect to the scattering plane. Note that sometimes the tilt angle is denoted by χ, where χ = 90° - ψ

where d_ψ is the interplanar spacing measured at a tilt angle ψ. A tensile (compressive) strain causes a peak shift to lower (higher) scattering angles, corresponding to higher (or lower) d values, respectively. By plotting d_ψ vs $\sin^2\psi$, the stress can be obtained, provided the elastic constants are known:

$$d_\psi = \sigma \frac{(1+\nu_f)}{E_f} d_n \sin^2\psi + d_n \quad \textbf{(82)}$$

where d_n corresponds to the lattice spacing at ψ = 0. The slope of the plot yields a linear behaviour when the film is under biaxial stress. A positive (negative) slope indicates that the film is under tensile (compressive) stress [315].

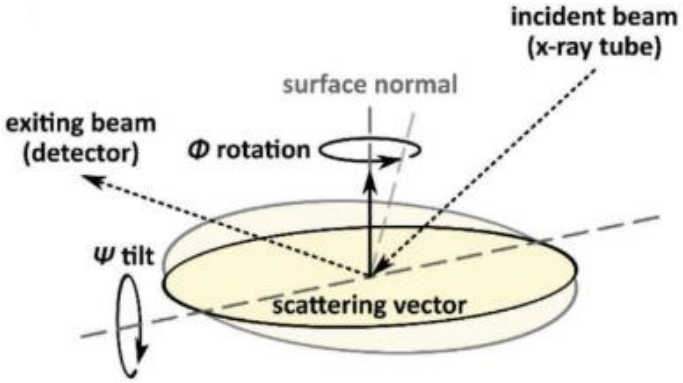

Figure 33 - Schematic of $\sin^2\psi$ X-ray diffraction configuration. Change of the sample orientation relative to the scattering vector via ψ tilts. Adapted from [332].

Pseudo-Voigt fitting function

In this study, the average crystallite size and microstrain were estimated using single-line profile analysis with a Pseudo-Voigt (f_{pV}) fitting function. This function combines a Cauchy-Lorentz function (f_C) with a Gaussian function (f_G), defined as:

$$f_{pV} = \eta f_C(2\theta) + (1-\eta) f_G(2\theta) \quad \textbf{(83)}$$

where the η is the profile shape factor, describing the contribution of the Cauchy-Lorentz component to the mixed profile. This factor is empirically related to the integral breadths of the Cauchy-Lorentzian (β_C) and Gaussian components (β_G), as well as the integral breadth of the Bragg peak (β), according to:

$$\beta_C = (0.017475 + 1.500484\eta - 0.534156\eta^2)\beta \quad \textbf{(84)}$$

$$\beta_G = \left(0.184446 + 0.812692\sqrt{1 - 0.998497\eta} - 0.659603\eta + 0.445542\eta^2\right)\beta \quad \textbf{(85)}$$

The average crystallite size (D) is determined using the Debye-Scherrer equation:

$$D = \frac{K\lambda}{(\beta_C - \beta_{C,inst})\cos(\theta)} \quad \textbf{(86)}$$

where K is the Scherrer constant (0.89 < K < 1.0) and $\beta_{C,inst}$ is the Cauchy-Lorentzian instrumental broadening, determined using a reference sample (corundum). This equation provides the crystallite size along the direction of the diffraction planes.

The Gaussian component of f_{pV} function is used to determine the microstrain ($\tilde{\varepsilon}$), defined as the average relative change in lattice spacing within the crystallites. This is given by:

$$\tilde{\varepsilon} = \frac{d - d_0}{d_0} = \frac{cotan(\theta)}{4}\sqrt{\beta_G^2 - \beta_{G,inst}^2} \quad \textbf{(87)}$$

where d and d_0 are the strained and unstrained lattice spacings, respectively, and $B_{G,inst}$ is the Gaussian instrumental broadening [315].

Chapter 4 – Characterisation of delafossite thin films

This chapter provides a thorough presentation and interpretation of the experimental results obtained during this research concerning the properties of the delafossite thin films.

It starts by examining the morphology of films deposited on different substrates, presenting and analysing micrographs obtained from Scanning Electron Microscopy (SEM) and Transmission Electron Microscopy (TEM). Following this, the chapter details the results from X-ray Photoelectron Spectroscopy (XPS), with a focus on the chemical environment and compositional analysis. A dedicated section then discusses the X-ray diffraction results, highlighting the use of the Pseudo-Voigt fitting function to estimate the average crystallite size and microstrain. The chapter concludes by addressing the stability of delafossite under various thermal post-treatments. Given the anticipation of high-temperature experiments at the outset of this research, it was essential to confirm that no phase changes occurred.

4.1. Thin films morphology

The morphology and thickness of copper chromium oxide delafossite thin films were analysed using SEM. To investigate the influence of strain on the electrical properties of delafossite thin films, two batches of films were intentionally grown on various substrates: one with minimal thickness and another with thicker films. According to Equation (80), the average stress is inversely proportional to the film thickness, indicating that thinner films experience higher average stress. It was observed that continuous and conductive films with thicknesses below approximately 70 nm could not be synthesized. When the deposition time (t_d) was less than 20 min, no continuous films were formed due to the particulate growth and nucleation process, resulting only in particle growth during these shorter deposition periods. This phenomenon is attributed to the insufficient surface diffusion and limited adatom mobility, which are crucial for the coalescence of nanoparticles into a uniform film. Figure 34 shows the growth of copper chromium oxide particles on silicon after 2 min of deposition, illustrating the incomplete coalescence of these delafossite particles. Therefore, the deposition times for delafossite films by MOCVD were set to 20 and 60 min, yielding thicknesses of approximately 70 and 200-300 nm, respectively. Under these conditions, continuous films are formed, and their room temperature electrical conductivity is measurable using the Linseis LSR-3 setup, with conductivity values exceeding 5 S cm^{-1}.

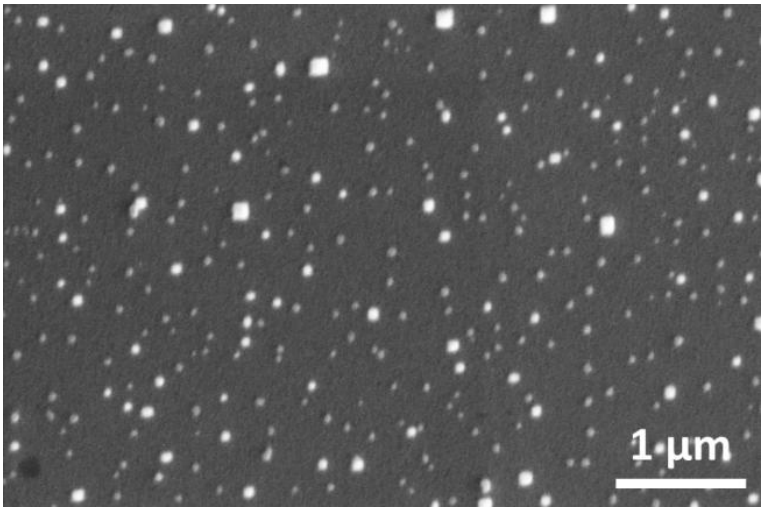

Figure 34 - Surface SEM image of CCO particles grown on Silicon for 2 min.

Figure 35 depicts top-view micrographs of films grown for 60 min at 630 K on various substrates used in this study. The films exhibit a granular structure, which can be attributed to differing thermal expansion coefficients between the delafossite films and these substrates, which influence the nucleation and growth kinetics during deposition. The granular nature indicates a polycrystalline growth mode where individual crystallites are separated by grain boundaries, which can impact the electrical and thermal properties of the films. The varying morphologies observed highlight the significant role of substrate choice in determining the microstructural properties of delafossite thin films. Figure 36 illustrates cross-sectional SEM micrographs of $Cu_{2/3}Cr_{4/3}O_2$ deposited on various substrates for 60 min at 370 °C. The films are compact and dense, with a granular appearance and small particle size, characteristic of the polycrystalline nature of delafossite.

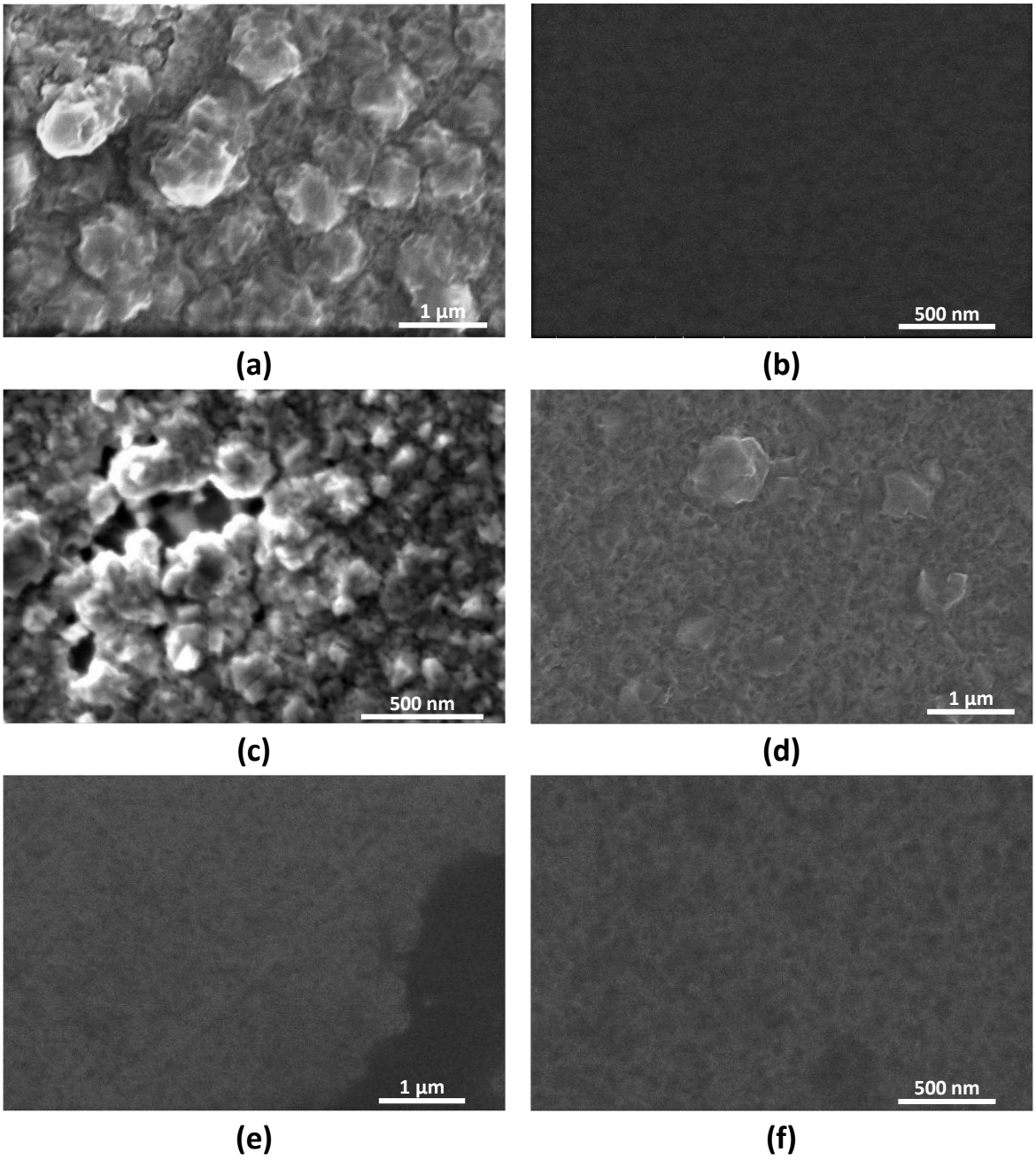

Figure 35 - Top-view SEM micrographs of delafossite films on (a) fused-silica quartz, (b) Schott AF 32® eco glass, (c) Schott D 263® T eco glass, (d) α-Al_2O_3, (e) $SrTiO_3$, and (f) MgO.

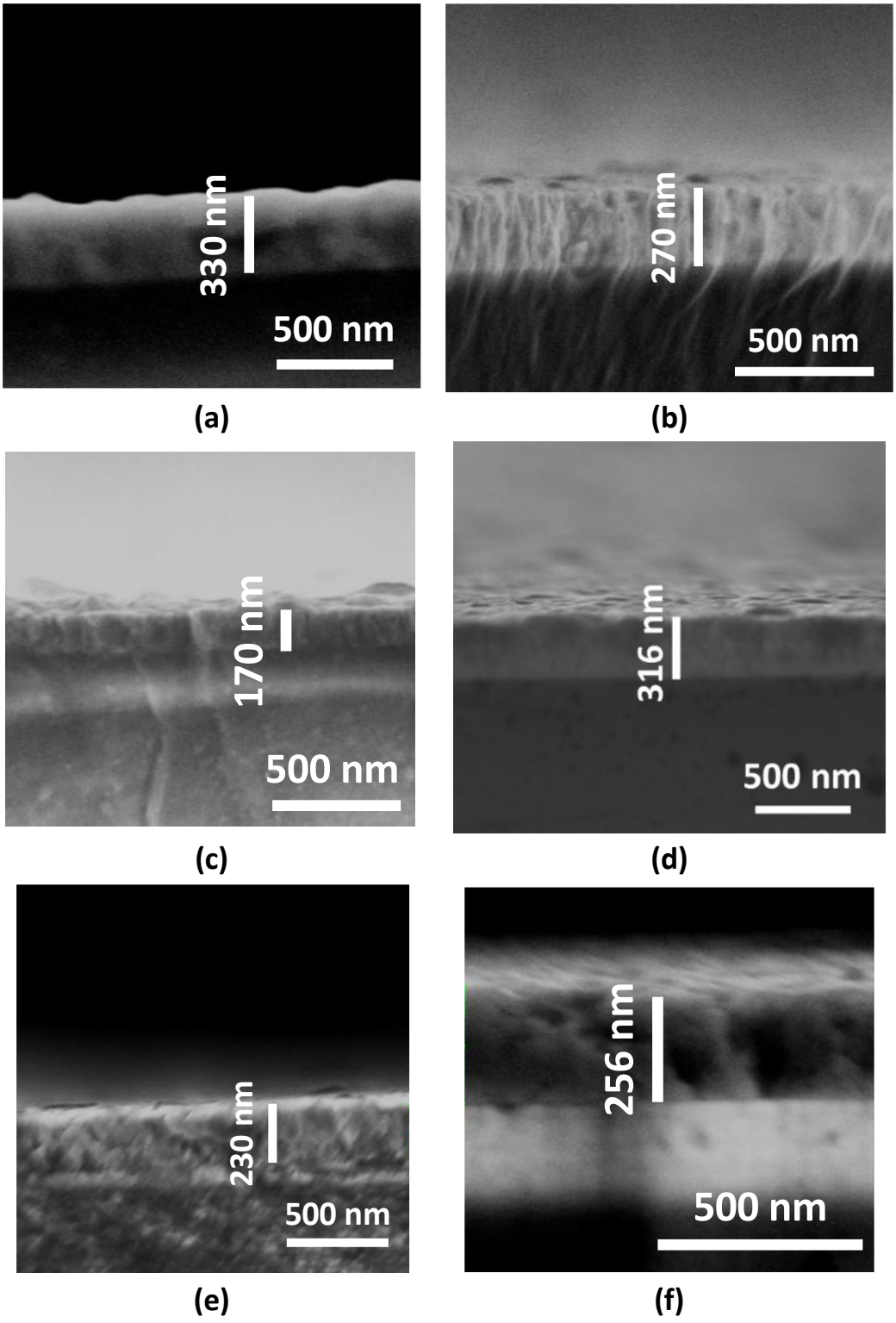

Figure 36 - Cross-section SEM micrographs of delafossite films on (a) fused-silica quartz, (b) Schott AF 32® eco glass, (c) Schott D 263® T eco glass, (d) α-Al_2O_3, (e) $SrTiO_3$ and (f) MgO.

4.2. Chemical composition

High-resolution X-ray photoelectron spectroscopy (XPS) depth profiles were analysed on 70-nm thick $Cu_{2/3}Cr_{4/3}O_2$ thin films deposited on α-Al_2O_3. This analysis aimed to assess the delafossite phase and examine the elemental composition as a function depth. Figure 37 shows XPS spectra, providing detailed profiles across the binding energy ranges of interest. The spectra were recorded both at the surface and after sputtering for intervals of 300, 600, 900, and 1200 seconds. The observed spectra revealed characteristic peaks corresponding to Cu^{2p}, Cr^{2p}, and O^{1s}.

Beginning with Figure 37a, two small satellite peaks (indicated by arrows) were detected at the sample surface, corresponding to the presence of Cu^{2+}, which indicates surface oxidation. These peaks disappear after sputtering, confirming the absence of CuO phase in the bulk sample [333].

In Figure 37b, the binding energies of $Cr^{2p}{}_{3/2}$, $Cr^{2p}{}_{1/2}$ at 586.4 and 576.5 eV, respectively, correspond to the +3 oxidation state of chromium [334]. The Auger Cu_{LMM} peak at 568.4 eV signals the presence of copper oxide phases.

Reference spectra for CuO (Cu^{2+}), Cu_2O (Cu^{+}), and metallic Cu (Cu^{0}) were used to elucidate the oxidation state of Cu, as shown in Figure 38 across the binding energy ranges of the respective copper oxide phases [335]. Two small shoulders (indicated by arrows) are visible, corresponding to contributions from Cu^0 and Cu^+. The presence Cu^+ is consistent with the pure delafossite phase, while Cu^0 results from Ar^+ sputtering reducing Cu^+ to metallic copper (Cu^0). As sputtering time increases, the amount of Cu^0 detected also increases, explaining the shift in the Cu_{LMM} peak with increasing sputtering time (Figure 37b).

Moreover, the position of the Auger Cu_{LMM} peak (568.4 eV) and the energy separation of 46.3 eV between $Cr^{2p}{}_{3/2}$ and O^{1s} peaks (Figure 37b, c) indicate the presence of pure delafossite phase. These findings are consistent with previous studies [190], [236], [160].

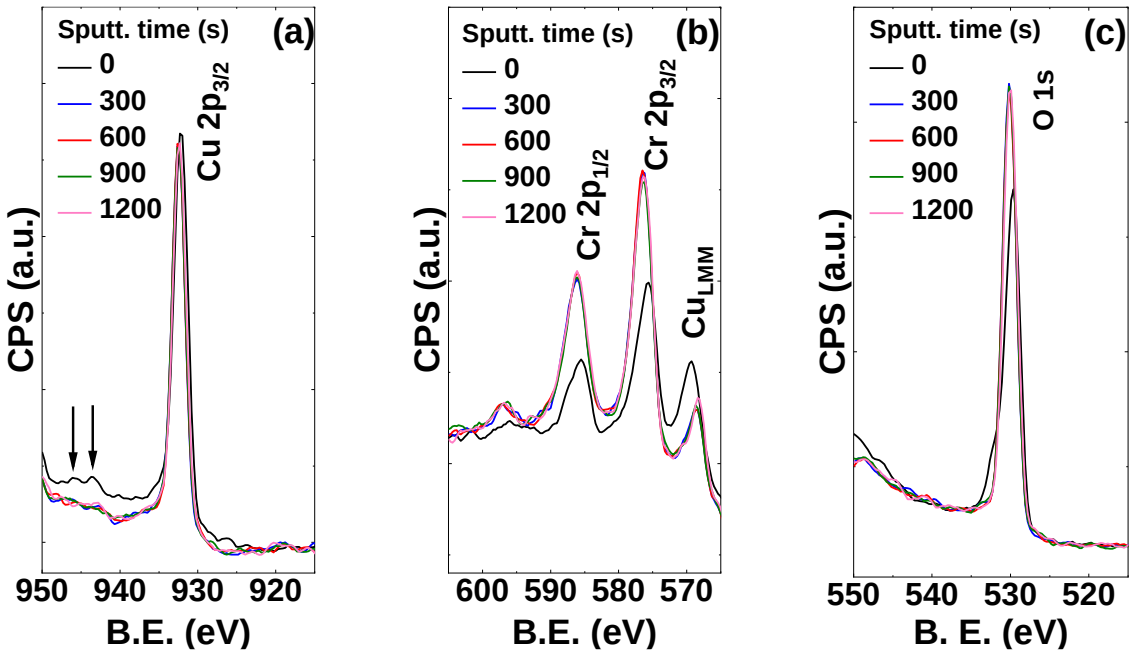

Figure 37 – High resolution XPS spectra in the binding energy range of (a) copper, (b) chromium and (c) oxygen.

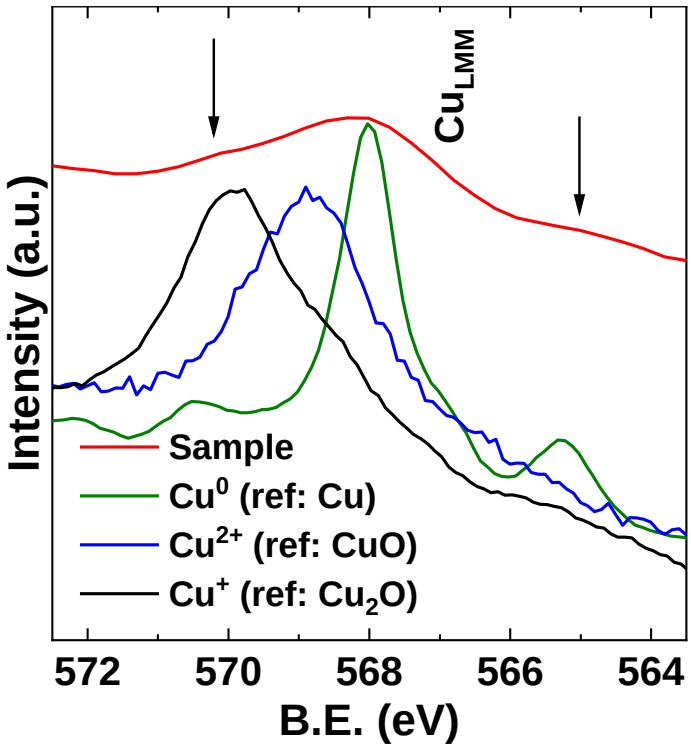

Figure 38 - XPS spectrum of 70-nm thick $Cu_{2/3}Cr_{4/3}O_2$, after sputtering for 300 s, over the binding energy range with Cu_{LMM} reference peaks of copper oxidation states Cu^0, Cu^+ and Cu^{2+} also displayed.

Figure 39 depicts the in-depth elemental quantification of as-deposited 70-nm thick $Cu_{2/3}Cr_{4/3}O_2$ thin films grown on both α-Al_2O_3 and silicon substrates. The depth profiling revealed average atomic percentages of approximately 17% for Cu, 33% for Cr, and 50% for O in the films, corresponding to a stoichiometry of $Cu_{2/3}Cr_{4/3}O_2$, with a Cr/Cu ratio of approximately 2. These values represent averages over the entire area covered by the XPS beam (3 mm x 3 mm), suggesting that variations in stoichiometry may occur in different regions of the film.

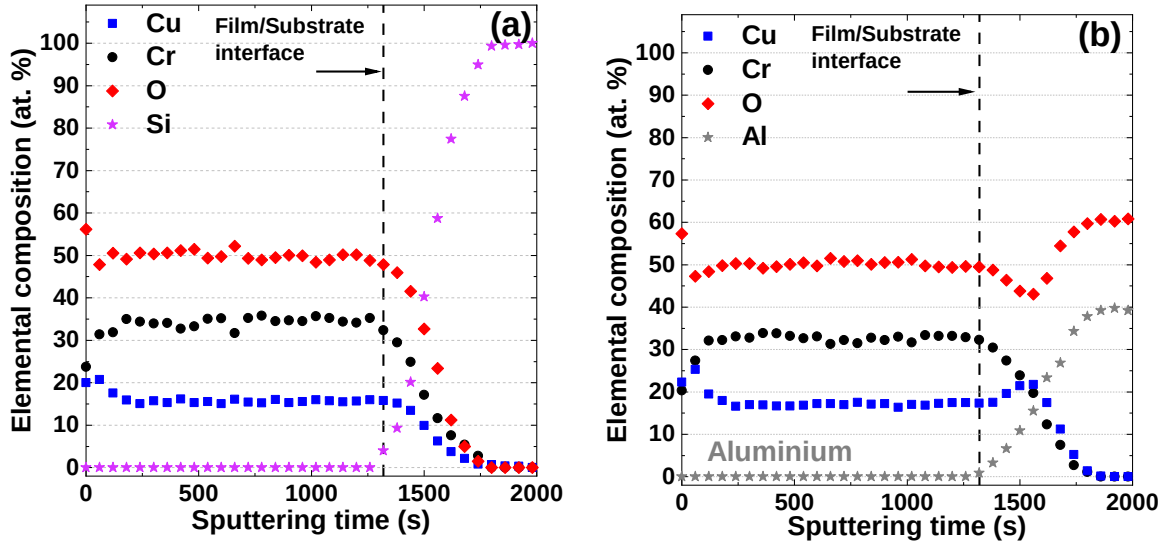

Figure 39 – In-depth elemental quantification of $Cu_{2/3}Cr_{4/3}O_2$ thin films grown on (a) silicon and (b) α-Al_2O_3 substrates [304].

4.3. Structural characterisation of thin films

The structure of $Cu_{2/3}Cr_{4/3}O_2$ films grown for 60 min on different substrates was assessed through XRD analysis. Figure 40 shows that the pure rhombohedral delafossite structure was observed in all samples, regardless of the substrate The characteristic peak reflection (012) at 2θ = 36.4° is the most intense, with minor contributions from (104), (018) and (110) reflections. No peaks related to non-conductive parasitic phases were identified, confirming the possibility of growth of pure delafossite on various substrates.

Moreover, the average crystallite size and microstrain were determined for each sample using Pseudo-Voigt fitting function (Figure 41). The average crystallite size is nearly double when delafossite is grown on both cubic substrates ($SrTiO_3$ and MgO). The values for the other three samples are similar between each other, with α-Al_2O_3 being the only non-amorphous substrate of these. Crystalline substrates such as $SrTiO_3$ and MgO offer well-defined nucleation sites and lower surface energy, which promotes the formation of larger crystallites. These substrates facilitate better nucleation and growth kinetics, resulting in larger average crystallite sizes. In contrast, amorphous substrates have higher surface energy and more random nucleation sites, leading to a higher density of smaller crystallites. Additionally, the structured surface of crystalline substrates can lead to more uniform and larger crystallite growth even in the absence of epitaxial alignment. This results in a significant increase in crystallite size on $SrTiO_3$ and MgO compared to amorphous substrates.

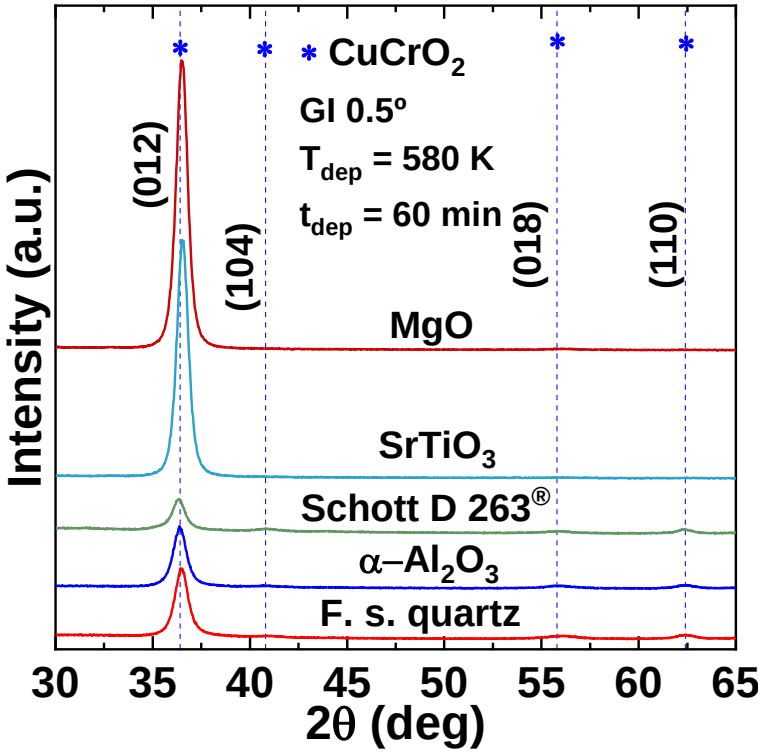

Figure 40 – GI-XRD diffractogram of as-deposited $Cu_{2/3}Cr_{4/3}O_2$ grown on various substrates (offsets for clarity).

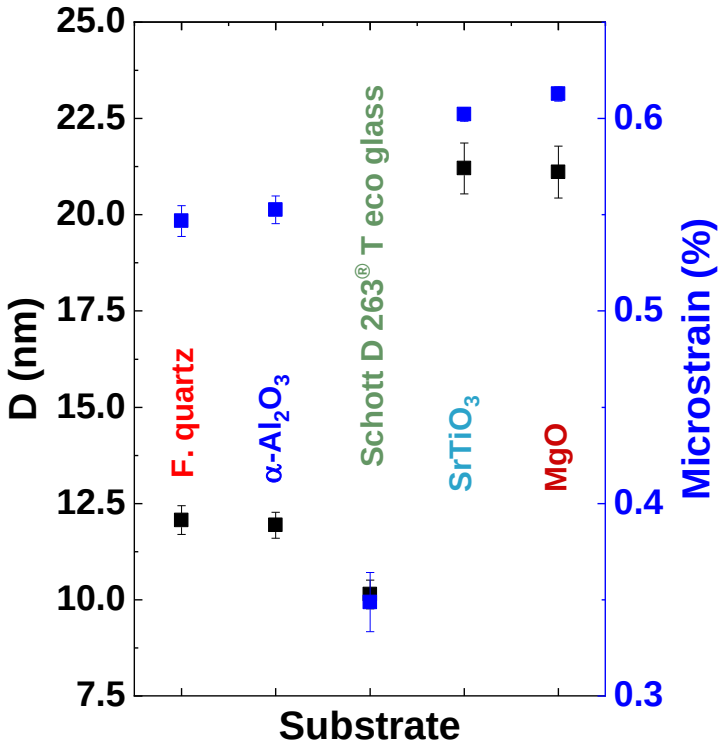

Figure 41 - Average crystallite size and microstrain from (012) diffraction peaks using pseudo-Voigt fitting function of as-deposited $Cu_{2/3}Cr_{4/3}O_2$ for 60 min, in different substrates.

However, in α-Al_2O_3, the epitaxial growth of rhombohedral $Cu_{2/3}Cr_{4/3}O_2$ on its surface is favourable due to the crystallographic compatibility between the two materials, which might restrict crystallite growth. To evaluate this, the structure of $Cu_{2/3}Cr_{4/3}O_2$ near the α-Al_2O_3 interface was inspected by HRTEM analysis (Figure 42). The corresponding FTT images (inset of Figure 42) show that the film aligns with the substrate (006 reflection) near the interface, implying epitaxial growth in the early stages of delafossite formation. Beyond approximately 40 nm, the delafossite exhibited random polycrystalline growth, suggesting that crystallite growth in the initial layers is limited by α-Al_2O_3. Lattice parameters. To further understand this phenomenon, the influence of growth time and temperature on crystallite size was examined.

Figure 43a illustrates the dependency of the average crystallite size and microstrain on the deposition time, as calculated using Pseudo-Voigt function. For t_d = 30 min, the crystallites grew up to 8 nm, and nearly doubled when t_d = 60 min. It is important to note that the crystallite size determined by Pseudo-Voigt profile analysis reflects the average size of crystallites throughout the entire depth of the measured spot in the thin film, accounting for both epitaxial and non-epitaxial regions. The initial increase in the microstrain might be attributed to the initial epitaxial growth of the delafossite film, which induces strain due to lattice mismatch. As t_d increases the crystallites growth larger and the microstrain decreases, likely due to the transition to a random polycrystalline growth. This growth mode allows for the accommodation of misfit dislocations more effectively, reducing overall internal strain. Larger crystallites distribute strain more uniformly, minimising localised stress concentrations. Additionally, as the overall grain boundary area decreases with the growth of larger crystallites, the number of strained interfacial areas also diminishes. This reduction in grain boundary area leads to fewer sites where dislocations and strain can accumulate, further contributing to the overall reduction in microstrain.

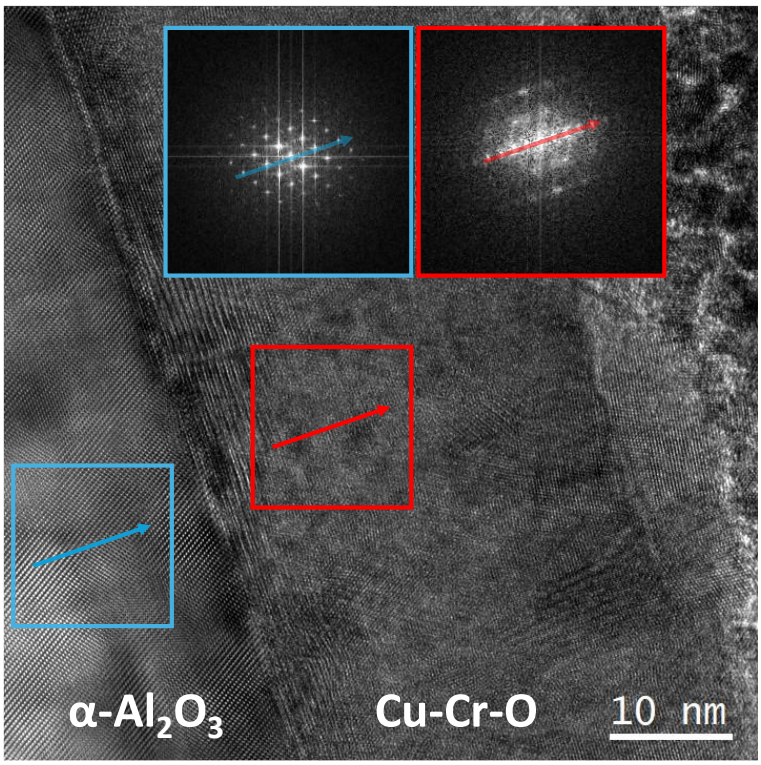

Figure 42 – HRTEM micrographs of $Cu_{2/3}Cr_{4/3}O_2$ deposited on α-Al_2O_3 substrate for 10 min at 580 K. The insets show the FFT images of both substrate and $Cu_{2/3}Cr_{4/3}O_2$ regions.

The effect of deposition temperature on crystallite size and microstrain was also investigated. These dependences are represented Figure 43b for films grown at 580, 605 and 680 K, with t_d = 60 min.

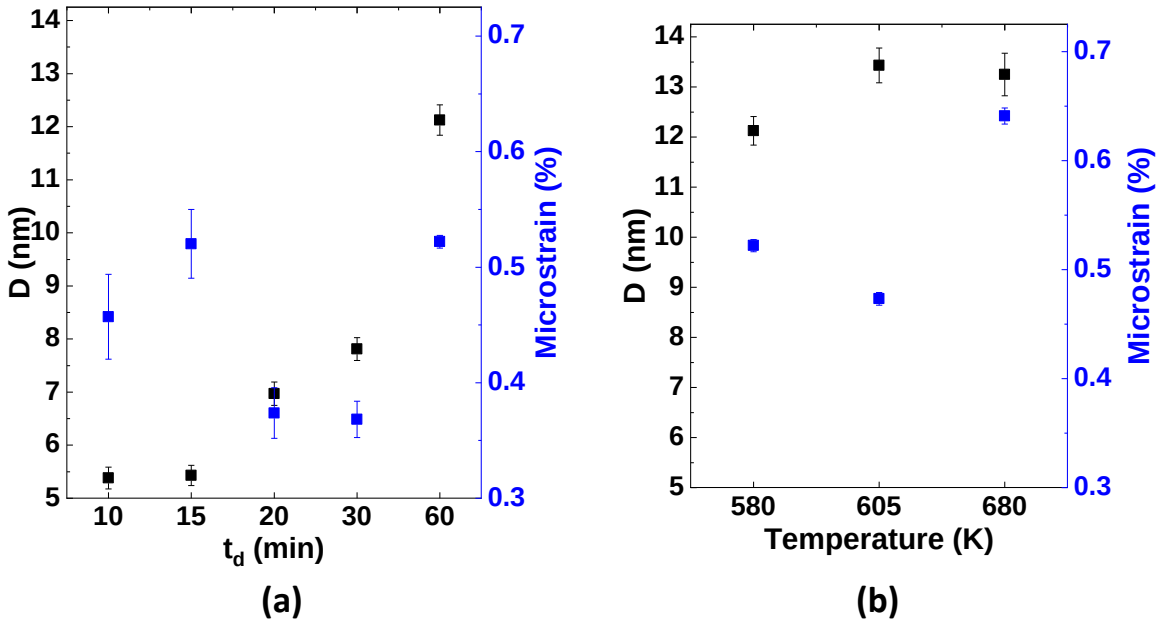

Figure 43 –Average crystallite size and microstrain from (012) diffraction peaks using the Pseudo-Voigt fitting function of as-deposited $Cu_{2/3}Cr_{4/3}O_2$ on α-Al_2O_3 (a) for different t_d at 580 K and (b) at different T_d for t_d = 60 min.

At higher temperatures, the crystallite sizes are similar, possibly due to the combined effects of growth time, growth temperature, and the constraints imposed by epitaxial growth in the early stages of thin film formation. The epitaxial substrate-film relationship observed in TEM micrographs suggests that the crystallite sizes are “restricted” by the substrate's lattice parameters during initial growth. This restriction likely sets an upper limit on crystallite size that is maintained even as temperature increases. Additionally, the growth time of 60 min may not be sufficient to allow significant further growth beyond the initial epitaxial alignment, further contributing to the similar crystallite sizes observed at these temperatures.

4.4. Stability of thin films upon thermal post-treatments

This section presents the characterisation results of off-stoichiometric delafossite ($Cu_{2/3}Cr_{4/3}O_2$) thin films grown by MOCVD and subjected to a post-treatment process. This evaluation aimed to assess the stability $Cu_{2/3}Cr_{4/3}O_2$ phase at high temperatures, in order to establish the optimal temperature range for Seebeck effect measurements. Specifically, three parameters were investigated for the $Cu_{2/3}Cr_{4/3}O_2$ thin films, which were deposited at 400 °C for 15 min on α-Al_2O_3: temperature, pressure and atmosphere.

Figure 44a depicts the ratio between the electrical conductivity after and before the post-treatment (σ_f/σ_i). The parameters adjusted were atmospheric gas (Ar, N_2 and O_2), temperature (400 and 600 °C) and pressure (1.6 mbar, 12 mbar and atmospheric pressure), for 10 min.

The as-deposited samples displayed an electrical conductivity of approximately 50 S cm^{-1}. Following post-treatment at 400 °C, this value remains stable across different pressures, indicating the inherent stability of the $Cu_{2/3}Cr_{4/3}O_2$ phase at this temperature. Moreover, the large radius of O_2, and the inert nature of Ar and N_2 gases, coupled with the thermal energy at this temperature, are insufficient to significantly intercalate and alter the delafossite structure.

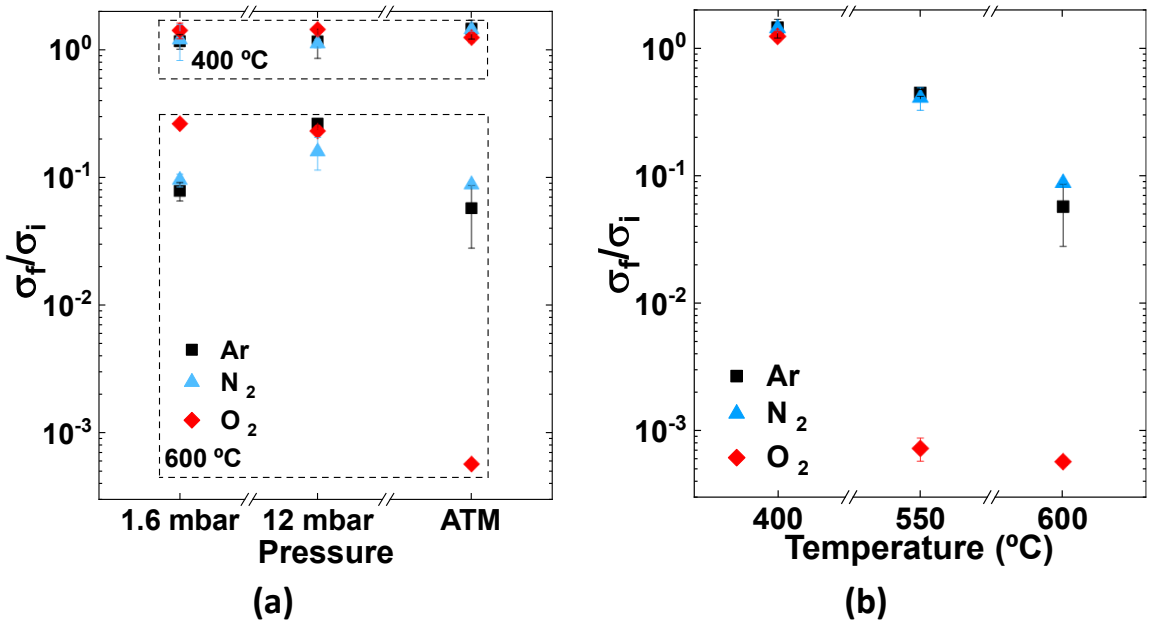

Figure 44 – (a) σ_f/σ_i for post-treatments on $Cu_{2/3}Cr_{4/3}O_2$ samples at three different pressures and two temperatures using three different atmosphere gases and (b) at three different temperatures using three different atmosphere gases, all at atmospheric pressure.

At 600 °C, the electrical conductivity of the samples post-annealed under pressures of 1.6 and 12 mbar decreased by an order of magnitude. Similarly, at atmospheric pressure, samples annealed in Ar and N_2 exhibit a reduction of approximately one order of magnitude. In contrast, under an O_2 atmosphere, the conductivity decreases by three orders of magnitude.

This substantial decline in conductivity can be attributed to two primary mechanisms. First, the $Cu_{2/3}Cr_{4/3}O_2$ phase contains structural defects, specifically chains of copper vacancies, which were reported to be responsible for high electrical conductivity. These defects start to heal at higher temperatures (above approximately 600 °C), leading to a decrease in the electrical conductivity

[305]. Second, the presence of O_2 at high temperatures favours the formation of parasitic phases with significantly lower electrical conductivity and optical transparency compared to the delafossite phase. O_2 reacts with the delafossite phase, oxidising Cu(I) species to form copper(I) oxide (CuO) and spinel ($CuCr_2O_4$), where Cu is in the +2 oxidation state. This reaction can be represented as follows [232],[336]:

$$2CuCrO_2 + \frac{1}{2}O_2 \rightarrow CuO + CuCr_2O_4 \quad \textbf{(88)}$$

The formation of CuO and $CuCr_2O_4$ results in a drastic reduction in electrical conductivity due to lower charge carrier concentration in these parasitic phases compared to the delafossite phase.

To further investigate the impact of temperature at atmospheric pressure, post-treatments were conducted at 400, 550 and 600 °C, as shown in Figure 44b. As previously observed, at 400 °C, the electrical conductivity remains unchanged regardless of the atmospheric gas. However, at 550 °C and 600 °C, the conductivity decreases, with the most significant reduction – up to three orders of magnitude – occurring in the presence of O_2. This effect is likely due to enhanced oxidation and the formation of non-conductive phases. In N_2 and Ar atmospheres, the slight decrease in conductivity can be attributed to partial healing of the copper vacancies, which also reduces the number of available charge carriers.

To verify the reliability of these findings, the presence of parasitic phases in the thin films was evaluated using GI-XRD measurements. The diffractograms of thin films post-treated at 600 °C under Ar, N_2, and O_2 atmospheres at atmospheric pressure are illustrated in Figure 45.

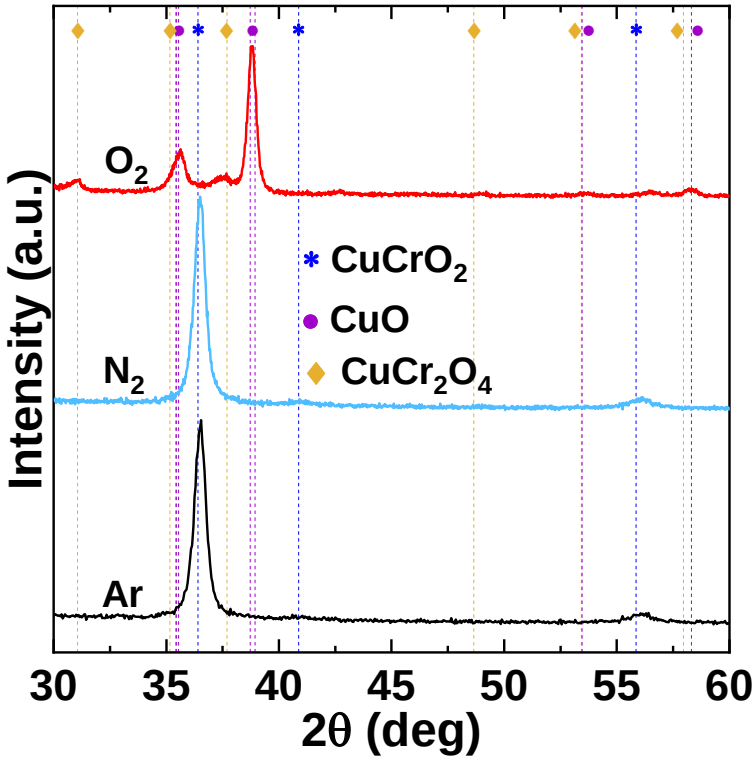

Figure 45 – GI-XRD diffractogram of delafossite samples post-annealed at 600 °C, under N_2, Ar and O_2 atmosphere.

According to ICDD, three phases were identified in the diffractograms. Table 11 details all identified phases and their corresponding Bragg angles reflections. The pure rhombohedral

delafossite structure belonging to the R-3m space group (ICDD PDF #04-010-3330) was observed in both samples post-treated in N_2 and Ar atmospheres, with the characteristic peak reflection (012) at 2θ = 36.4° being the most intense. Minor contributions from (104) and (018) reflections are observed. No characteristic peaks from parasitic non-conductive phases were identified in either delafossite thin films, which confirms that inert atmosphere helps to preserve of $Cu_{2/3}Cr_{4/3}O_2$ without inducing oxidation or phase transformations.

However, characteristic peaks from phases of CuO and $CuCr_2O_4$ (ICDD PDF #00-041-0254 and #00-034-0424, respectively) were identified in the samples post-treated in an O_2 atmosphere; moreover, the characteristic peak of the delafossite phase is absent. Additionally, the colour of this sample became dark grey, indicative of the presence of CuO and $CuCr_2O_4$, as their band gaps are both lower than the delafossite. These observations confirm the stability of the delafossite phase under inert atmospheres and its conversion to non-conductive phases under the presence of oxygen at higher temperatures.

The reversibility of the delafossite phase and the formation of parasitic phases were investigated using in situ XRD measurements, at various temperatures. Diffractograms of as-deposited $Cu_{2/3}Cr_{4/3}O_2$ were measured in situ at 30, 450, and 600 °C, and again at 30 °C after cooldown, under both ambient conditions and vacuum, to evaluate the thermal stability and phase transitions of the films. Each measurement took 2 h, with a heating step of 20 °C/min each between each temperature step. The cooldown took approximately 10 hours.

Table 11 - Phases identified in diffractograms from Figure 45 according to ICDD, and their corresponding Bragg angles and reflections.

2θ (°)	(hkl)	Phase
31.064	112	$CuCr_2O_4$
35.159	211	
35.437	002	CuO
36.409	012	$CuCrO_2$
37.692	103 202	$CuCr_2O_4$
38.730	111	CuO
38.940	200	
40.878	104	$CuCrO_2$
48.649	213	$CuCr_2O_4$
53.426	312	
53.465	020	CuO
55.853	018	$CuCrO_2$
56.172	321	$CuCr_2O_4$
57.965	303	

Figure 46 depicts the GI diffractogram measured under ambient air conditions. At 30 °C, it shows the characteristic peaks of the rhombohedral delafossite structure, confirming the presence of the delafossite phase. As the temperature increases to 450 °C, the diffractogram remains largely unchanged, indicating the stability of the delafossite structure up to this temperature. This is consistent with previous studies showing that delafossite phases, such as $CuCrO_2$, exhibit good

thermal stability at moderate temperatures [191]. At 600 °C, the diffractogram shows peaks corresponding to CuO and $CuCr_2O_4$ phases, suggesting the formation of parasitic non-conductive phases. The intensity of the delafossite main peak is also reduced at this stage. Upon cooling down to 30 °C, the diffractogram shows a further reduction in the intensity of the delafossite phase peaks, while the intensity of the parasitic phase peaks increases. As the system was cooling down, the delafossite phase was still converting into CuO and $CuCr_2O_4$ phases, which explains their higher peak intensities after cooling down. This also indicates that the phase transformation to CuO and $CuCr_2O_4$ is irreversible under ambient conditions, probably due to kinetic barriers preventing the reformation of the original delafossite phase from the parasitic phases. Additionally, the colour of this sample turned dark grey, further confirming the reduced band gap associated with the presence of parasitic phases.

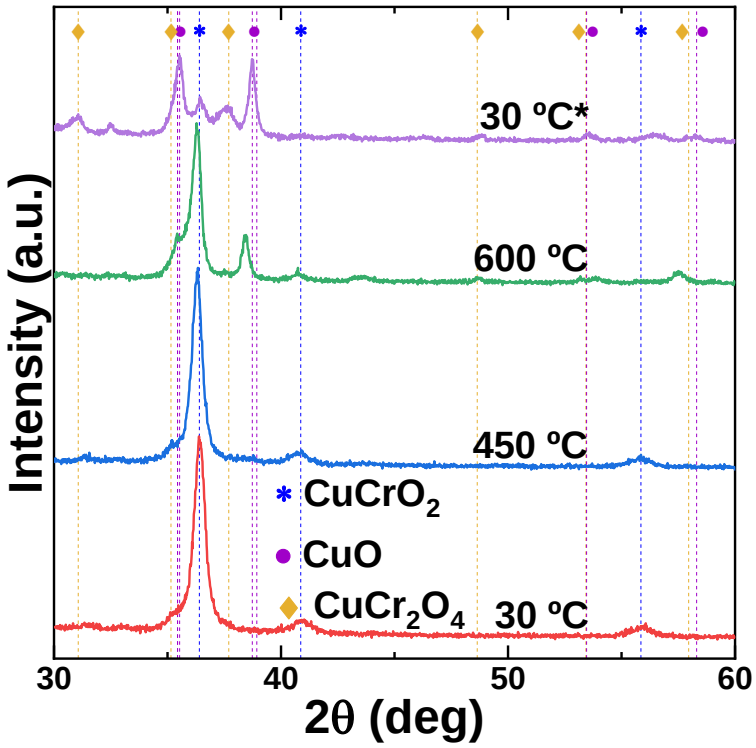

Figure 46 – GI-XRD diffractogram of as-deposited $Cu_{2/3}Cr_{4/3}O_2$ samples measured in situ at different temperatures, and after cooldown (marked by *), under ambient air.

The final experiment involved measuring in situ GI diffractograms of $Cu_{2/3}Cr_{4/3}O_2$ at different temperatures and under vacuum (Figure 47). It is clearly visible that the pure delafossite phase is maintained at each in situ temperature measurement, demonstrating the stability of delafossite phase in the absence of oxygen atmosphere. Additionally, the intensity of the main peak increases, which is associated with an increase in crystallite dimensions.

The average crystallite size and microstrain were extracted from (012) diffraction peaks using Pseudo-Voigt fitting function (Figure 48). In situ temperature XRD measurements on $Cu_{2/3}Cr_{4/3}O_2$ revealed that the delafossite crystallite size increases with temperature, while the microstrain decreases. This can be attributed to several factors. Higher temperatures facilitate the annealing process, where defects and dislocations within the crystals are reduced, leading to a decrease in internal strain. Additionally, as crystallites grow larger, they tend to have fewer grain

boundaries, which are common sources of microstrain. Each measurement took 120 min, during which the high temperatures promoted the growth of delafossite crystallites. The system was then allowed to cool down slowly to 30 °C, which explains the larger crystallites observed after the measurements.

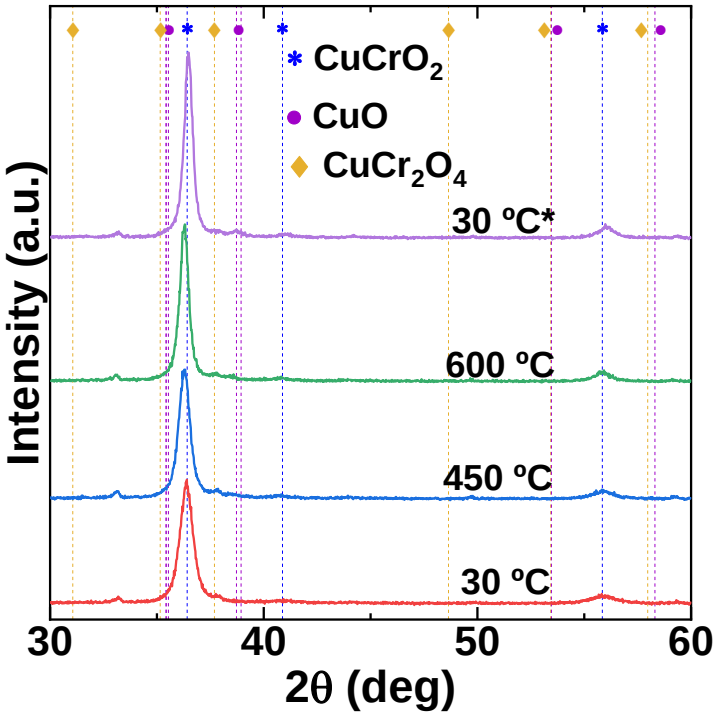

Figure 47 – GI-XRD diffractogram of as-deposited $Cu_{2/3}Cr_{4/3}O_2$ samples measured in situ at different temperatures, and after cooldown (marked by *), under vacuum.

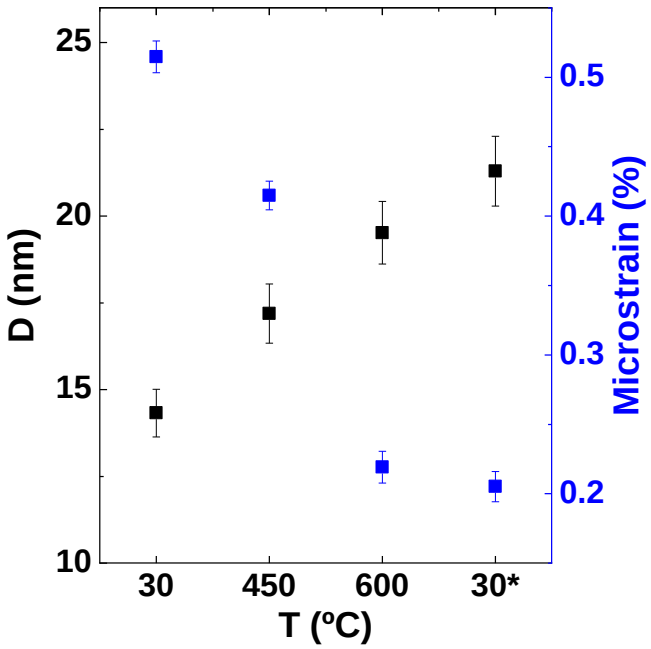

Figure 48 - Average crystallite size and microstrain from (012) diffraction peaks using Pseudo-Voigt fitting function of as-deposited $Cu_{2/3}Cr_{4/3}O_2$ samples measured in situ at different temperatures, and after cooldown (marked by *), under vacuum.

In summary, the delafossite phase is preserved under ambient air conditions up to 600 °C; beyond this temperature, it converts into parasitic non-conductive phases. Under inert gas or vacuum conditions, the delafossite phase remains stable at high temperatures. These results show that the delafossite phase is not affected by the thermoelectric measurements at high temperatures, as the measurements in LSR-3 Linseis setup are performed in vacuum environment. Still, the maximum measurement temperature should be taken carefully, as at around 600 °C the chains of copper vacancies start to heal, leading to a decrease in the electrical conductivity.

Chapter 5 – Impact of induced strain on delafossite thin films

This chapter is dedicated to experiments related to strain induced on delafossite thin films. Initially, it covers a discussion of experiments employing mechanical methods to generate strain. This is followed by investigations where internal stress is induced through doping with various materials. The final segment addresses studies where strain is thermally induced using substrates with differing thermal expansion coefficients. Electrical measurements are presented and analysed to elucidate the influence of strain on the electronic properties. This section includes a critical evaluation of the classical Seebeck coefficient in semimetals, proposing a novel approach. The implications of this new approach on electronic properties are then contextualised within the scope of the current research. The chapter ends by describing the mobility dependence on temperature when thermal energy transported by phonons is considered, as described in Emin-Wood model.

5.1. Effects of induced external strain

5.1.1. Magnetostriction

The first strategy envisioned in this case focused on inducing strain via the magnetostriction of the substrate. When a magnetic field is applied to a magnetostrictive substrate, it induces strain in the attached film. This method offers the advantage of dynamic strain control, allowing for real-time adjustment of the film's properties by varying the magnetic field, providing a non-invasive and reversible means of tuning material behaviour. This approach is particularly advantageous in applications requiring precise strain control.

However, two significant limitations were identified during our experiments. Firstly, the electrical conductivity of the substrates interfered with the precision of electronic measurements of the films, introducing noise and inaccuracies. Secondly, and most critically, the substrate needed to withstand the high deposition temperature of delafossite without melting or degrading its magnetic properties.

Unfortunately, this approach was not successful in our case. We selected a nickel foil with a thickness of 600 µm as the substrate and deposited a 50 nm layer of Al_2O_3 to prevent contact between the semiconductive delafossite film and the metallic foil. The delafossite films were then deposited on this structure, and the entire assembly was placed into a Helmholtz coil system. A more detailed description of the experimental setup is provided in the Methods chapter. However, no change in the resistivity of the material was observed when the magnetic field was varied up to 200 Oe.

This lack of change is likely due to the insufficient magnitude of the induced strain. The magnetostriction coefficient of nickel (λ_{Ni}) is approximately -1.6×10^{-6}. The change in dimensions, which directly correlates with the induced strain, can be calculated using the following formula:

$$\frac{\Delta L}{L} = \lambda H \qquad \textbf{(89)}$$

where ΔL is the change in length (or another dimension) of the material, L is the original length, and H is the applied magnetic field strength. Even at the maximum applied field, the induced strain is around 10^{-6}, equivalent to a mere 0.001%. This strain is too small to produce any observable effects on the resistivity of the delafossite films. Moreover, the cost and thermal stability requirements of alternative magnetostrictive materials made their use impractical for this experiment.

5.1.2. Mechanical bending

The second strategy focused on inducing strain externally by mechanical bending. A custom-built strain gauge bench setup was used to measure the variation of the electrical resistance of the delafossite sample as function of the strain induced externally by controlled bending. A more detailed description of the experimental setup is provided in the Methods chapter.

Films deposited on Schott D 263® T eco glass (flexible) were glued on the aluminium bars. Tensile or compressive strain is induced by bending the system upwards or downwards. The calibration gauge continuously monitors the strain values, while the Wheatstone bridge measures $\Delta R/R_0$. Measurements are conducted at a constant temperature (room temperature), ensuring that variations in resistivity are not attributed to changes in carrier concentration. Two possible explanations for the observed changes in resistivity remain: modifications in dimensions or alterations in carrier mobility. To differentiate these effects, the strain gauge factor (k) is monitored throughout the experiment (where k is calculated according to Equation (70)) . The gauge factor consistently remains negative, which indicates that piezoresistive effects dominate over geometric effects. Specifically, a negative k signifies that the contribution from piezoresistive effects outweighs that from changes in the size of the material. Figure 49a,b shows the dependence of k on ε. The product $\varepsilon\Delta\mu$ is always positive (compressive case both negative, tensile case both positive). Poisson's ratio is also positive, ranging from 0.1 to 0.5 for most materials. We assume that off-stoichiometric delafossite is not an auxetic material, meaning that when subjected to positive strain along a longitudinal axis, the transverse strain will be positive as well [304].

Figure 49 depicts the normalised mobility relative to the unstrained condition (μ/μ_0) under different strain conditions: (c) compressive strain regime and (d) tensile strain regime. Here, μ/μ_0 is calculated according to:

$$\frac{\mu}{\mu_0} = \frac{\rho_0}{\rho} \quad \textbf{(90)}$$

where the resistivity (ρ_0) of the unstrained sample is calculated according to:

$$\rho_0 = \frac{R_0 . w_f . h_f}{l_f} \quad \textbf{(91)}$$

Where w_f and l_f are the width and length of the unstrained delafossite film, respectively.

In the compressive regime, μ decreases with the increase in strain (absolute value), while in the tensile regime, the mobility increases with the strain. Overall, we can conclude that the mobility increases with increasing interatomic distances. Although the changes in μ are small, below 0.1%, the trends are clear. Unfortunately, the flexible substrate Schott D 263® T eco glass breaks at around

ε = 0.06%, in absolute value, making it impossible to evaluate its behaviour at higher strain values [304].

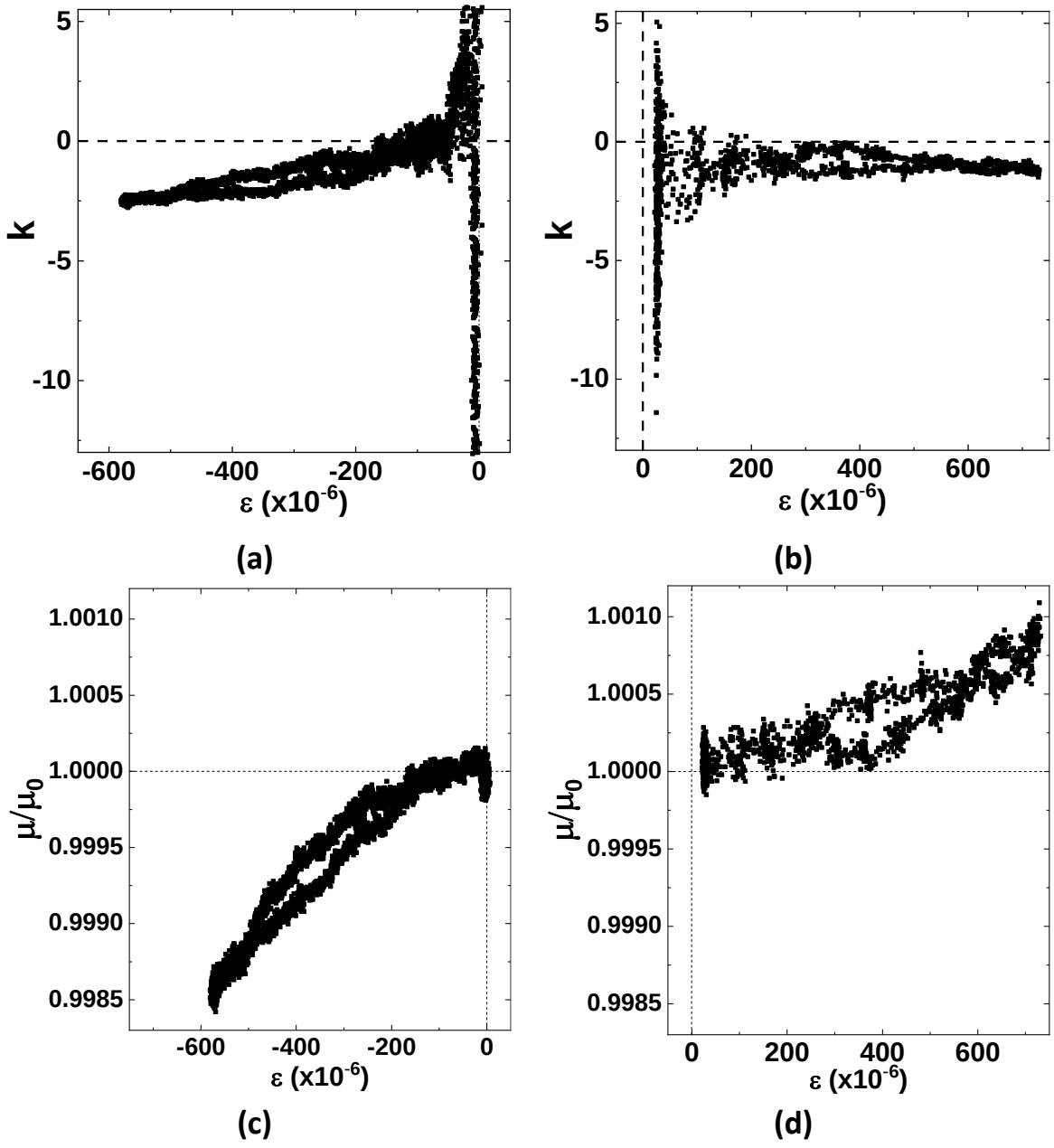

Figure 49 – Strain gauge factor k(ε) behaviour in (a) compressive and (b) tensile regimes. μ/μ_0 vs induced strain ε in (c) compressive and (d) tensile regimes [304].

The increase of mobility with interatomic distances seems to be related to phonon scattering as this mechanism is strongly dependent on lattice constants. Imposing strain changes the phonon speed and introduces phonon scattering centres by locally altering the phonon frequency. Lattice strain can weaken lattice anharmonicity, which is a key factor determining the rates of scattering processes. Anharmonicity is related to the interatomic potential and bond strengths that depend on the lattice structure [337]–[339].

To establish quantitative relationships, we need to relate the band dispersion with the strain sensor. The expression for the effective mass is given by Equation (34). Developing a comprehensive

theory linking energy with strain is challenging and almost impossible (and beyond the scope of this thesis) for this particular material. Most of the existing studies report empirical relationships derived from experimental data. For example, Shan et al. [340] use a quadratic relation for ZnO wires and sheets:

$$E(\xi) = E(0) + \alpha P + \beta P^2 \quad \textbf{(92)}$$

where P is the pressure and the coefficients α and β are determined by fitting experimental values. To evaluate the strain sensor, one should express the strain in reciprocal space. The strain tensor is a real-space quantity that characterises the deformation of a material. In contrast, **k**-space (reciprocal or Fourier space) is used to analyse the electronic structure and properties of materials. While strain can affect the electronic structure by modifying the band structure in **k**-space, there is no direct method to represent the strain tensor itself in reciprocal space. The connection between real-space strain and **k**-space electronic properties is indirect.

5.2. Effects of induced strain by extrinsic doping

5.2.1. Chemical composition

XPS measurements were conducted to chemically quantify as-deposited 300-nm thick Cu-Cr-O films on silicon substrates. These films were intentionally extrinsically doped with 5 at.% of Al, Mg, Mn, Sc, Y and Zn. Figure 50 depicts in-depth XPS spectra in the binding energy ranges of the dopant elements.

Upon initial analysis, surface contaminants, including carbon, silicon, calcium, and nitrogen and zinc (not shown in images) were identified through XPS. Apart from Zn, these contaminants are commonly found due to environmental exposure or sample handling. After sputtering, the contaminants were no longer detectable, indicating they were surface-bound and not present within the bulk material. Zn was observed on the surface of all doped films (as shown in Figure 50f for the case of Zn-doped film). Further analysis revealed that Zn was not present in the bulk of Zn non-doped films. This suggests that Zn contamination might have occurred post-deposition, potentially from environmental sources or cross-contamination during sample preparation. Moreover, all dopants were detected in the bulk films, except for Mg.

Figure 51 depicts the in-depth elemental quantification of as-deposited 300-nm thick Cu-Cr-O films grown on silicon substrates. The depth profiling revealed that among the six dopants, only Al (1.5 at.%) and Sc (2.2 at.%) were present in detectable quantities above the limit range. Conversely, Mn, Y and Zn were detected below the detection limit of 0.5%, while Mg was not detected at all. Notably, none of the intentionally extrinsically doped films exhibited dopant concentrations close to the targeted 5 at.%. The solubility limits of the dopants in the $CuCrO_2$ likely resulted in such lower incorporation levels. The absence of detectable Mg in the films could be due to its high volatility, which may have prevented its incorporation during the MOCVD process. Mg may have evaporated from the film surface or remained in the gas phase instead of being incorporated into the $CuCrO_2$ lattice.

Another significant observation was the stoichiometry of the delafossite structure. Unlike previous depositions, the Cr/Cu ratio was approximately 1, with the concentration of each element remaining below 25%. Furthermore, the oxygen concentration was around 57%, indicating the presence of an off-stoichiometric $CuCrO_{2+\delta}$ phase, with $\delta \approx 0.15$. This suggests that oxygen intercalated into the delafossite structure. Oxygen intercalation is frequently observed in delafossite structures containing larger trivalent cations (such as Y^{3+} and Sc^{3+}), where oxygen intercalates within the Cu-basal planes. For M^{3+} cations with ionic radius less than 0.70 Å, it is challenging to intercalate oxygen anions in the Cu-basal planes without causing lattice distortion because the crystallographic site for intercalated oxygen is too small [176]. Smaller cations like Cr^{3+} require more forceful conditions (high oxygen partial pressures or extended sintering) to achieve similar levels of intercalation. In our case, oxygen may have intercalated into vacant sites associated with Cu and/or Cr in the $CuCrO_2$ structure. This is supported by the detected concentrations of these elements (20.2-21.8% for Cu and 20.2-22.2% for Cr), which potentially led to the formation of the off-stoichiometric phase $CuCrO_{2+\delta}$. Higher values δ are expected for cations with a larger radius. In our case, the value of $\delta \approx 0.15$ is close to the one reported in literature for $CuFeO_{2+\delta}$, ($\delta = 0.18$), knowing that Fe^{3+} has an ionic radius very similar to that of Cr^{3+} [178].

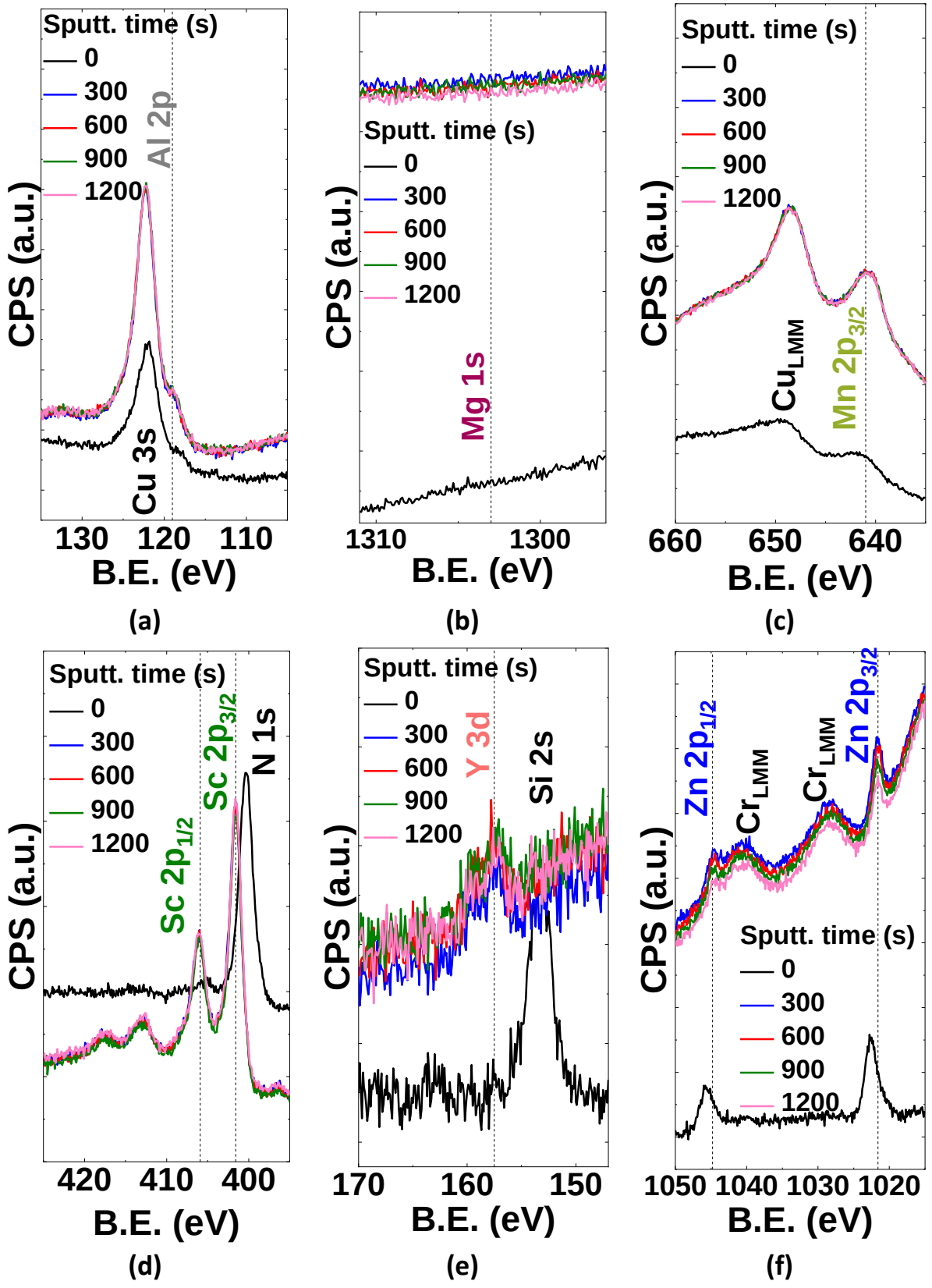

Figure 50 – In-depth XPS spectra in the binding energy range of (a) Al^{2p}, (b) Mg^{1s}, (c) Mn^{2p}, (d) Sc^{2p}, (e) Y^{3d} and (f) Zn^{2p}.

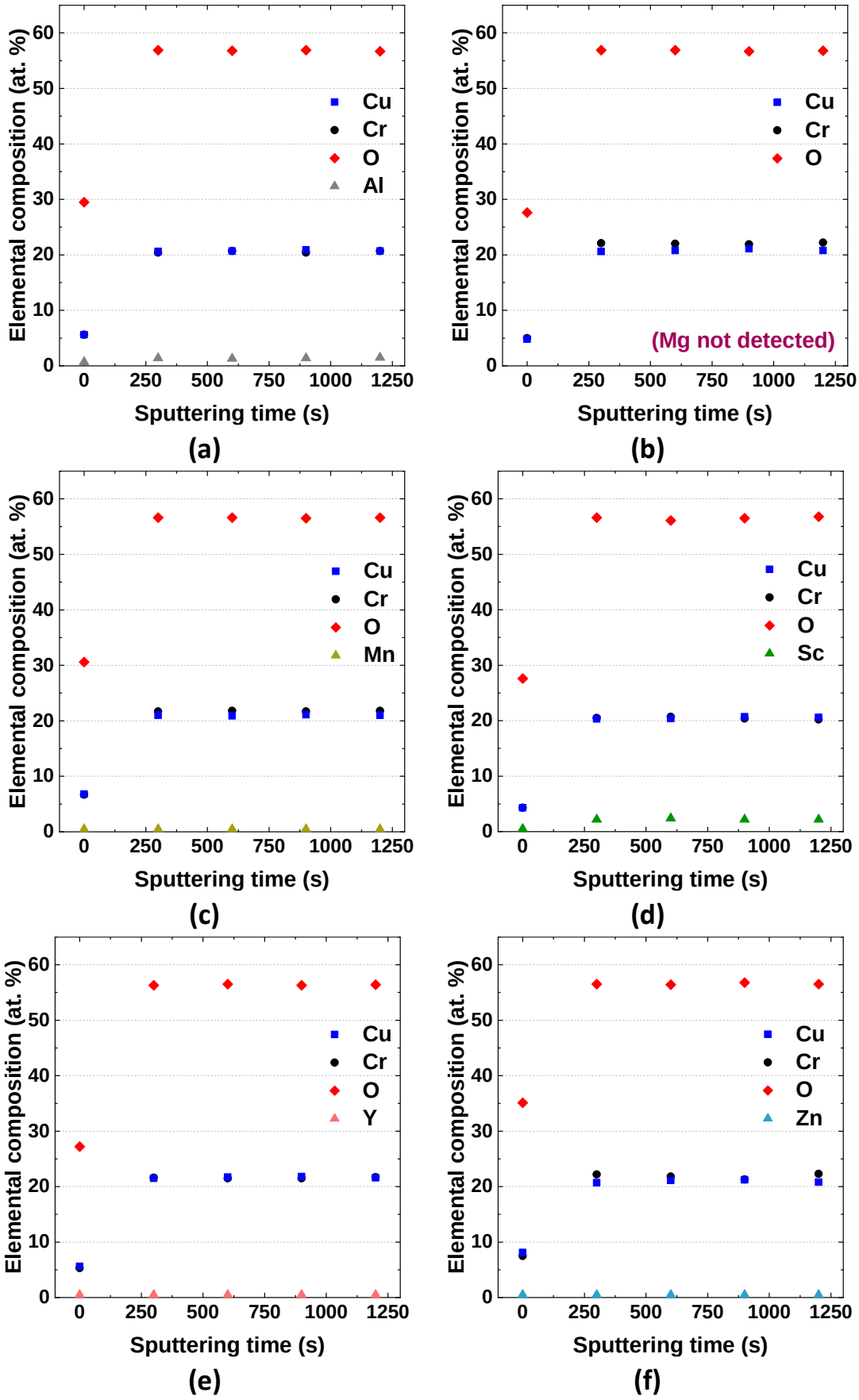

Figure 51 - Elemental composition of as-deposited intentionally extrinsically doped Cu-Cr-O samples with (a) Al, (b) Mg, (c) Mn, (d) Sc, (e) Y and (f) Zn on α-Al_2O_3 substrates.

5.2.2. Transmission electron microscopy

The structure of two delafossite samples intentionally extrinsically doped was inspected by TEM. Figure 52a shows HRTEM micrograph of the Sc-doped sample regions and the corresponding Fast Fourier Transform (FFT) images (inset) around the film/α-Al_2O_3 substrate. The FFT images show that Sc-doped film follows the same orientation as the substrate (006 reflection) when near the interface, inducing the sample is epitaxially grown on c-plane α-Al_2O_3. However, around 40 nm or above, the Cu-Cr-O exhibits a random polycrystalline orientation.

Figure 52b shows the HRTEM micrograph of the Y-doped sample regions and the corresponding FFT images (inset) around the film/silicon substrate. Here the film does not follow the same orientation as the substrate.

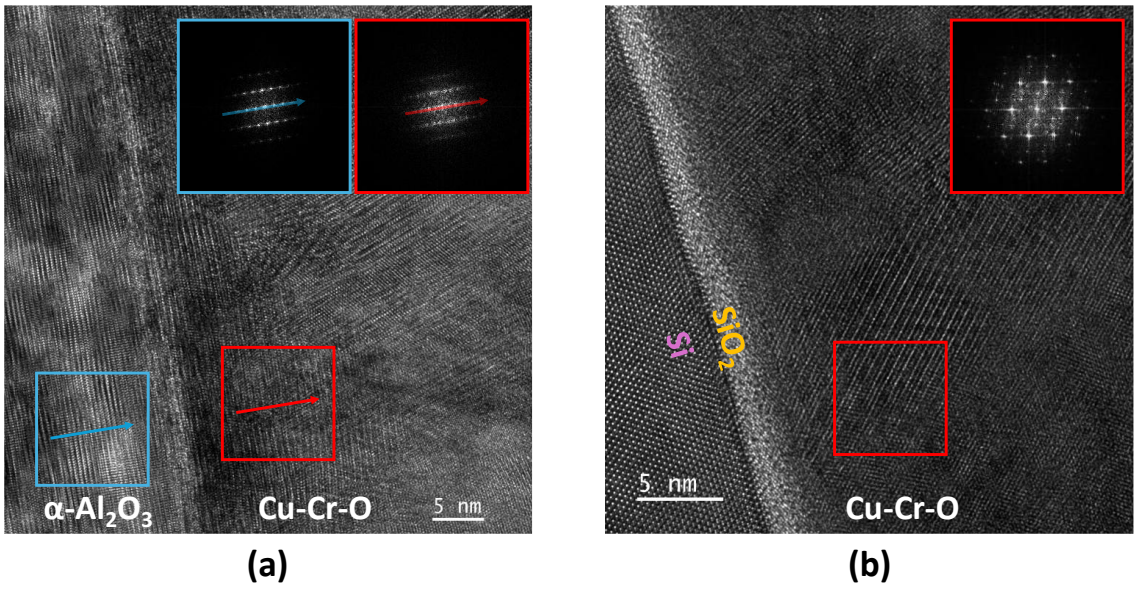

Figure 52 - HRTEM micrographs of Cu-Cr-O intentionally doped with (a) 5 at.% Sc, on α-Al_2O_3 substrate and (b) 5 at.% Y, on silicon substrate; the insets show the FFT images of both substrate and delafossite regions.

TEM was also used to obtain an average thin films' thickness over the mapped region by averaging the thickness along the mapped region. The measured values are on Table 12. The Y-doped sample has a thickness significantly less than the targeted 300 nm, likely due to inhomogeneities that occur during the chemical deposition process and the roughness of the film.

Table 12 – Minimum, average and maximum thicknesses of the intentionally doped delafossite films, measured by TEM.

Sample	Minimum h_f (nm)	Average h_f (nm)	Maximum h_f (nm)
Cu-Cr-O:Sc	265	298	330
Cu-Cr-O:Y	176	194	211

Scanning TEM (STEM) analysis was performed to do a chemical composition mapping of the scanned region of thin films. Figure 53 and Figure 54 depict the STEM analysis in a region of Cu-Cr-O thin film intentionally doped with 5 at.% Sc. and 5 at.% Y, respectively. Cu, Cr, and O are distributed homogeneously in the entire mapped regions of both doped samples.

The presence of Sc is significantly more evident than Y for the corresponding doped films, which is in good agreement with the chemical quantification performed by XPS (2.2 and less than 0.5 at.% of Sc and Y, respectively).

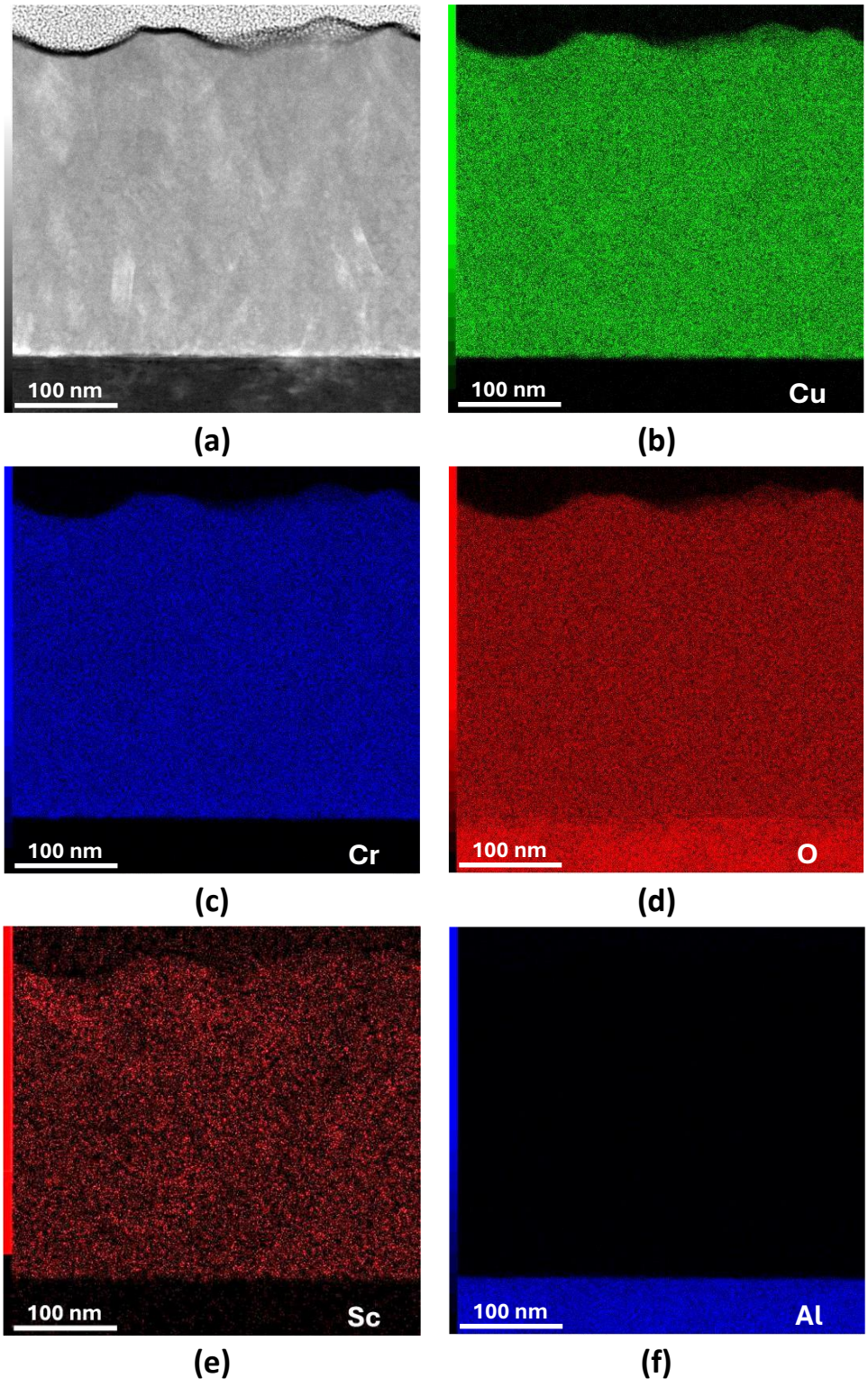

Figure 53 - (a) STEM analysis in a region of Cu-Cr-O thin film intentionally doped with 5 at.% Sc. (b) Cu (c) Cr (d) O (e) Sc and (f) Al from the α-Al_2O_3 substrate.

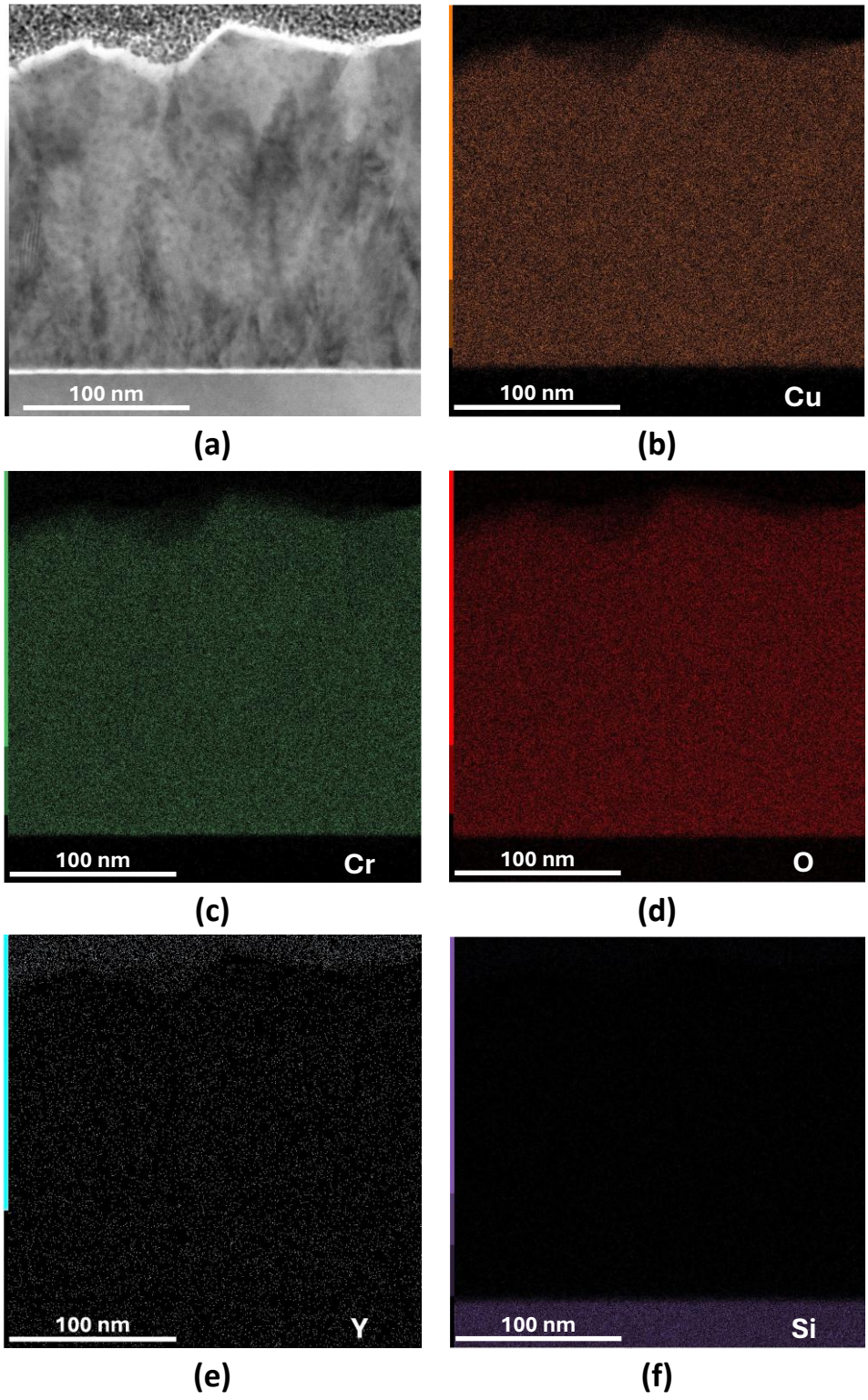

Figure 54 – (a) STEM analysis in a region of Cu-Cr-O thin film intentionally doped with 5 at.% Y. (b) Cu (c) Cr (d) O (e) Y and (f) Si from the substrate.

5.2.3. Surface topography

Figure 55 shows the AFM surface topography of Sc and Y-doped delafossite films. The surface morphologies of both films appear remarkably similar, exhibiting a nanometric grain structure. The root mean square (RMS) parameters were 11.6 nm for the Sc-doped film and 10.3 nm for the Y-doped film. Grain size distribution, obtained via watershed segmentation, also showed comparable values for grain diameter, with 71 nm ± 24 nm for the Sc-doped film and 76 nm ± 27 nm for the Y-doped film.

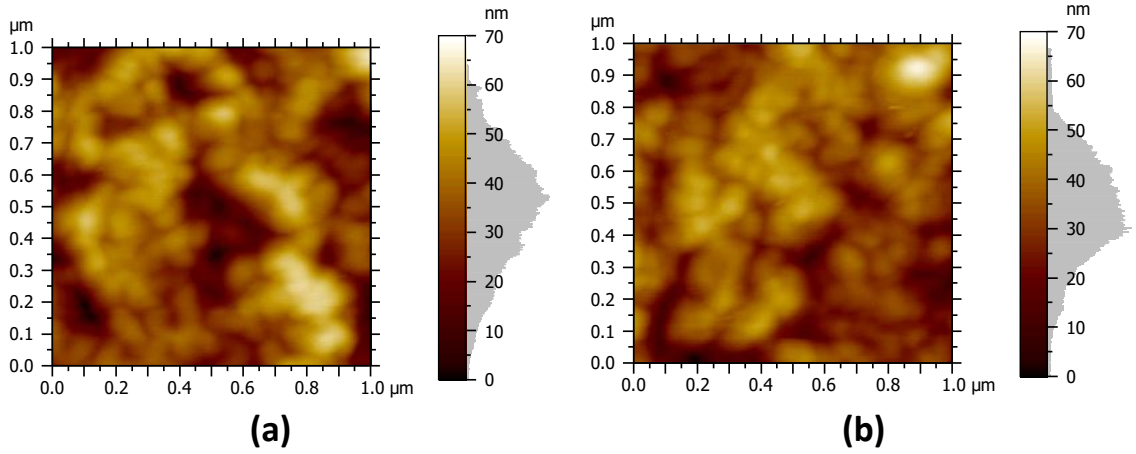

Figure 55 – Surface topography of (a) Sc and (b) Y doped Cu-Cr-O samples on silicon substrate, measured by AFM.

5.2.4. Optical characterisation

The transmission spectra were acquired for both undoped and doped samples over the wavelength range of 2500 to 250 nm. The absorption coefficient (α) was subsequently calculated, considering the sample thickness, according to:

$$\alpha = -\frac{1}{d}\ln(T) \qquad \textbf{(93)}$$

Where d is thickness of the sample and T is the transmittance. The results are depicted in Figure 56. We observed a significant difference between the absorption edges of the undoped and doped samples. A redshift of around 20 nm is clearly evident. However, no clear distinction can be made among the doped samples, even for those where the dopant was not detected by XPS measurements. It is very probable that the dopant concentrations are below the detection limit of XPS but still significant enough to influence the film properties. This observation warrants further discussion. The small polaron model describes charge transport in semiconductors where the charge carriers (electrons or holes) are strongly coupled to the lattice, forming small polarons. In such materials, optical absorption may not necessarily follow the same trends as in conventional semiconductors with delocalised charge carriers. The small polaron model can introduce additional features and complexities into the optical absorption spectrum. Consequently, the optical absorption edge may not be as well-defined as in conventional semiconductors due to the presence of polaron-related absorption features.

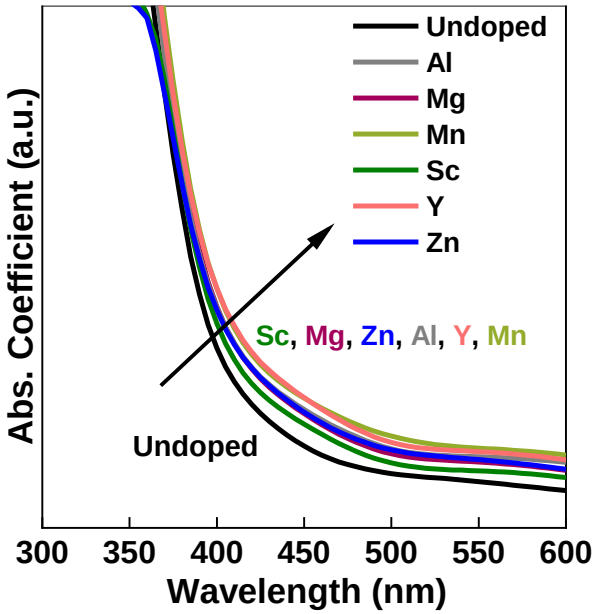

Figure 56 – Absorption coefficient curves for undoped and doped samples.

As in the vast majority of reports, the absorption coefficient is used to calculate the Tauc plot to determine the band gap. However, applying the Tauc plot to small polaron semiconductors requires careful consideration. The interpretation of the optical band gap obtained from the Tauc plot may be more complex, as it may not directly correspond to the electronic band gap due to strong electron-phonon coupling. Additional analysis, such as considering the temperature dependence of the optical absorption, may be necessary to fully understand the electronic structure and transport mechanisms in small polaron semiconductors. Unfortunately, we could not perform such an analysis throughout the thesis.

The exponent n in the Tauc plot may need to be adjusted to account for small polaron-related transitions, which may not follow the same selection rules as in a delocalised semiconductor. Small polaron semiconductors often exhibit significant structural disorder, leading to localised states in the band gap. This disorder can further complicate the interpretation of optical absorption data, as shown in Figure 57 for TiO_2 [341].

These localised states can cause an Urbach tail, an exponential absorption edge below the band gap, complicating the identification of the optical band gap using the Tauc plot method. The presence of small polarons can also introduce nonlinear absorption features that deviate from the assumptions underlying the Tauc plot. For example, the absorption might not follow a simple power-law dependence on photon energy, leading to ambiguous or misleading results when using the Tauc method.

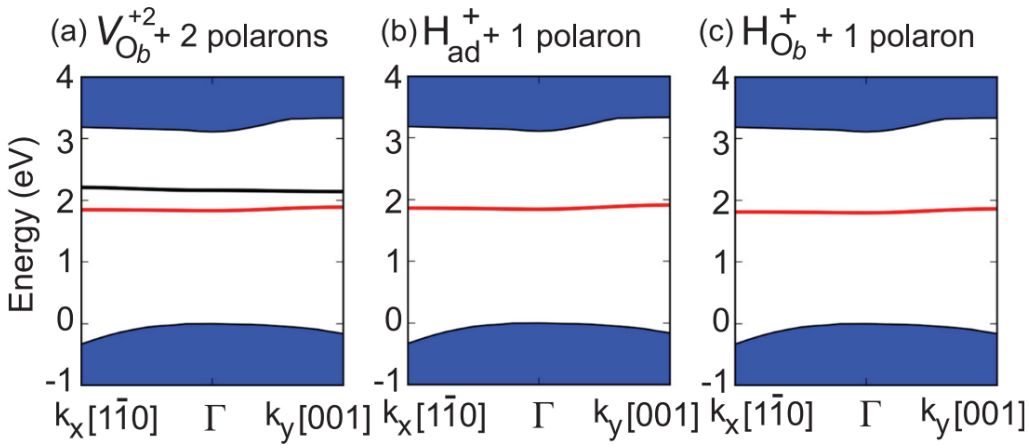

Figure 57 – Surface projected band structure for donor-polaron complexes on TiO_2 (110): (a) Oxygen vacancy in the +2 charge state (V^{+2}_{Ob}) with two polarons; (b) H adatom on a bridging O (H^{+}_{ad}) with one polaron; and (c) substitutional H on a bridging O site (H^{+2}_{Ob}) with one polaron. The states in the band gap are the polaronic states. Adapted from [341].

Despite these challenges, the band structure of a small polaronic material consists of the intrinsic band structure overlapped with states induced by polarons. Therefore, to a certain extent, the Tauc plot method can still be applied to small polaron semiconductors in a similar way as for band conduction semiconductors. Based on Equation (53), the corresponding Tauc plots for our samples are shown in Figure 58.

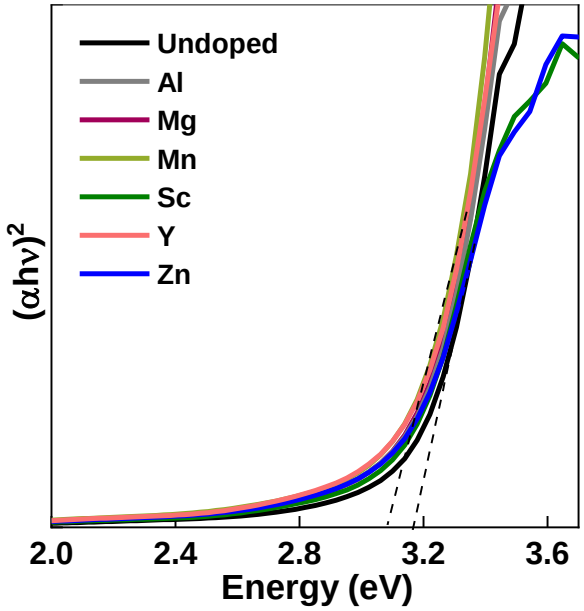

Figure 58 - Tauc plots of undoped and doped samples.

The optical direct band gap for the undoped sample is approximately 3.2 eV, consistent with off-stoichiometric samples and is consistent with most reports in the literature. The introduction of the dopant leads to a slight reduction in the band gap. This behaviour is observed for all dopants, regardless of their charge.

Two possible explanations exist for this phenomenon in the presence of high carrier concentration. First, it might be due to the inverse Burstein-Moss effect. The Burstein-Moss effect is

more pronounced in n-type semiconductors compared to p-type semiconductors because the DOS at the bottom of the CB is lower than at the top of the VB. In p-type semiconductors, as the doping concentration increases, the Fermi level moves closer to the VB edge, causing the apparent band gap to increase, though this effect is less dramatic than in n-type materials. The negative Burstein-Moss shifts can also occur in some cases due to changes in the band structure of the materials caused by doping or other effects. The effect is observed in various doped material such as IZO [342].

However, in our case, the optical changes upon doping do not coincide with alterations in electrical properties. As previously mentioned, the conductivity remains unchanged after doping with all elements. The only phenomenon that can explain this situation is band gap renormalisation. This refers to the reduction of the semiconductor band gap due to many-body effects, such as carrier-carrier or carrier-phonon interactions. This narrowing of the band gap can occur without a significant change in carrier concentration or mobility, which are the primary factors affecting electrical conductivity. Band gap renormalisation is known to occur due to exchange interactions and screening Coulomb interactions among free carriers in highly doped or excited semiconductors. This effect has been observed in highly doped semiconductors, photoexcited perovskites, and semiconductor quantum wells [343], [344]. A good description of band gap renormalisation is given for silicon-doped Ga_2O_3 [345]. Degenerate doping gives rise to an increase in the optical band gap $E_{opt} = Eg_0 + \Delta BM$ by Burstein-Moss shift (ΔBM) due to the occupation of bottom of CB (Figure 59 middle panel). However, the widening of E_{opt} is further counteracted by band gap renormalisation (ΔRN) (Figure 59 right panel).

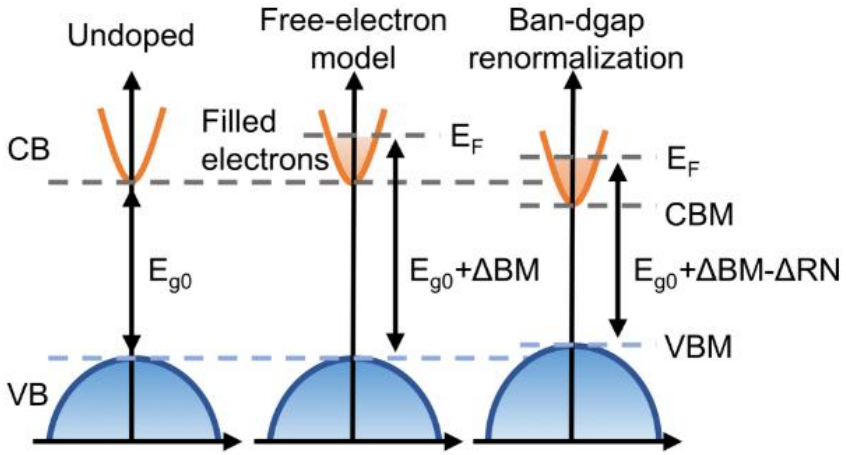

Figure 59 – Schematic diagram for change of the electron structure for Si doped Ga_2O_3.

Existing models do not explain such large relative changes in band gap and are not entirely self-consistent. The band gap renormalisation is usually quantitively explained by various numerical fittings techniques. For example, a coefficient law of 1/3 was used in the case of Iodine doped PbTe which reflects an electron–electron exchange interaction. The renormalisation effect in these samples is shown to be more than 0.1 eV, on the same order of magnitude as the band gap itself [346].

In conclusion, doping the delafossite samples induces a slight decrease in the band gap. We can exclude the possibility of an inverse Burstein-Moss effect, as the films do not exhibit any changes in electrical properties, and this effect is generally negligible in p-type materials. It is highly probable that band gap renormalisation occurs in our samples. This phenomenon is commonly reported in highly degenerate doped semiconductors with strong coupling to the lattice, conditions that are

perfectly met by the off-stoichiometric copper chromium delafossite. The strain induced by doping is the most frequently reported cause for band gap renormalisation in such materials. For example, the band gap wavelength was observed to red shift 0.2% for every 0.03 increase in the indium mole fraction, which introduces more strain into the InGaAsP system [347]. If we take closer look at the differences among the band gaps of films with different dopants, we can write the following relationship (although the errors, especially in linear interpolation, might seriously affect this).

$$E_{g,Mn} < E_{g,Y} < E_{g,Mg} < E_{g,Al} < E_{g,Sc} < E_{g,undoped}$$

These are correlated to some extent with our analysis of strain in these samples (for example the minimum strain is observed in scandium (Figure 62). However, the differences observed in the case of band gaps and the levels of doping are not sufficiently significant to confirm the band gap renormalisation in our samples.

5.2.5. X-ray diffraction characterisation

The structure of Cu-Cr-O films grown for 60 min, intentionally extrinsically doped with 5 at.% Al, Mg, Mn, Sc, Y and Zn, on α-Al_2O_3 was assessed by GI-XRD analysis (Figure 60). The same peak reflections corresponding to pure delafossite phase were identified as previously, with no peaks related to parasitic phases visible.

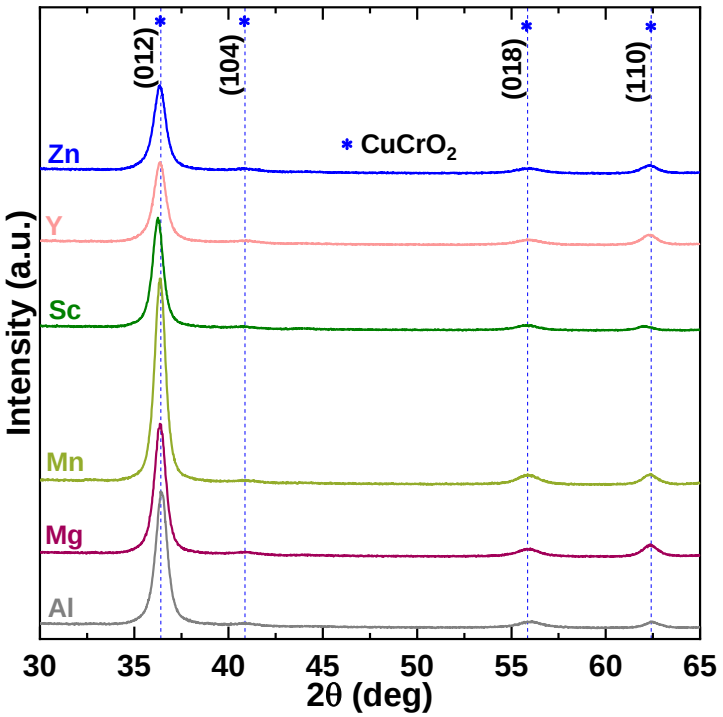

Figure 60 – GI-XRD diffractogram of as-deposited intentionally extrinsically doped Cu-Cr-O samples with Al, Mg, Mn, Sc, Y and Zn on α-Al_2O_3 substrates (offsets for clarity).

θ-2θ X-ray diffraction profiles for intentionally extrinsically doped Cu-Cr-O samples at different Ψ values are shown in Figure 61. The peak detected at 2θ = 37.7° in Sc and Zn doped samples probably corresponds to the α-Al_2O_3 substrate (110). The broad peak around 2θ = 31.5° (006) is a fingerprint of the epitaxial growth of delafossite on α-Al_2O_3 substrate. A shift in both (006) and (012) reflections with Ψ values is visible, suggesting the presence of residual stress.

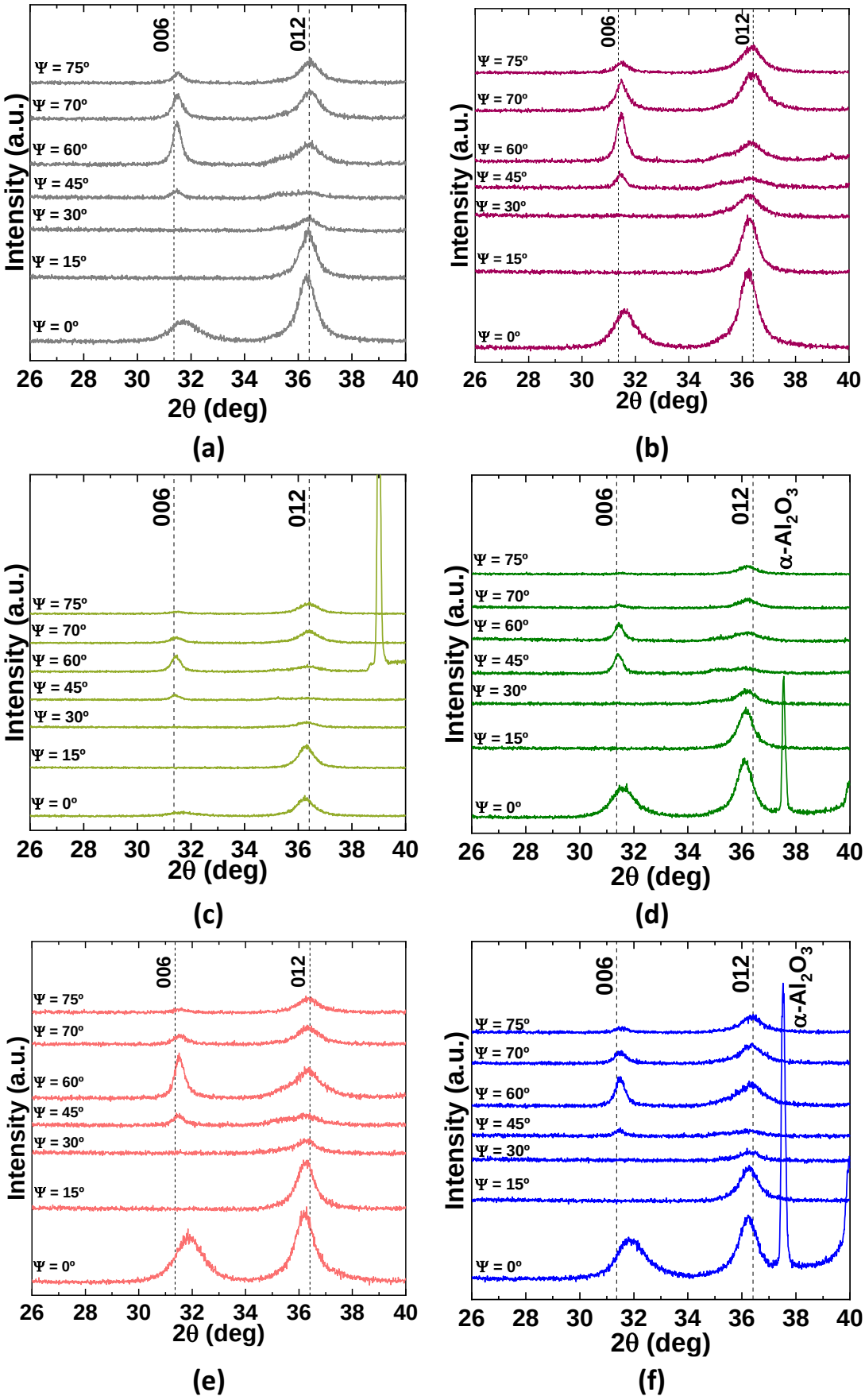

Figure 61 – θ-2θ X-ray diffraction profiles for intentionally extrinsically doped Cu-Cr-O samples with (a) Al, (b) Mg, (c) Mn, (d) Sc, (e) Y and (f) Zn on α-Al_2O_3 substrates, at different Ψ values.

Figure 62 depicts the $\sin^2\Psi$ method plots, for 300-nm thick intentionally extrinsically doped CCO films for (006) and (012) reflections. In (006), for $\sin^2\Psi = 0$ the d value is much smaller than the unstrained reported values, an indication of the epitaxial growth as observed in TEM micrographs. The approximate linear behaviour of the plots for other values of $\sin^2\Psi$ in both (006) and (012) reflections is an indication of compressive strain, as the slope is negative. This might indicate that the epitaxial strain overshadows the thermal strain in CCO films on α-Al_2O_3, because the expected thermal strain at room temperature is tensile in CCO grown on this substrate.

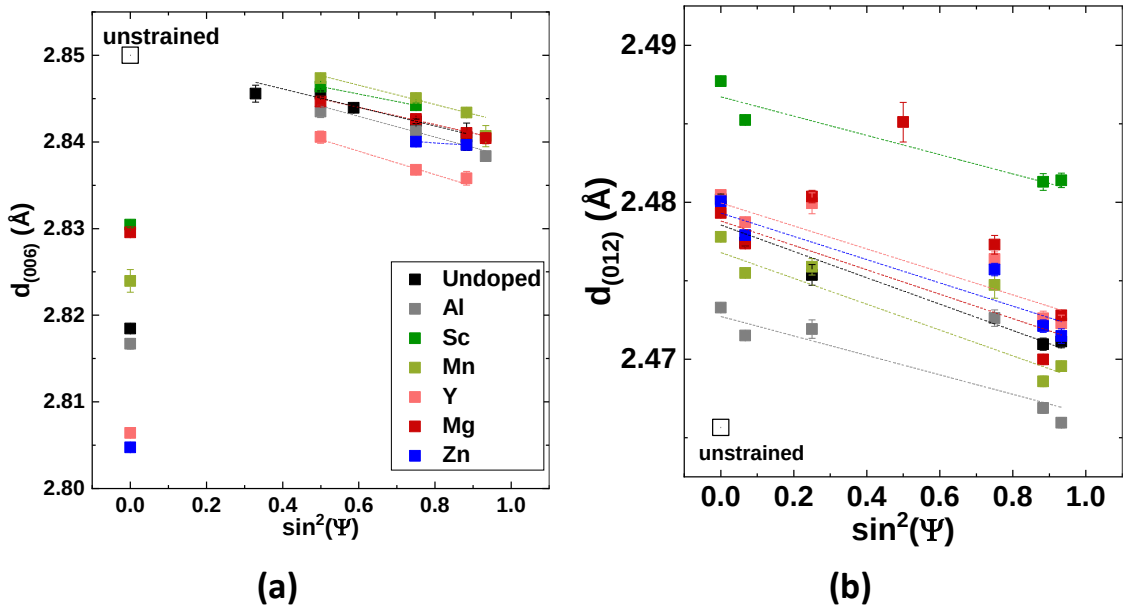

Figure 62 - $\sin^2\Psi$ plots for (a) 006 and (b) 012 reflections.

Finally, the small concentrations detected by XPS of some dopants, combined with the small variation of the linear behaviour of $\sin^2\Psi$ plots and the similarities of electrical conductivity of the films regardless the dopant, make it impossible to conclude the effect of dopant cation radii. The lack of elastic parameters for this material, makes it challenging to fully understand the impact of strain.

5.2.6. Electrical characterisation

Figure 63 shows the measured electrical conductivities of undoped and intentionally extrinsically doped delafossite films. The sheet resistance of each sample was measured at room temperature using the four-point probe technique, and the electrical conductivity was calculated according to Equation (56). These films demonstrated high levels of electrical conductivity, likely due to the oxygen excess detected by XPS analysis, undoped delafossite has much lower conductivity.

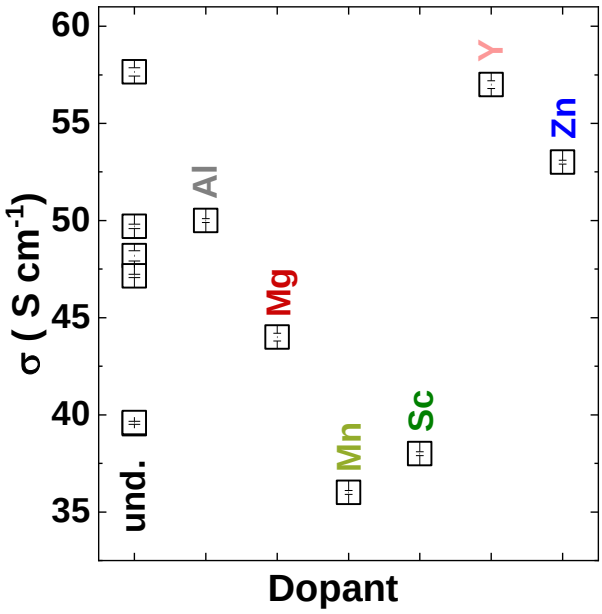

Figure 63 – Electrical conductivity of undoped and intentionally extrinsically doped Cu-Cr-O samples measured by the four-point probe method at room temperature on α-Al_2O_3 substrates.

However, it is impossible to conclusively determine the effect of each dopant on the electrical properties for two reasons. Firstly, the dopant concentrations vary, with three out of six dopants detected below the XPS detection limit of 0.5%, and Mg not detected at all. Secondly, inhomogeneities during the chemical deposition process and the roughness of the film can affect the film's thickness, leading to imprecise measurements of sheet resistance.

5.3. Effects of thermal strain

5.3.1. Electrical conductivity

As previously mentioned in the SEM characterisation section, two batches of off-stoichiometric delafossite thin films were deposited on various substrates: one with minimal thickness and another with thicker films, to investigate the influence of strain on the electrical properties. The electrical conductivity of the samples at room temperature was calculated, following the measurement of the sheet resistance using the four-point probe technique (Figure 64). All samples exhibited an electrical conductivity greater than 5 S cm^{-1}, which is the minimum measurable conductivity value for the LSR-3 setup. This confirms that all samples are within the detectable range for subsequent thermoelectric measurements.

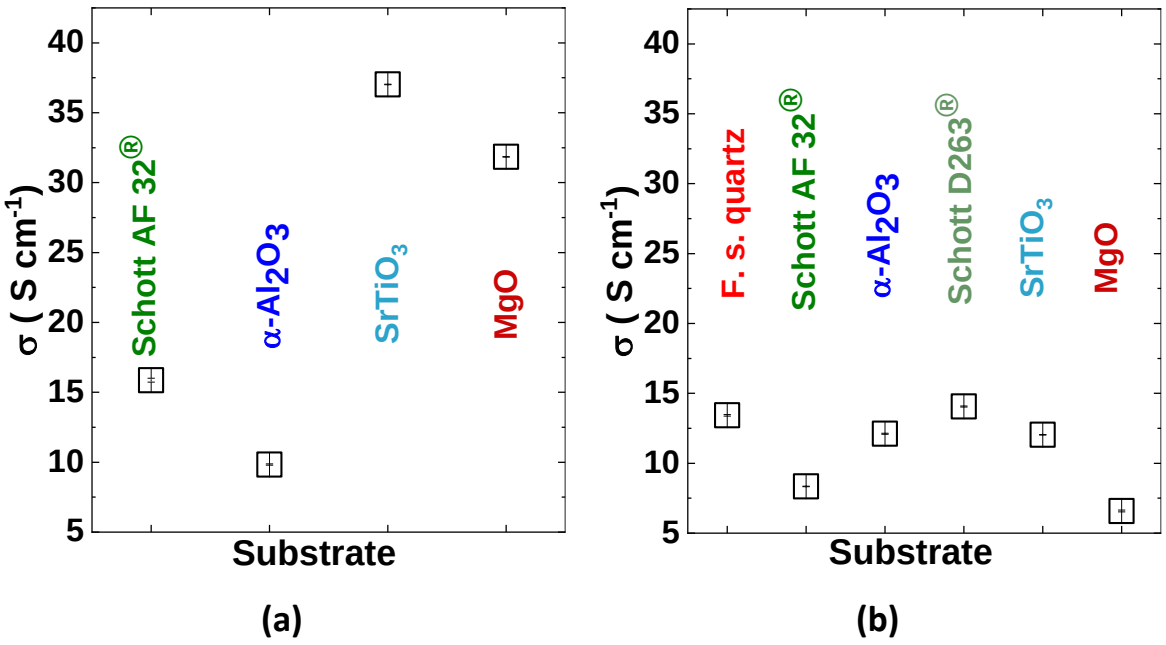

Figure 64 - Electrical conductivity of all samples characterised by the LSR-3 setup, measured by the four-point probe method at room temperature for (a) 70 nm and (b) 300 nm thick $Cu_{2/3}Cr_{4/3}O_2$ films on different substrates.

Following the initial conductivity measurements, thermoelectric and electrical characterisation were performed using the LSR-3 setup.

Figure 65 illustrates the electrical conductivity dependence on temperature for the delafossite thin films with two different thicknesses deposited on various substrates, up to temperatures around 580 K or 630 K. This was determined based on Equation (60). Measurements were conducted during both the heating and the cooling phases of the samples, with the plotted points in the figure corresponding exclusively to the heating phase measurements.

The electrical conductivity data exhibit typical semiconducting behaviour, with values increasing from approximately 5 S cm^{-1} to 70 S cm^{-1} as the temperature increases. The measured electrical conductivity varies depending on the substrate used, which may be attributed to small errors in precise thickness measurements, as SEM micrographs reveal slight differences across the film area. Inhomogeneities might also arise during the chemical deposition process. The σ(T) shows a

small kink remarkably close to the deposition temperature (T_d) of each batch (indicated by dashed vertical lines). The deposition temperature represents a transition from tensile to compressive stress, as described by Equation (78). In Figure 65b, it can be observed that this feature is less pronounced in the case of thicker samples [304].

The kink observed around T_d possibly indicates a phase transition or a stress relaxation phenomenon. In thin film materials, such thermal transitions can be attributed to changes in microstructure, grain boundary behaviour, or a shift from tensile to compressive stress, as mentioned. Thicker samples exhibit a less pronounced kink, possibly due to their ability to better accommodate or distribute the stress, leading to a more uniform strain across the film [304].

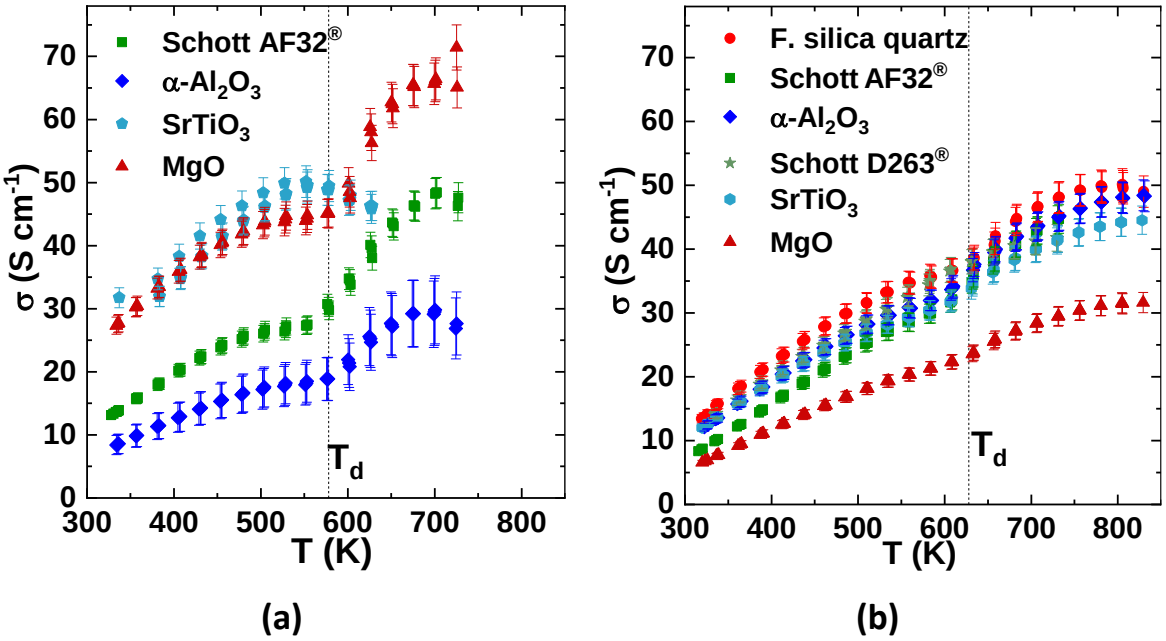

Figure 65 – Measured σ(T) for (a) 70 and (b) 300 nm thick $Cu_{2/3}Cr_{4/3}O_2$ films on different substrates.

Arrhenius fittings were conducted to determine the dominant conduction mechanism in delafossite films. In band conduction, the conductivity typically shows an Arrhenius-type behaviour, characterised by a linear relationship in the ln(σ) vs T plot. In contrast, in materials where small polaron hopping is the dominant conduction mechanism, the Arrhenius plots show linearity in the ln(σT) vs T^{-1} plot.

Figure 66 shows the Arrhenius plots for band conduction. These were obtained by taking the natural logarithm of both sides of Equation (9), yielding:

$$\ln(\sigma) = \ln(\sigma_0) - \frac{E_\sigma}{k_B T} \quad \textbf{(94)}$$

The plots exhibit an almost linear dependence at temperatures lower than T_d. The Arrhenius plots for small polaron hopping conduction (Figure 67) were obtained by taking the natural logarithm of both sides of Equation (28):

$$\ln(\sigma T) = \ln\left[\frac{gNc(1-c)q^2a^2\nu_0}{k_B}\right] - \frac{E_h}{k_B T} \quad \textbf{(95)}$$

Here, N, c and a are considered temperature-independent parameters. Under these assumptions, the linear fit improves significantly. Moreover, in both conduction mechanisms, it can be observed that the conductivity does not follow a linear trend at temperatures higher than T_d for the thinner films. For the thicker films, the behaviour remains almost linear at $T > T_d$. This behaviour might again be correlated with the previously mentioned explanation regarding the kink observed in the σ(T) curves.

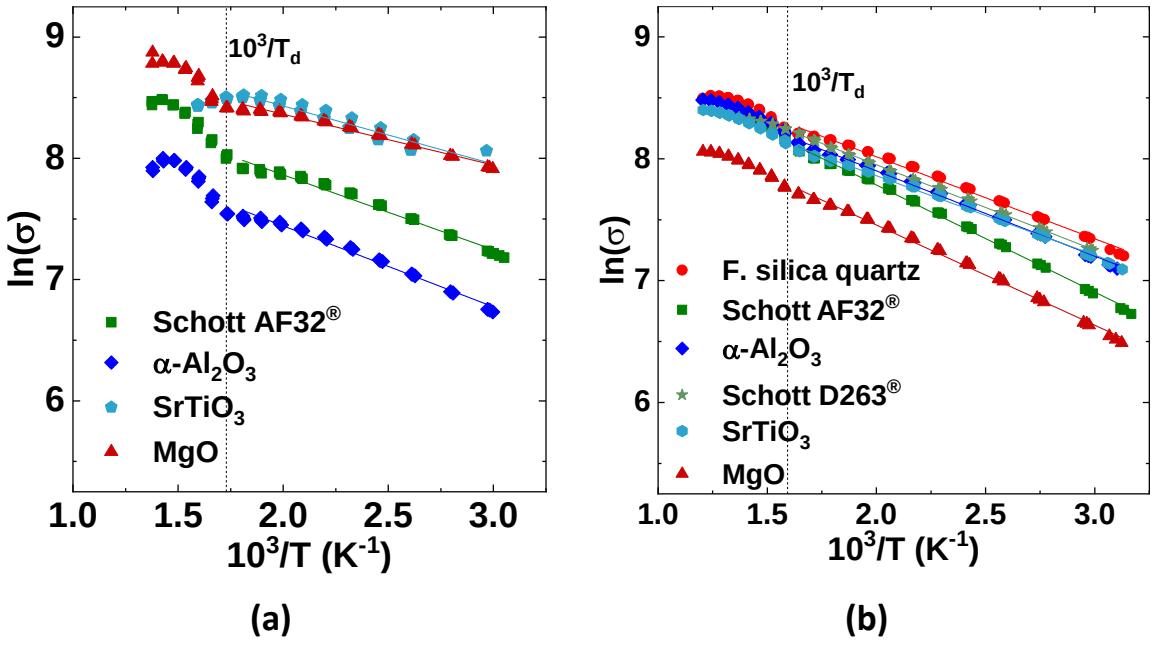

Figure 66 – Arrhenius plots in band conduction for (a) 70 and (b) 300 nm thick $Cu_{2/3}Cr_{4/3}O_2$ films on different substrates.

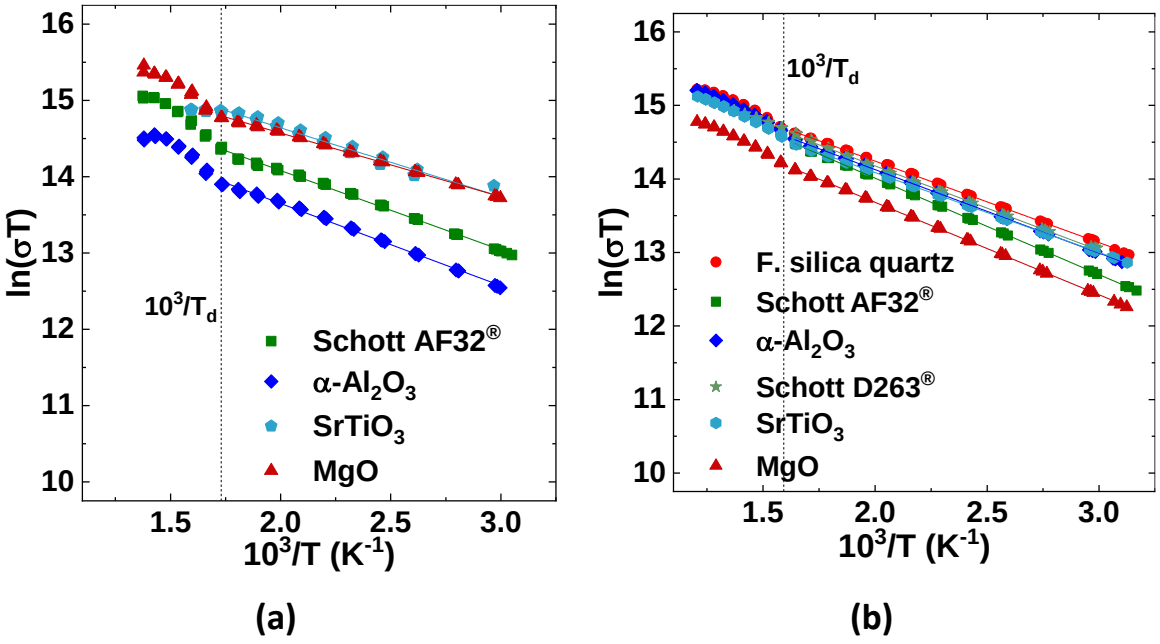

Figure 67 – Arrhenius plots in small-polaron model for (a) 70 and (b) 300 nm thick $Cu_{2/3}Cr_{4/3}O_2$ films on different substrates.

For the low-temperature range (below 200 K), the Mott variable-range hopping (VRH) is reported to be the dominant conduction mechanism in delafossite materials. Taking the natural logarithm of both sides of Equation (11), we obtain:

$$\ln(\sigma) = \ln(\sigma_0) - \left(\frac{T_M}{T}\right)^{\frac{1}{n+1}} \quad \textbf{(96)}$$

In our case, the best fittings were obtained for the transport dimensionality parameter n = 2, indicating that the hopping mechanism of holes is confined to two-dimensional motion within the Cu basal planes. The Arrhenius plot ln(σ) vs $T^{-1/3}$ (Figure 68) shows that a linear trend is only observed at lower temperatures.

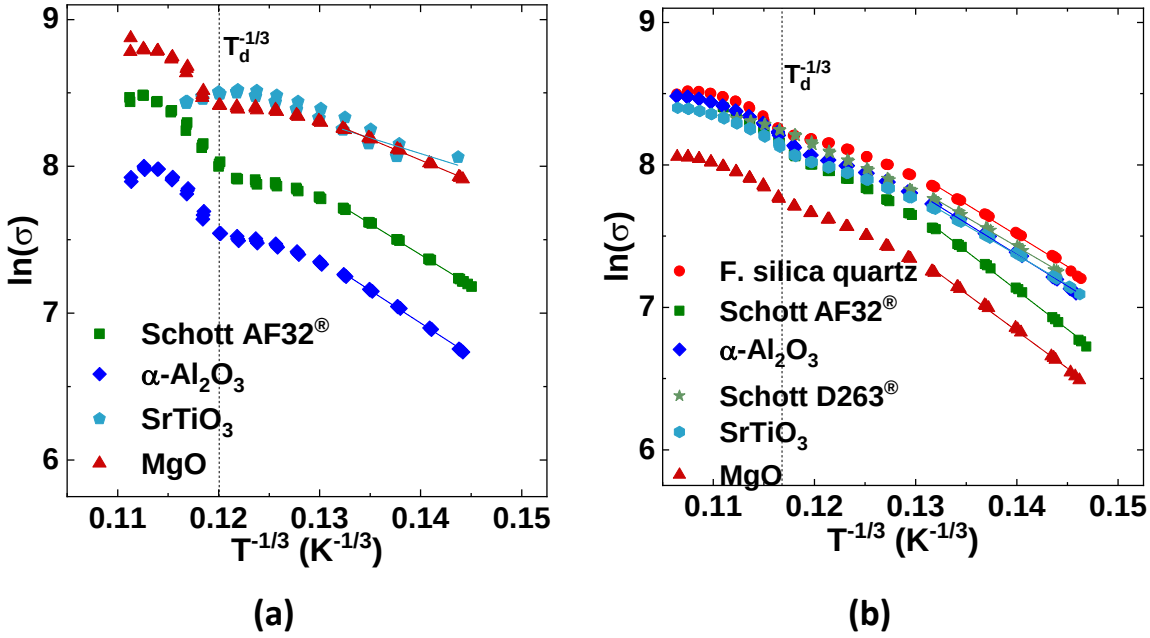

Figure 68 – Arrhenius plots in two-dimensional VRH model for (a) 70 and (b) 300 nm thick $Cu_{2/3}Cr_{4/3}O_2$ films on different substrates.

However, as previously mentioned, the Mott VRH mechanism is reported to dominate at temperatures below 200 K. In our measurements, the lowest temperature is 330 K, making it clear that the data is not within the expected temperature range where Mott VRH is the primary conduction mechanism.

5.3.2. Seebeck coefficient

Seebeck coefficient measurements were conducted on the same delafossite films described previously. As observed in Figure 69, the Seebeck coefficient exhibits positive values ranging from 100 to 200 μV K^{-1}. The S(T) shows an almost linear increase with temperature. Notably, deviations are observed for films deposited on $SrTiO_3$ substrates at elevated temperatures, which may be attributed to artefacts associated with the measurement setup.

A remarkably interesting feature, present in both batches of samples is the quasi-linear Seebeck coefficient dependence on temperature. In the case of thinner samples, within the 300-450 K range, the Seebeck coefficient remains almost constant at values around 150-180 μV K^{-1}. After 450

K, the coefficients increase up to approximately 300 μV K^{-1} at 700 K. For thicker samples, the linear dependence on temperature begins even at lower temperatures, but some saturation is observed after 700 K. The perfect reversibility of the curves indicates the same Seebeck coefficient before and after the heating-cooling measurement cycles, suggesting that the carrier concentration remains unchanged at the beginning and the end of the experiment.

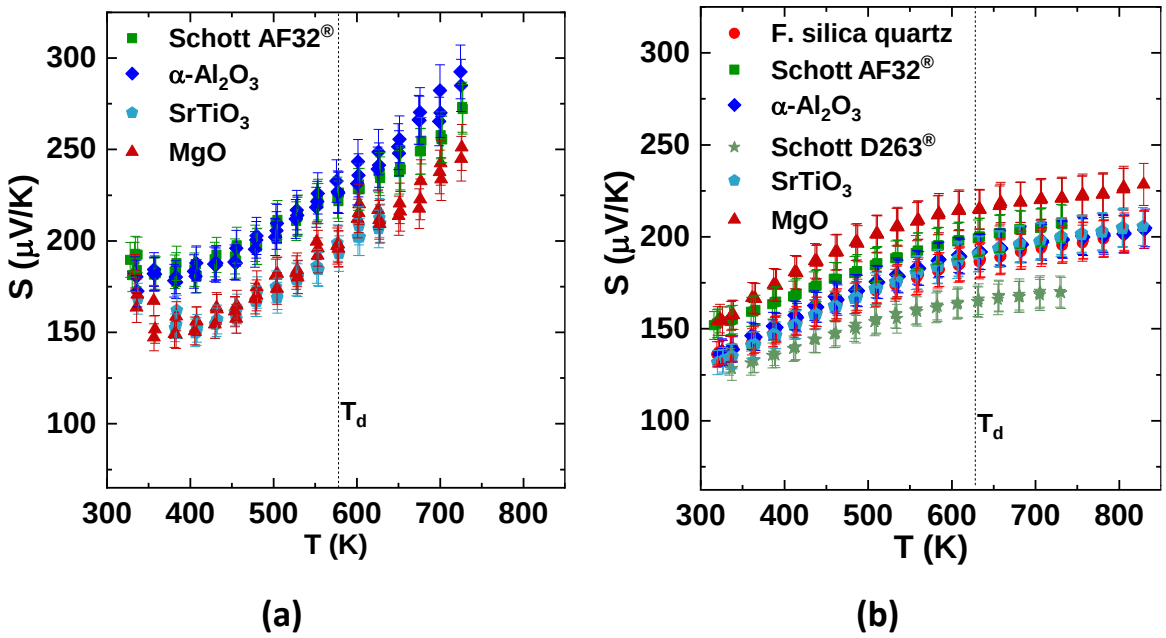

Figure 69 – Measured S(T) for (a) 70 and (b) 300 nm thick $Cu_{2/3}Cr_{4/3}O_2$ films on different substrates [304].

We used the Heikes formalism to estimate the carrier concentration and the mobility of the delafossite thin films (Equation (39)) [292]. Within the small polaron model, N_v is considered, leading to a temperature-independent S [256]. In contrast, the band conduction model predicts a temperature-dependent S. As previously mentioned, the predominant conduction mechanism in delafossite structure is small polaron hopping [272]. In the case of $CuCrO_2$, hopping occurs between the Cu^{2+} sites occupied by polarons, and "empty" Cu^{+} sites. Therefore, the density of sites occupied by polarons $[Cu^{2+}]$, i.e. the hole concentration (p), is given by:

$$[Cu^{2+}] = p = cN_{Cu} \quad \textbf{(97)}$$

where c is the fraction of sites occupied by polarons and N_{Cu} is the total density of sites of Cu sites in the crystal. In the context of small polarons, N_v is the total atomic density of Cu^{+} sites available for small polaron hopping [167]:

$$N_v = (1 - c)N_{Cu} \quad \textbf{(98)}$$

In rhombohedral R3-m $CuCrO_2$, there are 3 copper atoms per unit cell, and the unit cell has an approximate volume (V_{cell}) of 130.9 Å (ICDD PDF #04-010-3330). Therefore, in off-stoichiometric $Cu_{2/3}Cr_{4/3}O_2$, the Cu-site density is given by:

$$N_{Cu} = \frac{2}{3} \times \frac{3}{V_{cell}} \approx 1.5 \times 10^{22}\ cm^{-3} \quad \textbf{(99)}$$

Equation (39) for the hole concentration as function of S in a polaronic material is written as:

$$p = N_{Cu}\left[\frac{g_2}{g_1}\exp\left(\frac{Sq}{k_B}\right) + 1\right]^{-1} \quad \textbf{(100)}$$

The spin degeneracy (g_n) is given by:

$$g_n = (2S + 1)N \quad \textbf{(101)}$$

where S is the global spin and N is the number of orbital configurations. In $CuCrO_2$ structure, Cu^+ has a null spin with one configuration, whereas Cu^{2+} has spin equal to ½ and two possible configurations [205], [252], [275]:

$$g_1 = (2 \times 0 + 1) \times 1 = 1 \quad \textbf{(102)}$$

$$g_2 = \left(2 \times \frac{1}{2} + 1\right) \times 2 = 4 \quad \textbf{(103)}$$

However, Figure 69 reveals a temperature dependence of S, which contradicts the predictions of the Heikes formalism and thus questions the validity of small polaron model in this context. According to the small polaron model for semiconductors, the Seebeck coefficient should remain temperature-independent, reflecting a constant charge carrier concentration with temperature.

The observed reversibility in S(T) suggests that the vacancies generating the p-type charges are not healing. Previously, it was demonstrated that healing consists in Ostwald ripening mechanisms, based on the dissolution of shorter chains of vacancies into single Cu vacancies migrating to grain boundaries or longer chained vacancy defects [305]. This is further confirmed by literature indicating that the healing on defects in copper chromium delafossites occur at temperatures beyond 600 °C.

Finally, the post-treatment annealing experiments previously described at the beginning of this chapter indicate the stability of electronic properties within the range of temperatures studied here. In conclusion, there is no obvious reason why the carrier concentration should decrease with temperature.

One more aspect that must be discussed here is the difference in Seebeck coefficient values for thin and thick samples. For example, at room temperature the Seebeck coefficient has values in the 150-200 μV K^{-1} for thin samples and between 100 and 150 μV K^{-1} for thicker samples on

different substrates. This tendency is maintained over the whole large of temperatures. What we observed is a different "packing" of the values. For the thinner samples, the S spreads (S_{TMax}-S_{TMin}) over almost 150 µV K^{-1}, whilst for thicker ones the spreading is only about 50 µV K^{-1}. There is no doubt that error source relies on the measurement's errors. However, as the thermal power coefficient is independent on the geometry of the samples, errors related for example in the estimation of thickness might be neglected. Another possible explanation might come from strain altering the band gap of the materials, which leads to change in carrier concentration and thus affecting the coefficient numerical values. This is the case of InAs nanowire, where the lowest conduction band shifts down along the energy axis, whereas for the top valence band, the heavy-hole (HH) and light-hole (LH) bands will split [348]. Since both the valence and conduction bands shift with strain, the Fermi level must also shift. By applying solid state equations, Wortman [349] gave a formula for carrier concentration (holes) dependence on strain on silicon.

$$p = p_0 \sum_{i}^{min} \frac{m_i^{3/2}}{m_i^{*3/2}} \, exp\left(-\frac{\Delta E_F - \Delta E_{v,i}}{k_B T}\right) \qquad \textbf{(104)}$$

where p_0 is the carrier concentration with zero strain, the summation is over the number of maxima on the valence band (typically two terms, related to the heavy (HH) and light holes (LH)) and the $\Delta Ev_{v,i}$ is the change in energy of HH and LH branches under the strain. The reasoning might be applied in our case as we can consider that at room temperature all carrier charges are generated. Additionally, strain can induce the formation of defects and dislocations in the crystal lattice. These defects can act as trapping centres or recombination sites, thereby affecting carrier lifetime and concentration.

Generally, experimental and theoretical studies reported that tensile strain typically reduces the band gap, leading to increased carrier concentration, while compressive strain increases the band gap, potentially reducing carrier concentration [350]–[353]. This might apply in our case. However, the absence of an exact value for the delafossite CTE makes impossible the estimation of strain in the sample. Such change on carrier concentration, even small, might lead to an observable modification on the Seebeck coefficient values, as the formula contain an exponential function. However, the relative tighter spread of the values on the thicker samples might be explained, if we consider that the averaged strain is less significant in those samples. On the other hand, in the 70-nm thin films batch, the influence of stress is more important. This might lead to an augmented contribution of strain on carrier concentration, hence on Seebeck coefficient values.

In conclusion, the Seebeck coefficient dependence on temperature was studied for films deposited on substrates with different thermal coefficients of expansion and with different thicknesses. Portions with temperature linear dependence of S were observed for all samples. This cannot be explained by considering the classical small polaron transport model, used in the vast majority of reports on the topic. Using previous theories of Seebeck coefficient in semi-metals, where the contribution of vibrational energy transported is accounted for, we found a possible explanation of thermal behaviour. The delafossite films are polycrystalline and high degenerated. The hopping of holes occurs between two copper sites. As the samples demonstrate high off-stoichiometries (an important number of copper chained vacancies), it is then highly probable that the initial and the final sites are not equivalent in terms of energy and the coupling with the lattice. In this case, the second term of Seebeck coefficient cannot be neglected, and it leads to an

overestimating of its values. Consequently, this results in an underestimation of carrier concentration and finally to an overestimation of mobility values. In the dedicated paragraph we will try a quantitative estimation of these overvalues.

We also advanced the hypothesis in order to explain the minor but visible differences in Seebeck coefficient values for thinner and thicker samples. Our claim is that the strain, more significant in thinner samples, leads to changes in carrier concentrations that directly affects the quantitative estimation on thermopower values. Unfortunately, the level of strain induced by thermal coefficients expansion mismatch method is not allowing significant resolution to fully support the hypothesis.

5.3.3. Electrical mobility

The electrical mobility was calculated according to Equation (3), with the conductivity directly measured and the carrier concentration estimated from the Seebeck acquired values (Equation (100)). The carrier concentration, which is linked to the Seebeck coefficient, exhibits an approximately linear dependence within this temperature range. This suggests that the observed kink in σ(T) is likely attributable to variations in mobility. As shown in Figure 70, the mobility values are present for films from batches with two different thicknesses [304].

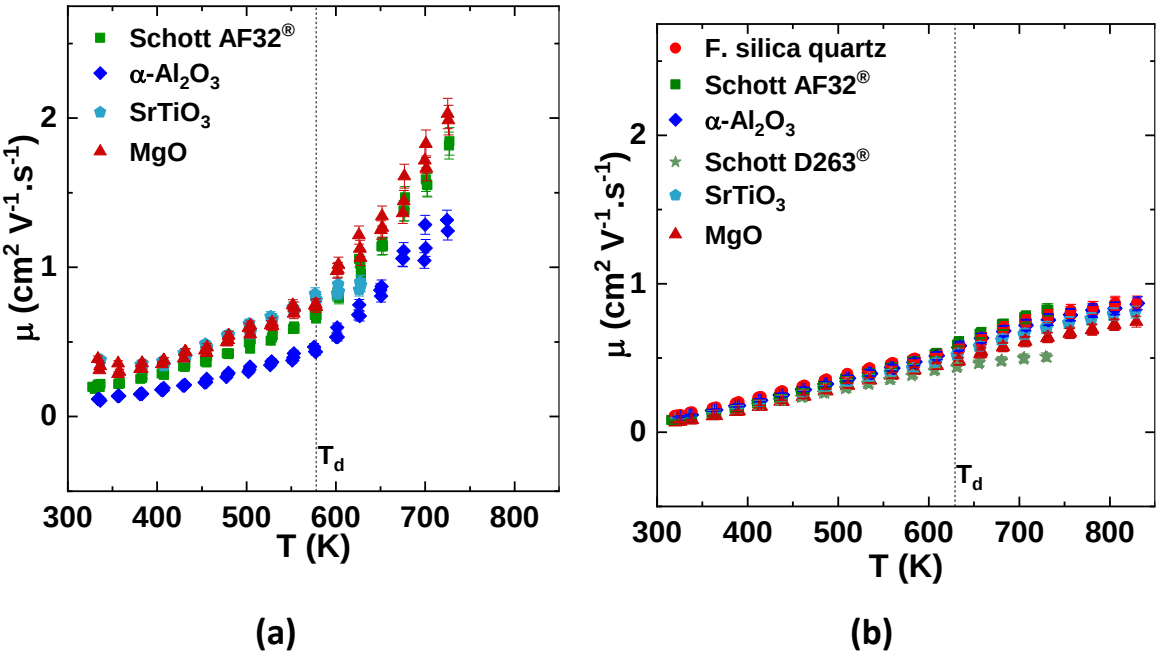

Figure 70 - Estimated μ(T) for (a) 70 nm and (b) 300 nm thick $Cu_{2/3}Cr_{4/3}O_2$ films on different substrates [304].

At room temperature, the mobility values range from 0.1 to 0.4 $cm^2 V^{-1} s^{-1}$. For the thinner samples, mobility increases almost linearly with temperature, exhibiting a crossover at the deposition temperature. In contrast, thicker films either show a less pronounced crossover or none at all. Moreover, the mobility values at higher temperatures are lower for thicker films compared to thinner ones. This behaviour, where the electronic properties vary with film thickness and temperature, was previously reported by Rastogi et al. for spray-deposited Mg-doped $CuCrO_2$ semiconductor oxide thin films [354]. In their study, which covered a temperature range including

the deposition temperature, a similar "kink" was observed in the σ(T) curve. However, the kink was less pronounced for thicker films and was not observed precisely at the deposition temperature. The authors attributed the observed changes to the influence of grain boundaries on conduction. Building on this, the hopping activation energies (E_h) and the hopping frequency (ν_0) or the films studied here were calculated. In the adiabatic regime of small polarons, the electrical conductivity follows an Arrhenius relationship, as given by [147],[304]:

$$\ln\left[\frac{\mu T}{(1-c)a^2(T)}\right] = \ln\left(\frac{q\nu_0}{k_B}\right) - \frac{E_h}{k_B T} \qquad \textbf{(105)}$$

In this expression, both the temperature-dependent Cu-Cu distance (a) and the unexpected temperature dependence of c were considered. From this equation, E_h and ν_0 can be extracted from the slope and intercept of the plot, respectively. The lattice parameter of the delafossite at deposition temperature ($a(T_d)$) was calculated according to Equation (77), knowing that the lattice parameter of the delafossite at room temperature is 2.97 Å (ICDD PDF #04-010-3330). Then, considering the thermal strain and re-arranging Equation (78), a(T) is given by:

$$a(T) = a(T_d)\left[(T - T_d)(\alpha_s - \alpha_f) + 1\right] \qquad \textbf{(106)}$$

The Arrhenius plots are depicted in Figure 71. The extracted E_h and the hopping frequency ν_0, as well as the S an σ at room temperature are shown in Table 13.

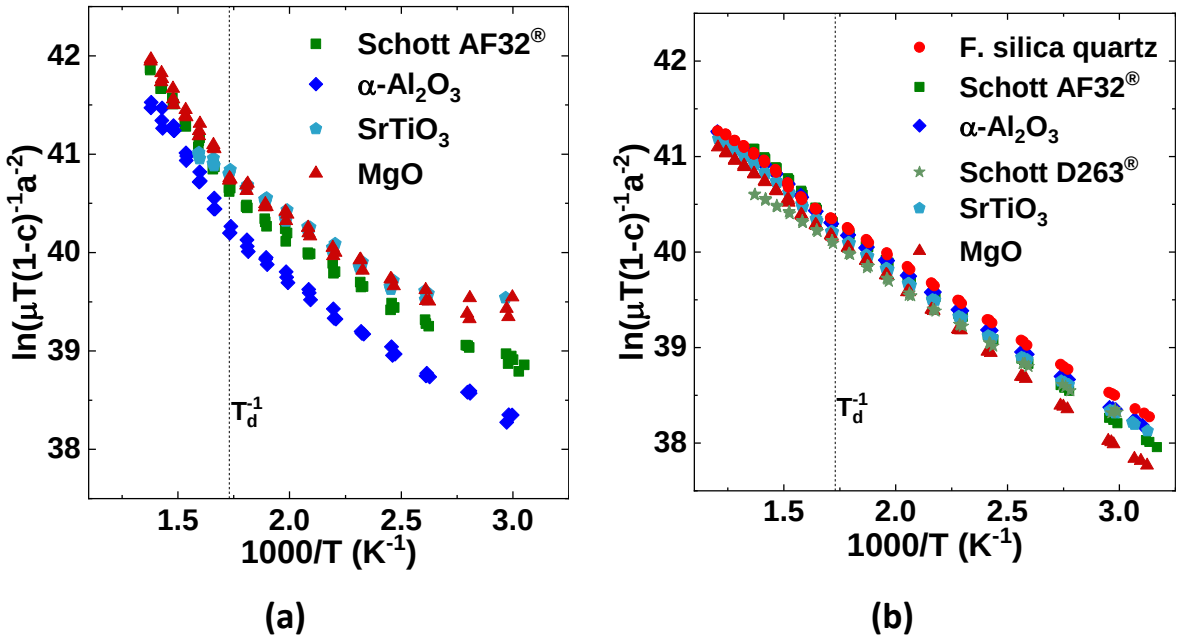

Figure 71 - Arrhenius plots for extraction of E_h for (a) 70 nm and (b) 300 nm thick $Cu_{2/3}Cr_{4/3}O_2$ films on different substrates.

Table 13 – S, σ, E_h, and ν_0 at room temperature for the studied films.

Substrate	h_f (nm)	S (μV K^{-1}) at RT	σ (S cm^{-1}) at RT	E_h (meV)	ν_0 (x 10^{14} Hz)
Schott AF 32® eco glass	≈ 70	123	16	132	5
α-Al_2O_3		107	10	145	5
$SrTiO_3$		105	37	126	5
MgO		94	32	124	5
Fused-silica quartz	≈ 300	118	13	131	4
Schott AF 32® eco glass		134	8	147	5
α-Al_2O_3		102	12	136	4
Schott D 263® T eco glass		105	14	128	3
$SrTiO_3$		109	12	133	5
MgO		109	7	150	5

For the thicker films, a linear behaviour of mobility was observed across the entire measured temperature range. In contrast, the thinner films exhibited two distinct slopes with a crossover occurring around the deposition temperature. E_h for the 70-nm films ranges from 124 to 145 meV (in the temperature range $T < T_d$), while for the 300-nm films, it ranges from 131 to 150 meV. This behaviour suggests that the thermal strain might influence the transport properties of the films. According to Equation (78), T_d represents the crossover between compressive and tensile ε_{th} regimes. The thermal strain induced by the substrate affects the Cu-Cu interatomic distances (lattice parameters) [147]. An increase (or decrease) in ε_{th} results in a longer (or shorter) distance for polarons to hop, thereby increasing (or decreasing) the mobility. In Figure 70b, the slope of μ(T) is nearly constant. According to Equation (80), ε_{th} is inversely proportional to the film thickness, suggesting that ε_{th} has a reduced impact on the electrical properties of thicker films, which is consistent with our observations. Figure 72 shows that the μ(T) data, normalised to the mobility at deposition temperature (μ_0), indicates no strain effects at this temperature ($\varepsilon_{th} = 0$).

Another noteworthy observation is the electrical behaviour of $Cu_{2/3}Cr_{4/3}O_2$ films grown on MgO. This substrate is unique among those studied, exhibiting a CTE greater than that of the film ($\alpha_s > \alpha_f$). If ε_{th} significantly influences the electrical properties of the thin films, the trend observed on MgO should be opposite to that on other substrates. Specifically, for a temperature $T \neq T_d$, the film on MgO would be in a tensile strain regime, while on other substrates it would be in a compressive strain regime. However, the real CTE of delafossite thin films might exceed that of MgO (12.8 ppm K^{-1}), potentially accounting for the similar trend observed across all substrates. Future studies should consider substrates with even higher CTE values to further explore this effect [304].

Additionally, the variation in mobility with different strain values at fixed temperatures was analysed (Figure 73). Here, for a fixed temperature, each datapoint corresponds to the normalised mobility of the delafossite films, on different substrates. This allows to analyse the effect of strain without interference of the temperature.

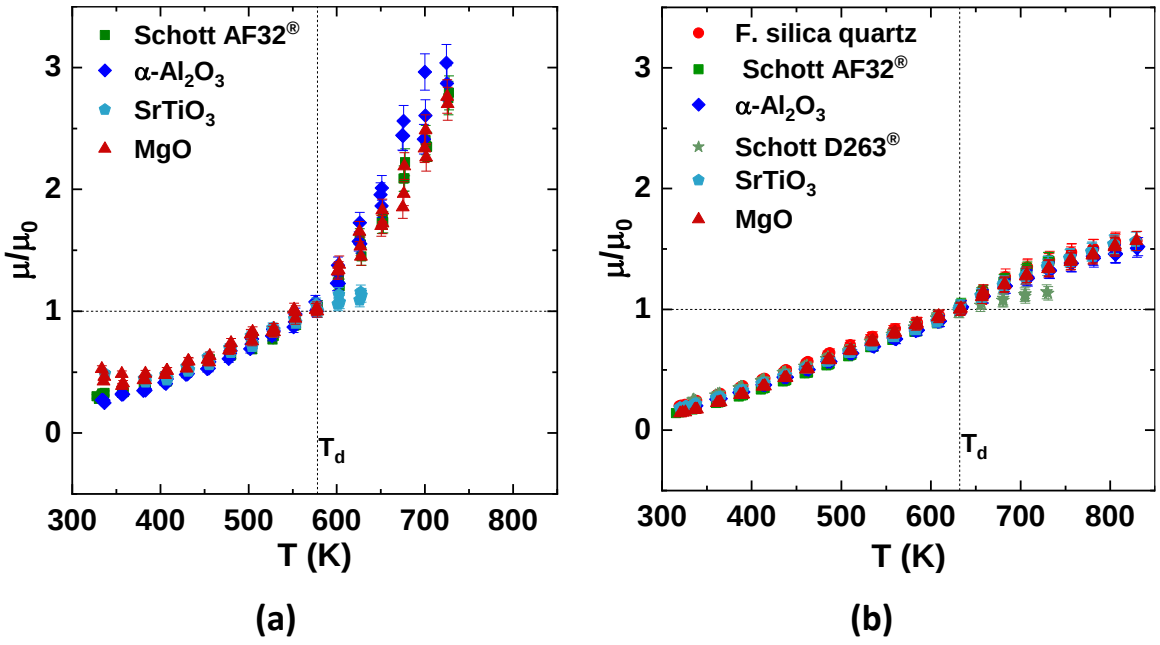

Figure 72 - $\mu/\mu_0(T)$ for (a) 70 nm and (b) 300 nm thick $Cu_{2/3}Cr_{4/3}O_2$ films on different substrates [304].

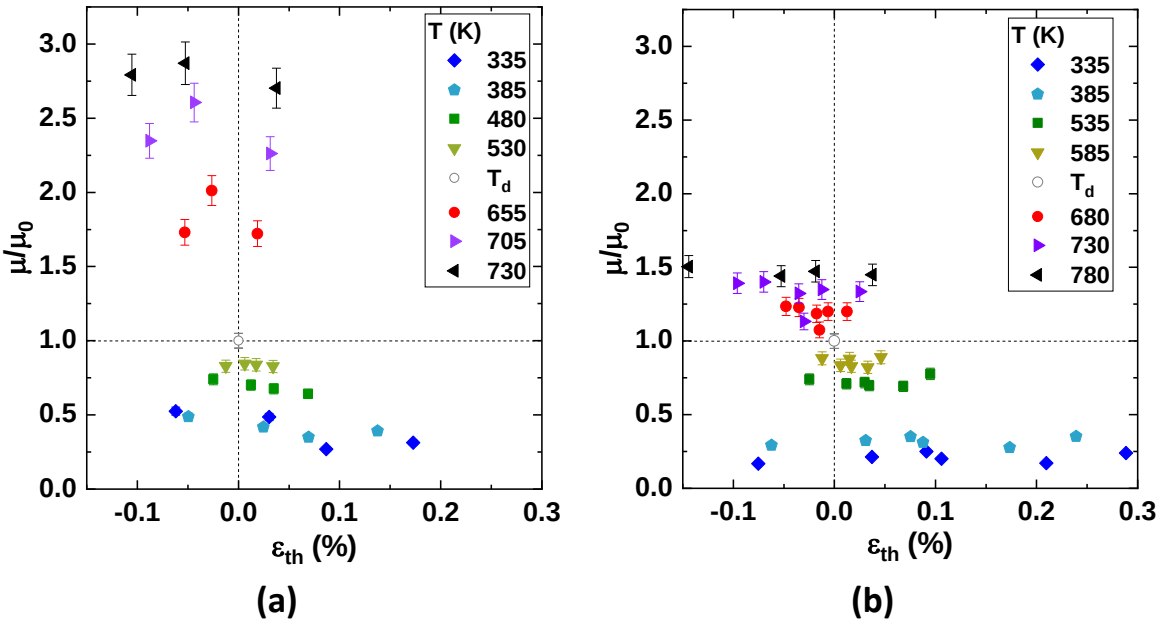

Figure 73 - $\mu/\mu_0(T)$ vs $\varepsilon_{th}(T)$ at fixed temperatures for (a) 70 nm and (b) 300 nm thick $Cu_{2/3}Cr_{4/3}O_2$ films on different substrates [304].

For temperatures $T < T_d$, the normalised mobility shows little variation with strain, with significant differences only at high temperatures for thinner films. If strain were to have a major impact on mobility, such effects would be expected to be more pronounced at temperatures $T > T_d$ [304].

5.3.4. Electrical mobility using Emin-Wood model

Considering the discussion from Chapter 2, we estimated the mobility based on Equations (3) and (100), where the carrier concentration was calculated considering S invariable with

temperature (Table 13). In this approach, the term accounting for the phonon transport energy is considered (Equation (49)) (Figure 74). The accounted value of S here corresponds to the one measured at room temperature. The calculated carrier concentrations of the thin films range from 8.5 to 12 x 10^{21} cm^{-3}.

Compared with the previous approach, two interesting features are now observed: firstly, the mobility decreased by one order of magnitude. These values are much closer to the Bosman-Van Daal limit, where mobilities around 0.1 $cm^2V^{-1}s^{-1}$ are typical for materials relying on small polaron transport [317]. Secondly, in the previous approach, the mobility seems to have an almost linear behaviour with temperature, with the slope changing at T_d (Figure 70). In Figure 74, the mobility shows a T^x dependence. Unexpectedly, the data can be fitted with a $T^{-3/2}$ dependence, consistent with the lattice scattering mechanism observed in free carriers.

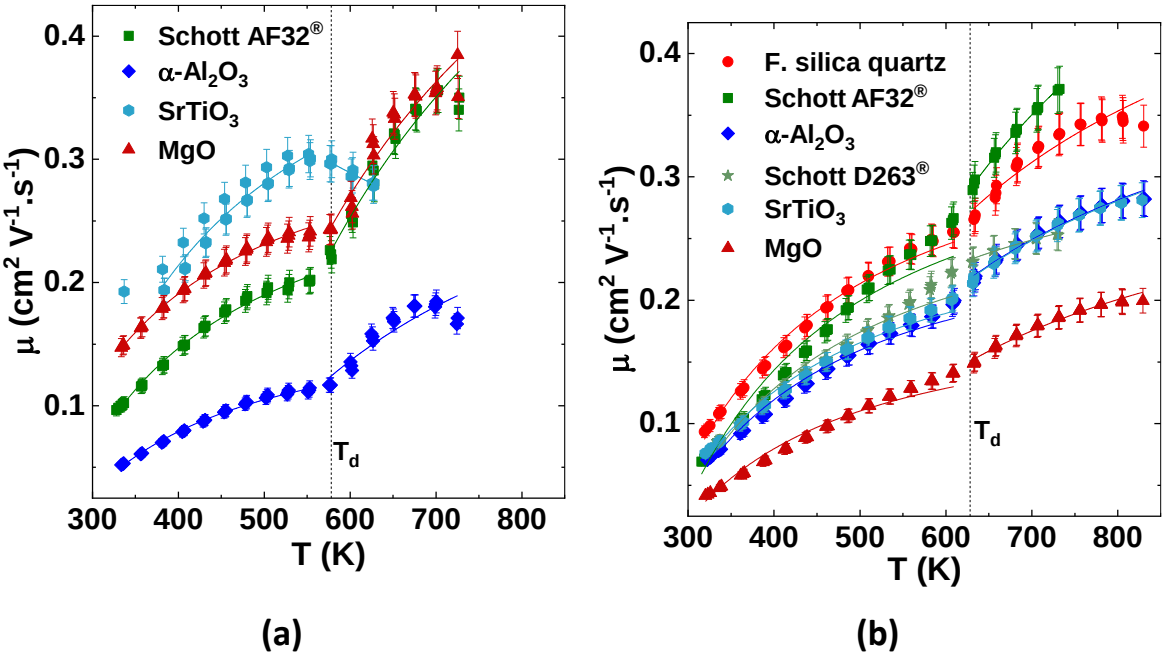

Figure 74 – μ(T) for (a) 70 nm and (b) 300 nm thick $Cu_{2/3}Cr_{4/3}O_2$ films on different substrates, considering S at room temperature for the calculation of the carrier concentration.

Next, we calculated the hopping frequency and activation energy for hopping by Arrhenius plots (Figure 75), considering the temperature dependence of mobility and hopping distance:

$$ln\left[\frac{\mu T}{a^2(T)}\right] = ln\left(\frac{q\nu_0}{k_B}\right) - \frac{E_h}{k_B T} \qquad (107)$$

The calculated values are shown on Table 14.

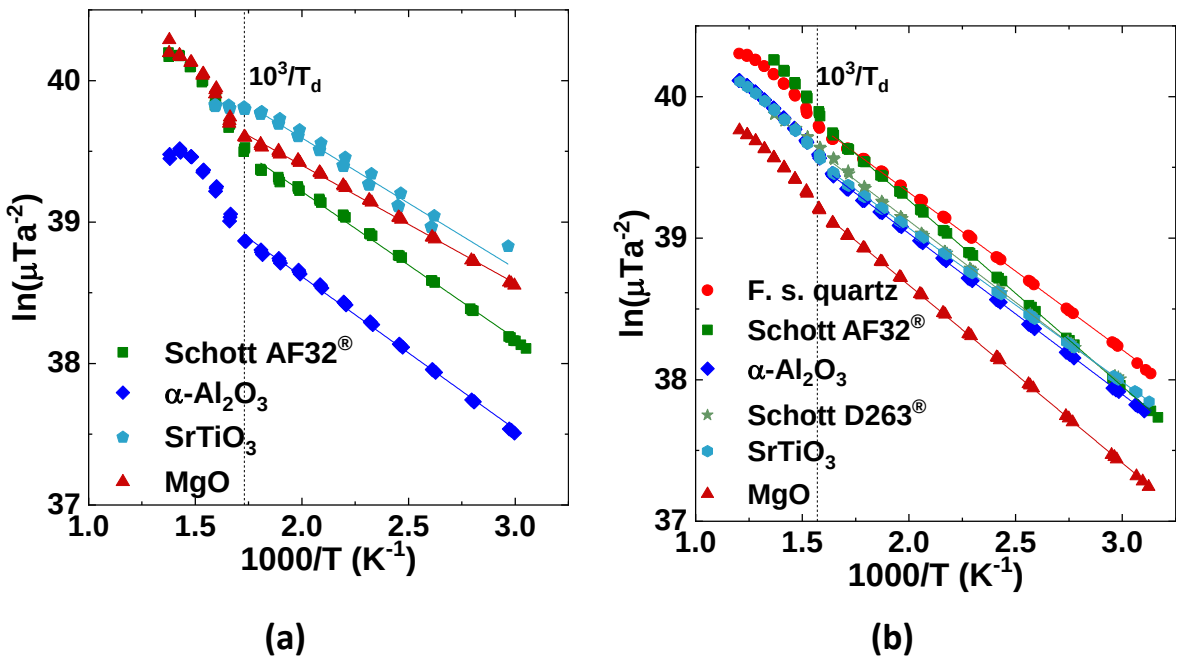

Figure 75 - Arrhenius plots for extraction of E_h and v_0 for (a) 70 nm and (b) 300 nm thick $Cu_{2/3}Cr_{4/3}O_2$ films on different substrates, considering S at room temperature for the calculation of the carrier concentration.

Table 14 - E_h, and v_0 for the studied films, considering S at room temperature for the calculation of the carrier concentration.

Substrate	h_f (nm)	E_h (meV)	v_0 (x 10^{12} Hz)
Schott AF 32® eco glass	≈ 70	90	74
α-Al_2O_3		94	46
$SrTiO_3$		79	86
MgO		73	61
Fused-silica quartz	≈ 300	96	95
Schott AF 32® eco glass		113	135
α-Al_2O_3		98	75
Schott D 263® T eco glass		99	84
$SrTiO_3$		94	71
MgO		108	66

The activation energies for hopping range from 79 to 113 meV, which are values closer to the reported ones in literature for copper chromium delafossite. Moreover, the hopping frequency values are closer to the ones reported literature (10^{12} Hz), in the order of 10^{13} Hz.

Chapter 6 – Conclusions and future perspectives

This thesis investigates the impact of strain on the electronic properties of off-stoichiometric copper chromium delafossite films grown by MOCVD. The study focuses on the relationship between structural characteristics and electronic behaviour, aiming to elucidate the unique transport mechanisms in this complex material. The primary objective was to modulate electrical mobility through induced strain. However, the research faced significant challenges due to the lack of available data on the elastic parameters for this material. Notably, only three studies have addressed this topic, and they focus exclusively on bulk and stoichiometric delafossite, leaving a gap in the literature for thin films.

In the initial experiments, strain was induced in the delafossite films by applying a magnetic field to films grown on a magnetostrictive nickel substrate. However, this approach did not lead to any measurable change in the electrical properties due to the minimal strain that was induced. In a subsequent experiment, mechanical bending was used to introduce strain, which resulted in varying mobility behaviour depending on whether the stress was tensile or compressive. Despite this, the maximum change in mobility observed was only around 0.1% within the applied strain range. The negative gauge factor values indicated that piezoresistive effects were more significant than geometric effects in these experiments.

Delafossite thin films were intentionally doped with trivalent (Al, Mn, Sc, and Y) and divalent (Mg and Zn) cations. Mg was the only dopant undetected by XPS. $Sin^2\Psi$ method plots, together with TEM analysis, showed that 300-nm thick films initially grew epitaxially along the (006) orientation of α-Al_2O_3 substrate. As growth progressed, the films became polycrystalline without preferential orientation. Additionally, $sin^2\Psi$ plots indicated that the films were under compressive strain in both the (006) and (012) reflections at room temperature, suggesting that epitaxial strain overshadowed thermal strain in delafossite films grown on α-Al_2O_3. The differences were too negligible to conclude a linear variation of strain with dopant cation radii. Unlike undoped films, the doped ones exhibited off-stoichiometry characterised by excess oxygen rather than Cu deficiency and Cr excess, which may be explained by the instability of the delafossite phase under doping conditions. Moreover, all intentionally doped films demonstrated similar room-temperature electrical conductivities.

A thorough analysis was performed on the strain induced in films deposited on substrates with different thermal expansion coefficients. The temperature dependence of resistivity and the Seebeck coefficient were studied to determine the electrical mobility, assuming small polaron transport as the governing mechanism. The resistivity dependence on temperature ($\rho(T)$) indicated semiconductive behaviour, while the Seebeck coefficient dependence on temperature ($S(T)$) suggested energy dispersion within the polaronic states in these polycrystalline films. A peculiar feature observed in the $\rho(T)$ curve at the deposition temperature corresponds to the transition between tensile and compressive regimes in the thin films. This feature was more prominent in thinner films and nearly disappeared in thicker films, suggesting that strain affects mobility. However, no quantitative assessments can be made at this stage, and experiments with substrates having larger thermal expansion coefficients should be considered.

A novel approach in regarding the Seebeck coefficient in delafossites was developed in this thesis. The acquired data shows an approximative linear dependency of the Seebeck coefficient on temperature, that is not a characteristic for small polaronic materials. We showed that in this case,

a second term involving the vibrational transport energy must be accounted in the Seebeck coefficient expression.

These results demonstrate that the hole effective mass in polaronic materials is inherently difficult to manipulate. Although strain can influence mobility, it does not significantly enhance it to the high levels required for many technological applications. However, it does offer insights into the fundamental physical properties of these films. There are numerous applications where high mobility is not a necessity, such as in gas sensors, rectifiers, photodetectors and n-type junction field-effect transistors. These applications can benefit from the unique properties of delafossites and other p-type TCMs without the stringent mobility requirements.

It can be concluded that delafossites have played a pivotal role in the development of p-type TCMs. These materials have garnered attention due to their relatively simple deposition methods and wide optical band gaps, which are advantageous for applications requiring transparency and conductivity, such as in optoelectronic devices. However, despite these favourable properties, the dominance of polaronic conductivity mechanisms, where charge carriers become localised and transport occurs through a hopping process, rather than a more efficient band conduction, remains a challenge. This polaronic behaviour results in lower mobility and, consequently, reduced overall conductivity, limiting the effectiveness of delafossites in high-performance applications. The deep acceptor levels contribute to the formation of small polarons, where the charge carriers are strongly coupled with lattice distortions. These distortions create localised states, making it difficult for the carriers to move freely through the material. This inherent flaw in the electronic structure of delafossites means that while they serve as an important model in the design of p-type TCMs, their practical application is often restricted to scenarios where high conductivity is not the primary requirement [242]. Despite these limitations, the delafossite structure remains a crucial template in materials science. Research continues to explore ways to overcome these challenges, such as by doping or alloying to modify the electronic structure and reduce the impact of polaronic effects. Advances in this area could potentially unlock new avenues for the use of delafossites in a broader range of applications, further cementing their role as a foundational material in the field of transparent conductors.

Broader implications and future perspectives

The search for high-performance p-type TCMs remains a significant challenge in materials science. Despite extensive research, no p-type material has yet matched the performance of n-type TCMs, which are widely used in applications such as solar cells, transparent electronics, and flat panel displays. Research in this field is focused on two primary directions: fundamental material discovery and technological application. In the pursuit of new materials, factors such as cost and sustainability play crucial roles. As the demand for transparent electronics, solar cells, and other optoelectronic devices increases, the need for materials that are not only high-performing but also economically viable becomes critical. Additionally, sustainability considerations are becoming increasingly important, with an emphasis on sourcing materials responsibly and minimizing their ecological footprints. The integration of lifecycle assessments in the material selection process ensures that environmental impacts of production and disposal are considered alongside performance metrics. The second research direction emphasizes the practical application of these materials, prioritizing cost-effectiveness and sustainability in their deployment.

However, given the current performance gap between p-type and n-type TCMs, prioritising further improvements may be premature before achieving fundamental breakthroughs in material performance. As of this writing, copper delafossites represent the best p-type TCMs available for pursuing technological applications, holding promise for future developments in transparent electronics, energy-efficient devices, and other optoelectronic applications. However, advancements in material processing and doping strategies are needed to fully unlock the potential of copper delafossites, which is currently limited by their low carrier mobility. Improving the mobility of charge carriers is essential to enhancing the electrical conductivity of these materials without sacrificing their transparency. A promising material in this context is copper iodide, which exhibits a band gap of 3.1 eV and mobility up to 40 $cm^2V^{-1}s^{-1}$. However, challenges related to its poor stability in air and moisture, especially at elevated temperatures, remain significant due to the ease of Cu migration.

It is evident that before bridging the gap toward technological applications, research should prioritize fundamental material discovery to identify a viable p-type archetypal material. Researchers are leveraging advanced techniques such as high-throughput computational screening to identify promising candidates. This approach allows for the rapid evaluation of a vast array of materials, but despite computational advancements, experimental validation of these materials remains limited. Challenges include the safe and controlled synthesis of elements like sulphur, phosphorus, and iodine, as well as ensuring the air stability of the materials.

The debate now centres on whether polaronic materials should be reconsidered in TCM research. The TCO community has been cautious about using materials that rely on small-polaron transport, often excluding them from the design of new TCOs, especially those guided by computational approaches. The avoidance of small-polaron formation has frequently been cited as key for developing high-performance TCOs. However, recent research reveals that TCOs using small-polaron transport can, in some cases, outperform those based on band transport. This advantage arises from the contrasting ways they respond to increasing carrier concentration. While band-based TCOs suffer a decline in optical transparency at high carrier concentrations, polaronic materials can maintain high transparency, making them potentially more effective in certain applications [37].

Computational studies have highlighted lately various materials as potential high-performance p-type TCMs. Boron phosphide has favourable electronic properties, including low hole effective mass, which is crucial for high p-type conductivity. Copper aluminium sulphide ($CuAlS_2$) offers an excellent between conductivity and transparency. Mixed-anion compounds such as such as (Zr,Hf)OS and $CsScS_2$ have been identified as promising due to their mixed-anion chemistry, which can lead to enhanced valence band dispersion and improved p-type dopability. Moreover, non-oxide materials such as phosphides, sulphides, and other compounds are being explored for their diffuse valence orbitals, which can provide better hole mobility compared to traditional oxides. This trend is supported by studies showing that phosphides have a significantly lower median hole effective mass than oxides, making them attractive for high-performance applications. Spinels, perovskites, and complex oxychalcogenides are also being intensively studied and have moved to the forefront of research. However, experimental challenges such as synthesis, stability, and scalability remain critical for their practical application.

In conclusion, the search for p-type TCMs is advancing through a dual focus on fundamental material discovery and practical technological applications. By tackling both the scientific challenges in developing new materials and the economic and environmental considerations of their implementation, researchers are well-positioned to make significant strides in transparent electronics, aligning with the ambitious market projections for the industry.

References

[1] A. Barnabé, E. Mugnier, L. Presmanes, and P. Tailhades, “Preparation of delafossite CuFeO2 thin films by rf-sputtering on conventional glass substrate,” *Mater. Lett.*, vol. 60, no. 29–30, pp. 3468–3470, Dec. 2006, doi: 10.1016/j.matlet.2006.03.033.

[2] U. Betz, M. Kharrazi Olsson, J. Marthy, M. F. Escolá, and F. Atamny, “Thin films engineering of indium tin oxide: Large area flat panel displays application,” *Surf. Coatings Technol.*, vol. 200, no. 20–21, pp. 5751–5759, May 2006, doi: 10.1016/j.surfcoat.2005.08.144.

[3] A. Janotti and C. G. Van De Walle, “Fundamentals of zinc oxide as a semiconductor,” *Reports Prog. Phys.*, vol. 72, no. 12, 2009, doi: 10.1088/0034-4885/72/12/126501.

[4] A. E. Rakhshani, Y. Makdisi, and H. A. Ramazaniyan, “Electronic and optical properties of fluorine-doped tin oxide films,” *J. Appl. Phys.*, vol. 83, no. 2, pp. 1049–1057, 1998, doi: 10.1063/1.366796.

[5] Z. Chen, W. Li, R. Li, Y. Zhang, G. Xu, and H. Cheng, “Fabrication of Highly Transparent and Conductive Indium–Tin Oxide Thin Films with a High Figure of Merit via Solution Processing,” *Langmuir*, vol. 29, no. 45, pp. 13836–13842, Nov. 2013, doi: 10.1021/la4033282.

[6] H. Hosono, *Handbook of Transparent Conductors*, 1st ed. Boston, MA: Springer US, 2011.

[7] H. Sato, T. Minami, S. Takata, and T. Yamada, “Transparent conducting p-type NiO thin films prepared by magnetron sputtering,” *Thin Solid Films*, vol. 236, no. 1–2, pp. 27–31, 1993, doi: 10.1016/0040-6090(93)90636-4.

[8] R. Woods-Robinson *et al.*, “Wide Band Gap Chalcogenide Semiconductors,” *Chem. Rev.*, vol. 120, no. 9, pp. 4007–4055, May 2020, doi: 10.1021/acs.chemrev.9b00600.

[9] H. Kawazoe, M. Yasukawa, H. Hyodo, M. Kurita, H. Yanagi, and H. Hosono, “P-type electrical conduction in transparent thin films of CuAlO2,” *Nature*, vol. 389, no. 6654, pp. 939–942, 1997, doi: 10.1038/40087.

[10] Z. Bai *et al.*, “Review in optoelectronic properties of p-type CuCrO2 transparent conductive films,” *Surfaces and Interfaces*, vol. 22, p. 100824, 2021, doi: 10.1016/j.surfin.2020.100824.

[11] J. Welser, J. L. Hoyt, and J. F. Gibbons, “Electron mobility enhancement in strained-Si n-type metal-oxide-semiconductor field-effect transistors,” *IEEE Electron Device Lett.*, vol. 15, no. 3, pp. 100–102, Mar. 1994, doi: 10.1109/55.285389.

[12] D. K. Nayak, J. C. S. Woo, J. S. Park, K. L. Wang, and K. P. MacWilliams, “High-mobility p - channel metal-oxide-semiconductor field-effect transistor on strained Si,” *Appl. Phys. Lett.*, vol. 62, no. 22, pp. 2853–2855, May 1993, doi: 10.1063/1.109205.

[13] A. Kudo, H. Yanagi, K. Ueda, H. Hosono, H. Kawazoe, and Y. Yano, “Fabrication of transparent p–n heterojunction thin film diodes based entirely on oxide semiconductors,” *Appl. Phys. Lett.*, vol. 75, no. 18, pp. 2851–2853, Nov. 1999, doi: 10.1063/1.125171.

[14] M. Grundmann *et al.*, “Oxide bipolar electronics: materials, devices and circuits,” *J. Phys. D. Appl. Phys.*, vol. 49, no. 21, p. 213001, Jun. 2016, doi: 10.1088/0022-3727/49/21/213001.

[15] J. Afonso, R. Leturcq, P. L. Popa, and D. Lenoble, “Transparent p-Cu0.66Cr1.33O2/n-ZnO heterojunction prepared in a five-step scalable process,” *J. Mater. Sci. Mater. Electron.*, vol. 30, no. 2, pp. 1760–1766, 2019, doi: 10.1007/s10854-018-0448-4.

[16] K. Nomura, T. Kamiya, and H. Hosono, “Ambipolar Oxide Thin-Film Transistor,” *Adv. Mater.*,

vol. 23, no. 30, pp. 3431–3434, Aug. 2011, doi: 10.1002/adma.201101410.

[17] K. Nomura, H. Ohta, A. Takagi, T. Kamiya, M. Hirano, and H. Hosono, “Room-temperature fabrication of transparent flexible thin-film transistors using amorphous oxide semiconductors,” *Nature*, vol. 432, no. 7016, pp. 488–492, 2004, doi: 10.1038/nature03090.

[18] K. Nomura, “Thin-Film Transistor Fabricated in Single-Crystalline Transparent Oxide Semiconductor,” *Science (80-.).*, vol. 300, no. 5623, pp. 1269–1272, May 2003, doi: 10.1126/science.1083212.

[19] C. G. Granqvist, “Electrochromics for smart windows: Oxide-based thin films and devices,” *Thin Solid Films*, vol. 564, pp. 1–38, Aug. 2014, doi: 10.1016/j.tsf.2014.02.002.

[20] M. Z. Sialvi *et al.*, “Electrochromic and Colorimetric Properties of Nickel(II) Oxide Thin Films Prepared by Aerosol-Assisted Chemical Vapor Deposition,” *ACS Appl. Mater. Interfaces*, vol. 5, no. 12, pp. 5675–5682, Jun. 2013, doi: 10.1021/am401025v.

[21] Q. Liu *et al.*, “In situ electrochromic efficiency of a nickel oxide thin film: origin of electrochemical process and electrochromic degradation,” *J. Mater. Chem. C*, vol. 6, no. 3, pp. 646–653, 2018, doi: 10.1039/C7TC04696K.

[22] H. Ohta, M. Orita, M. Hirano, and H. Hosono, “Fabrication and characterization of ultraviolet-emitting diodes composed of transparent p-n heterojunction, p-SrCu2O2 and n-ZnO,” *J. Appl. Phys.*, vol. 89, no. 10, pp. 5720–5725, May 2001, doi: 10.1063/1.1367315.

[23] S. Kim, S. jin Kim, K. heon Kim, H. Kim, and T. G. Kim, “Improved performance of Ga 2 O 3 /ITO-based transparent conductive oxide films using hydrogen annealing for near-ultraviolet light-emitting diodes,” *Phys. status solidi*, vol. 211, no. 11, pp. 2569–2573, Nov. 2014, doi: 10.1002/pssa.201431278.

[24] C. Battaglia, A. Cuevas, and S. De Wolf, “High-efficiency crystalline silicon solar cells: Status and perspectives,” *Energy Environ. Sci.*, vol. 9, no. 5, pp. 1552–1576, 2016, doi: 10.1039/c5ee03380b.

[25] F. Menchini *et al.*, “Application of NiO x thin films as p-type emitter layer in heterojunction solar cells,” *Phys. status solidi*, vol. 13, no. 10–12, pp. 1006–1010, Dec. 2016, doi: 10.1002/pssc.201600121.

[26] B. Tong *et al.*, “Oxygen Vacancy Defects Boosted High Performance p-Type Delafossite CuCrO2 Gas Sensors,” *ACS Appl. Mater. Interfaces*, vol. 10, no. 40, pp. 34727–34734, 2018, doi: 10.1021/acsami.8b10485.

[27] C. Baratto, R. Kumar, G. Faglia, K. Vojisavljević, and B. Malič, “p-Type copper aluminum oxide thin films for gas-sensing applications,” *Sensors Actuators B Chem.*, vol. 209, pp. 287–296, Mar. 2015, doi: 10.1016/j.snb.2014.11.116.

[28] D. Upadhyay, B. Roondhe, A. Pratap, and P. K. Jha, “Two-dimensional delafossite cobalt oxyhydroxide as a toxic gas sensor,” *Appl. Surf. Sci.*, vol. 476, no. January, pp. 198–204, May 2019, doi: 10.1016/j.apsusc.2019.01.057.

[29] T. P. Mokoena, H. C. Swart, and D. E. Motaung, “A review on recent progress of p-type nickel oxide based gas sensors: Future perspectives,” *J. Alloys Compd.*, vol. 805, pp. 267–294, Oct. 2019, doi: 10.1016/j.jallcom.2019.06.329.

[30] D. Bhattacharya *et al.*, “Delafossite type CuCo0.5Ti0.5O2 composite structure: A futuristic ceramics for supercapacitor and EMI shielding application,” *Ceram. Int.*, no. December, Dec. 2020, doi: 10.1016/j.ceramint.2020.12.135.

[31] A. N. Fioretti and M. Morales-Masis, “Bridging the p-type transparent conductive materials gap: synthesis approaches for disperse valence band materials,” *J. Photonics Energy*, vol. 10, no. 04, p. 1, Feb. 2020, doi: 10.1117/1.JPE.10.042002.

[32] K. Matsuzaki, K. Nomura, H. Yanagi, T. Kamiya, M. Hirano, and H. Hosono, “Epitaxial growth of high mobility Cu2 O thin films and application to p -channel thin film transistor,” *Appl. Phys. Lett.*, vol. 93, no. 20, pp. 3–6, 2008, doi: 10.1063/1.3026539.

[33] E. Fortunato *et al.*, “Thin-film transistors based on p-type Cu2 O thin films produced at room temperature,” *Appl. Phys. Lett.*, vol. 96, no. 19, pp. 2010–2013, 2010, doi: 10.1063/1.3428434.

[34] A. Tsukazaki *et al.*, “Repeated temperature modulation epitaxy for p-type doping and light-emitting diode based on ZnO,” *Nat. Mater.*, vol. 4, no. 1, pp. 42–45, 2005, doi: 10.1038/nmat1284.

[35] J. L. Lyons, A. Janotti, and C. G. Van de Walle, “Why nitrogen cannot lead to p-type conductivity in ZnO,” *Appl. Phys. Lett.*, vol. 95, no. 25, p. 252105, Dec. 2009, doi: 10.1063/1.3274043.

[36] M. Qiu *et al.*, “Effect of oxygen pressure on structural and electrical properties of pulsed laser deposition-derived Zn 0.95 Mg 0.05 O: Li thin films,” *J. Phys. D. Appl. Phys.*, vol. 40, no. 10, pp. 3229–3232, May 2007, doi: 10.1088/0022-3727/40/10/030.

[37] G. Hautier, A. Miglio, G. Ceder, G.-M. Rignanese, and X. Gonze, “Identification and design principles of low hole effective mass p-type transparent conducting oxides,” *Nat. Commun.*, vol. 4, no. 1, p. 2292, Oct. 2013, doi: 10.1038/ncomms3292.

[38] O. Bierwagen and J. S. Speck, “Mg acceptor doping of In 2 O 3 and overcompensation by oxygen vacancies,” *Appl. Phys. Lett.*, vol. 101, no. 10, p. 102107, Sep. 2012, doi: 10.1063/1.4751854.

[39] X. Chen, L. Zhao, and Q. Niu, “Electrical and Optical Properties of p-Type Li,Cu-Codoped NiO Thin Films,” *J. Electron. Mater.*, vol. 41, no. 12, pp. 3382–3386, Dec. 2012, doi: 10.1007/s11664-012-2213-4.

[40] A. Alshahrie, S. Joudakzis, A. A. Al-Ghamdi, L. M. Bronstein, and W. E. Mahmoud, “Synthesis and characterization of p-type transparent conducting Ni1-xRuxO ($0 \leq x \leq 0.1$) films prepared by pulsed laser deposition,” *Ceram. Int.*, vol. 45, no. 6, pp. 7984–7994, Apr. 2019, doi: 10.1016/j.ceramint.2018.09.214.

[41] T. Dutta, P. Gupta, A. Gupta, and J. Narayan, “Effect of Li doping in NiO thin films on its transparent and conducting properties and its application in heteroepitaxial p-n junctions,” *J. Appl. Phys.*, vol. 108, no. 8, p. 083715, Oct. 2010, doi: 10.1063/1.3499276.

[42] S. Yu, W. Zhang, L. Li, D. Xu, H. Dong, and Y. Jin, “Fabrication of p-type SnO2 films via pulsed laser deposition method by using Sb as dopant,” *Appl. Surf. Sci.*, vol. 286, pp. 417–420, Dec. 2013, doi: 10.1016/j.apsusc.2013.09.107.

[43] J. A. Caraveo-Frescas, P. K. Nayak, H. A. Al-Jawhari, D. B. Granato, U. Schwingenschlögl, and H. N. Alshareef, “Record Mobility in Transparent p-Type Tin Monoxide Films and Devices by Phase Engineering,” *ACS Nano*, vol. 7, no. 6, pp. 5160–5167, Jun. 2013, doi: 10.1021/nn400852r.

[44] Y. Ogo *et al.*, “p-channel thin-film transistor using p-type oxide semiconductor, SnO,” *Appl. Phys. Lett.*, vol. 93, no. 3, p. 032113, Jul. 2008, doi: 10.1063/1.2964197.

[45] E. Fortunato *et al.*, “Transparent p-type SnOx thin film transistors produced by reactive rf magnetron sputtering followed by low temperature annealing,” *Appl. Phys. Lett.*, vol. 97, no. 5, p. 052105, Aug. 2010, doi: 10.1063/1.3469939.

[46] E. Chikoidze *et al.*, “P-type β-gallium oxide: A new perspective for power and optoelectronic devices,” *Mater. Today Phys.*, vol. 3, pp. 118–126, Dec. 2017, doi: 10.1016/j.mtphys.2017.10.002.

[47] N. Ueda, H. Hosono, R. Waseda, and H. Kawazoe, “Synthesis and control of conductivity of ultraviolet transmitting β-Ga2O3 single crystals,” *Appl. Phys. Lett.*, vol. 70, no. 26, pp. 3561–3563, Jun. 1997, doi: 10.1063/1.119233.

[48] M. Orita, H. Hiramatsu, H. Ohta, M. Hirano, and H. Hosono, “Preparation of highly conductive, deep ultraviolet transparent β-Ga2O3 thin film at low deposition temperatures,” *Thin Solid Films*, vol. 411, no. 1, pp. 134–139, May 2002, doi: 10.1016/S0040-6090(02)00202-X.

[49] M. Ahmadi, M. Asemi, and M. Ghanaatshoar, “Mg and N co-doped CuCrO 2 : A record breaking p-type TCO,” *Appl. Phys. Lett.*, vol. 113, no. 24, 2018, doi: 10.1063/1.5051730.

[50] J. M. Ok, S. Yoon, A. R. Lupini, P. Ganesh, M. F. Chisholm, and H. N. Lee, “Interfacial stabilization for epitaxial CuCrO2 delafossites,” *Sci. Rep.*, vol. 10, no. 1, pp. 1–8, 2020, doi: 10.1038/s41598-020-68275-w.

[51] J. Tate *et al.*, “p-Type oxides for use in transparent diodes,” *Thin Solid Films*, vol. 411, no. 1, pp. 119–124, 2002, doi: 10.1016/S0040-6090(02)00199-2.

[52] R. S. Ajimsha, K. A. Vanaja, M. K. Jayaraj, P. Misra, V. K. Dixit, and L. M. Kukreja, “Transparent p-AgCoO2/n-ZnO diode heterojunction fabricated by pulsed laser deposition,” *Thin Solid Films*, vol. 515, no. 18, pp. 7352–7356, 2007, doi: 10.1016/j.tsf.2007.03.002.

[53] R. Wei *et al.*, “Facile chemical solution synthesis of p-type delafossite Ag-based transparent conducting AgCrO2 films in an open condition,” *J. Mater. Chem. C*, vol. 5, no. 8, pp. 1885–1892, 2017, doi: 10.1039/c6tc04848j.

[54] M. Tanaka, M. Hasegawa, and H. Takei, “Growth and Anisotropic Physical Properties of PdCoO2 Single Crystals,” *Journal of the Physical Society of Japan*, vol. 65, no. 12. pp. 3973–3977, 1996, doi: 10.1143/JPSJ.65.3973.

[55] C. W. Hicks, A. S. Gibbs, A. P. Mackenzie, H. Takatsu, Y. Maeno, and E. A. Yelland, “Quantum oscillations and high carrier mobility in the delafossite PdCoO 2,” *Phys. Rev. Lett.*, vol. 109, no. 11, pp. 1–5, 2012, doi: 10.1103/PhysRevLett.109.116401.

[56] C. W. Hicks *et al.*, “Quantum oscillations and magnetic reconstruction in the delafossite PdCrO2,” *Phys. Rev. B - Condens. Matter Mater. Phys.*, vol. 92, no. 1, pp. 1–9, 2015, doi: 10.1103/PhysRevB.92.014425.

[57] P. Kushwaha *et al.*, “Nearly free electrons in a 5d delafossite oxide metal,” *Sci. Adv.*, vol. 1, no. 9, pp. 1–7, 2015, doi: 10.1126/sciadv.1500692.

[58] K. H. L. Zhang *et al.*, “Perovskite Sr-Doped LaCrO 3 as a New p-Type Transparent Conducting Oxide,” *Adv. Mater.*, vol. 27, no. 35, pp. 5191–5195, Sep. 2015, doi: 10.1002/adma.201501959.

[59] E. Arca, K. Fleischer, and I. V. Shvets, “Magnesium, nitrogen codoped Cr2O3: A p-type transparent conducting oxide,” *Appl. Phys. Lett.*, vol. 99, no. 11, pp. 2011–2014, 2011, doi: 10.1063/1.3638461.

[60] E. Norton, L. Farrell, S. D. Callaghan, C. McGuinness, I. V. Shvets, and K. Fleischer, “X-ray

spectroscopic studies of the electronic structure of chromium-based p -type transparent conducting oxides," *Phys. Rev. B*, vol. 93, no. 11, pp. 1–8, 2016, doi: 10.1103/PhysRevB.93.115302.

[61] H. A. Mohamed, "P-Type transparent conducting copper-strontium oxide thin films for optoelectronic devices," *EPJ Appl. Phys.*, vol. 56, no. 3, pp. 1–7, 2011, doi: 10.1051/epjap/2011100463.

[62] C. . Windisch, G. . Exarhos, K. . Ferris, M. . Engelhard, and D. . Stewart, "Infrared transparent spinel films with p-type conductivity," *Thin Solid Films*, vol. 398–399, pp. 45–52, Nov. 2001, doi: 10.1016/S0040-6090(01)01302-5.

[63] K. Dileep, B. Loukya, P. Silwal, A. Gupta, and R. Datta, "Probing optical band gaps at nanoscale from tetrahedral cation vacancy defects and variation of cation ordering in NiCo 2 O 4 epitaxial thin films," *J. Phys. D. Appl. Phys.*, vol. 47, no. 40, p. 405001, Oct. 2014, doi: 10.1088/0022-3727/47/40/405001.

[64] M. Dekkers, G. Rijnders, and D. H. A. Blank, "ZnIr2O4, a p-type transparent oxide semiconductor in the class of spinel zinc-d6-transition metal oxide," *Appl. Phys. Lett.*, vol. 90, no. 2, p. 021903, Jan. 2007, doi: 10.1063/1.2431548.

[65] H. J. Kim *et al.*, "Electrical and magnetic properties of spinel-type magnetic semiconductor ZnCo2O4 grown by reactive magnetron sputtering," *J. Appl. Phys.*, vol. 95, no. 11, pp. 7387–7389, Jun. 2004, doi: 10.1063/1.1688571.

[66] H. Mizoguchi, M. Hirano, S. Fujitsu, T. Takeuchi, K. Ueda, and H. Hosono, "ZnRh2O4: A p -type semiconducting oxide with a valence band composed of a low spin state of Rh3+ in a 4d6 configuration," *Appl. Phys. Lett.*, vol. 80, no. 7, pp. 1207–1209, Feb. 2002, doi: 10.1063/1.1450252.

[67] N. Mansourian-Hadavi *et al.*, "Transport and band structure studies of crystalline ZnRh2 O4," *Phys. Rev. B - Condens. Matter Mater. Phys.*, vol. 81, no. 7, pp. 1–6, 2010, doi: 10.1103/PhysRevB.81.075112.

[68] J. Asbalter and A. Subrahmanyam, "p -type transparent conducting In2O3–Ag2O thin films prepared by reactive electron beam evaporation technique ," *J. Vac. Sci. Technol. A Vacuum, Surfaces, Film.*, vol. 18, no. 4, pp. 1672–1676, 2000, doi: 10.1116/1.582405.

[69] T. Minami, K. Shimokawa, and T. Miyata, "P-type transparent conducting In2O3–Ag2O thin films prepared by rf magnetron sputtering," *J. Vac. Sci. Technol. A Vacuum, Surfaces, Film.*, vol. 16, no. 3, pp. 1218–1221, May 1998, doi: 10.1116/1.581262.

[70] K. Ueda, S. Inoue, S. Hirose, H. Kawazoe, and H. Hosono, "Transparent p-type semiconductor: LaCuOS layered oxysulfide," *Appl. Phys. Lett.*, vol. 77, no. 17, pp. 2701–2703, 2000, doi: 10.1063/1.1319507.

[71] H. Hiramatsu, K. Ueda, H. Ohta, M. Hirano, T. Kamiya, and H. Hosono, "Degenerate p-type conductivity in wide-gap LaCuOS1-xSex (x = 0-1) epitaxial films," *Appl. Phys. Lett.*, vol. 82, no. 7, pp. 1048–1050, 2003, doi: 10.1063/1.1544643.

[72] K. Ueda, S. Inoue, H. Hosono, N. Sarukura, and M. Hirano, "Room-temperature excitons in wide-gap layered-oxysulfide semiconductor: LaCuOS," *Appl. Phys. Lett.*, vol. 78, no. 16, pp. 2333–2335, Apr. 2001, doi: 10.1063/1.1364656.

[73] H. Hiramatsu, K. Ueda, H. Ohta, M. Orita, M. Hirano, and H. Hosono, "Preparation of transparent p-type (La1-xSrxO)CuS thin films by r.f. sputtering technique," *Thin Solid Films*, vol. 411, no. 1, pp. 125–128, 2002, doi: 10.1016/S0040-6090(02)00200-6.

[74] H. Hiramatsu *et al.*, “Heavy hole doping of epitaxial thin films of a wide gap p-type semiconductor, LaCuOSe, and analysis of the effective mass,” *Appl. Phys. Lett.*, vol. 91, no. 1, p. 012104, Jul. 2007, doi: 10.1063/1.2753546.

[75] M.-L. Liu, L.-B. Wu, F.-Q. Huang, L.-D. Chen, and I.-W. Chen, “A promising p-type transparent conducting material: Layered oxysulfide [Cu2S2][Sr3Sc2O5],” *J. Appl. Phys.*, vol. 102, no. 11, p. 116108, Dec. 2007, doi: 10.1063/1.2817643.

[76] T. Kim *et al.*, “Material Design of New p-Type Tin Oxyselenide Semiconductor through Valence Band Engineering and Its Device Application,” *ACS Appl. Mater. Interfaces*, vol. 11, no. 43, pp. 40214–40221, 2019, doi: 10.1021/acsami.9b12186.

[77] A. Bhatia *et al.*, “High-Mobility Bismuth-based Transparent p -Type Oxide from High-Throughput Material Screening,” *Chem. Mater.*, vol. 28, no. 1, pp. 30–34, Jan. 2016, doi: 10.1021/acs.chemmater.5b03794.

[78] E. Bobeico, F. Varsano, C. Minarini, and F. Roca, “P-type strontium–copper mixed oxide deposited by e-beam evaporation,” *Thin Solid Films*, vol. 444, no. 1–2, pp. 70–74, Nov. 2003, doi: 10.1016/S0040-6090(03)01023-X.

[79] A. Kudo, H. Yanagi, H. Hosono, and H. Kawazoe, “SrCu2O2: A p -type conductive oxide with wide band gap,” *Appl. Phys. Lett.*, vol. 73, no. 2, pp. 220–222, Jul. 1998, doi: 10.1063/1.121761.

[80] H. Kawazoe, H. Yanagi, K. Ueda, and H. Hosono, “Transparent p -Type Conducting Oxides: Design and Fabrication of p-n Heterojunctions,” *MRS Bull.*, vol. 25, no. 8, pp. 28–36, Aug. 2000, doi: 10.1557/mrs2000.148.

[81] Z. Wang, P. K. Nayak, J. A. Caraveo-Frescas, and H. N. Alshareef, “Recent Developments in p-Type Oxide Semiconductor Materials and Devices,” *Adv. Mater.*, vol. 28, no. 20, pp. 3831–3892, May 2016, doi: 10.1002/adma.201503080.

[82] J. Crepelliere, “Metalorganic chemical vapour Deposition of p-type delafossite CuCrO2 thin-films: Characterization and application to transparent p-n junction,” PhD Thesis, University of Luxembourg, Luxembourg, 2016.

[83] A. N. Banerjee, S. Nandy, C. K. Ghosh, and K. K. Chattopadhyay, “Fabrication and characterization of all-oxide heterojunction p-CuAlO2 + x/n-Zn1 - xAlxO transparent diode for potential application in ‘invisible electronics,’” *Thin Solid Films*, vol. 515, no. 18, pp. 7324–7330, 2007, doi: 10.1016/j.tsf.2007.02.087.

[84] C. Friedel, “Sur une combinaison naturelle des oxydes de fer et de cuivre, et sur la reproduction de l’atacamite,” 1873.

[85] F. A. Benko and F. P. Koffyberg, “Opto-electronic properties of CuAlO2,” *J. Phys. Chem. Solids*, vol. 45, no. 1, pp. 57–59, Jan. 1984, doi: 10.1016/0022-3697(84)90101-X.

[86] D. O. Scanlon, K. G. Godinho, B. J. Morgan, and G. W. Watson, “Understanding conductivity anomalies in CuI -based delafossite transparent conducting oxides: Theoretical insights,” *J. Chem. Phys.*, vol. 132, no. 2, 2010, doi: 10.1063/1.3290815.

[87] W. Ketir, S. Saadi, and M. Trari, “Physical and photoelectrochemical characterization of CuCrO2 single crystal,” *J. Solid State Electrochem.*, vol. 16, no. 1, pp. 213–218, Jan. 2012, doi: 10.1007/s10008-011-1307-x.

[88] M. Han *et al.*, “Structural, electronic band transition and optoelectronic properties of delafossite CuGa 1-xCr xO 2 ($0 \leq x \leq 1$) solid solution films grown by the sol-gel method,” *J.*

Mater. Chem., vol. 22, no. 35, pp. 18463–18470, 2012, doi: 10.1039/c2jm33027j.

[89] K. H. L. Zhang, K. Xi, M. G. Blamire, and R. G. Egdell, "P-type transparent conducting oxides," *J. Phys. Condens. Matter*, vol. 28, no. 38, 2016, doi: 10.1088/0953-8984/28/38/383002.

[90] A. Thatribud, T. Tungsurat, and T. Pengpan, "First-principles study on electronic and optical properties of transparent conducting oxide CuBO2," *Comput. Mater. Sci.*, vol. 81, pp. 601–606, 2014, doi: 10.1016/j.commatsci.2013.09.023.

[91] R. B. Gall, N. Ashmore, M. A. Marquardt, X. Tan, and D. P. Cann, "Synthesis, microstructure, and electrical properties of the delafossite compound CuGaO2," *J. Alloys Compd.*, vol. 391, no. 1–2, pp. 262–266, 2005, doi: 10.1016/j.jallcom.2004.08.070.

[92] M. A. Marquardt, N. A. Ashmore, and D. P. Cann, "Crystal chemistry and electrical properties of the delafossite structure," *Thin Solid Films*, vol. 496, no. 1, pp. 146–156, 2006, doi: 10.1016/j.tsf.2005.08.316.

[93] A. P. Mackenzie, "The properties of ultrapure delafossite metals," *Reports Prog. Phys.*, vol. 80, no. 3, p. aa50e5, 2017, doi: 10.1088/1361-6633/aa50e5.

[94] M. N. Huda, Y. Yan, A. Walsh, S.-H. Wei, and M. M. Al-Jassim, "Group-IIIA versus IIIB delafossites: Electronic structure study," *Phys. Rev. B*, vol. 80, no. 3, p. 035205, Jul. 2009, doi: 10.1103/PhysRevB.80.035205.

[95] F. Mao, T. Nyberg, T. Thersleff, A. M. Andersson, and U. Jansson, "Combinatorial magnetron sputtering of AgFeO2 thin films with the delafossite structure," *Mater. Des.*, vol. 91, pp. 132–142, 2016, doi: 10.1016/j.matdes.2015.11.092.

[96] I. Ross, "Investigation and development of cuprous delafossites for solid oxide fuel cell cathodes," PhD Thesis, University of St Andrews, St Andrews, 2017.

[97] T. Harada, "Thin-film growth and application prospects of metallic delafossites," *Mater. Today Adv.*, vol. 11, p. 100146, 2021, doi: 10.1016/j.mtadv.2021.100146.

[98] T. Harada, K. Fujiwara, and A. Tsukazaki, "Highly conductive PdCoO2 ultrathin films for transparent electrodes," *APL Mater.*, vol. 6, no. 4, 2018, doi: 10.1063/1.5027579.

[99] H. Takatsu, S. Yonezawa, S. Mouri, S. Nakatsuji, K. Tanaka, and Y. Maeno, "Roles of high-frequency optical phonons in the physical properties of the conductive delafossite PdCoO 2," *J. Phys. Soc. Japan*, vol. 76, no. 10, pp. 1–7, 2007, doi: 10.1143/JPSJ.76.104701.

[100] M. E. Ketfi, S. S. Essaoud, S. Al Azar, A. Y. Al-Reyahi, A. A. Mousa, and A. Mufleh, "Insight into the spin-polarized structural, optoelectronic, magnetic, thermodynamic, and thermoelectric properties of PdBO2 (B = Al, Cr, and Rh) Delafossite semiconductor," *Opt. Quantum Electron.*, vol. 55, no. 11, 2023, doi: 10.1007/s11082-023-05259-w.

[101] W. C. Sheets, E. Mugnier, A. Barnabé, T. J. Marks, and K. R. Poeppelmeier, "Hydrothermal Synthesis of Delafossite-Type Oxides," *Chem. Mater.*, vol. 18, no. 1, pp. 7–20, Jan. 2006, doi: 10.1021/cm051791c.

[102] R. Nagarajan *et al.*, "p-Type conductivity in the delafossite structure," *Int. J. Inorg. Mater.*, vol. 3, no. 3, pp. 265–270, 2001, doi: 10.1016/S1466-6049(01)00006-X.

[103] B. J. Ingram, T. O. Mason, R. Asahi, K. T. Park, and A. J. Freeman, "Electronic structure and small polaron hole transport of copper aluminate," *Phys. Rev. B - Condens. Matter Mater. Phys.*, vol. 64, no. 15, pp. 1551141–1551147, 2001, doi: 10.1103/PhysRevB.64.155114.

[104] R. D. Shannon, D. B. Rogers, and C. T. Prewitt, "Chemistry of noble metal oxides. I. Syntheses

and properties of ABO2 delafossite compounds," *Inorg. Chem.*, vol. 10, no. 4, pp. 713–718, Apr. 1971, doi: 10.1021/ic50098a011.

[105] R. D. Shannon, C. T. Prewitt, and D. B. Rogers, "Chemistry of noble metal oxides. II. Crystal structures of platinum cobalt dioxide, palladium cobalt dioxide, coppper iron dioxide, and silver iron dioxide," *Inorg. Chem.*, vol. 10, no. 4, pp. 719–723, Apr. 1971, doi: 10.1021/ic50098a012.

[106] D. B. Rogers, R. D. Shannon, C. T. Prewitt, and J. L. Gillson, "Chemistry of Noble Metal Oxides. III. Electrical Transport Properties and Crystal Chemistry of ABO2 Compounds with the Delafossite Structure," *Inorg. Chem.*, vol. 10, no. 4, pp. 723–727, 1971, doi: 10.1021/ic50098a013.

[107] M. Moreira, J. Afonso, J. Crepelliere, D. Lenoble, and P. Lunca-Popa, "A review on the p-type transparent Cu–Cr–O delafossite materials," *J. Mater. Sci.*, vol. 57, no. 5, pp. 3114–3142, 2022, doi: 10.1007/s10853-021-06815-z.

[108] K. Ueda, H. Hiramatsu, M. Hirano, T. Kamiya, and H. Hosono, "Wide-gap layered oxychalcogenide semiconductors: Materials, electronic structures and optoelectronic properties," *Thin Solid Films*, vol. 496, no. 1, pp. 8–15, 2006, doi: 10.1016/j.tsf.2005.08.268.

[109] H. Yanagi, S. I. Inoue, K. Ueda, H. Kawazoe, H. Hosono, and N. Hamada, "Electronic structure and optoelectronic properties of transparent p-type conducting CuAlO2," *J. Appl. Phys.*, vol. 88, no. 7, pp. 4159–4163, 2000, doi: 10.1063/1.1308103.

[110] J. E. Sansonetti and W. C. Martin, "Handbook of Basic Atomic Spectroscopic Data," *J. Phys. Chem. Ref. Data*, vol. 34, no. 4, pp. 1559–2259, Dec. 2005, doi: 10.1063/1.1800011.

[111] S. Kumar, M. Miclau, and C. Martin, "Hydrothermal synthesis of AgCrO2 delafossite in supercritical water: A new single-step process," *Chem. Mater.*, vol. 25, no. 10, pp. 2083–2088, 2013, doi: 10.1021/cm400420e.

[112] D. Xiong *et al.*, "Preparation of p-type AgCrO2 nanocrystals through low-temperature hydrothermal method and the potential application in p-type dye-sensitized solar cell," *J. Alloys Compd.*, vol. 642, pp. 104–110, 2015, doi: 10.1016/j.jallcom.2015.04.072.

[113] S. Ouyang, Z. Li, Z. Ouyang, T. Yu, J. Ye, and Z. Zou, "Correlation of Crystal Structures, Electronic Structures, and Photocatalytic Properties in a Series of Ag-based Oxides: AgAlO 2 , AgCrO 2 , and Ag 2 CrO 4," *J. Phys. Chem. C*, vol. 112, no. 8, pp. 3134–3141, Feb. 2008, doi: 10.1021/jp077127w.

[114] A. M. L. Lopes *et al.*, "Local distortions in multiferroic AgCrO2 triangular spin lattice," *Phys. Rev. B*, vol. 84, no. 1, p. 014434, Jul. 2011, doi: 10.1103/PhysRevB.84.014434.

[115] M. F. Iozzi, P. Vajeeston, R. Vidya, P. Ravindran, and H. Fjellvåg, "Structural and electronic properties of transparent conducting delafossite: A comparison between the AgBO2 and CuBO2 families (B = Al, Ga, in and Sc, Y)," *RSC Adv.*, vol. 5, no. 2, pp. 1366–1377, 2015, doi: 10.1039/c3ra47531j.

[116] A. N. Banerjee, C. K. Ghosh, and K. K. Chattopadhyay, "Effect of excess oxygen on the electrical properties of transparent p-type conducting CuAlO2+x thin films," *Sol. Energy Mater. Sol. Cells*, vol. 89, no. 1, pp. 75–83, 2005, doi: 10.1016/j.solmat.2005.01.003.

[117] T.-W. Chiu, Y.-C. Yang, A.-C. Yeh, Y.-P. Wang, and Y.-W. Feng, "Antibacterial property of CuCrO2 thin films prepared by RF magnetron sputtering deposition," *Vacuum*, vol. 87, pp. 174–177, Jan. 2013, doi: 10.1016/j.vacuum.2012.04.026.

[118] Y.-T. Nien, M.-R. Hu, T.-W. Chiu, and J.-S. Chu, “Antibacterial property of CuCrO2 nanopowders prepared by a self-combustion glycine nitrate process,” *Mater. Chem. Phys.*, vol. 179, pp. 182–188, Aug. 2016, doi: 10.1016/j.matchemphys.2016.05.026.

[119] D. Li *et al.*, “Electrical, optical and structural properties of CuCrO2 films prepared by pulsed laser deposition,” *J. Phys. D. Appl. Phys.*, vol. 40, no. 16, pp. 4910–4915, 2007, doi: 10.1088/0022-3727/40/16/023.

[120] L. Bottiglieri, J. Resende, M. Weber, O. Chaix-Pluchery, C. Jiménez, and J.-L. Deschanvres, “Out of stoichiometry CuCrO 2 films as promising p-type TCO for transparent electronics,” *Mater. Adv.*, 2021, doi: 10.1039/D1MA00156F.

[121] A. Jacob *et al.*, “Luminescent properties of delafossite-type oxides LaCuO2 and YCuO2,” *Solid State Commun.*, vol. 103, no. 9, pp. 529–532, Sep. 1997, doi: 10.1016/S0038-1098(97)00224-X.

[122] J. P. Doumerc, C. Parent, Z. J. Chao, G. Le Flem, and A. Ammar, “Luminescence of the Cu+ ion in CuLaO2,” *J. Less-Common Met.*, vol. 148, no. 1–2, pp. 333–337, 1989, doi: 10.1016/0022-5088(89)90048-9.

[123] A. N. Banerjee and K. K. Chattopadhyay, “Size-dependent optical properties of sputter-deposited nanocrystalline p -type transparent CuAl O 2 thin films,” *J. Appl. Phys.*, vol. 97, no. 8, 2005, doi: 10.1063/1.1866485.

[124] Y. Wang, Y. Gu, T. Wang, and W. Shi, “Structural, optical and electrical properties of Mg-doped CuCrO2 thin films by sol-gel processing,” *J. Alloys Compd.*, vol. 509, no. 19, pp. 5897–5902, 2011, doi: 10.1016/j.jallcom.2011.02.175.

[125] T. Okuda *et al.*, “Hole-doping effect on the magnetic state of delafossite oxide CuCrO 2,” *J. Phys. Conf. Ser.*, vol. 150, no. 4, pp. 0–4, 2009, doi: 10.1088/1742-6596/150/4/042157.

[126] T. Okuda, N. Jufuku, S. Hidaka, and N. Terada, “Magnetic, transport, and thermoelectric properties of the delafossite oxides CuCr1-xMgxO2 (0 x 0.04),” *Phys. Rev. B - Condens. Matter Mater. Phys.*, vol. 72, no. 14, pp. 4–8, 2005, doi: 10.1103/PhysRevB.72.144403.

[127] M. Amami, C. V. Colin, P. Strobel, and A. Ben Salah, “Al-doping effect on the structural and physical properties of delafossite-type oxide CuCrO2,” *Phys. B Condens. Matter*, vol. 406, no. 11, pp. 2182–2185, 2011, doi: 10.1016/j.physb.2011.03.027.

[128] A. Maignan *et al.*, “On the strong impact of doping in the triangular antiferromagnet CuCrO2,” *Solid State Commun.*, vol. 149, no. 23–24, pp. 962–967, 2009, doi: 10.1016/j.ssc.2009.02.026.

[129] F. Lin, C. Gao, X. Zhou, W. Shi, and A. Liu, “Magnetic, electrical and optical properties of p-type Fe-doped CuCrO 2 semiconductor thin films,” *J. Alloys Compd.*, vol. 581, pp. 502–507, 2013, doi: 10.1016/j.jallcom.2013.07.160.

[130] T. Okuda *et al.*, “Magnetic and transport properties of delafossite oxides CuCr1-x(Mg,Ca)xO2,” *J. Magn. Magn. Mater.*, vol. 310, no. 2, pp. 890–892, Mar. 2007, doi: 10.1016/j.jmmm.2006.10.1141.

[131] M. O ’sullivan, P. Stamenov, J. Alaria, M. Venkatesan, and J. M. D. Coey, “Magnetoresistance of CuCrO 2 -based delafossite films,” *J. Phys. Conf. Ser*, vol. 200, p. 052021, 2010, [Online]. Available: http://iopscience.iop.org/1742-6596/200/5/052021.

[132] J. Y. Yang *et al.*, “Strain Induced Relaxor-type Ferroelectricity Near Room Temperature in Delafossite CuCrO 2,” *AIP Adv.*, vol. 101, no. 1, pp. 0–7, 2020, doi: 10.1063/1.5121454.

[133] H. Sun, M. Arab Pour Yazdi, F. Sanchette, and A. Billard, “Optoelectronic properties of delafossite structure CuCr 0.93 Mg 0.07 O 2 sputter deposited coatings,” *J. Phys. D. Appl. Phys.*, vol. 49, no. 18, p. 185105, May 2016, doi: 10.1088/0022-3727/49/18/185105.

[134] C. Taddee, T. Kamwanna, and V. Amornkitbamrung, “Characterization of transparent superconductivity Fe-doped CuCrO 2 delafossite oxide,” *Appl. Surf. Sci.*, vol. 380, pp. 237–242, 2016, doi: 10.1016/j.apsusc.2016.01.120.

[135] J. F. H. L. Monteiro, A. R. Jurelo, and E. C. Siqueira, “Raman spectroscopy of the superconductor CuCrO2 delafossite oxide,” *Solid State Commun.*, vol. 252, no. January, pp. 64–67, 2017, doi: 10.1016/j.ssc.2017.01.014.

[136] Y. Ono, K. Satoh, T. Nozaki, and T. Kajitani, “Structural, Magnetic and Thermoelectric Properties of Delafossite-type Oxide, CuCr 1- x Mg x O 2 (0 ≤ x ≤0.05),” *Jpn. J. Appl. Phys.*, vol. 46, no. 3A, pp. 1071–1075, Mar. 2007, doi: 10.1143/JJAP.46.1071.

[137] K. Hayashi, K. Sato, T. Nozaki, and T. Kajitani, “Effect of Doping on Thermoelectric Properties of Delafossite-Type Oxide CuCrO 2,” *Jpn. J. Appl. Phys.*, vol. 47, no. 1, pp. 59–63, Jan. 2008, doi: 10.1143/JJAP.47.59.

[138] S. Zhou *et al.*, “Room temperature ozone sensing properties of p-type CuCrO2 nanocrystals,” *Sensors Actuators, B Chem.*, vol. 143, no. 1, pp. 119–123, 2009, doi: 10.1016/j.snb.2009.09.026.

[139] M. Isacfranklin, R. Yuvakkumar, G. Ravi, M. Pannipara, A. G. Al-Sehemi, and DhayalanVelauthapillai, “CuCoO2 electrodes for supercapacitor applications,” *Mater. Lett.*, vol. 296, p. 129930, Aug. 2021, doi: 10.1016/j.matlet.2021.129930.

[140] A. M. Fathi, S. A. M. Abdel-Hameed, F. H. Margha, and N. A. A. Ghany, “Electrocatalytic oxygen evolution on nanoscale crednerite (CuMnO2) composite electrode,” *Zeitschrift fur Phys. Chemie*, vol. 230, no. 10, pp. 1519–1530, 2016, doi: 10.1515/zpch-2015-0627.

[141] H. Chfii, A. Bouich, and B. M. Soucase, “The Use of Copper-Based Delafossite to Improve Hydrogen Production Performance: A Review,” *Hydrogen*, vol. 5, no. 1, pp. 39–58, Jan. 2024, doi: 10.3390/hydrogen5010004.

[142] A. H. Reshak, “First principle calculations of transition metal oxide, AgAlO2, as active photocatalyst: Sustainable alternative sources of energy,” *Int. J. Electrochem. Sci.*, vol. 8, no. 7, pp. 9371–9383, 2013.

[143] S. Saadi, A. Bouguelia, and M. Trari, “Photocatalytic hydrogen evolution over CuCrO2,” *Sol. Energy*, vol. 80, no. 3, pp. 272–280, Mar. 2006, doi: 10.1016/j.solener.2005.02.018.

[144] Q.-L. Liu, Z.-Y. Zhao, R.-D. Zhao, and J.-H. Yi, “Fundamental properties of delafossite CuFeO2 as photocatalyst for solar energy conversion,” *J. Alloys Compd.*, vol. 819, no. xxxx, p. 153032, Apr. 2020, doi: 10.1016/j.jallcom.2019.153032.

[145] D. H. Youn, Y. H. Choi, J. Kim, S. Han, A. Heller, and C. B. Mullins, “Simple Microwave-Assisted Synthesis of Delafossite CuFeO 2 as an Anode Material for Sodium-Ion Batteries,” *ChemElectroChem*, vol. 5, no. 17, pp. 2419–2423, Sep. 2018, doi: 10.1002/celc.201800548.

[146] H. C. Kandpal and R. Seshadri, “First-principles electronic structure of the delafossites ABO2 (A=Cu, Ag, Au; B=Al, Ga, Sc, In, Y): evolution of d10–d10 interactions,” *Solid State Sci.*, vol. 4, no. 8, pp. 1045–1052, Aug. 2002, doi: 10.1016/S1293-2558(02)01363-8.

[147] B. J. Ingram *et al.*, “Transport and Defect Mechanisms in Cuprous Delafossites. 1. Comparison of Hydrothermal and Standard Solid-State Synthesis in CuAlO 2,” *Chem. Mater.*, vol. 16, no.

26, pp. 5616–5622, Dec. 2004, doi: 10.1021/cm048983c.

[148] C. Ruttanapun, “Optical and electronic properties of delafossite CuBO2 p-type transparent conducting oxide,” *J. Appl. Phys.*, vol. 114, no. 11, 2013, doi: 10.1063/1.4821960.

[149] D. O. Scanlon, A. Walsh, and G. W. Watson, “Understanding the p-type conduction properties of the transparent conducting oxide cuBO2: A density functional theoryanalysis,” *Chem. Mater.*, vol. 21, no. 19, pp. 4568–4576, 2009, doi: 10.1021/cm9015113.

[150] M. Snure and A. Tiwari, “CuB O2: A p -type transparent oxide,” *Appl. Phys. Lett.*, vol. 91, no. 9, pp. 3–6, 2007, doi: 10.1063/1.2778755.

[151] K. Ueda *et al.*, “Epitaxial growth of transparent p-type conducting CuGaO2 thin films on sapphire (001) substrates by pulsed laser deposition,” *J. Appl. Phys.*, vol. 89, no. 3, pp. 1790–1793, 2001, doi: 10.1063/1.1337587.

[152] R. Srinivasan *et al.*, “Tuning the size and color of the p-type wide band gap delafossite semiconductor CuGaO2 with ethylene glycol assisted hydrothermal synthesis,” *J. Mater. Chem.*, vol. 18, no. 46, pp. 5647–5653, 2008, doi: 10.1039/b810064k.

[153] H. Yanagi, T. Hase, S. Ibuki, K. Ueda, and H. Hosono, “Bipolarity in electrical conduction of transparent oxide semiconductor CuInO2 with delafossite structure,” *Appl. Phys. Lett.*, vol. 78, no. 11, pp. 1583–1585, Mar. 2001, doi: 10.1063/1.1355673.

[154] L. Liu, K. Bai, H. Gong, and P. Wu, “First-principles study of Sn and Ca doping in CuInO2,” *Phys. Rev. B*, vol. 72, no. 12, p. 125204, Sep. 2005, doi: 10.1103/PhysRevB.72.125204.

[155] M. Sasaki and M. Shimode, “Fabrication of bipolar CuInO2 with delafossite structure,” *J. Phys. Chem. Solids*, vol. 64, no. 9–10, pp. 1675–1679, 2003, doi: 10.1016/S0022-3697(03)00071-4.

[156] M. Singh, V. N. Singh, and B. R. Mehta, “Synthesis and Properties of Nanocrystalline Copper Indium Oxide Thin Films Deposited by Rf Magnetron Sputtering,” *J. Nanosci. Nanotechnol.*, vol. 8, no. 8, pp. 3889–3894, Aug. 2008, doi: 10.1166/jnn.2008.178.

[157] Z. Du *et al.*, “A low temperature hydrothermal synthesis of delafossite CuCoO2 as an efficient electrocatalyst for the oxygen evolution reaction in alkaline solutions,” *Inorg. Chem. Front.*, vol. 5, no. 1, pp. 183–188, 2018, doi: 10.1039/c7qi00621g.

[158] H. Chfii, A. Bouich, B. M. Soucase, and M. Abdlefdil, “Structural and physical properties of Mg-doped CuCoO2 delafossite thin films,” *Mater. Chem. Phys.*, p. 128006, 2023, doi: 10.1016/j.matchemphys.2023.128006.

[159] R. Nagarajan, A. D. Draeseke, A. W. Sleight, and J. Tate, “p-type conductivity in CuCr1-xMgxO2 films and powders,” *J. Appl. Phys.*, vol. 89, no. 12, pp. 8022–8025, 2001, doi: 10.1063/1.1372636.

[160] T. Arnold *et al.*, “X-ray spectroscopic study of the electronic structure of CuCrO 2,” *Phys. Rev. B*, vol. 79, p. 075102, 2009, doi: 10.1103/PhysRevB.79.075102.

[161] J.-S. Kang *et al.*, “Phase separation in thermoelectric delafossite CuFe 1− x Ni x O 2 observed by soft x-ray magnetic circular dichroism,” *Appl. Phys. Lett.*, vol. 99, no. 1, p. 012108, Jul. 2011, doi: 10.1063/1.3609248.

[162] A. Wuttig, J. W. Krizan, J. Gu, J. J. Frick, R. J. Cava, and A. B. Bocarsly, “The effect of Mg-doping and Cu nonstoichiometry on the photoelectrochemical response of CuFeO2,” *J. Mater. Chem. A*, vol. 5, no. 1, pp. 165–171, 2017, doi: 10.1039/c6ta06504j.

[163] C. Ruttanapun, W. Prachamon, and A. Wichainchai, “Optoelectronic properties of Cu1-

xPtxFeO2 (0 ≤ x ≤ 0.05) delafossite for p-type transparent conducting oxide," *Curr. Appl. Phys.*, vol. 12, no. 1, pp. 166–170, 2012, doi: 10.1016/j.cap.2011.05.028.

[164] Q. Zhang, D. Xiong, H. Li, D. Xia, H. Tao, and X. Zhao, "A facile hydrothermal route to synthesize delafossite CuMnO2 nanocrystals," *J. Mater. Sci. Mater. Electron.*, vol. 26, no. 12, pp. 10159–10163, 2015, doi: 10.1007/s10854-015-3702-z.

[165] S. Shibasaki, W. Kobayashi, and I. Terasaki, "Transport properties of the delafossite Rh oxide Cu1−xAgxRh1−yMgyO2: Effect of Mg substitution on the resistivity and Hall coefficient," *Phys. Rev. B*, vol. 74, no. 23, p. 235110, Dec. 2006, doi: 10.1103/PhysRevB.74.235110.

[166] N. Duan, A. W. Sleight, M. K. Jayaraj, and J. Tate, "Transparent p-type conducting CuScO2+x films," *Appl. Phys. Lett.*, vol. 77, no. 9, pp. 1325–1326, 2000, doi: 10.1063/1.1289906.

[167] B. J. Ingram, B. J. Harder, N. W. Hrabe, T. O. Mason, and K. R. Poeppelmeier, "Transport and defect mechanisms in cuprous delafossites. 2. CuScO 2 and CuYO2," *Chem. Mater.*, vol. 16, no. 26, pp. 5623–5629, 2004, doi: 10.1021/cm048982k.

[168] Y. Kakehi *et al.*, "Optical and electrical properties of CuScO2 epitaxial films prepared by combining two-step deposition and post-annealing techniques," *J. Cryst. Growth*, vol. 311, no. 4, pp. 1117–1122, Feb. 2009, doi: 10.1016/j.jcrysgro.2008.11.060.

[169] Y. Kakehi, K. Satoh, T. Yotsuya, A. Ashida, T. Yoshimura, and N. Fujimura, "Electrical and optical properties of excess oxygen intercalated CuScO2(0001) epitaxial films prepared by oxygen radical annealing," *Thin Solid Films*, vol. 516, no. 17, pp. 5785–5789, 2008, doi: 10.1016/j.tsf.2007.10.038.

[170] M. K. Jayaraj, R. Manoj, M. Nisha, and K. A. Vanaja, "Effect of oxygen intercalation on properties of sputtered CuYO2 for potential use as p-type transparent conducting films," *Bull. Mater. Sci.*, vol. 31, no. 1, pp. 49–53, 2008, doi: 10.1007/s12034-008-0009-1.

[171] M. K. Jayaraj, A. D. Draeseke, J. Tate, and A. W. Sleight, "p-type transparent thin films of CuY1-xCaxO2," *Thin Solid Films*, vol. 397, no. 1–2, pp. 244–248, 2001, doi: 10.1016/S0040-6090(01)01362-1.

[172] S. Saadi, A. Bouguelia, A. Derbal, and M. Trari, "Hydrogen photoproduction over new catalyst CuLaO2," *J. Photochem. Photobiol. A Chem.*, vol. 187, no. 1, pp. 97–104, 2007, doi: 10.1016/j.jphotochem.2006.09.017.

[173] G. Dong *et al.*, "Synthesis, electrical and optical properties of CuNdO2 compound," *J. Phys. Chem. Solids*, vol. 73, no. 9, pp. 1170–1172, Sep. 2012, doi: 10.1016/j.jpcs.2012.05.004.

[174] N. Miyasaka, Y. Doi, and Y. Hinatsu, "Synthesis and magnetic properties of ALnO2 (A=Cu or Ag; Ln=rare earths) with the delafossite structure," *J. Solid State Chem.*, vol. 182, no. 8, pp. 2104–2110, Aug. 2009, doi: 10.1016/j.jssc.2009.05.035.

[175] J. Lindén, K. Isawa, J. Miettinen, M. Karppinen, and H. Yamauchi, "151Eu Mössbauer study of the CuEuO2+δ delafossite," *Phys. B Condens. Matter*, vol. 271, no. 1–4, pp. 223–229, Nov. 1999, doi: 10.1016/S0921-4526(99)00225-2.

[176] B. Y. R. D. Shannon, M. H, N. H. Baur, O. H. Gibbs, M. Eu, and V. Cu, "Revised Effective Ionic Radii and Systematic Studies of Interatomie Distances in Halides and Chaleogenides Central Research and Development Department , Experimental Station , E . L Du Pont de Nemours The effective ionic radii of Shannon & Prewitt [Acta ," 1976.

[177] F. A. Benko and F. P. Koffyberg, "Opto-electronic properties of p- and n-type delafossite, CuFeO2," *J. Phys. Chem. Solids*, vol. 48, no. 5, pp. 431–434, Jan. 1987, doi: 10.1016/0022-

3697(87)90103-X.

[178] E. Mugnier, A. Barnabé, and P. Tailhades, “Synthesis and characterization of CuFeO2+δ delafossite powders,” *Solid State Ionics*, vol. 177, no. 5–6, pp. 607–612, 2006, doi: 10.1016/j.ssi.2005.11.026.

[179] D. O. Scanlon and G. W. Watson, “Conductivity limits in CuAlO2 from screened-hybrid density functional theory,” *J. Phys. Chem. Lett.*, vol. 1, no. 21, pp. 3195–3199, 2010, doi: 10.1021/jz1011725.

[180] D. O. Scanlon and G. W. Watson, “Understanding the p-type defect chemistry of CuCrO2,” *J. Mater. Chem.*, vol. 21, no. 11, pp. 3655–3663, 2011, doi: 10.1039/c0jm03852k.

[181] N. Barot, P. K. Mehta, A. Rao, R. Thomas, and Y. K. Kuo, “Effects of iso- and polyvalent substitutions on the short/long-range crystalline order in CuCrO2 compounds,” *J. Alloys Compd.*, vol. 791, pp. 134–143, 2019, doi: 10.1016/j.jallcom.2019.03.291.

[182] P. Lunca Popa, J. Crêpellière, R. Leturcq, and D. Lenoble, “Electrical and optical properties of Cu-Cr-O thin films fabricated by chemical vapour deposition,” *Thin Solid Films*, vol. 612, pp. 194–201, 2016, doi: 10.1016/j.tsf.2016.05.052.

[183] D. O. Scanlon, A. Walsh, B. J. Morgan, G. W. Watson, D. J. Payne, and R. G. Egdell, “Effect of Cr substitution on the electronic structure of CuAl 1-xCrxO2,” *Phys. Rev. B - Condens. Matter Mater. Phys.*, vol. 79, no. 3, pp. 1–7, 2009, doi: 10.1103/PhysRevB.79.035101.

[184] T. Yokobori *et al.*, “Electronic structure of the hole-doped delafossite oxides CuCr 1-xMgxO2,” *Phys. Rev. B - Condens. Matter Mater. Phys.*, vol. 87, no. 19, pp. 1–8, 2013, doi: 10.1103/PhysRevB.87.195124.

[185] M. Lalanne, A. Barnabé, F. Mathieu, and P. Tailhades, “Synthesis and thermostructural studies of a CuFe1-xCr xO2 delafossite solid solution with 0 ≤ × ≤ 1,” *Inorg. Chem.*, vol. 48, no. 13, pp. 6065–6071, 2009, doi: 10.1021/ic900437x.

[186] H. Sun, M. Arab Pour Yazdi, P. Briois, J. F. Pierson, F. Sanchette, and A. Billard, “Towards delafossite structure of Cu-Cr-O thin films deposited by reactive magnetron sputtering: Influence of substrate temperature on optoelectronics properties,” *Vacuum*, vol. 114, pp. 101–107, 2015, doi: 10.1016/j.vacuum.2015.01.009.

[187] O. Crottaz and F. Kubel, “Crystal structure of copper (I) chromium (III) oxide , 2H-CuCrCO2,” vol. 47, no. I, p. 2646, 1996.

[188] O. Crottaz and F. Kubel, “Crystal structure of copper (I) chromium (III) oxide , 3R-$CuCrO_2$,” *Z. Krist.*, vol. 10, no. I, p. 1996, 1996.

[189] F. Lin, W. Shi, and A. Liu, “Optical bandgap modulation and magnetic characterization of Fe-doped CuCrO 2 nanopowders,” *J. Alloys Compd.*, vol. 529, pp. 21–24, 2012, doi: 10.1016/j.jallcom.2012.03.059.

[190] P. Lunca-Popa *et al.*, “Invisible electronics: Metastable Cu-vacancies chain defects for highly conductive p-type transparent oxide,” *Appl. Mater. Today*, vol. 9, pp. 184–191, 2017, doi: 10.1016/j.apmt.2017.07.004.

[191] A. P. Amrute *et al.*, “Solid-state chemistry of cuprous delafossites: Synthesis and stability aspects,” *Chem. Mater.*, vol. 25, no. 21, pp. 4423–4435, Nov. 2013, doi: 10.1021/cm402902m.

[192] O. Crottaz, F. Kubel, and H. Schmid, “Preparation of Trigonal and Hexagonal Cuprous Chromite and Phase Transition Study Based on Single Crystal Structure Data,” *J. Solid State Chem.*, vol. 122, no. 1, pp. 247–250, Feb. 1996, doi: 10.1006/jssc.1996.0109.

[193] R. Gillen and J. Robertson, “Band structure calculations of CuAlO2, CuGaO2, CuInO2, and CuCrO2 by screened exchange,” *Phys. Rev. B - Condens. Matter Mater. Phys.*, vol. 84, p. 035125, 2011, doi: 10.1103/PhysRevB.84.035125.

[194] X. Wang, W. Meng, and Y. Yan, “Electronic band structures and excitonic properties of delafossites: A GW -BSE study,” *J. Appl. Phys.*, vol. 122, no. 8, 2017, doi: 10.1063/1.4991913.

[195] Y. Xu, G.-Z. Nie, D.-F. Zou, J.-W. Tang, and Z. Ao, “N–Mg dual-acceptor co-doping in CuCrO2 studied by first-principles calculations,” *Phys. Lett. A*, vol. 1, pp. 1–5, 2016, doi: 10.1016/j.physleta.2016.08.029.

[196] J. Shook, L. M. Scolfaro, P. D. Borges, and W. J. Geerts, “Structural stability and electronic properties of XTO 2 (X= Cu, Ag; T=Al, Cr): An ab initio study including X vacancies and Mg doping,” *Solid State Sci.*, vol. 88, no. November 2018, pp. 48–56, 2019, doi: 10.1016/j.solidstatesciences.2018.12.009.

[197] J. Shook, P. D. Borges, L. M. Scolfaro, and W. J. Geerts, “Effects of vacancies and p -doping on the optoelectronic properties of Cu- And Ag-based transparent conducting oxides,” *J. Appl. Phys.*, vol. 126, no. 7, p. 075702, 2019, doi: 10.1063/1.5088711.

[198] M. Schwarting, S. Siol, K. Talley, A. Zakutayev, and C. Phillips, “Automated algorithms for band gap analysis from optical absorption spectra,” *Mater. Discov.*, vol. 10, no. 2010, pp. 43–52, 2017, doi: 10.1016/j.md.2018.04.003.

[199] F. A. Benko and F. P. Koffyberg, “Preparation and opto-electronic properties of semiconducting CuCrO2,” *Mater. Res. Bull.*, vol. 21, no. 6, pp. 753–757, Jun. 1986, doi: 10.1016/0025-5408(86)90156-X.

[200] L. Farrell, E. Norton, C. M. Smith, D. Caffrey, I. V. Shvets, and K. Fleischer, “Synthesis of nanocrystalline Cu deficient CuCrO2-a high figure of merit p-type transparent semiconductor,” *J. Mater. Chem. C*, vol. 4, no. 1, pp. 126–134, 2015, doi: 10.1039/c5tc03161c.

[201] M. Poienar *et al.*, “Revisiting the properties of delafossite CuCrO 2: A single crystal study,” *J. Solid State Chem.*, vol. 185, pp. 56–61, 2012, doi: 10.1016/j.jssc.2011.10.047.

[202] Y. Ruei-Sung and C. M. Wu, “Characteristics of p-type transparent conductive CuCrO 2 thin films,” *Appl. Surf. Sci.*, vol. 282, pp. 92–97, 2013, doi: 10.1016/j.apsusc.2013.05.061.

[203] P. W. Sadik, M. Ivill, V. Craciun, and D. P. Norton, “Electrical transport and structural study of CuCr1 - xMgxO2 delafossite thin films grown by pulsed laser deposition,” *Thin Solid Films*, vol. 517, no. 11, pp. 3211–3215, 2009, doi: 10.1016/j.tsf.2008.10.097.

[204] T. Okuda, Y. Beppu, Y. Fujii, T. Onoe, N. Terada, and S. Miyasaka, “Specific heat of delafossite oxide CuCr1-x Mgx O2 (0≤x≤0.03),” *Phys. Rev. B - Condens. Matter Mater. Phys.*, vol. 77, no. 13, pp. 1–5, 2008, doi: 10.1103/PhysRevB.77.134423.

[205] A. Barnabé, Y. Thimont, M. Lalanne, L. Presmanes, and P. Tailhades, “P-Type conducting transparent characteristics of delafossite Mg-doped CuCrO2 thin films prepared by RF-sputtering,” *J. Mater. Chem. C*, vol. 3, no. 23, pp. 6012–6024, 2015, doi: 10.1039/c5tc01070e.

[206] M. Amami, S. Smari, K. Tayeb, P. Strobel, and A. Ben Salah, “Cationic doping effect on the structural, magnetic and spectroscopic properties of delafossite oxides CuCr1-x(Sc,Mg)xO 2,” *Mater. Chem. Phys.*, vol. 128, no. 1–2, pp. 298–302, 2011, doi: 10.1016/j.matchemphys.2011.03.021.

[207] K. Moto, R. Yoshimine, T. Suemasu, and K. Toko, “Improving carrier mobility of polycrystalline

Ge by Sn doping," *Sci. Rep.*, vol. 8, no. 1, pp. 4–10, 2018, doi: 10.1038/s41598-018-33161-z.

[208] K. L. Kovalenko, S. I. Kozlovskiy, and N. N. Sharan, "Strain induced mobility enhancement in p-type silicon structures: Bulk and quantum well (quantum kinetic approach)," *J. Appl. Phys.*, vol. 125, no. 8, 2019, doi: 10.1063/1.5045620.

[209] B. Wang, Y. Puzyrev, and S. T. Pantelides, "Strain enhanced defect reactivity at grain boundaries in polycrystalline graphene," *Carbon N. Y.*, vol. 49, no. 12, pp. 3983–3988, 2011, doi: 10.1016/j.carbon.2011.05.038.

[210] X. Li *et al.*, "Temperature-dependent band gap, interband transitions, and exciton formation in transparent p-type delafossite CuCr1−xMgxO2 films," *Phys. Rev. B*, vol. 90, no. 3, p. 035308, Jul. 2014, doi: 10.1103/PhysRevB.90.035308.

[211] İ. C. Kaya, M. A. Sevindik, and H. Akyıldız, "Characteristics of Fe- and Mg-doped CuCrO2 nanocrystals prepared by hydrothermal synthesis," *J. Mater. Sci. Mater. Electron.*, vol. 27, no. 3, pp. 2404–2411, Mar. 2016, doi: 10.1007/s10854-015-4038-4.

[212] C. Gao, F. Lin, X. Zhou, W. Shi, and A. Liu, "Fe concentration dependences of microstructure and magnetic properties for Cu(Cr1−xFex)O2 ceramics," *J. Alloys Compd.*, vol. 565, pp. 154–158, Jul. 2013, doi: 10.1016/j.jallcom.2013.02.161.

[213] M. A. Madre, M. A. Torres, J. A. Gomez, J. C. Diez, and A. Sotelo, "Effect of alkaline earth dopant on density, mechanical, and electrical properties of Cu0.97AE0.03CrO2 (AE = Mg, Ca, Sr, and Ba) delafossite oxide," *J. Aust. Ceram. Soc.*, vol. 55, no. 1, pp. 257–263, Mar. 2019, doi: 10.1007/s41779-018-0230-3.

[214] T. W. Chiu, S. W. Tsai, Y. P. Wang, and K. H. Hsu, "Preparation of p-type conductive transparent CuCrO 2:Mg thin films by chemical solution deposition with two-step annealing," *Ceram. Int.*, vol. 38, no. SUPPL. 1, pp. S673–S676, 2012, doi: 10.1016/j.ceramint.2011.09.048.

[215] D. Li *et al.*, "Characteristics of CuCr1-xMgxO2 films prepared by pulsed laser deposition," *J. Alloys Compd.*, vol. 486, no. 1–2, pp. 462–467, 2009, doi: 10.1016/j.jallcom.2009.06.174.

[216] J. F. H. L. Monteiro, F. C. Monteiro, A. R. Jurelo, and D. H. Mosca, "Conductivity in (Ag,Mg)-doped delafossite oxide CuCrO2," *Ceram. Int.*, vol. 44, no. 12, pp. 14101–14107, 2018, doi: 10.1016/j.ceramint.2018.05.008.

[217] L. Deng *et al.*, "Improved ferromagnetic behavior and novel near-infrared photoluminescence in Mg/Mn-codoped CuCrO2 ceramics," *J. Mater. Sci.*, vol. 51, no. 16, pp. 7491–7501, Aug. 2016, doi: 10.1007/s10853-016-0028-z.

[218] P. Mandal *et al.*, "A scheme of simultaneous cationic–anionic substitution in CuCrO 2 for transparent and superior p -type transport," *J. Phys. D. Appl. Phys.*, vol. 49, no. 27, p. 275109, Jul. 2016, doi: 10.1088/0022-3727/49/27/275109.

[219] G. Dong, M. Zhang, X. Zhao, H. Yan, C. Tian, and Y. Ren, "Improving the electrical conductivity of CuCrO2 thin film by N doping," *Appl. Surf. Sci.*, vol. 256, pp. 4121–4124, 2010, doi: 10.1016/j.apsusc.2010.01.094.

[220] D. Li *et al.*, "Magnetic and electrical properties of p-type Mn-doped CuCrO2 semiconductors," *J. Phys. D. Appl. Phys.*, vol. 42, no. 5, p. 055009, 2009, doi: 10.1088/0022-3727/42/5/055009.

[221] X. Zhou, F. Lin, W. Shi, and A. Liu, "Structural, electrical, optical and magnetic properties of p-type Cu(Cr1-xMnx)O2 thin films prepared by pulsed laser deposition," *J. Alloys Compd.*, vol. 614, pp. 221–225, 2014, doi: 10.1016/j.jallcom.2014.06.127.

[222] S. Y. Zheng, G. S. Jiang, J. R. Su, and C. F. Zhu, "The structural and electrical property of CuCr1

- xNixO2 delafossite compounds," *Mater. Lett.*, vol. 60, no. 29–30, pp. 3871–3873, 2006, doi: 10.1016/j.matlet.2006.03.132.

[223] S.-Y. Kim, J.-H. Lee, J.-J. Kim, and Y.-W. Heo, "Effect of Ni doping on the structural, electrical, and optical properties of transparent CuCrO2 films grown using pulsed laser deposition," *Ceram. Int.*, vol. 44, no. 15, pp. 17743–17748, Oct. 2018, doi: 10.1016/j.ceramint.2018.06.241.

[224] M. Amami, F. Jlaiel, P. Strobel, and A. Ben Salah, "Synthesis, structural and magnetic studies of the CuCr1-xRh xO2 delafossite solid solution with 0 ≤ x ≤ 0.2," *Mater. Res. Bull.*, vol. 46, no. 10, pp. 1729–1733, Oct. 2011, doi: 10.1016/j.materresbull.2011.05.033.

[225] T. Elkhouni, M. Amami, P. Strobel, and A. Ben Salah, "Structural and Magnetic Properties of Substituted Delafossite-Type Oxides CuCr1−xScxO2," *World J. Condens. Matter Phys.*, vol. 03, no. 01, pp. 1–8, 2013, doi: 10.4236/wjcmp.2013.31001.

[226] S. Jantrasee and C. Ruttanapun, "Impact of Sn4+ Substitution at Cr3+ Sites on Thermoelectric and Electronic Properties of p-Type Delafossite CuCrO2," *J. Electron. Mater.*, vol. 49, no. 1, pp. 601–610, Jan. 2020, doi: 10.1007/s11664-019-07780-9.

[227] T. Elkhouni, M. Amami, P. Strobel, and A. Ben Salah, "Structural, Raman spectroscopy, and magnetic ordering in new delafossite-type oxide CuCr 1-x Ti x O 2 (0≤x≤0.1)," *J. Supercond. Nov. Magn.*, vol. 26, no. 9, pp. 2795–2802, Sep. 2013, doi: 10.1007/s10948-013-2256-7.

[228] H.-Y. Chen and C.-C. Yang, "Transparent p-type Zn-doped CuCrO2 films by sol-gel processing," *Surf. Coatings Technol.*, vol. 231, pp. 277–280, 2013, doi: 10.1016/j.surfcoat.2012.06.006.

[229] R.-S. Yu and C. Chu, "Synthesis and Characteristics of Zn-Doped CuCrO2 Transparent Conductive Thin Films," *Coatings*, vol. 9, no. 5, p. 321, May 2019, doi: 10.3390/coatings9050321.

[230] A. N. Banerjee, S. Kundoo, and K. K. Chattopadhyay, "Synthesis and characterization of p-type transparent conducting CuAlO 2 thin film by DC sputtering," *Thin Solid Films*, vol. 440, no. 1–2, pp. 5–10, 2003, doi: 10.1016/S0040-6090(03)00817-4.

[231] J. Tate *et al.*, "Origin of p -type conduction in single-crystal CuAlO2," *Phys. Rev. B - Condens. Matter Mater. Phys.*, vol. 80, no. 16, pp. 1–8, 2009, doi: 10.1103/PhysRevB.80.165206.

[232] S. H. Lim, S. Desu, and A. C. Rastogi, "Chemical spray pyrolysis deposition and characterization of p-type CuCr1-xMgxO2 transparent oxide semiconductor thin films," *J. Phys. Chem. Solids*, vol. 69, no. 8, pp. 2047–2056, 2008, doi: 10.1016/j.jpcs.2008.03.007.

[233] L. Farrell, E. Norton, B. J. O'dowd, D. Caffrey, I. V. Shvets, and K. Fleischer, "Spray pyrolysis growth of a high figure of merit, nano-crystalline, p -type transparent conducting material at low temperature," *Appl. Phys. Lett.*, vol. 107, no. 3, pp. 1–7, 2015, doi: 10.1063/1.4927241.

[234] E. Norton *et al.*, "Bending stability of Cu0.4CrO2 - A transparent p-type conducting oxide for large area flexible electronics," *AIP Adv.*, vol. 8, no. 8, pp. 4–11, 2018, doi: 10.1063/1.5027038.

[235] D. C. Ling, C. W. Chiang, Y. F. Wang, Y. J. Lee, and P. H. Yeh, "Effect of Cr deficiency on physical properties of triangular-lattice antiferromagnets CuCr1-xO2 (0≦x≦0.10)," *J. Appl. Phys.*, vol. 109, no. 7, pp. 54–57, Apr. 2011, doi: 10.1063/1.3544498.

[236] J. Crepelliere *et al.*, "Transparent conductive CuCrO2 thin films deposited by Pulsed Injection Metal Organic Chemical Vapor Deposition: up-scalable process technology for an improved transparency/conductivity trade-off," *J. Mater. Chem. C*, vol. 4, p. 4728, 2016, doi:

doi.org/10.1039/C6TC00383D10.1039.

[237] P. Lunca-Popa *et al.*, “Tuneable interplay between atomistic defects morphology and electrical properties of transparent p-type highly conductive off-stoichiometric Cu-Cr-O delafossite thin films,” *Sci. Rep.*, vol. 10, no. 1, pp. 1–9, 2020, doi: 10.1038/s41598-020-58312-z.

[238] G. L. W. Hart and A. Zunger, “Origins of nonstoichiometry and vacancy ordering in Sc1−x□xS,” *Phys. Rev. Lett.*, vol. 87, no. 27, pp. 275508-1-275508–4, 2001, doi: 10.1103/PhysRevLett.87.275508.

[239] A. Zunger, “The fundamentals of Transparent Oxides revisited: Band gap formation in classic Mott insulators and spontaneous non-stoichiometry in degenerate oxides.”

[240] Z. J. Fang, J. Z. Zhu, J. Zhou, and M. Mo, “Defect properties of CuCrO 2: A density functional theory calculation,” *Chinese Phys. B*, vol. 21, no. 8, 2012, doi: 10.1088/1674-1056/21/8/087105.

[241] N. Ashcroft and N. D. Mermin, *Solid State Physics*, 1st Editio. Holt, Rinehart and Winston.

[242] J. Willis and D. O. Scanlon, “Latest directions in p-type transparent conductor design,” *J. Mater. Chem. C*, vol. 9, no. 36, pp. 11995–12009, 2021, doi: 10.1039/d1tc02547c.

[243] J. Robertson and S. J. Clark, “Limits to doping in oxides,” *Phys. Rev. B*, vol. 83, no. 7, p. 075205, Feb. 2011, doi: 10.1103/PhysRevB.83.075205.

[244] H. Raebiger, S. Lany, and A. Zunger, “Origins of the p-type nature and cation deficiency in Cu2 O and related materials,” *Phys. Rev. B - Condens. Matter Mater. Phys.*, vol. 76, no. 4, p. 045209, Jul. 2007, doi: 10.1103/PhysRevB.76.045209.

[245] A. Zunger, “Practical doping principles,” *Appl. Phys. Lett.*, vol. 83, no. 1, pp. 57–59, Jul. 2003, doi: 10.1063/1.1584074.

[246] R. F. Pierret, *Advanced Semiconductor Fundamentals*, 1st ed. Reading, MA: Addison-Wesley, 1987.

[247] P. Y. Yu and M. Cardona, *Fundamentals of Semiconductors*, vol. 1, no. April. Berlin, Heidelberg: Springer Berlin Heidelberg, 2010.

[248] S. Kasap and P. Capper, Eds., *Springer Handbook of Electronic and Photonic Materials*. Springer.

[249] D. H. Zhang and H. L. Ma, “Scattering mechanisms of charge carriers in transparent conducting oxide films,” *Appl. Phys. A Mater. Sci. Process.*, vol. 62, no. 5, pp. 487–492, May 1996, doi: 10.1007/BF01567122.

[250] J. Y. W. Seto, “The electrical properties of polycrystalline silicon films,” *J. Appl. Phys.*, vol. 46, no. 12, pp. 5247–5254, Dec. 1975, doi: 10.1063/1.321593.

[251] M. Grundmann, *The Physics of Semiconductors*, 1st ed. Berlin, Heidelberg, New York: Springer, 2006.

[252] P. Mele, *Thermoelectric Thin Films*, 1s ed. Cham, Switzerland: Springer International Publishing, 2019.

[253] D. P. Karim and A. T. Aldred, “Localized level hopping transport in La(Sr)CrO3,” *Phys. Rev. B*, vol. 20, no. 6, pp. 2255–2263, Sep. 1979, doi: 10.1103/PhysRevB.20.2255.

[254] N. F. Mott, “Conduction in non-crystalline materials,” *Philos. Mag.*, vol. 19, no. 160, pp. 835–

852, Apr. 1969, doi: 10.1080/14786436908216338.

[255] N. F. Mott and E. A. Davis, *Electronic processes in non-crystalline materials*, 2nd ed. Oxford University Press Inc.: New York, USA, 1979.

[256] J. Nell, B. J. Wood, S. E. Dorris, and T. O. Mason, "Jonker-type analysis of small polaron conductors," *J. Solid State Chem.*, vol. 82, no. 2, pp. 247–254, Oct. 1989, doi: 10.1016/0022-4596(89)90289-2.

[257] J. T. Devreese, "Polarons," in *digital Encyclopedia of Applied Physics*, vol. 2, no. 6, Weinheim, Germany: Wiley-VCH Verlag GmbH & Co. KGaA, 2003, pp. 24–29.

[258] E. Chikoidze *et al.*, "Control of p-type conduction in Mg doped monophase CuCrO2 thin layers," *J. Phys. D. Appl. Phys.*, vol. 49, no. 20, 2016, doi: 10.1088/0022-3727/49/20/205107.

[259] B. I. Shklovskii and A. L. Efros, *Electronic Properties of Doped Semiconductors*. Berlin, Heidelberg, Germany: Springer-Verlag, 1984.

[260] L. J. H. Alvin, "Characterisation of Thermoelectric Properties in R0.65Ca0.35MnO3 Perovskites (R = La, Pr, Nd, Sm, Y, Bi) and Constsruction of High Temperature Measurement Setup," National University of Singapore, Singapore, 2015.

[261] A. S. Alexandrov, *Polarons in Advanced Materials*, 1st ed., vol. 103, no. 9. Springer: P.O. Box 17, 3300 AA Dordrecht, The Netherlands, 2007.

[262] M. Pollak and B. I. Shklovskii, *Hopping Transport in Solids*. Amsterdam, Netherlands: North-Holland, 1991.

[263] S. Jung, "Physically-Based Compact Modelling of Organic Electronic Devices," Université Paris-Saclay, 2016.

[264] S. M. Sze and K. K. Ng, *Physics of Semiconductor Devices*. Wiley, 2006.

[265] T. Ivanov, "Piezoresistive cantilevers with an integrated bimorph actuator," PhD Thesis, University of Kassel, Kassel, 2004.

[266] K. Ellmer, "Past achievements and future challenges in the development of optically transparent electrodes," *Nat. Photonics*, vol. 6, no. 12, pp. 809–817, 2012, doi: 10.1038/nphoton.2012.282.

[267] T. Pisarkiewicz, K. Zakrzewska, and E. Leja, "Scattering of charge carriers in transparent and conducting thin oxide films with a non-parabolic conduction band," *Thin Solid Films*, vol. 174, no. PART 1, pp. 217–223, 1989, doi: 10.1016/0040-6090(89)90892-4.

[268] J. Bardeen and W. Shockley, "Deformation Potentials and Mobilities in Non-Polar Crystals," *Phys. Rev.*, vol. 80, no. 1, pp. 72–80, Oct. 1950, doi: 10.1103/PhysRev.80.72.

[269] D. C. Look, R. C. Scott, K. D. Leedy, and B. Bayraktaroglu, "Donor and acceptor concentrations from a single mobility measurement in degenerate semiconductors: ZnO," in *Oxide-based Materials and Devices II*, Feb. 2011, vol. 7940, p. 794003, doi: 10.1117/12.877072.

[270] B. M. Askerov, *Electron Transport Phenomena in Semiconductors*, 1st ed. World Scientific Publishing Company, 1994.

[271] A. Bikowski and K. Ellmer, "Analytical model of electron transport in polycrystalline, degenerately doped ZnO films," *J. Appl. Phys.*, vol. 116, no. 14, Oct. 2014, doi: 10.1063/1.4896839.

[272] H. L. Tuller and A. S. Nowick, "Small polaron electron transport in reduced CeO2 single

crystals," *J. Phys. Chem. Solids*, vol. 38, no. 8, pp. 859–867, Feb. 1977, doi: 10.1016/0022-3697(77)90124-X.

[273] C. Franchini and M. Reticcioli, "Polarons in materials," *Nat. Rev. Mater.*, vol. 0123456789, doi: https://doi.org/10.1038/s41578-022-00424-1.

[274] H. P. Myers, *Introductory Solid State Physics*, 1st ed. London, United Kingdom: Taylor & Francis, 1990.

[275] I. Sinnarasa, Y. Thimont, L. Presmanes, A. Barnabé, and P. Tailhades, "Thermoelectric and transport properties of delafossite CuCrO2: Mg thin films prepared by RF magnetron sputtering," *Nanomaterials*, vol. 7, no. 7, 2017, doi: 10.3390/nano7070157.

[276] H. L. Tuller, "Mixed Conduction in Nonstoichiometric Oxides," in *Nonstoichiometric Oxides*, Elsevier, 1981, pp. 271–335.

[277] T. Holstein, "Studies of polaron motion," *Ann. Phys. (N. Y).*, vol. 8, no. 3, pp. 343–389, Nov. 1959, doi: 10.1016/0003-4916(59)90003-X.

[278] A. S. Alexandrov and J. T. Devreese, *Advances in Polaron Physics*, vol. 159. Berlin, Heidelberg: Springer Berlin Heidelberg, 2010.

[279] I. G. Austin and N. F. Mott, "Polarons in crystalline and non-crystalline materials," *Adv. Phys.*, vol. 18, no. 71, pp. 41–102, Jan. 1969, doi: 10.1080/00018736900101267.

[280] P. A. Cox, *Transition Metal Oxides: An Introduction to Their Electronic Structure and Properties*. Oxford, United Kingdom: Oxford University Press, 1992.

[281] V. Ha, "High throughput computing for high mobility p-type transparent conducting materials," UC Louvain, 2019.

[282] H. K. Hideo Hosono, Masahiro Yasakawa, "Novel oxide amorphous semiconductors : transparent conducting amorphous oxides Possible Candidate for HMCs," *J. Non. Cryst. Solids*, vol. 203, pp. 334–344, 1996.

[283] H. Hosono, "Ionic amorphous oxide semiconductors: Material design, carrier transport, and device application," *J. Non. Cryst. Solids*, vol. 352, no. 9–20, pp. 851–858, Jun. 2006, doi: 10.1016/j.jnoncrysol.2006.01.073.

[284] H. Hosono, N. Kikuchi, N. Ueda, and H. Kawazoe, "Working hypothesis to explore novel wide band gap electrically conducting amorphous oxides and examples," *J. Non. Cryst. Solids*, vol. 198–200, no. PART 1, pp. 165–169, May 1996, doi: 10.1016/0022-3093(96)80019-6.

[285] Y. Sun, S. E. Thompson, and T. Nishida, "Physics of strain effects in semiconductors and metal-oxide-semiconductor field-effect transistors," *J. Appl. Phys.*, vol. 101, no. 10, 2007, doi: 10.1063/1.2730561.

[286] Y. Sun, S. E. Thompson, and T. Nishida, *Strain Effect in Semiconductors: Theory and Device Applications*. Boston, MA: Springer US, 2010.

[287] N. B. Ekreem, A. G. Olabi, T. Prescott, A. Rafferty, and M. S. J. Hashmi, "An overview of magnetostriction, its use and methods to measure these properties," *J. Mater. Process. Technol.*, vol. 191, no. 1–3, pp. 96–101, Aug. 2007, doi: 10.1016/j.jmatprotec.2007.03.064.

[288] A. S. Fiorillo, C. D. Critello, and S. A. Pullano, "Theory, technology and applications of piezoresistive sensors: A review," *Sensors Actuators A Phys.*, vol. 281, pp. 156–175, Oct. 2018, doi: 10.1016/j.sna.2018.07.006.

[289] A. A. Barlian, W.-T. Park, J. R. Mallon, A. J. Rastegar, and B. L. Pruitt, “Review: Semiconductor Piezoresistance for Microsystems,” *Proc. IEEE*, vol. 97, no. 3, pp. 513–552, Mar. 2009, doi: 10.1109/JPROC.2009.2013612.

[290] A. Priydarshi, Y. S. Chauhan, S. Bhowmick, and A. Agarwal, “Strain-tunable charge carrier mobility of atomically thin phosphorus allotropes,” *Phys. Rev. B*, vol. 97, no. 11, p. 115434, Mar. 2018, doi: 10.1103/PhysRevB.97.115434.

[291] M. S. Hossain, R. Islam, M. Shahjahan, and K. A. Khan, “Studies on the thermoelectric effect in semiconducting ZnTe thin films,” *J. Mater. Sci. Mater. Electron.*, vol. 19, no. 11, pp. 1114–1121, Nov. 2008, doi: 10.1007/s10854-007-9483-2.

[292] R. R. Heikes and R. W. Ure, *Thermoelectricity: Science and Engineering*. New York, USA: Interscience Publishers, 1961.

[293] I. Sinnarasa, Y. Thimont, L. Presmanes, C. Bonningue, A. Barnabé, and P. Tailhades, “Influence of thickness and microstructure on thermoelectric properties of Mg-doped CuCrO 2 delafossite thin films deposited by RF-magnetron sputtering,” *Appl. Surf. Sci.*, vol. 455, pp. 244–250, 2018, doi: 10.1016/j.apsusc.2018.05.104.

[294] T. S. Tripathi and M. Karppinen, “Structural Optical and Electrical Transport Properties of ALD-Fabricated CuCrO2 Films,” *Phys. Procedia*, vol. 75, pp. 488–494, 2015, doi: 10.1016/j.phpro.2015.12.061.

[295] C. Wood and D. Emin, “Conduction mechanism in boron carbide,” *Phys. Rev. B*, vol. 29, no. 8, pp. 4582–4587, Apr. 1984, doi: 10.1103/PhysRevB.29.4582.

[296] H. Qiu *et al.*, “Hopping transport through defect-induced localized states in molybdenum disulphide,” *Nat. Commun.*, vol. 4, no. 1, p. 2642, Oct. 2013, doi: 10.1038/ncomms3642.

[297] G. C. Tewari, T. S. Tripathi, H. Yamauchi, and M. Karppinen, “Thermoelectric properties of layered antiferromagnetic CuCrSe2,” *Mater. Chem. Phys.*, vol. 145, no. 1–2, pp. 156–161, May 2014, doi: 10.1016/j.matchemphys.2014.01.053.

[298] K. Choy, “Chemical vapour deposition of coatings,” *Prog. Mater. Sci.*, vol. 48, no. 2, pp. 57–170, 2003, doi: 10.1016/S0079-6425(01)00009-3.

[299] S. Mahapatra and S. A. Shivashankar, “Low-pressure metal-organic CVD of transparent and p-type conducting CuCrO2 thin films with high conductivity,” *Chem. Vap. Depos.*, vol. 9, no. 5, pp. 238–240, 2003, doi: 10.1002/cvde.200304147.

[300] H. Wen *et al.*, “Advancements in Transparent Conductive Oxides for Photoelectrochemical Applications,” *Nanomaterials*, vol. 14, no. 7, p. 591, Mar. 2024, doi: 10.3390/nano14070591.

[301] J. L. Yang, S. J. An, W. Il Park, G. C. Yi, and W. Choi, “Photocatalysis using ZnO thin films and nanoneedles grown by metal-organic chemical vapor deposition,” *Adv. Mater.*, vol. 16, no. 18, pp. 1661–1664, 2004, doi: 10.1002/adma.200306673.

[302] A. M. B. van Mol, Y. Chae, A. H. McDaniel, and M. D. Allendorf, “Chemical vapor deposition of tin oxide: Fundamentals and applications,” *Thin Solid Films*, vol. 502, no. 1–2, pp. 72–78, Apr. 2006, doi: 10.1016/j.tsf.2005.07.247.

[303] J. P. Sénateur *et al.*, “Synthesis and characterisation of YBCO thin films grown by injection-MOCVD,” *J. Alloys Compd.*, vol. 251, no. 1–2, pp. 288–291, Apr. 1997, doi: 10.1016/S0925-8388(96)02699-0.

[304] M. Moreira *et al.*, “Electrical properties of strained off-stoichiometric Cu–Cr–O delafossite thin films,” *J. Phys. Condens. Matter*, vol. 36, no. 21, p. 215702, May 2024, doi: 10.1088/1361-

648X/ad2a07.

[305] P. Lunca-Popa, J. Afonso, P. Grysan, J. Crêpellière, R. Leturcq, and D. Lenoble, “Tuning the electrical properties of the p-type transparent conducting oxide Cu1-xCr1+xO2 by controlled annealing,” *Sci. Rep.*, vol. 8, no. 1, pp. 1–8, 2018, doi: 10.1038/s41598-018-25659-3.

[306] A. Barnabe *et al.*, “P-Type conducting transparent characteristics of delafossite Mg-doped CuCrO2 thin films prepared by RF-sputtering,” *J. Mater. Chem. C*, vol. 3, no. 23, pp. 6012–6024, 2015, doi: 10.1039/c5tc01070e.

[307] G. Haugstad, *Atomic Force Microscopy: Understanding Basic Modes and Advanced Applications*. John Wiley & Sons, 2012.

[308] H. Bluhm, “X-ray photoelectron spectroscopy (XPS) for in situ characterization of thin film growth,” in *In Situ Characterization of Thin Film Growth*, Elsevier, 2011, pp. 75–98.

[309] D. B. Williams and C. B. Carter, *Transmission Electron Microscopy*. Boston, MA: Springer US, 2009.

[310] L. Reimer, *Transmission Electron Microscopy*, vol. 36. Berlin, Heidelberg: Springer Berlin Heidelberg, 1997.

[311] K. Torigoe, “Electron Microscopy Observation of Solid Particles,” in *Measurement Techniques and Practices of Colloid and Interface Phenomena*, Singapore: Springer Singapore, 2019, pp. 111–118.

[312] K. Fleischer, E. Norton, D. Mullarkey, D. Caffrey, and I. V. Shvets, “Quantifying the performance of P-type transparent conducting oxides by experimental methods,” *Materials (Basel).*, vol. 10, no. 9, pp. 19–22, 2017, doi: 10.3390/ma10091019.

[313] J. Tauc, “Optical properties and electronic structure of amorphous Ge and Si,” *Mater. Res. Bull.*, vol. 3, no. 1, pp. 37–46, Jan. 1968, doi: 10.1016/0025-5408(68)90023-8.

[314] M. A. Moram and M. E. Vickers, “X-ray diffraction of III-nitrides,” *Reports Prog. Phys.*, vol. 72, no. 3, p. 036502, Mar. 2009, doi: 10.1088/0034-4885/72/3/036502.

[315] M. Birkholz, *Thin Film Analysis by X-ray Scattering*. Weinheim, Germany: Wiley-VCH, 2006.

[316] I. C. Noyan and J. B. Cohen, *Residual Stress*. New York, NY: Springer New York, 1987.

[317] A. J. Bosman and H. J. van Daal, “Small-polaron versus band conduction in some transition-metal oxides,” *Adv. Phys.*, vol. 19, no. 77, pp. 1–117, 1970, doi: 10.1080/00018737000101071.

[318] F. A. Benko and F. P. Koffyberg, “The optical bandgap and band-edge positions of semiconducting p -type CuYO 2,” *Can. J. Phys.*, vol. 63, no. 10, pp. 1306–1308, Oct. 1985, doi: 10.1139/p85-215.

[319] F. Werner, “Hall measurements on low-mobility thin films,” *J. Appl. Phys.*, vol. 122, no. 13, p. 135306, Oct. 2017, doi: 10.1063/1.4990470.

[320] “Linseis Messgeraete GmbH.” https://www.linseis.com/en/products/thermoelectric/lsr-3/#description.

[321] X. Liang *et al.*, “A Review of Thin-Film Magnetoelastic Materials for Magnetoelectric Applications,” *Sensors*, vol. 20, no. 5, p. 1532, Mar. 2020, doi: 10.3390/s20051532.

[322] K. Seeger, *Semiconductor Physics: An Introduction*, 9th ed. Berlin, Heidelberg, Germany: Springer, 2004.

[323] D. Van Hoang *et al.*, “Fine-tuning high electrical conductivity of Mg-Doped CuCrO2 delafossite thin films through preferred-(110) orientation and film thickness control,” *Phys. B Condens. Matter*, vol. 667, no. July, p. 415185, Oct. 2023, doi: 10.1016/j.physb.2023.415185.

[324] W. C. Young and R. G. Budynas, *Roark’s formulas for stress and strain*, 7th ed. McGraw Hill, USA, 2002.

[325] R. G. Munro, “Evaluated material properties for a sintered α-alumina,” *J. Am. Ceram. Soc.*, vol. 80, no. 8, pp. 1919–1928, 1997, doi: 10.1111/j.1151-2916.1997.tb03074.x.

[326] B. M. Patil, G. C. Wadhawa, A. C. Chaskar, and P. S. Walke, “Low temperature synthesis and thermal expansion study of nanocrystalline CaTiO3,” *Mater. Lett.*, vol. 333, no. December 2022, p. 133627, Feb. 2023, doi: 10.1016/j.matlet.2022.133627.

[327] G. Abadias *et al.*, “Review Article: Stress in thin films and coatings: Current status, challenges, and prospects,” *J. Vac. Sci. Technol. A Vacuum, Surfaces, Film.*, vol. 36, no. 2, p. 020801, Mar. 2018, doi: 10.1116/1.5011790.

[328] Y. Lee, H. W. Jeong, S. H. Kim, K. Yang, and M. H. Park, “Effect of stress on fluorite-structured ferroelectric thin films for semiconductor devices,” *Mater. Sci. Semicond. Process.*, vol. 160, no. February, p. 107411, 2023, doi: 10.1016/j.mssp.2023.107411.

[329] K. Barmak and K. Coffey, *Metallic films for electronic, optical and magnetic applications*, 1st ed. Woodhead Publishing Limited: 80 High Street, Sawston, Cambridge CB22 3HJ, UK, 2014.

[330] J. O. Carneiro, V. Teixeira, and S. Azevedo, *Residual stresses in thin films evaluated by different experimental techniques*. Encyclopedia of Thermal Stresses. Dordrecht, Netherlands: Springer (2014): 4222-4231., 2014.

[331] H. Oettel and R. Wiedemann, “Residual stresses in PVD hard coatings,” *Surf. Coatings Technol.*, vol. 76–77, pp. 265–273, 1995, doi: 10.1016/0257-8972(95)02581-2.

[332] T. Schenk *et al.*, “On the Origin of the Large Remanent Polarization in La:HfO 2,” *Adv. Electron. Mater.*, vol. 5, no. 12, p. 1900303, Dec. 2019, doi: 10.1002/aelm.201900303.

[333] N. Pauly, S. Tougaard, and F. Yubero, “Determination of the Cu 2p primary excitation spectra for Cu, Cu2O and CuO,” *Surf. Sci.*, vol. 620, pp. 17–22, Feb. 2014, doi: 10.1016/j.susc.2013.10.009.

[334] C. D. Wagner, W. M. Riggis, L. E. Davis, J. F. Moulder, and G. E. Mulenberg, *Handbook of X-Ray Photoelectron Spectroscopy*. Eden Prairie, Minnesota, USA: Perkin-Elmer Corporation, 1979.

[335] M. C. Biesinger, “Advanced analysis of copper X-ray photoelectron spectra,” *Surf. Interface Anal.*, vol. 49, no. 13, pp. 1325–1334, Dec. 2017, doi: 10.1002/sia.6239.

[336] L. De Los Santos Valladares *et al.*, “Crystallization and electrical resistivity of Cu2O and CuO obtained by thermal oxidation of Cu thin films on SiO2/Si substrates,” *Thin Solid Films*, vol. 520, no. 20, pp. 6368–6374, Aug. 2012, doi: 10.1016/j.tsf.2012.06.043.

[337] R. Korlacki *et al.*, “Strain and stress relationships for optical phonon modes in monoclinic crystals with β-Ga2O3 as an example,” *Phys. Rev. B*, vol. 102, no. 18, p. 180101, Nov. 2020, doi: 10.1103/PhysRevB.102.180101.

[338] R. Hanus *et al.*, “Lattice Softening Significantly Reduces Thermal Conductivity and Leads to High Thermoelectric Efficiency,” *Adv. Mater.*, vol. 31, no. 21, pp. 1–10, May 2019, doi: 10.1002/adma.201900108.

[339] X. Jin *et al.*, “Strain-driven phonon topological phase transition impedes thermal transport in

titanium monoxide," *Cell Reports Phys. Sci.*, vol. 5, no. 4, p. 101895, Apr. 2024, doi: 10.1016/j.xcrp.2024.101895.

[340] W. Shan *et al.*, "Pressure-dependent photoluminescence study of ZnO nanowires," *Appl. Phys. Lett.*, vol. 86, no. 15, pp. 1–3, Apr. 2005, doi: 10.1063/1.1901827.

[341] P. G. Moses, A. Janotti, C. Franchini, G. Kresse, and C. G. Van de Walle, "Donor defects and small polarons on the TiO2(110) surface," *J. Appl. Phys.*, vol. 119, no. 18, May 2016, doi: 10.1063/1.4948239.

[342] K. G. Saw, N. M. Aznan, F. K. Yam, S. S. Ng, and S. Y. Pung, "New insights on the burstein-moss shift and band gap narrowing in indium-doped zinc oxide thin films," *PLoS One*, vol. 10, no. 10, pp. 1–17, 2015, doi: 10.1371/journal.pone.0141180.

[343] B. Yu *et al.*, "Ultrafast dynamics of photoexcited carriers in perovskite semiconductor nanocrystals," *Nanophotonics*, vol. 10, no. 8, pp. 1943–1965, Jun. 2021, doi: 10.1515/nanoph-2020-0681.

[344] H. Kalt and M. Rinker, "Band-gap renormalization in semiconductors with multiple inequivalent valleys," *Phys. Rev. B*, vol. 45, no. 3, pp. 1139–1154, Jan. 1992, doi: 10.1103/PhysRevB.45.1139.

[345] J. Zhang *et al.*, "Direct determination of band-gap renormalization in degenerately doped ultrawide band gap β-Ga2O3 semiconductor," *Phys. Rev. B*, vol. 106, no. 20, p. 205305, Nov. 2022, doi: 10.1103/PhysRevB.106.205305.

[346] Z. M. Gibbs, A. LaLonde, and G. J. Snyder, "Optical band gap and the Burstein–Moss effect in iodine doped PbTe using diffuse reflectance infrared Fourier transform spectroscopy," *New J. Phys.*, vol. 15, no. 7, p. 075020, Jul. 2013, doi: 10.1088/1367-2630/15/7/075020.

[347] Mi-Ra Kim, Cheol-Hoi Kim, and Baik-Hyung Han, "Band-gap renormalization and strain effects in semiconductor quantum wells," *Phys. B Condens. Matter*, vol. 245, no. 1, pp. 45–51, Jan. 1998, doi: 10.1016/S0921-4526(97)00450-X.

[348] L. Zeng *et al.*, "Correlation between Electrical Transport and Nanoscale Strain in InAs/In0.6Ga0.4As Core-Shell Nanowires," *Nano Lett.*, vol. 18, no. 8, pp. 4949–4956, 2018, doi: 10.1021/acs.nanolett.8b01782.

[349] J. J. Wortman, "Effect of mechanical strain on p-n junctions," Washington, D. C., USA, 1965.

[350] W. Jia-Xin, L. Gui-Li, W. Lin, J. Gan, and Z. Guo-Ying, "Effect of tensile and compressive strains on the electronic structure of O-atom-doped monolayer MoS2," *Int. J. Mod. Phys. B*, no. 2550012, 2024.

[351] Y. Li *et al.*, "Ultrasensitive tunability of the direct bandgap of 2D InSe flakes via strain engineering," *2D Mater.*, vol. 5, no. 2, p. 021002, Jan. 2018, doi: 10.1088/2053-1583/aaa6eb.

[352] B. Mondal and R. Tonner-Zech, "Systematic strain-induced bandgap tuning in binary III–V semiconductors from density functional theory," *Phys. Scr.*, vol. 98, no. 6, p. 065924, Jun. 2023, doi: 10.1088/1402-4896/acd08b.

[353] J. Pető *et al.*, "Moderate strain induced indirect bandgap and conduction electrons in MoS2 single layers," *npj 2D Mater. Appl.*, vol. 3, no. 1, p. 39, Oct. 2019, doi: 10.1038/s41699-019-0123-5.

[354] A. C. Rastogi, S. H. Lim, and S. B. Desu, "Structure and optoelectronic properties of spray deposited Mg doped p-CuCrO2 semiconductor oxide thin films," *J. Appl. Phys.*, vol. 104, no. 2, 2008, doi: 10.1063/1.2957056.